NUREG/CR-6929
PNNL-16253

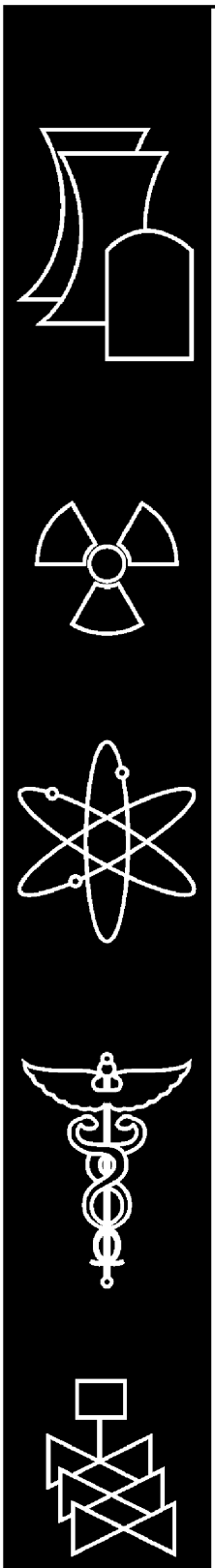

Assessment of Eddy Current Testing for the Detection of Cracks in Cast Stainless Steel Reactor Piping Components

Pacific Northwest National Laboratory

U.S. Nuclear Regulatory Commission
Office of Nuclear Regulatory Research
Washington, DC 20555-0001

NUREG/CR-6929
PNNL-16253

Assessment of Eddy Current Testing for the Detection of Cracks in Cast Stainless Steel Reactor Piping Components

Manuscript Completed: November 2006
Date Published: February 2007

Prepared by
A.A. Diaz, R.A. Mathews,
J. Hixon[1], S.R. Doctor

Pacific Northwest National Laboratory
Richland, WA 99352

D.A. Jackson and W.E. Norris, NRC Project Managers

Prepared for
Division of Fuel, Engineering and Radiological Research
Office of Nuclear Regulatory Research
U.S. Nuclear Regulatory Commission
Washington, DC 20555-0001
NRC Job Code Y6604

[1]Visiting Intern - U.S. Nuclear Regulatory Commission
Division of Fuel, Engineering and Radiological Research
Office of Nuclear Regulatory Research
Washington, DC 20555-0001

Abstract

Studies conducted at the Pacific Northwest National Laboratory (PNNL) in Richland, Washington, have focused on assessing the effectiveness and reliability of novel approaches to nondestructive examination (NDE) for inspecting coarse-grained, cast stainless steel reactor components. The primary objective of this work is to provide information to the U.S. Nuclear Regulatory Commission (NRC) on the utility, effectiveness, and reliability of advanced NDE methods as related to the inservice inspection of primary piping components in pressurized water reactors. This report describes progress, recent developments, and results from the assessment of eddy current testing (ET) for detection of surface-breaking cracks in cast stainless steel (CSS) reactor piping components from the inside surface of the pipe wall.

In assessing the ET inspection technique, PNNL used a range of specimens from four different sources:

- cast stainless steel pipe segments with thermal and mechanical fatigue cracks (Westinghouse Owners Group)
- specimens containing thermal fatigue cracks (PNNL)
- a blank spool piece from a Spanish nuclear plant (loaned by the Electric Power Research Institute NDE Center)
- three smaller segments of highly coarse-grained blank spool pieces (Southwest Research Institute)
- a blank spool piece of vintage cast stainless steel on loan from Westinghouse
- a blank spool piece of vintage cast stainless steel on loan from IHI Southwest Technologies Inc.

Eddy current studies were conducted on the inner-diameter surface of piping using a Zetec MIZ-27SI eddy current instrument and a Zetec C Z0000857-1 plus-point spot probe with an operating frequency of 250 kHz. To reduce noise effects, a subset of the CSS specimens was degaussed, resulting in noticeable improvements. In this report, results from laboratory studies for assessing detection, localization, and length sizing effectiveness are provided, and issues and anticipated future work are discussed.

Foreword

Cast stainless steel (CSS) material was used extensively in the primary pressure boundary of pressurized water reactors (PWRs) due to its relatively low cost and resistance to corrosion. The American Society of Mechanical Engineers (ASME) Boiler and Pressure Vessel (BPV) Code requires periodic inservice inspection (ISI) of welds in the primary pressure boundary. Because of background radiation and access limitations, inspection personnel use ultrasonic testing (UT) techniques rather than radiography to inspect these welds. In most applications, UT can reliably detect and accurately size flaws that may occur during service. This is not the case for CSS material.

The coarse-grained and anisotropic microstructure of CSS material makes it difficult to inspect CSS components such as statically cast elbows, statically cast pump bowls, and centrifugally cast stainless steel piping. Similar inspection problems exist for dissimilar metal welds and weld-overlay-repaired pipe joints. The large grain sizes of these materials strongly affect the propagation of ultrasound by causing severe attenuation, change in velocity, and scattering of ultrasonic energy. Thus, the signal patterns originating from flaws can be difficult to distinguish from scatter. In addition, the result of redirection of the sound beam may be that some portions of the material are not examined.

Based on operating history, the unreliability of volumetric examination of CSS material, and the occupational dose incurred by inspection personnel while performing these inspections, industry representatives proposed removing the BPV Code requirement to inspect CSS piping welds. The U.S. Nuclear Regulatory Commission (NRC) did not support the proposal as these welds are in safety-related systems. In addition, there are safety-related component welds that can only be examined from the CSS material side because of geometry limitations. Finally, CSS materials can be susceptible to thermal fatigue under certain conditions. While thermal fatigue issues have, to date, occurred infrequently at operating plants, more frequent occurrences cannot be discounted as plants continue to age. Thus, the NRC requested that the ASME table the proposal to allow time for further study. The staff searched the literature and inquired at national and international research organizations but discovered no active research programs. The staff then initiated a study at Pacific Northwest National Laboratory (PNNL) to research the feasibility of an effective and reliable inspection technique.

Inspection personnel typically employ volumetric UT methods from the outside-surface (OD) of piping components where they have ready access. However, these OD inspection methods have not been demonstrated to be reliable for coarse-grained materials such as CSS. Inspection personnel have successfully employed inside-surface (ID) eddy-current test (ET) protocols in certain nuclear applications. A direct-contact method that is sensitive to surface-breaking cracks likely has an inherently higher probability of successful detection than an OD inspection method. PNNL thus evaluated the applicability and effectiveness of an ID inspection technique. PNNL (1) studied advanced eddy-current probe configurations that provide sensitivity to both axially and circumferentially oriented, near-surface flaws and (2) investigated the reliability and effectiveness of an ID inspection technique. The studied specimens contained cracks created by methods proven to produce realistic, surface-connected mechanical and thermal fatigue cracks.

This report provides a firm engineering basis for evaluating the feasibility of performing more reliable inspection of CSS material. An eddy-current method is described—as verified by the PNNL study—which is very effective at detecting surface-breaking cracks when the ID is accessible. This report also describes a number of implementation details that must be resolved before this method can be employed for ISI.

A feasible and effective inspection method for CSS material has been identified. This material is located in safety-related systems. The NRC will present the results of this study to the cognizant ASME committees as technical justification for initiating the efforts necessary to add ET to the arsenal of nondestructive examination tools to effectively examine CSS material.

Brian W. Sheron, Director
Office of Nuclear Regulatory Research
U.S. Nuclear Regulatory Commission

Contents

Figures

Tables

Executive Summary

Research is under way at the Pacific Northwest National Laboratory (PNNL) to determine the effectiveness and reliability of advanced nondestructive examination (NDE) techniques on light water reactor components containing cast stainless steel (CSS) material and other coarse-grained components that encompass dissimilar metal welds, piping with corrosion-resistant cladding, and far-side examinations of austenitic piping welds. The specific objective of this work is to evaluate and enhance various NDE methods to directly improve our ability to detect, localize, and, if possible, size cracks in coarse-grained steel components.

This report provides a synopsis of laboratory investigations at PNNL to evaluate the effectiveness and determine the capabilities of eddy current testing (ET) as applied to the inspection of CSS welds in nuclear reactor piping. Progress, recent developments, and results from the assessment of ET for detection of surface-breaking cracks in CSS reactor piping components from the inside surface of the pipe wall are described.

The work described here includes a study of the use of advanced eddy current probe configurations that provide sensitivity to both axial and circumferentially oriented flaws and an investigation of the reliability and effectiveness of an inside-surface inspection technique in which direct contact with the surface from which flaws emanate, enhances the probability of detection.

The component specimens used in this study do not represent worst-case field conditions with regard to weld root conditions, counterbore facets, surface roughness, or mismatch, but provide a wide range of grain structure conditions. The set of PNNL specimens has inner diameter (ID) conditions that may be considered optimal, as the inside surfaces and root conditions have been ground smooth while the counterbore facets are shallow and do not hinder inspections to any great degree. With regard to the Westinghouse Owners Group (WOG) specimens, these ID conditions are considered to be of intermediate difficulty regarding the impact of the ID surface geometry on the inspection process. These specimens were fabricated from a diverse array of materials that include stainless steel cladding, Inconel buttering, forged stainless steel and Inconel welds, statically cast and centrifugally cast stainless steel (CCSS), wrought austenitic stainless steel, carbon steel, and more. Other specimens exhibiting very coarse-grained and multibanded macrostructures (such as those on loan from IHI Southwest Technologies Inc.) are considered to represent material used in the earliest nuclear power plants that were constructed, probably providing the worst-case grain structure conditions.

Magnitude and phase responses were plotted using ID surface ET techniques to generate topographical C-scan (x-y) representations of the data for enhanced visualization. For analysis of the ET data, loss of signal was used for length sizing the indications. From this analysis, all 19 specimens that contained surface-breaking cracks on the inside surface were detected by this inspection methodology.

With regard to length sizing, 16 of the 19 specimens containing flaws were slightly undersized, and the associated length root-mean-square error (RMSE) was 7.7 mm (0.30 in.). As the ASME Code requires the length sizing RMSE to be less than 19 mm (0.75 in.), the ET data provided here are well under half of this value. Three flaws were oversized, and the largest length difference was oversized by 3.0 mm (0.12 in.). Noise signals that would be confused with crack signals having high amplitude and correct

phase, and of substantial length, shape, and continuity to be called a crack, were not prevalent in the data. No false calls were made in this study.

Sparsely scattered anomalous but dimensionally small high-amplitude responses (on the order of 2 mm (0.08 in.) to 10 mm (0.4 in.) in diameter or length dimension) were observed on approximately 20% of the specimens. These high-amplitude responses that typically occur only in the magnitude representation appear to be random occurrences of noise, clutter, grain effects, permeability effects, or other probe translational factors and would not be considered sufficiently continuous to have any structure or to be called a crack, based upon the general criteria used for detection in this study. These criteria include relying primarily on the magnitude responses for detection of initial hot spots and then looking to the phase response plots for possible validation. The surrounding pattern of clutter and background noise also must be considered in visually discriminating between anomalous amplitude responses and those responses that are clustered and show some shape and consistent continuity. Finally, the associated length or extent also is considered, where typical responses 10 mm (0.4 in.) and smaller in length are considered noncrack responses unless detected in proximity to other amplitude responses of similar intensity or where a pattern starts to develop.

In reviewing the composite noise data, researchers derived no correlation between background noise levels (ET magnitude or phase response) and the variables of microstructural classification (i.e., columnar, equiaxed, mixed/banded), grain size, orientation, or casting method (static or centrifugal). The only significant measured differences in background noise levels occurred when comparing the background noise to the clutter resulting from isotropic, homogeneous, fine-grained materials like forged stainless steel and carbon steel or clad carbon steel. These materials (in contrast to the cast steels) exhibited significantly lower levels of background noise and clutter, on the order of 10 dB to 15 dB less than their statically or centrifugally cast counterparts.

Demagnetizing the inspection zones proved useful in 8 out of 19 cases (42% of the time) where the degaussing process resulted in a quantifiably higher signal-to-noise ratio (SNR). It is unclear why this process improves the magnitude response from the flaws and reduces background noise and surrounding clutter in nearly half of the specimens but fails to show any improvement in the other half.

Overall, the ET methodology was very effective with regard to detection performance in that all of the cracks were detected, and both magnitude and phase response images often were useful in detecting the cracks. As with all NDE inspections, advances in probe design eventually lead to improved detection performance; off-angle sensitivity issues play a key role in defining the detection performance for ET as a function of crack orientation and directionality. It is evident from this study that even by employing a plus-point probe for enhanced dual-axis sensitivity, one must consider a multiple scan protocol where the probe is rotated incrementally as a function of angle, to provide suitable sensitivity for detection of cracking across the full spectrum of angles. Slight variations in background noise were evident as a function of probe rotation relative to the orientation of the grain distribution/microstructure, but these variations were not significant. The data here do not indicate that probe orientation will significantly affect background noise levels as microstructures and grain size/distribution varies, but there is direct evidence from this work that shows increased sensitivity to off-angle flaws by reorienting the probe by 45º. Probe decoupling was evident on a few data sets, requiring subsequent re-scanning of these areas.

The need to employ smaller, highly sensitive ET probes that allow for more effective coupling at the counterbore transitions is key to addressing field ID conditions not represented in this study.

In summary, if the inner surface is accessible, the ET method demonstrated here is very effective for detection of these types of surface-breaking cracks. The cracks in the specimens studied were created using methods that have proven useful in producing realistic surface-connected mechanical and thermal fatigue cracks. These flaws are considered to be planar cracks, parallel to the weld centerline, perpendicularly oriented to and connected with the ID surface. Some transverse cracking and off-axis branching are also evident with some of these cracks. It should be noted that this technique provided valuable detection and length sizing capabilities but will not provide depth sizing information. The crack identification criteria employed in this study essentially eliminated all responses less than 12.5 mm (0.50 in.) from consideration as a crack, and as such, no false calls were reported from these data. Both magnitude and phase response information provided value in detecting cracks in these materials, while demagnetization enhanced the overall SNR of approximately 42% of the specimens.

Acknowledgments

The work reported here was sponsored by the U.S. Nuclear Regulatory Commission (NRC) and conducted under NRC Job Code Number Y6604. During the period of this work, two NRC program managers led the effort and provided valuable guidance and technical direction. The Pacific Northwest National Laboratory (PNNL) acknowledges both Ms. Deborah Jackson and Mr. Wallace Norris for their contributions. The authors are very grateful to have had the opportunity to host Mr. Jeff Hixon during the conduct of work reported here. Mr. Hixon was participating in an NRC rotating internship program and was assigned to support ongoing NRC work in the NDE field at PNNL. During this period, Mr. Hixon was a key contributor to every phase of the work reported here and was influential in guiding the technical aspects of data acquisition and analysis.

The authors express their sincere gratitude to the staff at the Electric Power Research Institute NDE Center in Charlotte, North Carolina, for their support through loaned cast stainless steel (CSS) specimens and their flexibility in allowing PNNL to extract a specimen of the Spanish spool piece for subsequent polishing and chemical etching. Also we wish to acknowledge Southwest Research Institute, IHI Southwest Technologies Inc., and Westinghouse Electric Company for providing CSS specimens to PNNL for ongoing research in this area. Southwest Research Institute provided sectioned segments of larger Centrifugally Cast Stainless Steel spool pieces to PNNL many years ago, prior to the existence of IHI Southwest Technologies Inc. Both organizations have provided specimens over the years, and PNNL is very appreciative of their ongoing support.

At PNNL, the authors wish to thank Mr. George Schuster for his technical contributions and support of data acquisition and analysis activities, Dr. Robert Harris for providing plus-point probe sensitivity data, Dr. Ronald Hockey (now at Applied Research Associates Inc., in Albuquerque, New Mexico) for supporting the data analysis, and Mrs. Earlene Prickett for her support in finalizing this document. The authors also acknowledge Lila Andor and Mike Parker for preparing the final manuscript and Andrea Currie for editing. PNNL is operated by Battelle for the U.S. Department of Energy under Contract DE-AC05-76RL01830.

Abbreviations and Acronyms

AC	alternating current
ASME	American Society of Mechanical Engineers
ASTM	American Society for Testing and Materials
CCSS	centrifugally cast stainless steel
CS	carbon steel
CSS	cast stainless steel
dB	decibel
EDM	electrical discharge machining
EPRI	Electric Power Research Institute
ET	electromagnetic testing (eddy current testing)
Hz	hertz
ID	inner diameter or inside diameter
ISI	inservice inspection
kHz	kilohertz
LWR	light water reactor
NDE	nondestructive examination or nondestructive evaluation
NRC	U.S. Nuclear Regulatory Commission
OD	outer diameter or outside diameter
PIRR	piping inspection round robin
PISC	Program for Inspection of Steel Components
PNNL	Pacific Northwest National Laboratory
POD	probability of detection
PWR	pressurized water reactor
RMSE	root-mean-square error
SCSS	statically cast stainless steel
SNR	signal-to-noise ratio
SS	stainless steel
UT	ultrasonic testing
V	volts

VT	visual testing
WOG	Westinghouse Owners Group

1 Introduction

Since 1977, Pacific Northwest National Laboratory (PNNL) has conducted research in support of U.S. Nuclear Regulatory Commission (NRC) guidance to evaluate state-of-the-art technical approaches for inspecting coarse-grained reactor components. This work recently has focused on assessing the viability of both ultrasonic nondestructive examination (NDE) methods from the outside pipe surface and eddy current methods as implemented from the inside surface of the components. Regarding ultrasonic methods, PNNL's strategy has been to evaluate low-frequency (500 kHz to 1 MHz) phased-array methods and an ultrasonic technique that uses a zone-focused, multi-incident angle, low-frequency (250 to 450 kHz) inspection protocol coupled with the synthetic aperture focusing technique (SAFT). These approaches were employed to assess the viability in using long-wavelength (low-frequency) outside-surface inspection techniques that are inherently less sensitive to the effects of the coarse-grained microstructure. More recently, PNNL has studied an alternate approach that essentially eliminates the attenuation and scattering effects of long path-length propagation in these coarse-grained metals. The approach involves applying an NDE method along the inside surface of these components, where detection sensitivity to surface-breaking cracks is not compromised. Thus, PNNL has focused efforts on assessing an eddy current (ET) technique for the direct detection of cracks originating on the inside surface of reactor components.

The objective of this research is to determine the effectiveness and reliability of advanced NDE methods on light water reactor (LWR) components containing cast stainless steel (CSS) material and other coarse-grained components that encompass dissimilar metal welds, piping with corrosion-resistant cladding, and far-side examinations of austenitic piping welds. The specific goal of this work is to enhance various NDE methods to directly improve our ability to detect, localize, and, if possible, size cracks in coarse-grained steel components.

This report provides a synopsis of the laboratory investigations at PNNL to evaluate the effectiveness and determine capabilities of ET as applied to the inspection of CSS welds in nuclear reactor piping. Progress, recent developments, and results from the assessment of ET for the detection of surface-breaking cracks in CSS reactor piping components from the inside surface of the pipe wall are described.

The purpose of inservice inspection (ISI) of nuclear reactor piping and related components is to reliably detect, localize, and accurately size material defects before they challenge the structural integrity of the component. Before defects can be sized, they must first be detected. For many years, engineering studies and research activities were focused primarily on developing and enhancing NDE methods employed from the outside surface of the ferritic and austenitic piping components where access is readily obtained (Diaz et al. 1998; Doctor et al. 2005). However, outside surface ISI examination has proven to be less effective and unreliable on coarse-grained, anisotropic, and inhomogeneous materials such as CSS (Taylor 1984; Diaz et al. 1998; Doctor et al. 2005) Most difficulties in testing CSS components come from the compound effects of coarse grains and their distribution patterns. The problem becomes one of effective discrimination between coherent energy scattered from these coarse grains or weldment structure and the coherent energy scattered from existing cracks. Even advanced, state-of-the-art NDE approaches such as low-frequency ultrasonic methods and phased-array methodologies are limited with

regard to detection probability for cracks on the order of 1.27 cm (0.5 in.) in depth and smaller (Diaz et al. 1998; Doctor et al. 2005).

PNNL evaluated the applicability and effectiveness of an inside-surface inspection technique based upon the premise that if access to the inner-diameter (ID) surface were readily available, a direct contact methodology that is sensitive to surface-breaking cracks would have an inherently higher probability of success for detection than conducting inspections from the outer diameter (OD). In support of this hypothesis, ID eddy current test protocols had been employed successfully in Sweden in blind test qualifications and on primary piping nozzle-to-pipe welds at the V.C. Summer Nuclear Station in the United States (Rao et al. 2001). At V.C. Summer, there were some challenging ID geometry conditions that adversely affected the ultrasonic testing, but they were easily handled by the small footprint of the eddy current probe. The eddy current inspection results were validated by destructive testing, with all indications being confirmed to be cracks, with the exception of one indication that was caused by an iron-rich subsurface inclusion (Rao et al. 2001). PNNL employed a similar eddy current method for this study.

The underlying objectives of the work presented here are two-fold:

- to study the use of advanced eddy current probe configurations that provide sensitivity to both axial and circumferentially oriented, near-surface flaws

- to investigate the reliability and effectiveness of an inside-surface inspection technique, where direct contact is used on the surface from which the flaws emanate.

The work described here was performed to provide a firm engineering basis for evaluating the utility of this technical approach for the inspection of CSS components. Section 2 of this report describes the technical and physical aspects associated with CSS materials that define the inspection problem. Section 3 provides a description of the fundamentals of ET as they pertain to automated surface scanning of reactor components. Section 4 provides a discussion of the experimental approach employed in this work, and Section 5 describes the various CSS specimens used in these laboratory studies. Section 6 provides a discussion of the results of the eddy current data acquisition and analysis activities, while Section 7 provides a discussion and conclusions from the work presented here.

2 The Cast Stainless Steel Inspection Problem

The relatively low cost and corrosion resistance of CSS have resulted in extensive use of this material in the primary piping systems of Westinghouse-designed pressurized water reactors (PWRs). Inservice inspection requirements dictate that piping welds in the primary pressure boundary of LWRs be subjected to periodic volumetric examination based on the requirements of Section XI of the ASME Boiler and Pressure Vessel Code. The volumetric examination may be either radiographic or ultrasonic. For inservice examinations, background radiation and access limitations generally prevent the use of radiography. Hence, cast austenitic welds in primary piping loops of LWRs generally receive an ultrasonic ISI. The purpose of ultrasonic ISI of nuclear reactor piping and pressure vessels is the reliable detection and accurate sizing of degradation-induced flaws that may be occurring during service. Detection, the initial priority, is accomplished by analyzing ultrasonic echo waveforms from reflections. Due to the coarse microstructure of CSS material, many inspection problems exist and are common to structures such as statically cast elbows, statically cast pump bowls, centrifugally cast stainless steel (CCSS) piping, dissimilar metal welds (DMWS), and weld-overlay-repaired pipe joints. Far-side weld inspection of stainless steels is an inspection technique that also encounters these inspection problems because the ultrasonic field must pass through the coarse-grained, anisotropic weld material.

Because Westinghouse Electric Corporation manufactured and implemented CCSS piping in the primary reactor coolant loop network of 27 PWRs in the United States, there exists a need to develop effective and reliable inspection techniques for these components. Examination of CCSS materials is difficult to perform due to the coarse microstructure that characterizes these materials. The general microstructural classifications for CCSS are columnar, equiaxed, and a mixed and banded columnar-equiaxed condition, of which most field material is believed to be the latter. Figures 2.1 and 2.2 illustrate the general classes of microstructures and the diverse variations in grain orientations, mixing, and banding.

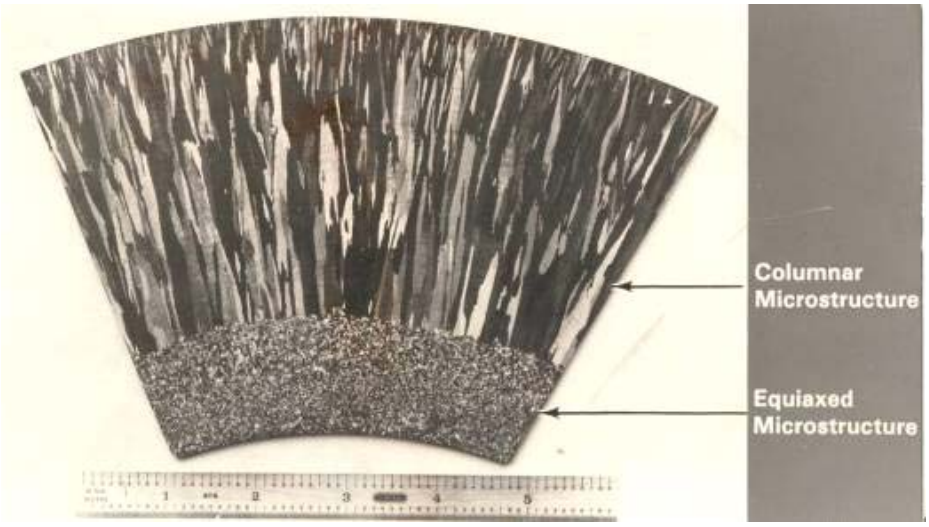

Figure 2.1 Specially Fabricated Specimen Illustrating Both Columnar (dendritic) and Equiaxed Microstructures in Centrifugally Cast Stainless Steel

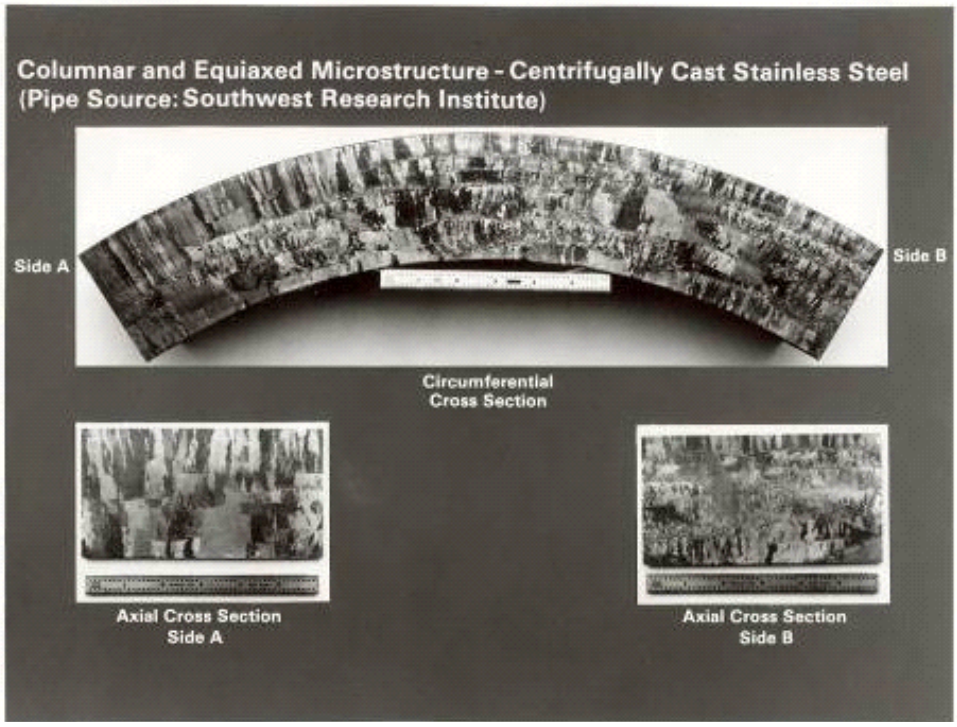

Figure 2.2 Circumferential and Axial Cross Sections of a Centrifugally Cast Stainless Steel Pipe Section Provided by Southwest Research Institute

Centrifugally cast stainless steel is an anisotropic and inhomogeneous material. The manufacturing process can result in the formation of a long columnar (dendritic) grain structure (approximately normal to the surface), with grain growth oriented along the direction of heat dissipation, often several centimeters in length. During the cooling and solidification process, columnar, equiaxed (randomly speckled microstructure), or a mixed structure can result, depending on chemical content, control of the cooling, and other variables in the casting process. The OD and ID surfaces of the specimens used in this study were machined smooth to remove surface imperfections resulting from the casting process.

To lay the foundation for justifying the technical approach in this study, it is important to familiarize the reader with the inspection problems inherent to ultrasonic propagation. The large size of the anisotropic grains, relative to the acoustic pulse wavelength, strongly affects the propagation of ultrasound by causing severe attenuation, changes in velocity, and scattering of ultrasonic energy. Refraction and reflection of the sound beam occur at the grain boundaries, resulting in defects being incorrectly reported, specific volumes of material not being examined, or both. When coherent reflection and scattering of the sound beam occur at grain boundaries, ultrasonic indications occur that are difficult to distinguish from signals originating from flaws. When inspecting piping components from the outside surface, where the returning signal-to-noise background ratio (SNR) is relatively low, ultrasonic examination can be confusing, unpredictable, and unreliable (Taylor 1984).

In order to reduce the impact of the microstructure on the inspection technique, the work reported here focuses on bypassing energy propagation through long distances in the material by performing ID surface inspection, using ET to detect crack initiation sites. The eddy current technique is most effective by

providing a means for direct inspection at the surface where cracks initiate, essentially enhancing the probability of detection relative to OD or outer-surface inspection methods. It is not implied that CSS anisotropy and microstructural variations have no effect on the magnitude of the signal strength or phase angle shift as eddy current data is acquired. On the contrary, it is shown here that CSS material does indeed affect ET SNR. However, these effects do not appear to preclude crack detection altogether as they are apt to do with ultrasonic tests from the OD for smaller cracks (Diaz et al. 1998; Doctor et al. 2005). Of primary importance in ET of anisotropic CSS materials is the ferritic content and variations in grain size and orientation, which have an effect on the directionality of conductivity (Libby 1971).

3 The Eddy Current Testing Technique

Eddy current testing has gained worldwide acceptance over the past 50 years in the automotive, petrochemical, aviation, nuclear, and aerospace industries, including a diverse array of manufacturing, quality, and integrity assurance applications (Libby 1971; General Dynamics 1979; McMaster et al. 1986; Lamtenzan et al. 2000). In principle, a typical application is conducted when an eddy current probe (consisting of an electromagnetic coil or array of conductors) is placed in proximity to (or scanned over) the surface of a conductive material. An alternating current (AC) is applied to the coil, which produces a varying (AC) magnetic field. This varying magnetic field induces circulating currents (called eddy currents) in the material under test, as the material attempts to counter the coil's primary magnetic field. Eddy currents are closed loops of current that circulate in a plane perpendicular to the direction of magnetic flux, where their normal direction of propagation is parallel to the coil windings and parallel to the surface of the test material. These eddy currents, in turn, produce a secondary magnetic field that opposes (and interacts) with the coil's magnetic field, essentially changing the impedance of the test coil. When the coil is scanned over a discontinuity or surface-breaking crack, the secondary magnetic field is distorted, essentially changing the load on the test coil. A load change on the coil directly affects the impedance of the coil, and because the coil impedance is continually monitored by an instrument, any factor in the material that influences the eddy currents can be detected (McMaster et al. 1986). The eddy current field that is induced at the surface of the test material has a specific magnitude and phase as a function of time. Discontinuities, cracks, and material properties disturb the flow-path of the eddy current field and, in turn, affect the magnitude and phase of the induced current. As the impedance of the coil changes, both the circuit resistance and the inductive reactance of the coil also are affected. These changes (to both resistance and inductive reactance) do not occur at the same time and therefore cannot simply be added together to determine the impedance of the circuit. Using automated vector analysis algorithms, an eddy current instrument can rapidly determine the magnitude and phase angle associated with the actual impedance at that particular point in the scan. These data are computed in real time and stored for subsequent data representation (magnitude plots, phase plots, or line plots) and analysis as a function of the two-dimensional probe's position on the test material (Cecco et al. 1983).

Eddy current testing is specifically sensitive to a variety of factors (apart from flaws) that affect the response of the eddy current probe. Typical ET inspectors aim to eliminate, reduce, or compensate for these factors to achieve consistent and reliable results. These factors include the electrical conductivity and magnetic permeability of the test material, the operational frequency of the eddy current probe, geometric properties of the test material, and proximity of the probe to the surface (termed *liftoff*).

Electrical conductivity describes the ability of a material to conduct electric current. The greater the conductivity of a material, the greater the flow of eddy currents on the surface of the material. Factors that affect conductivity include material composition (for example, whether an alloy or not), ambient temperature and internal residual stresses, heat treatment, work hardening, and conductive coatings (such as cladding) (Libby 1971; Hagemaier 1990).

Magnetic permeability is the ability of a material to concentrate magnetic lines or, in other words, the ease with which a material can be magnetized. Nonferrous metals such as brass, aluminum, copper, and austenitic stainless steels have essentially the same numeric relative permeability as that of a vacuum or air; that being 1. For ferrous metals, however, the value for permeability may be orders of magnitude

greater than 1. Typical values for iron can range between 100 and 5000. Additionally, this parameter can vary greatly as a function of spatial position within a material due to localized stresses, heating effects, and so on. Permeability is dimensionless as it is a ratio that compares two flux densities (Hagemaier 1990).

The operating frequency chosen for the inspection also can have a significant effect on the eddy current probe response. Frequency selection affects both the phase relationship and the relative signal strength of the response from different flaws. Choosing the proper frequency is critical to acquiring optimal resolution between flaw signals and noise contributors from the material under test. However, frequency is a parameter that is controlled by the inspector. In this study, an eddy current probe with a nominal operating frequency of 250 kHz was chosen, to balance the trade-offs between detection sensitivity, probe size, and depth of penetration. In this application, minimal probe size was required to achieve consistent coupling and contact of the probe to the inside surface as it was translated over the ID surface geometry that included the weld root and the counterbore facets. The depth of penetration of an induced eddy current field is not uniformly distributed throughout the test material but is most dense near the surface and decreases in magnitude with distance from the surface (Hagemaier 1990). The effective zone for flaw detection of the eddy current field (and essentially the strength of the flaw response) is defined by the value of the standard depth of penetration. Libby (1971) and the American Society for Testing and Materials (ASTM 1997) give the eddy current density at a given depth, x, as

$$J_x = J_0 \exp - x\sqrt{\pi f \mu \sigma} \tag{3.1}$$

where J_0 = current density at the surface in amps/m^2
π = 3.14159
f = frequency in hertz
μ = magnetic permeability
x = depth from surface in m, known as *skin depth*
σ = electrical conductivity in mho/m.

Hagemaier (1990) defines standard depth of penetration, assuming plane-wave electromagnetic field excitation within the test material, as

$$\delta = \left(\pi f \mu \sigma\right)^{-1/2} \tag{3.2}$$

Figure 3.1 illustrates the relationship between frequency, conductivity, and permeability on the depth of penetration for an eddy current field. Therefore, the depth of penetration decreases with increasing frequency, conductivity, and permeability. In the work reported here, with the given operational frequency of 250 kHz using type 304 stainless steel as the base material, our standard depth of penetration is 0.9 mm. This is the distance down from the surface of the material where the eddy current energy density has decreased by 37%. This can be significant to an ET examination, as penetration into ferrous materials at practical frequencies is quite small. Figure 3.2 depicts the standard depth of penetration for an eddy current field for materials of varying conductivity as a function of frequency.

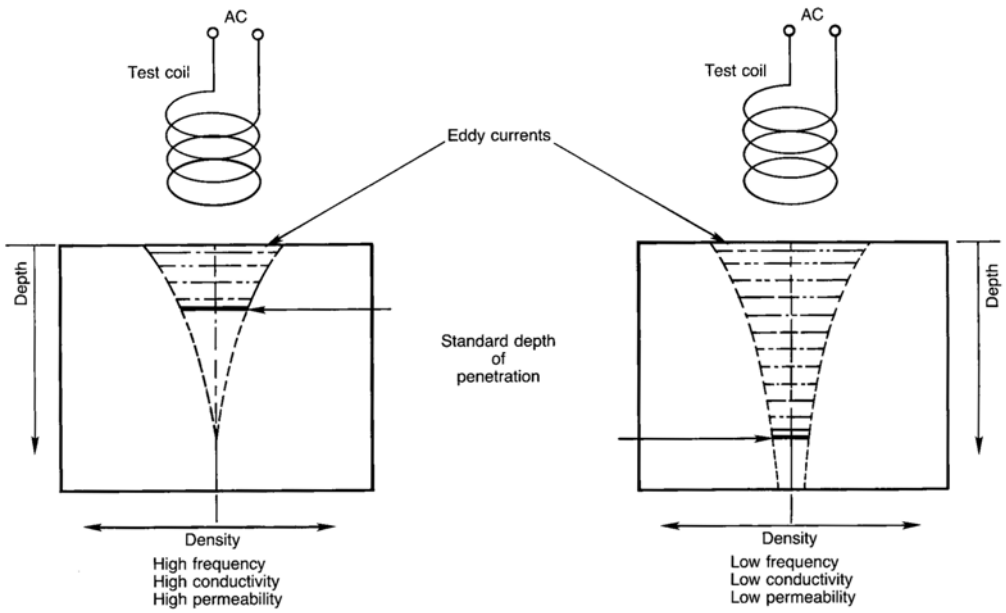

Figure 3.1 Relative Effect of Frequency, Conductivity, and Permeability on the Depth of Penetration for a Typical Single-Coil ET Probe (from Hagemaier 1990)

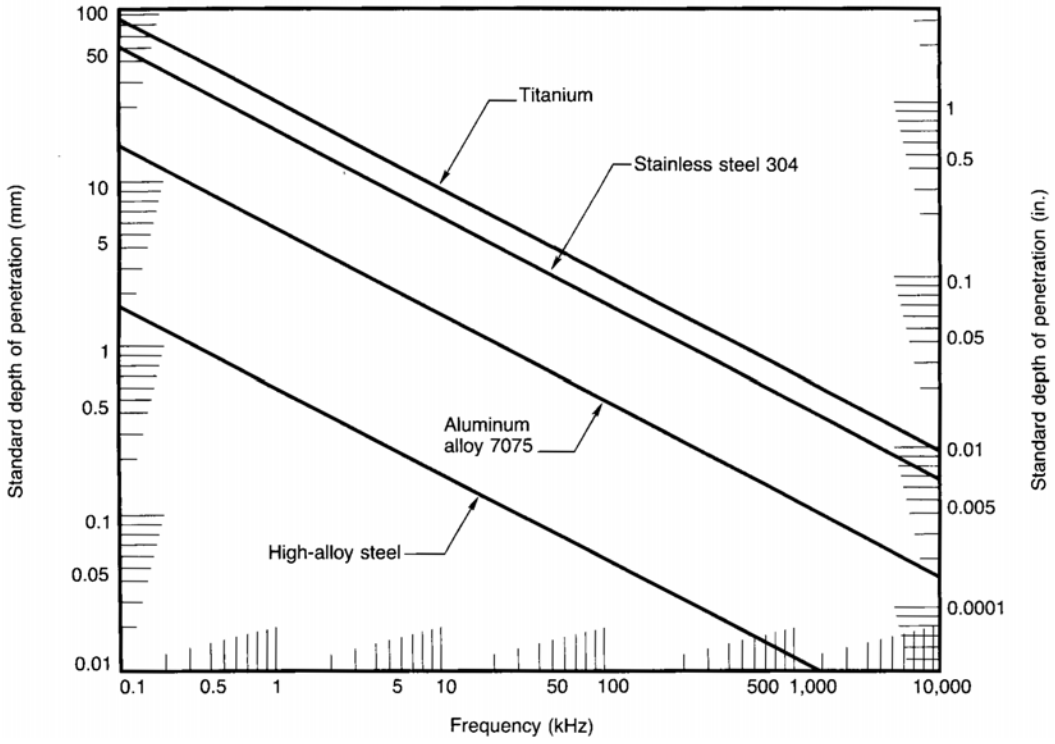

Figure 3.2 Eddy Current Testing Standard Depth of Penetration for Assorted Materials of Varying Conductivity as a Function of Frequency (from Hagemaier 1990)

Dimensional factors or geometric characteristics of the test material can also influence the eddy current response. These factors can generally be categorized into two types—the dimension/shape of the test material and the presence of discontinuities in the material (General Dynamics 1979; McIntire 1986). Geometric features, such as part curvature, grooves, surface conditions (corrosion, porosity), edges, and weldment structure (counterbore, weld root) will affect the eddy current response. Material thickness also can influence the measurements, especially when the material thickness is less than the effective depth of penetration. The inspection protocol must recognize these conditions and adapt the inspection procedure to reduce or eliminate these effects. Edge effects can occur when the ET probe approaches the edge of a specimen where the current has no place to flow, resulting in a false indication. Surface conditions and weldment geometry contributed to minor challenges in consistent coupling of the ET probe in this study. Eliminating or reducing liftoff (when the spacing between the probe and material surface becomes too large) is critical to maintaining sensitivity and suitable signal strength. The closer an ET probe is to the surface of the material, the greater the effect of liftoff on the coil itself. This effectively decreases the magnitude of the signals from the material and the sensitivity of the eddy current field to cracks and discontinuities. To achieve reproducible eddy current results, it is critical to maintain perpendicularity between the ET probe coil windings and the surface of the test material. The effects of probe tilt and wobble can produce liftoff or partial liftoff conditions. Thus, part curvature, surface geometry, and employment of a suitable gimbal that is robust and stable are required to ensure constant and effective coupling and probe position over the entire scan aperture when using automated scanning techniques.

4 Experimental Approach

Eddy current testing can be used for a variety of applications such as the detection of cracks, measurement of metal thickness, detection of metal thinning due to corrosion and erosion, determination of coating thickness, and the measurement of electrical conductivity and magnetic permeability. As discussed in Section 3, eddy current inspection is an excellent method for detecting surface-breaking and near-surface defects. Defects such as cracks are detected when they disrupt the path of the eddy current field.

In this study, eddy current data were collected using an automated scanning system to improve the quality of the measurements and to construct images of the scanned areas. Typically, the most common type of scanning is line scanning in which an automated system is used to translate the probe over the surface of the part at a fixed speed. Two-dimensional scanning systems are used to scan a two-dimensional area. This is typically embodied in a scanning system that scans in an x-y raster mode. The data are then displayed as a false-color plot of signal strength (magnitude) or phase-angle shift as a function of position, similar to an ultrasonic C-scan presentation. A third method of data representation includes generation of composite peak-amplitude line plots that provide peak ET signal amplitude data as a function of circumferential position on the test specimen. Finally, a fourth method of data representation is the surface plot that illustrates ET magnitude measurements (amplitude) versus spatial position in both x- and y-axes. The entire set of data presentations for all specimens examined in this study can be reviewed in the appropriate appendix. Magnitude plots can be found in Appendix B, phase plots in Appendix C, and line plots in Appendix D. Surface plot representations were not generated.

Automated scanning has advantages for ET methods that include

- minimizing changes in liftoff resulting from probe wobble, tilt, uneven surfaces, part shape/geometry, and curvature (in this case on the ID of the pipe specimens)
- accurate indexing
- repeatability
- high-resolution mapping.

The CSS examinations in this study were implemented using a PC-controlled x-y scanning system connected to a Zetec MIZ27-SI eddy current instrument. A digital photograph of the ET scanning system configuration is shown in Figure 4.1. A Zetec plus-point probe (Model Z0000857-1) configured with two small coils oriented 90º from each other was chosen. This probe configuration (sometimes referred to as a plus-point probe) consists of a differential pair of coils that interrogate the same spatial area on the material under test. These types of probes are generally insensitive to extraneous factors and most effective for detection of cracks and other surface material discontinuities. These operational characteristics permit the suppression of localized geometry variations (curved surfaces, corners, weld splatter) and variations in material composition (filler metals, heat-affected zone). Plus-point probes are

Figure 4.1 Automated x-y Eddy Current Testing Scanning System

less sensitive to permeability changes as well and can therefore be employed on both ferromagnetic and nonferromagnetic materials. Plus-point probes tend to suppress unwanted noise and exhibit enhanced sensitivity to the detection of surface-breaking cracks. These differential probes provide bidirectional sensitivity and are sensitive to both circumferential and axially oriented flaws.

The probe used in this study was designed by, and procured from Zetec, Inc. (Snoqualmie, Washington). The probe was developed to detect surface-breaking cracks in the weldment region of steel components while effectively reducing signal responses generated by variations in conductivity or permeability. This probe configuration has been employed successfully in ET examinations conducted in Sweden and at the V.C. Summer Nuclear Station by WesDyne NDT personnel in 2000.

Researchers at the Federal Highway Administration NDE Validation Center also have used this probe to inspect welds in structural steel for bridges (Lamtenzan et al. 2000). The probe, shown in Figure 4.2, consists of two intersecting and orthogonal circular coils with their axes parallel to the surface of the test material. The probe is spring-loaded; the coil width dimension is 3 mm (0.12 in.) in a 12.5-mm

(0.5-in.)-diameter spot probe assembly using PP11a twin coils (one coil is longitudinal, the second coil is circumferential) with special nylon wear surface material. The nominal operating frequency of this probe is 240 kHz using a 100-ohm instrument. Because the probe coils are very close to one another, essentially one inset within the other, gradual changes caused by permeability and conductivity are limited. Liftoff effects are reduced but not eliminated because both coils are affected simultaneously by distance-to-probe surface variations (Lamtenzan et al. 2000).

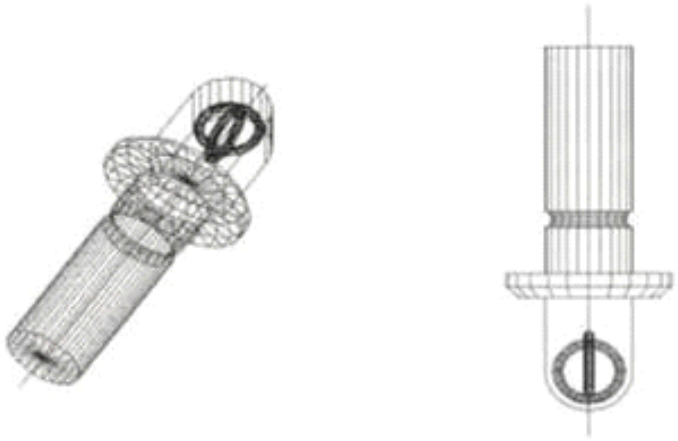

Figure 4.2 Mechanical Drawing of Plus-Point Probe Design, Showing Internal Coil Configuration and Orientation. Source: Lamtenzan et al. (2000)

The probe was fitted to a spring-loaded probe sled capable of pivoting and gimbaling to ensure adequate contact of the probe face to the specimen surface throughout the scanning operation. A calibration block was used to set the instrument parameters (liftoff, probe drive, and gain) and scanner parameters (speed and spacing between scans) to achieve the best signal response. Three driving frequencies were evaluated—100 kHz, 250 kHz, and 500 kHz. The frequency of 250 kHz resulted in the best overall response for small surface defects and provided lower noise, resulting in a higher signal-to-noise ratio (SNR) for the detected indications.

The scans were indexed (incremental steps in both x- and y-axis coordinates) at 1.02 cm (0.04 in.) with a data sampling rate of one measurement every 0.064 cm (0.025 in.). The study was focused on evaluating the performance of this ET method as it pertains to circumferentially oriented cracking in CSS materials. This inspection protocol was based upon the work conducted at V.C. Summer and focused phase sensitivity for cracks over two ranges of phase responses near 90º and 270º where maximum sensitivity to circumferential cracking could be achieved.

The scan area was defined as 6.35 cm (2.5 in.) on each side and parallel to the centerline of the weld and 2.54 cm (1.0 in.) from the top and bottom edges of the test specimen, to minimize the edge effects on the probe that could suppress signals from defects near the edge of the scan area. Probe sensitivity was calibrated to a 0.5-mm x 50-mm (0.019-in. x 1.968-in.) electrical discharge machining (EDM) notch, and the ET measurement system was configured to detect phase shift responses over the ranges of 65º to 105º or 245º to 285º at an operational frequency of 250 kHz using three successive sweeps and employing no amplitude threshold. Valid flaw indications resulting from planar crack-like defects had a typical phase response ranging between 65º and 105º or 245º and 285º and a length greater than 0.64 cm (0.25 in.).

Indicated flaws were checked and then subsequently re-scanned to validate flaw detection. The lengths and locations of the flaws were determined using Transform 2D (SpyGlass) data analysis software (Fortner Research LLC 1996).

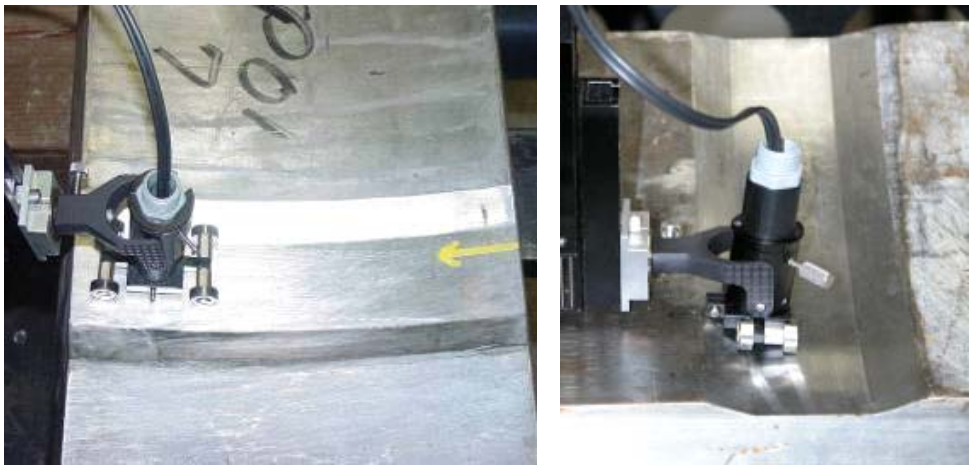

Figure 4.3 Top and Side Views of Inner Diameter Scan Configuration Using Eddy Current Testing Probe and Spring-Loaded Probe Sled for Translation over the Inner-Diameter Surface

As many of these specimens contained cracks with a primarily circumferential orientation, some of these cracks exhibited significant crazing and branching at off-angle directions from both axial and circumferential perspectives. Knowing this, the ET plus-point probe was anticipated to provide strong sensitivity to circumferential cracking and potentially axial cracking as well, due to the additional orthogonal coil, but with reduced detection sensitivity to off-angle cracks that potentially meander at 45º, 135º, 225º and 315º relative to the longitudinal axis of the pipe specimen. To quantify the reduced probe sensitivity as a function of angle, tests were conducted by using a calibration block and rotating the ET probe through a set of angles while recording the magnitude. Figure 4.4 illustrates the relative magnitude sensitivity for the plus-point probe as a function of probe rotation, to both axial and circumferential flaw orientations. The reflectors used to study this effect were both circumferentially and axially oriented EDM notches, machined into an aluminum mock-up of a control rod drive mechanism penetration tube.

PNNL chose to use existing EDM notch reflectors to aid in evaluating and understanding probe sensitivity issues and noise levels. These tests demonstrated that the reduction in probe sensitivity to off-angle cracking, crazing, and branching can be significant and is on the order of 14 dB, or a factor of 5.

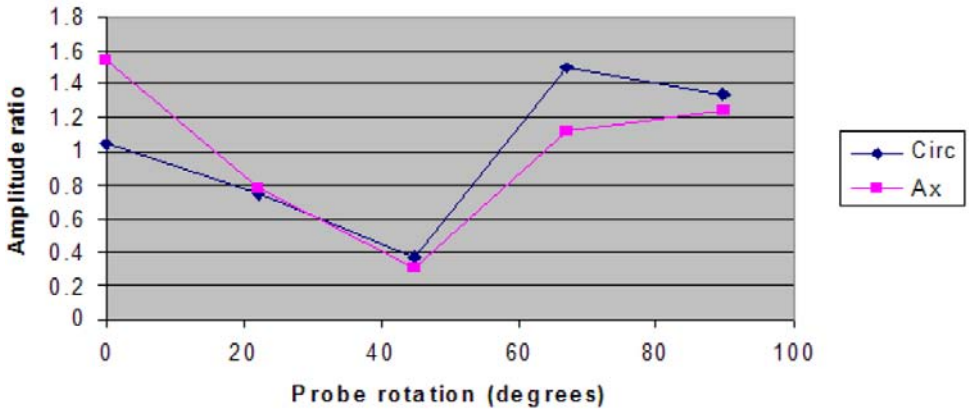

Figure 4.4 Relative Sensitivity of the Plus-Point Probe to a Calibration Block Reflector

Those specimens that exhibited high noise levels in the scan area were degaussed and then re-scanned, with favorable results obtained on half of the specimens. Areas in which results were difficult to interpret or otherwise anomalous were also re-scanned and categorized as hot spots. These discontinuities generally ranged between 0.64 cm (0.25 in.) and 1.0 cm (0.39 in.) in length. The general crack detection criteria employed in the analysis includes relying primarily upon the magnitude responses for detection of initial hot spots and then looking to the phase response plots for validation. The surrounding pattern of clutter and background noise must also be considered in visually discriminating between anomalous amplitude responses and those responses that are clustered and show some shape and consistent continuity. Finally, the associated length or extent is also considered, where typical responses under 12.5 mm (0.5 in.) long are considered non-crack–like responses unless detected in proximity to other amplitude responses of similar intensity or where a pattern starts to develop.

5 Cast Stainless Steel Specimens Used in the Study

This section contains a detailed description of the specimens examined in this study. Fifteen WOG CSS pipe segments (the traveling specimen set from the EPRI NDE Center) with thermal and mechanical fatigue cracks were loaned to PNNL for conducting the ET examinations. Also, a number of PNNL specimens containing thermal fatigue cracks were identified for use in this study. The PNNL specimens originally were fabricated for use in the PNNL piping inspection round robin (PIRR) and CCSS round robin tests as part of the Program for Inspection of Steel Components (PISC) in the early to mid 1980s. A large blank spool piece loaned to PNNL from the EPRI NDE Center (acquired from a cancelled Spanish nuclear plant) also was used for assessing the ET inspection technique. Eddy current testing scans were conducted on the ID of some additional large spool pieces that were provided by Westinghouse and IHI Southwest Technologies Inc. These pieces were cut from vintage CSS material and subsequently prepared, polished, and chemically etched to enhance the microstructure of the grains for visual appearance. The photograph in Figure 5.1 illustrates a local zone of the grain microstructure of the IHI Southwest Technologies Inc. specimen. While conventional ultrasonic NDE methodologies are significantly challenged by these types of microstructures, the ET technique with its shallow depth of penetration is not affected by banding, layering and other depth-dependent changes in grain size and orientation.

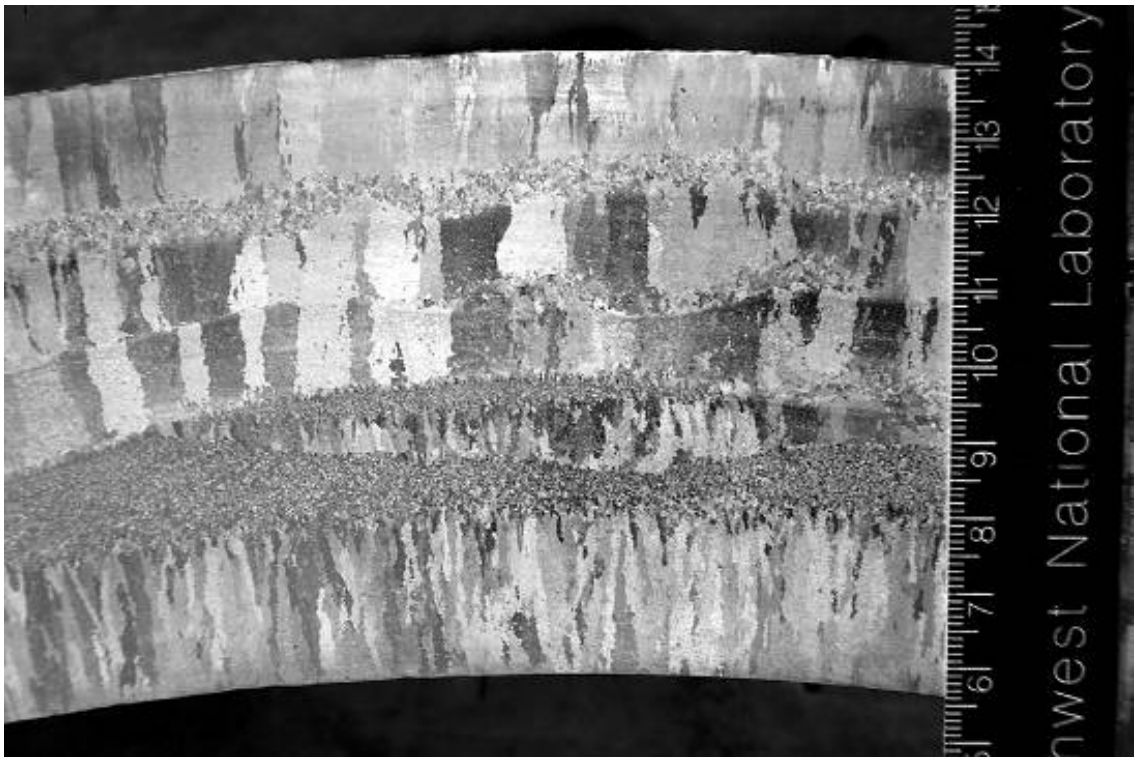

Figure 5.1 Photograph of Polished and Chemically Etched Surface of the IHI Southwest Technologies Inc. 8.0-cm-Thick Spool Piece Showing Bands of Columnar Grains and Bands of Equiaxed Grains

The Westinghouse spool piece exhibited a dendritic (columnar) microstructure that can be seen in Figure 5.2.

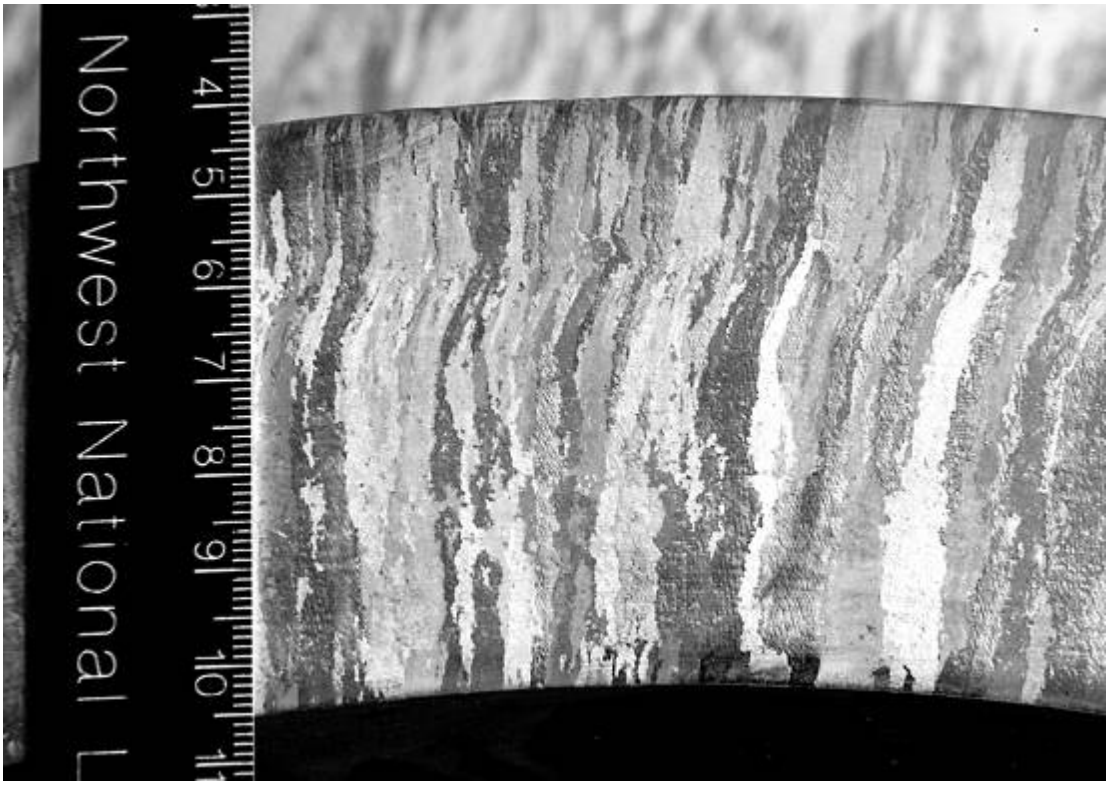

Figure 5.2 Photograph of Polished and Chemically Etched Surface of the Westinghouse CSS Spool Piece Showing Bands of Columnar Grains

Three smaller sections of very coarse-grained blank spool pieces (from Southwest Research Institute) also were examined to study the effects of coarse-grained parent material on the ET responses. Digital photographs of each individual specimen examined in this study can be found in Appendix A. A review of this appendix shows the various inside and outside diameter surface conditions indicative of piping geometries installed in the field. It is worthy to note that some of these components also contain fine grain wrought stainless steel, where the very fine microstructure is made up of randomly distributed equiaxed grains of very small dimension (less than 0.5 mm diameter) relative to those grain diameters found in CSS microstructures.

5.1 Westinghouse Owners Group Specimens

The WOG specimens represent a variety of reactor piping configurations, including

- statically cast stainless steel (SCSS) elbow to centrifugally cast pipe
- carbon steel inlet nozzle to forged stainless steel (SS) safe-end to statically cast elbow
- SCSS pump outlet nozzle to CCSS pipe
- clad carbon steel outlet nozzle to forged SS safe-end to centrifugally cast pipe.

The represented microstructures were described as coarse and coarse-mixed microstructures, consisting of combined dendritic (columnar) and equiaxed grains. Figure 5.3 shows the WOG specimens in the laboratory prior to data acquisition.

Figure 5.3 Westinghouse Owners Group Set of Cast Stainless Steel Specimens Used in This Study

The cracks in the WOG pipe sections were created using methods that have proven useful in producing realistic surface-connected mechanical and thermal fatigue cracks. The flaws in the WOG specimens are basically considered to be planar cracks, parallel to the weld centerline and perpendicular to and connected to the ID. However, the fabrication process also has created some transverse cracking in some of these specimens. The tightness and roughness of the thermal fatigue cracks generally make them more difficult to detect in comparison to mechanical fatigue cracks. Typical pipe ID surface conditions for these types of components are more problematic with regard to surface roughness, counterbore conditions, root conditions, and mismatch, where the latter can be substantial on cold-leg, statically cast elbow fit-ups. In the field, typical ID surface preparations include employing a feathering tool to generally buff out rough edges that are generated after fit-up and welding, according to David Kurek (personal communication, September 2003). In comparison, the WOG specimens are generally regarded as exhibiting moderate ID surface conditions that do not represent worst-case scenarios (based upon the opinions and experiences of several ISI vendors who have conducted inspections from the ID of field-welded CSS piping). In contrast to this, the PNNL specimens discussed later in this section exhibit even smoother conditions that are considered relatively easy and represent best-case conditions due to the lack of root conditions, smoothly tapered counterbore facets, and machined ID surfaces.

The piping configurations and crack details for the WOG specimens used in this study are described in Table 5.1.

Table 5.1 Westinghouse Owners Group Specimens Available for This Study

WOG Specimen	Mock-Up Configuration	Crack Type	Crack Through-Wall (%)	Crack Location (Side of Weld)
APE-1	CCSS pipe-to-SCSS elbow	MF	13	SCSS
APE-4	CCSS pipe-to-SCSS elbow	MF	14	SCSS
INE-A-1	SCSS elbow-to-WSS safe end	MF	42	SCSS
INE-A-4	SCSS elbow-to-WSS safe end	TF	29	SCSS
INE-A-5	SCSS elbow-to-WSS safe end	MF	34	WSS
MPE-3	CCSS pipe-to-SCSS elbow	MF	30	SCSS
MPE-6	CCSS pipe-to-SCSS elbow	TF	18	SCSS
ONP-D-2	CCSS pipe-to-WSS safe end	TF	28	CCSS
ONP-D-5	CCSS pipe-to-WSS safe end	MF	18	CCSS
ONP-3-5	CCSS pipe-to-WSS safe end	TF	28	WSS
ONP-3-8	CCSS pipe-to-WSS safe end	MF	28	WSS
OPE-2	CCSS pipe-to-SCSS elbow	MF	18	SCSS
OPE-5	CCSS pipe-to-SCSS elbow	TF	23	SCSS
POP-7	CCSS pipe-to-SCSS pump nozzle	MF	31	SCSS
POP-8	CCSS pipe-to-SCSS pump nozzle	TF	18	CCSS

The following physical descriptions of each specimen used in this study includes information relating to the general grain size, grain orientation/distribution, and material microstructure. In order to visually represent these various microstructures, the reader is referred to Appendix A, where color-coded digital images illustrate the banding associated with various layers of grains that were formed as a result of the casting processes used during fabrication for each specimen. Grain size data acquired using visual analyses from these digital illustrations are summarized in Table 5.2. These data represent only the maximum grain size information (through the mean-lineal-intercept method) found along the inner surface (ID) of each specimen. Since the ET methodology is a surface detection method, the depth of penetration is minimal and any microstructural effects on ET measurement performance would be attributed only to the near surface grains along the ID. Table 5.2 provides data representing each of the WOG specimen configurations from actual data acquired from specimens that were polished and chemically etched to highlight the grains for visual analysis and measurement. Since each individual specimen was not polished and etched, the reader should assume similar grain size and orientation for those specimens of similar configuration. For example, visual grain size data were physically measured for WOG specimen APE-1 and documented in Table 5.2, but not APE-4, which represents the same component configuration (CCSS pipe to SCSS elbow). The reader must extrapolate the dimensional information among like specimens from Table 5.2. It should be noted that for the CCSS pipe-side of WOG specimens APE-1 and POP-8, the quality of the digital images were insufficient for providing

accurate grain size determination using the mean-lineal-intercept method. In these cases, the data for the next band above the ID band is provided.

Table 5.2 Range of Grain Sizes in Cast Stainless Steel Specimens

Specimen	CCSS (ID) Maximum	SCSS (ID) Maximum	WSS (ID) Maximum
EPRI Ring	2.89 mm (0.02 in.)	n/a	n/a
IHI Southwest	Left ID Band: 1.26 mm (0.05 in.) Center ID Band: 1.58 mm (0.06 in.) Right ID Band: 3.21 mm (0.13 in.)	n/a	n/a
Westinghouse	3.75 mm (0.15 in.)	n/a	n/a
APE-1	Insufficient Image Quality (ID Band); Next Band Above: 1.77 mm (0.07 in.)	1.67 mm (0.07 in.)	n/a
INE-A-5	n/a	1.00 mm (0.004 in.)	<0.5 mm (0.02 in.)
MPE-6	3.0 mm (0.12 in.)	1.89 mm (0.07 in.)	n/a
ONP-3-8	5.9 mm (0.23 in.)	n/a	<0.5 mm (0.02in.)
ONP-D-5	3.89 mm (0.15 in.)	n/a	<0.5 mm (0.02in.)
OPE-5	1.68 mm (0.07 in.)	1.15 mm (0.05 in.)	n/a
POP-8	Insufficient Image Quality (ID Band); Next Band Above: 1.89 mm (0.07 in.)	1.64 mm (0.06 in.)	n/a

Westinghouse Owners Group specimen APE-1 is 25.4 cm (10.0 in.) wide (circumferential distance) and 60.96 cm (24.0 in.) long in axial extent. This specimen is a statically cast elbow to centrifugally cast pipe section in which the elbow side is 8.89 cm (3.5 in.) thick and the pipe side is 6.6 cm (2.6 in.) thick. The statically cast microstructure is defined as thin-band equiaxed grains, while the centrifugally cast microstructure is defined as bands of coarse columnar mixed with bands of small equiaxed grains (see the micrograph in Figure A.32 for a visual depiction of the microstructure for this specimen). The crack in APE-1 is a mechanical fatigue crack located on the elbow side of the weld centerline, with a circumferential extent (length) of 3.94 cm (1.55 in.) and a depth of 1.14 cm (0.45 in.).

Specimen APE-4 is 20.3 cm (8.0 in.) wide (circumferential distance) and 60.96 cm (24.0 in.) long in axial extent. This specimen is a statically cast elbow to centrifugally cast pipe section, where the elbow side is 8.89 cm (3.5 in.) thick and the pipe side is 6.6 cm (2.6 in.) thick. The statically cast microstructure is defined as thin-band equiaxed grains, while the centrifugally cast microstructure is defined as bands of coarse columnar mixed with bands of small equiaxed grains (the micrograph in Figure A.32 depicts a similar microstructure for this specimen). The crack in APE-4 is a mechanical fatigue crack on the pipe side of the weld centerline, with a circumferential extent (length) of 4.19 cm (1.65 in.) and a depth of 1.27 cm (0.5 in.).

Specimen INE-A-1 is 26.0 cm (10.25 in.) wide (circumferential distance) and 60.96 cm (24.0 in.) long in axial extent. This specimen is a clad carbon steel inlet nozzle to forged stainless steel safe end to statically cast elbow section, where the nozzle side consists of 6.6-cm (2.6-in.)-thick carbon steel and 0.76-cm (0.3-in.)-thick cladding. The forged SS safe end is 7.37 cm (2.9 in.) thick, and the SCSS elbow segment is 6.35 cm (2.5 in.) thick. Both clad carbon steel and forged SS segments are defined as

consisting of a fine-grained equiaxed microstructure, while the statically cast microstructure is defined as a coarse matrix of grains (the micrograph in Figure A.33 depicts a similar microstructure for this specimen). The crack in INE-A-1 is a mechanical fatigue crack on the elbow side of the weld centerline between the forged SS-elbow segment, with a circumferential extent (length) of 6.99 cm (2.75 in.) and a depth of 2.64 cm (1.04 in.).

Specimen INE-A-4 is 20.3 cm (8.0 in.) wide (circumferential distance) and 60.96 cm (24.0 in.) long in axial extent. This specimen is a clad carbon steel inlet nozzle to forged SS safe end to statically cast elbow section, where the nozzle side consists of 6.6-cm (2.6-in.)-thick carbon steel and 0.76-cm (0.3-in.)-thick cladding. The forged SS safe end is 7.37 cm (2.9 in.) thick, and the SCSS elbow segment is 6.35 cm (2.5 in.) thick. Both clad carbon steel and forged SS segments are defined as consisting of a fine-grained equiaxed microstructure, while the statically cast microstructure is defined as a coarse matrix of grains (the micrograph in Figure A.33 depicts a similar microstructure for this specimen). The crack in INE-A-4 is a thermal fatigue crack on the elbow side of the weld centerline between the forged SS-elbow segment, with a circumferential extent (length) of 6.86 cm (2.7 in.) and a depth of 1.85 cm (0.73 in.).

Specimen INE-A-5 is 25.4 cm (10.0 in.) wide (circumferential distance) and 60.96 cm (24.0 in.) long in axial extent. This specimen is a clad carbon steel inlet nozzle to forged stainless steel safe end to statically cast elbow section, where the nozzle side consists of 6.6-cm (2.6-in.)-thick carbon steel and 0.76-cm (0.3-in.)-thick cladding. The forged SS safe end is 7.37 cm (2.9 in.) thick, and the SCSS elbow segment is 6.35 cm (2.5 in.) thick. Both clad carbon steel and forged SS segments are defined as consisting of a fine-grained equiaxed microstructure, while the statically cast microstructure is defined as a coarse matrix of grains (see the micrograph in Figure A.33 for a visual depiction of the microstructure for this specimen). The crack in INE-A-5 is a mechanical fatigue crack on the safe end side of the weld centerline between the forged SS-elbow segment, with a circumferential extent (length) of 6.73 cm (2.65 in.) and a depth of 2.54 cm (1.0 in.).

Specimen MPE-3 is 20.3 cm (8.0 in.) wide (circumferential distance) and 60.96 cm (24.0 in.) long in axial extent. This specimen is a statically cast elbow to centrifugally cast pipe section, where the elbow side is 8.38 cm (3.3 in.) thick and the pipe side is 6.6 cm (2.6 in.) thick. Both the statically cast and centrifugally cast microstructures are defined as a coarse-mixed matrix of grains (the micrograph in Figure A.34 depicts a similar microstructure for this specimen). The crack in MPE-3 is a mechanical fatigue crack located on the pipe side of the weld centerline, with a circumferential extent (length) of 6.73 cm (2.65 in.) and a depth of 2.54 cm (1.0 in.).

Specimen MPE-6 is 26.0 cm (10.25 in.) wide (circumferential distance) and 60.96 cm (24.0 in.) long in axial extent. This specimen is a statically cast elbow to centrifugally cast pipe section, where the elbow side is 8.38 cm (3.3 in.) thick and the pipe side is 6.6 cm (2.6 in.) thick. Both the statically cast and centrifugally cast microstructures are defined as a coarse-mixed matrix of grains (see the micrograph in Figure A.34 for a visual depiction of the microstructure for this specimen). The crack in MPE-6 is a thermal fatigue crack on the elbow side of the weld centerline, with a circumferential extent (length) of 5.92 cm (2.33 in.) and a depth of 1.50 cm (0.59 in.).

Specimen ONP-D-2 is 25.4 cm (10.0 in.) wide (circumferential distance) and 61.6 cm (24.25 in.) long in axial extent. This specimen is a clad carbon steel outlet nozzle to forged stainless steel safe end to centrifugally cast pipe section, where the nozzle side consists of 6.86-cm (2.7-in.)-thick carbon steel and

0.51-cm (0.2-in.)-thick cladding. The forged SS safe end is 7.37 cm (2.9 in.) thick, and the CCSS pipe segment is 6.35 cm (2.5 in.) thick. Both clad carbon steel and forged SS segments are defined as consisting of a fine-grained microstructure, while the centrifugally cast microstructure is defined as a coarse-mixed matrix of grains (the micrograph in Figure A.35 depicts a similar microstructure for this specimen). The crack in ONP-D-2 is a thermal fatigue crack on the pipe side of the weld centerline between the forged SS-CSS pipe segment, with a circumferential extent (length) of 6.6 cm (2.6 in.) and a depth of 1.78 cm (0.7 in.).

Specimen ONP-D-5 is 25.4 cm (10.0 in.) wide (circumferential distance) and 61.6 cm (24.25 in.) long in axial extent. This specimen is a clad carbon steel outlet nozzle to forged stainless steel safe end to centrifugally cast pipe section, where the nozzle side consists of 6.86-cm (2.7-in.)-thick carbon steel and 0.51-cm (0.2-in.)-thick cladding. The forged SS safe end is 7.37 cm (2.9 in.) thick, and the CCSS pipe segment is 6.35 cm (2.5 in.) thick. Both clad carbon steel and forged SS segments are defined as consisting of a fine-grained microstructure, while the centrifugally cast microstructure is defined as a coarse-mixed matrix of grains (see the micrograph in Figure A.35 for a visual depiction of the microstructure for this specimen). The crack in ONP-D-5 is a mechanical fatigue crack on the pipe side of the weld centerline between the forged SS-CSS pipe segment, with a circumferential extent (length) of 4.06 cm (1.6 in.) and a depth of 1.19 cm (0.47 in.).

Specimen ONP-3-5 is 20.3 cm (8.0 in.) wide (circumferential distance) and 61.6 cm (24.25 in.) long in axial extent. This specimen is a clad carbon steel outlet nozzle to forged stainless steel safe end to centrifugally cast pipe section, where the nozzle side consists of 6.60-cm (2.6-in.)-thick carbon steel and 0.51-cm (0.2-in.)-thick clad. The forged SS safe end is 7.11 cm (2.8 in.) thick, and the CCSS pipe segment is 6.35 cm (2.5 in.) thick. Both clad carbon steel and forged SS segments are defined as consisting of a fine-grained microstructure, while the centrifugally cast microstructure is defined as a coarse matrix of grains (the micrograph in Figure A.36 depicts a similar microstructure for this specimen). The crack in ONP-3-5 is a thermal fatigue crack on the safe-end side of the weld centerline between the nozzle segment and the forged SS safe-end segment, with a circumferential extent (length) of 6.6 cm (2.6 in.) and a depth of 1.78 cm (0.7 in.).

Specimen ONP-3-8 is 20.3 cm (8.0 in.) wide (circumferential distance) and 61.6 cm (24.25 in.) long in axial extent. This specimen is a clad carbon steel outlet nozzle to forged stainless steel safe end to centrifugally cast pipe section, where the nozzle side consists of 6.60-cm (2.6-in.)-thick carbon steel and 0.51-cm (0.2-in.)-thick clad. The forged SS safe end is 7.11 cm (2.8 in.) thick, and the CCSS pipe segment is 6.35 cm (2.5 in.) thick. Both clad carbon steel and forged SS segments are defined as consisting of a fine-grained microstructure, while the centrifugally cast microstructure is defined as a coarse matrix of grains (see the micrograph in Figure A.36 for a visual depiction of the microstructure for this specimen). The crack in ONP-3-8 is a mechanical fatigue crack on the outlet nozzle side of the weld centerline between the nozzle segment and the forged SS safe-end segment, with a circumferential extent (length) of 5.13 cm (2.02 in.) and a depth of 1.78 cm (0.7 in.).

Specimen OPE-2 is 25.4 cm (10.0 in.) wide (circumferential distance) and 52.1 cm (20.5 in.) long in axial extent. This specimen is a statically cast elbow to centrifugally cast pipe section, where the elbow side is 7.11 cm (2.8 in.) thick and the pipe side is 5.84 cm (2.3 in.) thick. Both the statically cast and centrifugally cast microstructures are defined as a coarse matrix of grains (see the micrograph in Figure A.37 for a visual depiction of the microstructure for this specimen). The crack in OPE-2 is a

mechanical fatigue crack on the elbow side of the weld centerline, with a circumferential extent (length) of 4.19 cm (1.65 in.) and a depth of 1.27 cm (0.5 in.).

Specimen OPE-5 is 20.3 cm (8.0 in.) wide (circumferential distance) and 52.1 cm (20.5 in.) long in axial extent. This specimen is a statically cast elbow to centrifugally cast pipe section, where the elbow side is 7.11 cm (2.8 in.) thick and the pipe side is 5.84 cm (2.3 in.) thick. Both the statically cast and centrifugally cast microstructures are defined as a coarse matrix of grains (the micrograph in Figure A.37 depicts a similar microstructure for this specimen). The crack in OPE-5 is a thermal fatigue crack on the elbow side of the weld centerline, with a circumferential extent (length) of 6.15 cm (2.42 in.) and a depth of 1.63 cm (0.64 in.).

Specimen POP-7 is 25.4 cm (10.0 in.) wide (circumferential distance) and 53.3 cm (21 in.) long in axial extent. This specimen is a statically cast pump outlet nozzle to centrifugally cast pipe section, where the nozzle segment is 8.38 cm (3.3 in.) thick and the pipe side is 6.6 cm (2.6 in.) thick. Both the statically cast and centrifugally cast microstructures are defined as a coarse-mixed matrix of grains (the micrograph in Figure A.38 depicts a similar microstructure for this specimen). The crack in POP-7 is a mechanical fatigue crack on the elbow side of the weld centerline, with a circumferential extent (length) of 6.78 cm (2.67 in.) and a depth of 2.57 cm (1.01 in.).

Specimen POP-8 is 25.4 cm (10.0 in.) wide (circumferential distance) and 53.3 cm (21 in.) long in axial extent. This specimen is a statically cast pump outlet nozzle to centrifugally cast pipe section, where the nozzle segment is 8.38 cm (3.3 in.) thick and the pipe side is 6.6 cm (2.6 in.) thick. Both the statically cast and centrifugally cast microstructures are defined as a coarse-mixed matrix of grains (see the micrograph in Figure A.38 for a visual depiction of the microstructure for this specimen). The crack in POP-8 is a thermal fatigue crack on the pipe side of the weld centerline, with a circumferential extent (length) of 5.72 cm (2.25 in.) and a depth of 1.50 cm (0.59 in.).

Digital photographs depicting side-profile views that illustrate the ID surface conditions and weldment geometry for each of the WOG specimens described here, can be found in Appendix A.

5.2 Pacific Northwest National Laboratory Specimens

The PNNL specimens consist of sections cut from butt-welded, 845-mm (33.3-in.)-OD, 60-mm (2.4-in.)-thick CCSS pipe. This pipe material was from two different heats of ASTM A-351 Grade CF-8A, a cast 304 material (Diaz et al. 1998). Many of these specimens have been used in a variety of other studies, and many have labels and identification numbers scribed on them; those labels/scribe numbers are used in this report to aid in distinguishing individual specimens. Many of these specimens contain welds approximately in the middle of each section and were made by welders qualified to meet Section III requirements of the ASME Code. The welds in these specimens were made under shop conditions but are typical of field practice. The weld crowns were ground relatively smooth and blended with the parent pipe, although troughs between weld paths are still present. The ID surface contours are significantly smoother than those of the WOG specimens described earlier. Although these specimens exhibit shallow counterbore facets, the ID surface conditions are relatively smooth, with more fluid contours between the weld root, counterbore, and parent material segments.

The cracks in these pipe sections were created using laboratory methods developed at PNNL that have proven useful in producing realistic surface-connected thermal fatigue cracks. The flaws in these specimens are basically considered to be planar cracks, parallel to the weld centerline and perpendicular to and connected to the ID. The tightness and roughness of the thermal fatigue cracks generally make them more difficult to detect in comparison to mechanical fatigue cracks. Some specimens were stamped with an identifying code in the upper left corner. These specimens had a scribe line located near, but not necessarily coincident with, the weld centerline, which was to be used as the reference line for axial offset measurements. One side of these specimens was marked "-" and the other side "+" to indicate which half of the specimen was to be examined and also to give the directional sign to put on the axial scribe offset measurement for any indications. Specimens marked with "C" or "E" denote columnar microstructure or equiaxed microstructure, respectively.

PNNL Specimen #B-501 is 18.19 cm (7.16 in.) wide (circumferential distance) and 40.4 cm (15.92 in.) long in axial extent. This specimen is configured as a pipe-to-pipe segment with the (-) side consisting of intermediate-size columnar grains and the (+) side consisting of intermediate-size equiaxed grains. The weldment is located approximately in the center of the pipe-to-pipe segment, and the weld crown was ground relatively smooth and blended with the parent pipe. The equiaxed segment of this specimen is 5.84 cm (2.3 in.) thick, and the columnar segment of this specimen is 5.59 cm (2.2 in.) thick. The segment thickness at the weld centerline is 5.51 cm (2.17 in.). Originally, this specimen was intentionally fabricated as a blank specimen and contained no crack for the PIRR and the PISC II assessments. Subsequently, however, a thermal fatigue crack was introduced into this specimen by Trueflaw Ltd. (Espoo, Finland) using its patented crack production technology. This work was performed to compare the thermal fatigue crack produced by Trueflaw with those manufactured by PNNL.

PNNL used a process of placing a small starter notch (approximately 0.5 mm [0.020 in.] deep) at the site where the flaw was to be introduced. After the crack was grown, the starter notch was carefully machined away. This results in some modifications to the material and has always been a concern as to whether this might be detectable by the NDE method being employed. The Trueflaw method does not require the use of a starter notch. Rather, it employs a technique that concentrates the heating in the area where crack formation is desired; thus, that is the only place where the crack can initiate and grow. Because this is a different process for introducing thermal fatigue cracks, PNNL wanted to assess this process and compare it to the process that PNNL has previously used. Trueflaw introduced a crack into this specimen 2.92 cm (1.15 in.) long. The intent was to grow something that has a depth of about 20 mm (0.79 in.) because this would make it approximately one-third of the wall thickness. The actual depth of this crack as well as all of the cracks in CSS are not well known because it is very difficult to obtain any tip signals.

PNNL Specimen #B-504 is 17.78 cm (7.0 in.) wide (circumferential distance) and 40.4 cm (15.91 in.) long in axial extent. This specimen is configured as a pipe-to-pipe segment with the (+) side consisting of intermediate-size columnar grains and the (-) side consisting of intermediate-size equiaxed grains. The weldment is located approximately in the center of the pipe-to-pipe segment, and the weld crown was ground relatively smooth and blended with the parent pipe. This specimen has a thermal fatigue crack on the columnar side of the weld with an offset of 0.56 cm (0.22 in.) from the weld centerline. The crack is 6.15 cm (2.42 in.) in length (circumferential extent) and 2.79 cm (1.10 in.) deep. The equiaxed segment of this specimen is 5.84 cm (2.3 in.) thick; the columnar segment is 5.84 cm (2.3 in.) thick. The segment thickness at the weld centerline is 5.51 cm (2.17 in.).

Specimen # B-505 is a pipe section 40 cm (15.75 in.) long (axial extent), 17.15 cm (6.75 in.) wide, and 5.8 cm (2.28 in.) thick containing microstructures both fine-grained equiaxed (on the plus side of the weld) and fine-grained columnar (located on the minus side of the weld). This CSS calibration block was a section cut from a butt-welded, 845-mm-OD, 60-mm-thick (33.267-in.-OD, 2.362-in.-thick) CCSS pipe containing a weld located approximately in the middle of the section. It was fabricated by welders qualified to meet Section III requirements of ASME Code. The weld crown was ground relatively smooth and blended with the parent pipe, although troughs between weld paths are still present. This specimen also contains three 10% through-wall notches, 5.72 cm. (2.25 in.) in length and 0.635 cm. (0.25 in.) in width, two on the columnar side and one on the equiaxed side of the weld root, as well as a gouged-out area (defined as a minor surface indication) along the ID of the weld root with small dimensions. This specimen also contains a number of 4.76-mm (0.188-in.)-diameter side-drilled holes at ¼ T, ½ T, and ¾ T depths on both sides of the weld.

Specimen #B-515 is 18.16 cm (7.15 in.) wide (circumferential distance) and 40.4 cm (15.91 in.) long in axial extent. This specimen is configured as a pipe-to-pipe segment with the (-) side consisting of intermediate-size columnar grains and the (+) side consisting of intermediate-size equiaxed grains. The weldment is located approximately in the center of the pipe-to-pipe segment, and the weld crown was ground relatively smooth and blended with the parent pipe. This specimen has a thermal fatigue crack on the equiaxed (+) side of the weld with an offset of 0.13 cm (0.05 in.) from the weld centerline. The crack is 2.92 cm (1.15 in.) in length (circumferential extent) and 1.52 cm (0.6 in.) deep. The equiaxed segment of this specimen is 5.84 cm (2.3 in.) thick, and the columnar segment of this specimen is 6.05 cm (2.38 in.) thick. The segment thickness at the weld centerline is 5.49 cm (2.16 in.). This specimen is special in that #B-515 has been thermally stress-relieved, mechanically bent open, and then bent back to its original shape. This resulted in an open, easier-to-detect crack, which may not mimic defects anticipated to be found in service.

Specimen #B-519 is 18.16 cm (7.15 in.) wide (circumferential distance) and 40.4 cm (15.91 in.) long in axial extent. This specimen is configured as a pipe-to-pipe segment with the (-) side consisting of intermediate-size columnar grains and the (+) side consisting of intermediate-size equiaxed grains. The weldment is approximately in the center of the pipe-to-pipe segment, and the weld crown was ground relatively smooth and blended with the parent pipe. This specimen has a thermal fatigue crack on the equiaxed (+) side of the weld with an offset of 0.25 cm (0.1 in.) from the weld centerline. The crack is 5.72 cm (2.25 in.) in length (circumferential extent) and 2.79 cm (1.10 in.) deep. The equiaxed segment of this specimen is 5.79 cm (2.28 in.) thick, and the columnar segment of this specimen is 6.05 cm (2.38 in.) thick. The segment thickness at the weld centerline is 5.49 cm (2.16 in.).

Digital photographs depicting side-profile views that illustrate the ID surface conditions and weldment geometry for each of these PNNL specimens can be found in Appendix A.

5.3 Electric Power Research Institute Blank Spool Piece

The large blank spool piece was extracted from a Spanish nuclear power plant and consists of a fine-grained CCSS microstructure. The EPRI NDE Center acquired the piece and loaned it to PNNL for NDE assessments of advanced inspection methodologies. A segment at one end of the spool piece was cut off, polished, and chemically etched to obtain digital micrographs of the material structure. Figure 5.4

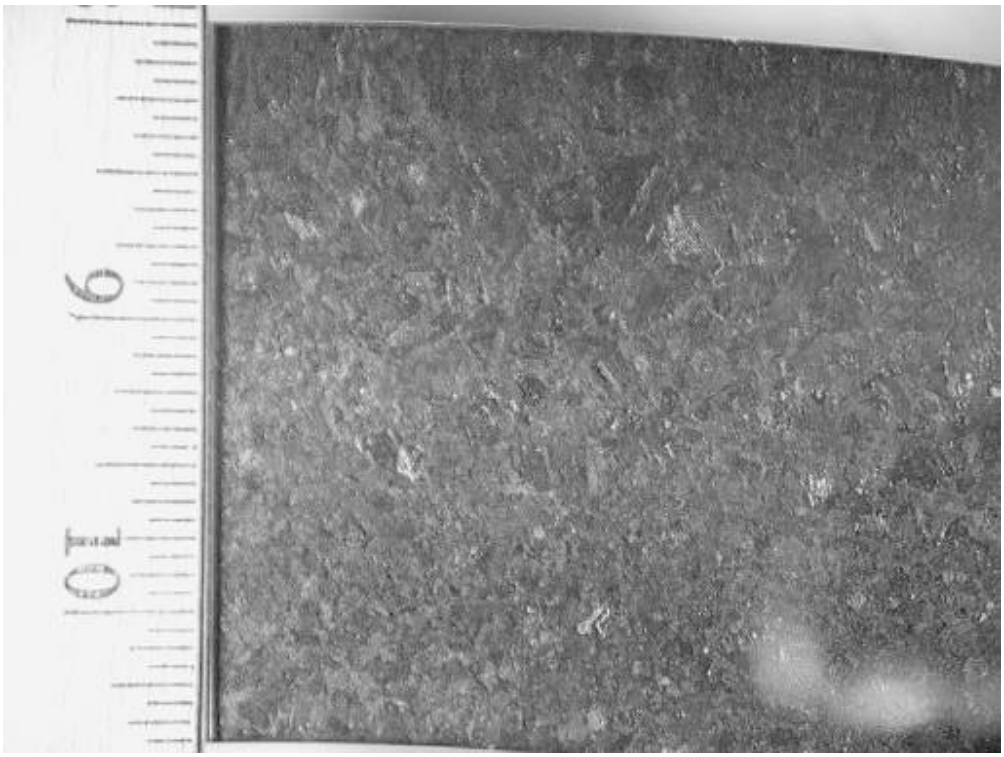

Figure 5.4 Polished and Chemically Etched Ring Segment Extracted from Spanish Spool Piece for Microstructural Visualization

is a digital photograph of a small region of the polished and chemically etched ring depicting a microstructure consisting of fine equiaxed grains.

This information provides a visual mechanism to better understand the average grain size, distribution, and orientation, and to more effectively correlate microstructural data with NDE data from ultrasonic and eddy current examinations. The spool piece does not contain any thermal or mechanical fatigue cracks and was used solely to study the eddy current responses that result from large areas of blank, fine-grained cast material microstructures. The entire spool piece component is illustrated in Figure 5.5.

The piece is 1.86 m (6.1 ft) in length, with a 6.35-cm (2.5-in.) wall thickness and an OD value of 86.4 cm (34.0 in.). Other digital photographs of the spool piece that illustrate the ID surface conditions and general geometry for this component can be found in Appendix A.

5.4 Southwest Research Institute Spool Piece Segments

The specimens described here were provided to PNNL by Southwest Research Institute. Specimen AAD#1 is a thick spool piece segment measuring 28.7 cm (11.3 in.) in length, 15.6 cm (6.14 in.) in width, and 8.41 cm (3.31 in.) in thickness. Specimen AAD#2 is a thick pipe section measuring 36.7 cm (14.4 in.) long, 31.1 cm (12.2 in.) wide, and 6.5 cm (2.6 in.) thick. Specimen AAD#3 is a thick pipe

Figure 5.5 Large Blank Cast Spool Piece, Extracted from a Cancelled Spanish Nuclear Power Plant, Acquired by the EPRI NDE Center, and Loaned to PNNL for Advanced NDE Assessment Work

section measuring 28.7 cm (11.3 in.) long, 15.6 cm (6.14 in.) wide, and 8.41 cm (3.31 in.) thick. These specimens exhibit multibanded and mixed coarse-grained columnar and equiaxed microstructures. There are no flaws in these specimens, as these pipe sections were used to study the eddy current responses that result from blank, very coarse-grained, and anisotropic material microstructures.

Details of these spool piece segments are illustrated in Appendix A.

5.5 Westinghouse Spool Piece

The Westinghouse spool piece was a segment 25.4 cm (10 in.) in axial extent by 130 cm (51 in.) in circumferential extent, with a 6.4-cm (2.5-in.) wall thickness and an approximately 71-cm (28-in.) OD. This segment consisted of a coarse-grained, dendritic (columnar) microstructure with a banding condition evident as well (refer to Figure 5.2). This specimen contained some minor surface defects, sawcuts, and notches machined into the surface but no fabricated or implanted cracks (see Appendix A).

5.6 IHI Southwest Technologies Inc. Spool Piece

The IHI Southwest Technologies Inc. spool piece was a segment 15.24 cm (6 in.) in axial extent by 127 cm (50 in.) in circumferential extent, with an 8.4-cm (3.3-in.) wall thickness and an approximately 91-cm (36-in.) OD. It consisted of a coarse-grained, mixed, and banded microstructure and had some surface defects, sawcuts, and notches machined into the specimen but no fabricated or implanted cracks (see Appendix A).

5.7 Grain Size Considerations

Although the actual metallurgical structure of piping at U.S. nuclear power plants is currently unknown, the piping segments available to PNNL are believed to represent generic vintage classes of CCSS that were used for fabricating Class 1 reactor coolant piping in all Westinghouse-designed PWRs. Specific fabrication parameters used during casting processes that may have produced resultant structures are unclear at the present and not within the scope of the research described in this report. In addition, grain size considerations for both specimen types (specimens with weld flaws and unflawed specimens) are presented here.

Cross sections in the circumferential-radial plane of the unflawed piping segments were polished, etched, and photographed to document the grain structures in these materials. The photographs were enlarged and used to determine average grain-size measurements via the lineal intercept method. Engineering judgment was employed to define separate regions (if existing) of the CCSS piping cross sections containing similar grain sizes and orientations; a circumferentially oriented line bisecting each of these regions was then applied and used to measure each grain that was intercepted. Measurements of the intercepted grains along this line were averaged to assess approximate grain size by region. The measurements specific to the banded region comprising the ID of the specimens are most relevant to the ET work presented here since the depth of penetration is minimal. Color coded illustrations of the various banded regions for the unflawed specimens are found in Appendix A. A review of Figures A.29, A.30, and A.31 show the variation of grain types as a function of circumferential location. Because of the large variation of grains in these specimens, different regions of the cross section have been false-colored to enable the reader to better visualize the significant range of sizes and shapes present in this early vintage CCSS.

The grain sizes listed in Table 5.1 are a function of an intercept line drawn normal to primary grain growth, which for CCSS is the radial direction. The result is that grain sizes listed are representative of the minor axis of each grain, which, in some cases, also exhibit major axes of extensive lengths.

Intermediate vintage CCSS microstructures are represented by the piping segment on loan from Westinghouse, Inc. This segment is believed to have been fabricated in the late 1960s to mid-1970s and shows consistent grain orientation and size throughout the circumference, which may indicate the casting process was becoming more refined. This segment exhibits a coarse-grained, dendritic (columnar) microstructure with a banding condition evident as well.

The most recently fabricated CCSS base material was loaned to PNNL by EPRI and was extracted from a cancelled nuclear power plant in Spain. This large blank spool piece has consistent fine-grained CCSS microstructure. Figure A.31 depicts a region of the polished and chemically etched ring, which shows the relatively fine (for CCSS) equiaxed microstructure and approximate grain size, present over the entire circumference of the segment. Again, the grain size determination was performed by the lineal intercept method as described previously. This type of microstructure is believed to represent the latest class of CCSS piping installed in primary coolant systems of later vintage Westinghouse-designed plants (circa mid-1970s through mid-1980s).

As shown in Appendix A, the cumulative average size of grains in varied regions of the CSS materials has been measured by a lineal mean intercept method. However, this average is not a reliable indicator of overall dominant grain sizes and distributions for the specimens used in this study. Table 5.2 provides more insight into a dominant ID grain size by listing the maximum measurement for each type of piping segment examined along the ID surface.

6 Eddy Current Testing Results

From a review of the data provided in Appendixes B through D, this section provides an interpretation of results of the ET data from each specimen examined in this study. To provide the reader with a baseline of information with which to make comparisons, Table 6.1 summarizes key information and true state data for each specimen. The results discussed in this section pertain specifically to the ET data acquired with a 250-kHz driving frequency. As expected, this set of data provided the best results, as the peak operating frequency (where the ET probe is most sensitive) is nominally rated at 240 kHz. Data acquired at 100 kHz and 500 kHz resulted in decreased probe sensitivity and reduced SNR. Therefore, this discussion will target the 250-kHz data. Phase plots were not generated for the Spanish spool piece, and line plots were generated for only the WOG specimens as provided in Appendix D.

Table 6.1 Summary Table of Key Information and True State Data for All Flawed Specimens in This Study

Specimen ID Descriptor	Flaw Location (Weld Side) and Material Type	Fatigue Crack Type	True State Flaw Depth (cm)	True State Flaw Length (cm)
APE-1	Elbow - SCSS	Mechanical	1.1	3.94
APE-4	Elbow - SCSS	Mechanical	1.2	4.19
INE-A-1	Elbow - SCSS	Mechanical	2.64	6.99
INE-A-4	Elbow - SCSS	Thermal	1.8	6.86
MPE-3	Elbow - SCSS	Mechanical	2.54	6.73
MPE-6	Elbow - SCSS	Thermal	1.5	5.92
ONP-D-2	Pipe - CCSS	Thermal	1.78	6.6
ONP-D-5	Pipe - CCSS	Mechanical	1.19	4.06
INE-A-5	Safe End - Wrought SS	Mechanical	2.54	6.73
ONP-3-5	Safe End - Wrought SS	Thermal	1.78	6.6
ONP-3-8	Nozzle - Wrought SS	Mechanical	1.78	5.13
OPE-2	Elbow - SCSS	Mechanical	1.27	4.19
OPE-5	Elbow - SCSS	Thermal	1.63	6.15
POP-7	Nozzle - SCSS	Mechanical	2.55	6.78
POP-8	Pipe - CCSS	Thermal	1.5	5.72
B-501	(+) Equiaxed	Thermal	2	2.92
B-504	(+) Columnar	Thermal	2.79	6.15
B-515	(+) Equiaxed	Thermally Stress Relieved- Mechanically Bent	1.52	2.92
B-519	(+) Equiaxed	Thermal	2.79	5.72
Metric units can be converted to English units by dividing by 2.54 (2.54 cm = 1 in.).				

Of the 26 specimens examined in this study, 19 contained flaws (either mechanical or thermal fatigue cracks). PNNL Specimen B-505 was designed as a calibration block for ultrasonic examinations and thus contained no cracks. The remaining spool piece segments from Southwest Research Institute, IHI Southwest Technologies Inc., Westinghouse, and the EPRI NDE Center were examined to study the effects of varying microstructures on the ET measurement response and did not contain cracks. A summary of the composite detection results for this study is found in Table 6.2.

Table 6.2 Detection Results and Measured Length Sizing for All Flawed Specimens in This Study. Signal-to-noise ratio values are listed after the specimen was degaussed.

Specimen ID Descriptor	Was Flaw Detected?/ Did Degaussing Improve SNR?	Peak Magnitude from Flaw (volts) and SNR (decibels)		Range of Phase Response from Flaw (deg.)	Measured Flaw Length (cm)	True State Flaw Length (cm)	True State Flaw Depth (cm)
		V	dB				
APE-1	Yes/No	9.77	11.8	92º - 97º	3.82	3.94	1.1
APE-4	Yes/No	8.00	16.1	50º - 115º	4.11	4.19	1.27
INE-A-1	Yes/Yes	10.12	10.6	275º- 292º	6.6	6.99	2.64
INE-A-4	Yes/No	10.20	11.4	270º- 282º	5.9	6.86	1.85
INE-A-5	Yes/Yes	10.0	15.1	200º- 290º	6.35	6.73	2.54
MPE-3	Yes/No	10.11	14.1	270º- 285º	6.12	6.73	2.54
MPE-6	Yes/No	8.42	10.5	270º- 285º	3.8	5.92	1.5
ONP-3-5	Yes/No	5.75	21.2	70º- 110º	6.4	6.6	1.78
ONP-3-8	Yes/Yes	1.20	10.7	50º- 120º	4.21	5.13	1.78
ONP-D-2	Yes/Yes	9.18	13.9	250º- 285º	5.49	6.6	1.78
ONP-D-5	Yes/No	6.58	16.4	260º- 275º	3.73	4.06	1.19
OPE-2	Yes/Yes	6.25	8.0	105º- 130º 7º - 38º	4.37	4.19	1.27
OPE-5	Yes/Yes	8.06	11.1	70º- 105º	5.58	6.15	1.63
POP-7	Yes/Yes	7.52	11.5	273º- 280º	6.72	6.78	2.55
POP-8	Yes/No	9.25	15.8	230º- 258º 80º- 150º	6.02	5.72	1.5
B-501	Yes/No	8.42	12.5	45º - 130º	2.84	2.92	2
B-504	Yes/No	6.47	14.3	260º- 285º	6.19	6.15	2.79
B-515	Yes/Yes	5.86	13.4	85º - 105º	2.87	2.92	1.52
B-519	Yes/No	4.90	16.3	260º- 285º	4.18	5.72	2.79
Root-mean-square error					0.77		
Metric units can be converted to English units by dividing by 2.54 (2.54 cm = 1 in.).							

In reviewing the data for specimen APE-1 (see Figures A.1, B.1, C.1, and D.1 in the respective appendixes), the magnitude plots provided a high-SNR (11.8-dB) flaw response. Two discontinuous facets of this crack are evident in the magnitude image plot of Figure B.1. The phase plot did not provide a suitable perspective to allow one to discern the shape, position, or continuity of the flaw to any degree. Degaussing the specimen did not improve the SNR. This flaw was readily detected above the noise and clutter and was slightly undersized in the length dimension, by 1.2 mm (0.047 in.). Length sizing results were determined by using loss-of-signal criteria.

In the case of specimen APE-4 (see Figures A.2, B.2, C.2, and D.2 in the respective appendixes), only the magnitude plots provided the capability to discriminate the crack from surrounding noise and clutter. Only a very small portion of the crack (circumferential extent) could be detected by analyzing the phase response. The SNR for the magnitude data was 16.1 dB, and the physical position of the crack relative to the surrounding noise allowed for a rather easy detection. Small high-amplitude blips (on the order of 5 mm to 10 mm in diameter or length dimension) can be observed, but these blips appear to be random occurrences of noise, clutter, grain effects, or other factors and would not be considered sufficiently continuous to have any structure or to be called a crack. Again, degaussing did not improve the SNR for this specimen. This crack was detected and slightly undersized in length by 0.8 mm (0.032 in.).

For specimen INE-A-1 (see Figures A.3, B.3, C.3, and D.3 in the respective appendixes), both magnitude and phase representations were valuable for detection, localization, and length sizing of the crack. Surrounding noise and clutter were low, and the SNR for the magnitude data was 10.6 dB. No other anomalies were detected in this specimen. In this case, degaussing the specimen did improve the eddy current response to the flaw by providing a noticeable enhancement to the peak magnitude response across the length of the crack on the image. This crack was detected and undersized in the length dimension by 3.9 mm (0.154 in.).

INE-A-4 is a specimen that contains a crack with branching (off-angle to the circumferential direction) at the ends and some slight crazing and branching throughout the middle portion of the crack as well. The data are found in Figures A.4, B.4, C.4, and D.4 in the respective appendixes. The magnitude plot representations were well suited for depicting the circumferential extent of the crack, but the off-angle branching at each end was not detected. The phase plots did provide some validation of the circumferential portion of the crack, but these images did not provide a high SNR. The SNR of the magnitude data was 11.4 dB, allowing for clear and concise detection, localization, and length sizing of the circumferential aspect of the crack. This crack was undersized by 9.6 mm (0.378 in.). Degaussing this specimen did not help improve the SNR.

In reviewing the ET data for specimen INE-A-5 (see Figures A.5, B.5, C.5 and D.5 in the respective appendixes), both magnitude and phase plot representations were useful for detection, localization, and length sizing of the crack. This is, in part, because the flaw is physically located on the forged SS safe-end side of the weld, where the surrounding noise and clutter are minimal, so a contrast between the crack and the background is significant. The SNR for the magnitude data was 15.1 dB. Once again, small high-amplitude blips (on the order of 5 mm (0.197 in.) to 8 mm (0.315 in.) in diameter or length dimension) can be observed, but they appear to be random occurrences of noise, clutter, grain effects, or other factors and were not considered sufficiently continuous to have any structure or to be called a crack. The degaussing process did provide a slight improvement toward reducing the magnitude of the surrounding background noise and clutter for this specimen. This crack was undersized in the length dimension by 3.8 mm (0.15 in.).

In the case of specimen MPE-3 (see Figures A.6, B.6, C.6, and D.6 in the respective appendixes), both magnitude and phase plots were very useful for detection, localization, and length sizing of the crack. The SNR for the magnitude data was 14.1 dB. The crack was easily detected from the ET data, as the surrounding background noise and clutter are minimal. It is evident that the ID surface conditions relative to the size of the probe were somewhat problematic, as the phase plots show circumferential loss of signal response, indicating consistent coupling issues that correspond to the sharp counterbore facets on this

specimen. Degaussing did not improve the SNR for this specimen. The crack was undersized in the length dimension by 6.1 mm (0.24 in.).

Similar to specimen INE-A-4, MPE-6 contains a crack with both axial and circumferential branching (off-angle to both directions) at the ends and along the middle of its extent. The data can be found in Figures A.7, B.7, C.7, and D.7 in the respective appendixes. The magnitude plot representations were well suited for depicting the circumferential extent of the crack, but the off-angle branching (both axial and circumferential aspects) was not detected. The phase plots did provide some validation of the circumferential portion of the crack, but these images did not provide a high SNR. The SNR of the magnitude data was 10.5 dB, allowing for clear detection, localization, and length sizing of the primary circumferential aspect of the crack. This crack was undersized by 21.2 mm (0.835 in.). Degaussing this specimen did not help improve the SNR.

Specimen ONP-3-5 contains a crack with branching at the ends and minimal branching from the middle segments of the crack. However, this crack lies on the forged SS safe-end side of a nozzle-to-safe-end weld where the background noise and surrounding clutter are very low, allowing the ET probe to show great contrast between the magnitude of the crack and the surrounding parent material. The data for this specimen can be found in Figures A.8, B.8, C.8 and D.8 in the respective appendixes. Both phase and magnitude representations were quite suitable for crack detection, localization, and length sizing, as the magnitude SNR was 21.2 dB, the highest for all of the specimens scanned. The phase response between 70º and 110º showed a high contrast in the C-scan image. The crack was undersized in the length dimension by 2.0 mm (0.079 in.).

In reviewing data for specimen ONP-3-8, the SNR for the magnitude data was 10.7 dB. The data for this specimen can be found in Figures A.9, B.9, C.9, and D.9 in the respective appendixes. Again, this crack was located on the forged SS safe-end side of a nozzle-to-safe-end weld where the surrounding background noise and clutter were low. Both the magnitude and phase representations were useful in detecting and length sizing this crack, as the phase response showed sensitivity to the crack over the range of 50º to 120º. This crack was undersized in length by 9.2 mm (0.362 in.). Degaussing did provide an improvement toward the reduction of background clutter on the magnitude plots for this specimen.

Specimen ONP-D-2 contains a crack with multiple facets, significant off-angle crazing and branching in the axial direction, and a circumferentially oriented crack with branching on the ends as well. The crack is located on the centrifugally cast pipe side of the weld. The data for this specimen can be found in Figures A.10, B.10, C.10, and D.10 in the respective appendixes. The two areas of agglomeration of miniature cracks were difficult to detect; however, some of the larger facets of this crazing and branching were evident in both phase and magnitude plots. Degaussing provided significant enhancement to the reduction of clutter and background noise while providing an increase to the signal response from the primary portion of the circumferentially oriented crack. The SNR for the magnitude data was 13.9 dB. The crack length was undersized by 11.1 mm (0.437 in.).

In the case of specimen ONP-D-5, both magnitude and phase plots were very useful for detection, localization, and length sizing of the crack. The data for this specimen can be found in Figures A.11, B.11, C.11, and D.11 in the respective appendixes. The SNR for the magnitude data was 16.4 dB. The crack is easily detected from the ET data, as the surrounding background noise and clutter are minimal

from both safe-end and cast pipe sides of the weld. Degaussing did not improve the SNR for this specimen. The crack was undersized in the length dimension by 3.3 mm (0.13 in.).

In reviewing data for specimen OPE-2 (see Figures A.12, B.12, C.12, and D.12 in the respective appendixes), only the magnitude and line plot representations exhibit enough contrast to visually detect the crack and effectively discriminate it from the background clutter and surrounding noise. Some portion of the crack can be seen from the phase response, which showed minimal sensitivity over the ranges between 7º and 38º and additionally between 105º and 130º. The SNR for the magnitude data was 8.0 dB. Once again, small high-amplitude blips (on the order of 2 mm (0.079 in.) to 4 mm (0.158 in.) in diameter or length dimension) can be observed, but they appear to be random occurrences of noise, clutter, grain effects, or other factors and were not considered sufficiently continuous to have any structure or to be called a crack. Degaussing did indeed improve the contrast and reduce the amplitude of clutter for the magnitude data for this specimen. This crack was oversized in the length dimension by 1.8 mm (0.071 in.).

Specimen OPE-5 contains a crack that has long and extended branching from one end that traverses off-angle in the axial direction, relative to the circumferential extent of the primary segment of the crack. The data for this specimen can be found in Figures A.13, B.13, C.13, and D.13 in the respective appendixes. Both phase and magnitude representations depict most of the circumferential portion of the crack, but only short segments of the branching portions are detectable from these data. The SNR for the magnitude data was 11.1 dB. From the magnitude data, it is evident that the clutter and noise from background factors are significantly higher in amplitude on the centrifugally cast pipe side than from the statically cast elbow side. Degaussing resulted in an improved magnitude image where the crack response was increased in amplitude and the general clutter and background noise were slightly reduced in amplitude. The primary circumferential portion of this crack was easily detected. The crack was undersized in length by 5.7 mm (0.224 in.).

In reviewing the data for specimen POP-7 (see Figures A.14, B.14, C.14, and D.14 in the respective appendixes), it is evident from both magnitude and phase representations that the crack is detectable. The SNR for magnitude data was 11.5 dB. This crack does not exhibit branching or crazing and was undersized in length by 0.6 mm (0.024 in.). Degaussing the specimen improved the magnitude response from the crack and resulted in a slight reduction of the background clutter and surrounding noise as well. On the elbow side of the weld, small high-amplitude blips (on the order of 5 mm (0.197 in.) to 8 mm (0.315 in.) in diameter or length dimension) can be observed, but again, these appear to be random occurrences of noise, clutter, grain effects, or other factors and were not considered sufficiently continuous to have any structure or to be called a crack.

Specimen POP-8 contains a crack with multiple facets, significant off-angle crazing and branching in the axial direction, and a circumferentially oriented crack with branching on the ends as well. The data for this specimen can be found in Figures A.15, B.15, C.15, and D.15 in the respective appendixes. This crack does not have much circumferential extent but rather exhibits a near star-like pattern with short facets emanating in multiple directions. The cracking network is located on both sides of the weld, with most of the deepest portions located on the elbow side of the weld. These miniature cracks were difficult to detect; primarily the shorter, circumferential aspect of the crack was detected. Both phase and magnitude plots showed sufficient contrast between background noise/clutter and crack response, so that this portion of the crack could be detected, localized, and length-sized. Degaussing did not provide any

improvements to these data. The SNR for the magnitude data was 15.8 dB. The crack length was oversized by 3.0 mm (0.118 in.).

Specimen B501 contains a thermal fatigue crack on the columnar side of the weld centerline, with both axial and circumferential branching (off-angle to both directions) in a swirling pattern. The data for this specimen can be found in Figures A.16, B.16, C.16, and D.16 in the respective appendixes. This crack was difficult to detect with the probe in the conventional orientation for maximum sensitivity to circumferentially oriented flaws. When the probe was oriented at 45º to the normal scanning convention, the probe was more sensitive to the off-angle crack branching and was better at detecting this flaw. Both magnitude and phase plot representations were well suited for depicting this crack as well as some aspects of the off-angle branching. The phase plots did provide good validation of the circumferential aspects of the crack. The SNR of the magnitude data was 12.5 dB, allowing for clear detection, localization, and length sizing. This crack was undersized by 0.8 mm (0.032 in.). Degaussing did not help improve the SNR; however, the background clutter and surrounding noise were relatively low in this specimen.

Specimen B504 contains a crack with both axial and circumferential branching (off-angle to both directions) at one end and along the middle of its extent. The data for this specimen can be found in Figures A.17, B.17, C.17, and D.17 in the respective appendixes. Both magnitude and phase plot representations were well suited for depicting this crack as well as the off-angle branching. The phase plots did provide good validation of the crack branching and the circumferential extent of the crack. The SNR of the magnitude data was 14.3 dB, allowing for clear detection, localization, and length sizing. This crack was oversized by 0.4 mm (0.016 in.). Degaussing did not help improve the SNR; however, the background clutter and surrounding noise were very low in this specimen.

Specimen B515 contains a rather short circumferentially oriented crack with an axial component that branches from the middle segment of the crack length almost like the letter T. The data for this specimen can be found in Figures A.18, B.18, C.18, and D.18 in the respective appendixes. Only the magnitude plot representation was well suited for depicting this crack as well as the off-angle branching. The phase plots did not provide good validation of the crack branching or the circumferential extent of the crack. The SNR of the magnitude data was 13.4 dB, allowing for clear detection, localization, and length sizing. This crack was undersized by 0.5 mm (0.02 in.). Degaussing did indeed improve the SNR by slightly magnifying the amplitude of the crack while simultaneously reducing the background clutter and surrounding noise.

Specimen B519 contains a crack with both axial and circumferential branching and some crazing in a hemispherical pattern (sometimes referred to as a crack cluster). The data for this specimen can be found in Figures A.19, B.19, C.19, and D.19 in the respective appendixes. Both magnitude and phase plot representations were well suited for depicting this crack as well as the off-angle branching and crazing. The phase plots did provide good validation of the crack branching and the circumferential extent of the crack as well. The SNR of the magnitude data was 16.3 dB, allowing for clear detection, localization, and length sizing. This crack was undersized by 15.4 mm (0.606 in.). Degaussing of this specimen did not help improve the SNR; however, the background clutter and surrounding noise were very low in this specimen.

Seven other specimens were evaluated to assess the effects of microstructure variation on eddy current response and sensitivity levels. These specimens were blank (containing no cracks) and consisted of a

diverse array of microstructures, grain distributions, sizes, and orientations. Table 6.3 summarizes the key outcomes from these evaluations.

Table 6.3 Eddy Current Testing Measurement Results for All Unflawed Specimens in This Study

Specimen ID Descriptor	Did Degaussing Reduce Noise?	False Call (called a crack in a blank specimen)	Average Background Noise Levels (volts)	Peak Magnitude from Anomalous Blips on the Specimens (volts)
EPRI Spool Piece	N/A	No	1.6	6
PNNL B-505	N/A	No	1.1	5.75
AAD #1	N/A	No	1.25	5
AAD #2	N/A	No	1.25	5
AAD #3	N/A	No	1	4.5
Westinghouse Specimen	N/A	No	1.8	6
IHI Southwest Technologies Inc. Specimen	N/A	No	2.75	7.5

The Spanish spool piece on loan from the EPRI NDE Center was a complete pipe segment. The data acquisition system configuration precluded full 360º scanning, so the entire spool piece was scanned in quadrants, where the full circumference was divided into 10 partitioned quadrants. Scans were conducted at both end locations (one from the right end and two from the left end) of the spool piece. The scanned area dimensions for each quadrant were approximately 25.4 cm (10.0 in.) in axial extent (longitudinal axes of the spool piece) by 22.2 cm. (8.75 in.) in circumferential distance. Although this piece was considered a relatively fine-grained equiaxed microstructure, the measured background noise and general clutter varied significantly from quadrant to quadrant, as seen in Table 6.4. Also noteworthy is the comparison of the general noise and clutter levels of the two different ends of the spool piece, revealing that the right end exhibited consistently higher background noise levels than the opposite (left) end of the spool piece. No phase plots were generated for this specimen.

Data acquisition settings and gain were identical for scans acquired at both ends of the spool piece. Access limitations precluded scanning of quadrants 9 and 10 on the left end of this specimen. A review of the background noise indicates that the left end exhibited approximately 5 dB less background noise related to microstructure than that of the opposite end. Quadrants 1 and 2 on the right side of the spool piece contained a number of ID surface anomalies that included surface scratches, surface gouges, and slag mounds (from the flame cutting process used to remove the pipe) that were readily detected by the plus-point ET probe.

PNNL specimen B-505 was fabricated with a number of calibration reflectors, but many were not surface breaking. This specimen was considered blank in the areas scanned and exhibited rather low background noise and clutter levels. Two anomalous but small high-amplitude blips (on the order of 3 mm (0.118 in.) to 5 mm (0.197 in.) in diameter or length dimension) can be observed on the columnar side of the weld, but these blips appear to be random occurrences of noise, clutter, grain effects, or other factors and would

Table 6.4 Eddy Current Testing Average Magnitude Values (volts) for Background Noise as a Function of Spatial Position (by quadrant) and as a Function of Either End of the Spool Piece

Spanish Spool Piece Quadrant Number	Right End of Spool Piece Average Background Noise Level – Magnitude (volts)	Left End of Spool Piece Average Background Noise Level – Magnitude (volts)
1	1.5	0.5
2	1.9	1
3	2.1	0.75
4	3	1.1
5	2.8	1.8
6	1.75	0.9
7	2	1.8
8	1.8	1.3
9	1.8	Access Restricted
10	1.6	Access Restricted
Average Noise Response	2.03	1.14

not be considered sufficiently continuous to have any structure or to be called a crack. Once again, however, the phase plots did not validate the detectability of these hot spots. This specimen contained both columnar and equiaxed microstructures. Both magnitude and phase representations indicated a moderate background noise level on the columnar side of the weld and reduced background noise on the equiaxed side of the weld. Degaussing did not improve the overall noise levels for this specimen.

Specimens AAD#1, AAD#2, and AAD#3 provided a diverse array of very coarse-grained microstructures, randomly patterned distributions, and large average grain diameters. These specimens exhibited anisotropic and highly nonhomogeneous microstructures, but no welds were fabricated into these specimens. The magnitude and phase representations resulting from these thick and coarse-grained specimens exhibited surprisingly low background noise conditions and little clutter over the entire scanned areas. Specimens AAD#1 and AAD#3 had x-y scan dimensions of 16.5 cm (6.5 in.) in circumferential extent by 12.7 cm (5.0 in.) in axial extent, while AAD#2 (the larger of the three specimens) had scan dimensions of 19.7 cm (7.75 in.) in circumferential extent and 15.2 cm (6.0 in.) in axial length. Degaussing did not reduce the background noise or clutter in any of these specimens.

Eddy current testing results from raster scans of the ID of the Westinghouse and IHI Southwest Technologies Inc. spool pieces provided information related to background noise effects as a function of microstructural parameters such as grain size, orientation, ferritic content, and distribution patterns. An example of the magnitude image of the background ET response from the IHI Southwest Technologies Inc. specimen can be seen in Figure 6.1.

Signal-to-noise ratios from baseline ID surface scans varied somewhat but did not show significant differences in background noise values (attributed to the microstructural variations, permeability variations, changes in ferritic content) across different sections of the same spool piece. It was noted that probe orientation did have an effect on the background noise when two scans of identical sections on the

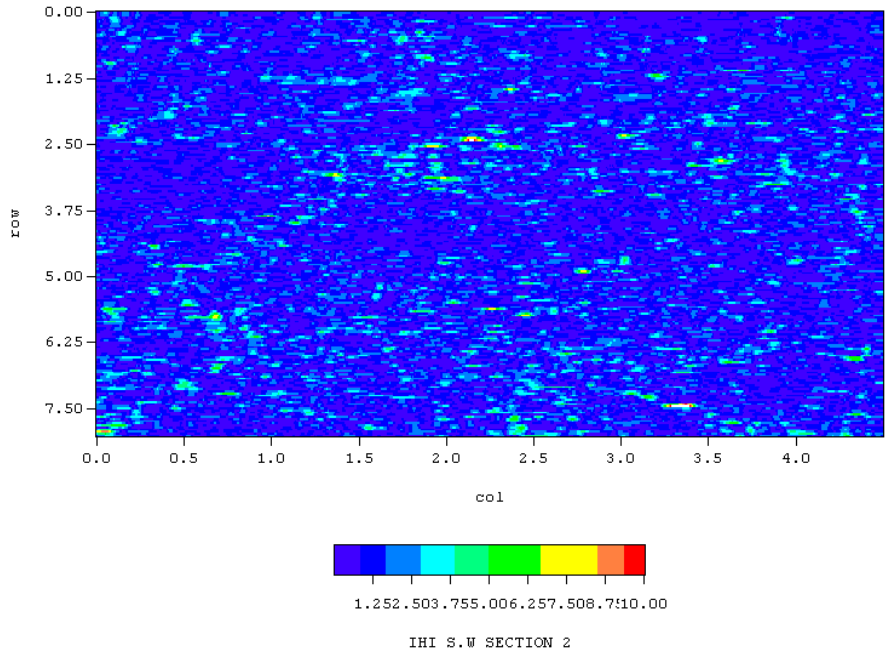

Figure 6.1 Eddy Current Testing Magnitude Image Showing Background Noise from the Microstructural Variations in the IHI Southwest Technologies Inc. Specimen. English units can be converted to metric units by multiplying by 2.54 (1 in. = 2.54 cm).

spool piece were compared. Figure 6.2 illustrates the impact on signal-to-noise of the ET data based upon a 45º shift in probe orientation. The data here show an increase of more than 10 dB in the background noise due to the probe orientation shift.

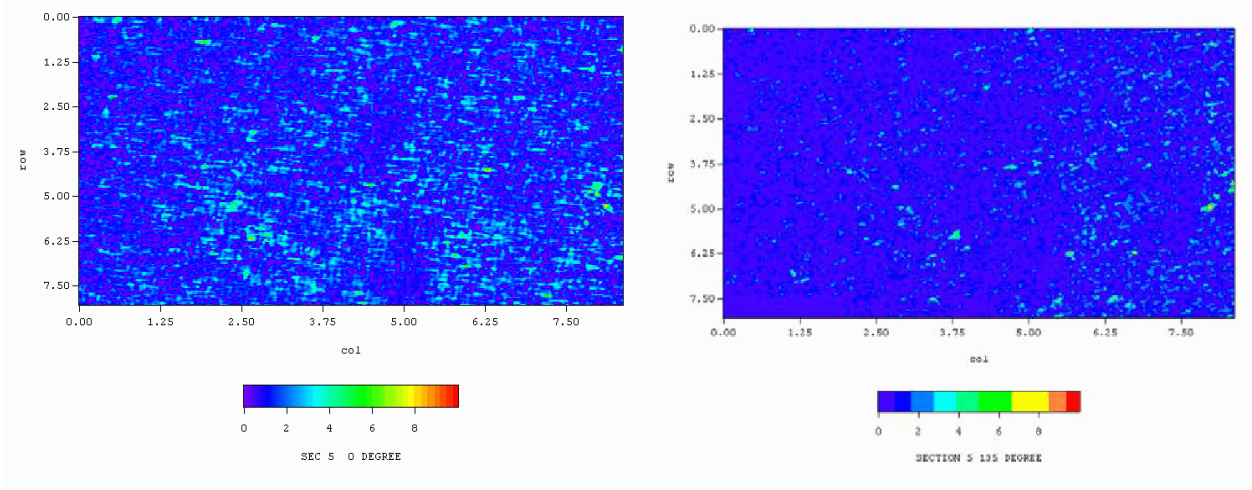

Figure 6.2 Eddy Current Testing Magnitude Image of Section 5 of the Westinghouse Spool Piece. English units can be converted to metric units by multiplying by 2.54 (1 in. = 2.54 cm).

A visual analysis indicates a slight increase in background signal amplitudes based solely upon probe orientation and the effects attributed to microstructural grain orientation relative to the ET probe axis. Although the IHI Southwest Technologies Inc. spool piece exhibited a highly nonuniform, coarse-grained microstructure relative to the columnar grain orientation of the Westinghouse specimen, the ET data did not provide a means to correlate grain patterns, size, and distribution with magnitude data. In general, the noise levels were comparable to those seen from the WOG specimens. Eddy current testing magnitude plots of all unflawed specimens and spool pieces can be found in Appendix B.

7 Discussion and Conclusions

The WOG specimens used in this study do not represent worst-case field conditions with regard to weld root conditions, counterbore facets, surface roughness, or mismatch. The IHI Southwest Technologies Inc. specimen exhibiting very coarse-grained and multibanded macrostructures is more representative of field conditions in some plants constructed in the late 1960s and early 1970s and is considered to represent worst-case conditions. This specimen provided a high level of difficulty for coherent sound propagation and ultrasonic inspection. The ID conditions of the PNNL specimens may be considered optimal as the inside surfaces and root conditions have been ground smooth, while the counterbore facets are shallow and do not hinder the inspections. With regard to the WOG specimens, the ID conditions are considered to be of intermediate difficulty in terms of the impact of the ID surface geometry on the inspection process. These specimens were fabricated from a diverse array of materials that include stainless steel cladding, alloy 182/82 buttering, forged stainless steel, alloy 182/82 welds, statically cast and centrifugally cast stainless steel, wrought austenitic stainless steel, and carbon steel.

Data obtained via ET techniques to characterize the ID surface of each specimen were used to plot magnitude and phase responses, generating topographical C-scan x-y representations of the data for enhanced visualization. An example of the imaged eddy current data is shown in Figure 7.1. In analyzing the ET data, loss of signal was used for length sizing the indications.

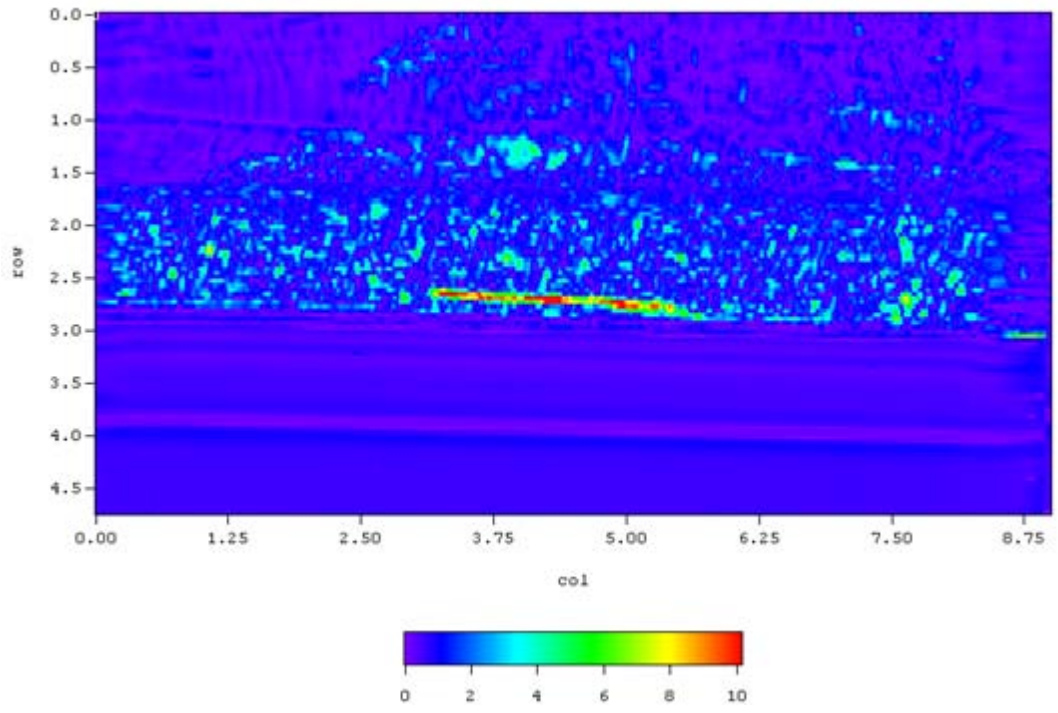

Figure 7.1 Degaussed Magnitude Plot of WOG Specimen INE-A-1 at 250 kHz. English units can be converted to metric units by multiplying by 2.54 (1 in. = 2.54 cm).

From this analysis, all 19 specimens that contained surface-breaking cracks on the inside surface were detected by the loss-of-signal methodology. With regard to length sizing, 16 of the 19 specimens containing flaws in the study were undersized, and the associated length root-mean-square error (RMSE) was 7.7 mm (0.30 in.). As the ASME Code requires the length sizing RMSE to be less than 19 mm (0.75 in.), the ET data provided here are well under 50% of this value. Three flaws were oversized, and the largest length difference was oversized by 3.0 mm (0.12 in.). Noise signals having high amplitude and correct phase, and of substantial length, shape, and continuity that could be confused with crack signals, were not prevalent in the data. This study eliminated all responses less than 12.5 mm (0.50 in.) from consideration as a crack, and, as such, no false calls were reported.

Sparsely scattered anomalous, but dimensionally small high-amplitude responses (on the order of 2 mm to 10 mm (0.394 in.) in diameter or length dimension) were observed on approximately 20% of the specimens. These high-amplitude responses that typically occur only in the magnitude representation appear to be random occurrences of noise, clutter, grain effects, or other probe translational factors and would not be considered sufficiently continuous to have any structure or to be called a crack, based upon the general criteria used for detection in this study. These criteria include relying primarily on the magnitude responses for detection of initial hot spots and then looking to the phase response plots for possible validation. The surrounding pattern of clutter and background noise also must be considered in visually discriminating between anomalous amplitude responses and those responses that are clustered and show some shape and continuity. Finally, the associated length or extent also is considered, where typical responses 12.5 mm (0.5 in.) and less in length are considered noncrack responses unless detected in proximity to other amplitude responses of similar intensity or where a pattern starts to develop.

A review of the composite noise data derived a correlation between background noise levels (from the ET magnitude or phase response) and the variables of microstructural grain size and casting method (static versus centrifugal). When comparing ET data acquired from CSS versus that from isotropic, homogeneous, fine-grained materials like forged stainless steel and carbon steel or clad carbon steel, significant measured differences in background noise levels were evident in the data. These materials (in contrast to the cast steels) exhibited significantly lower levels of background noise and clutter, on the order of 10 dB to 15 dB lower than their statically or centrifugally cast counterparts. Slight variations in background noise were evident as a function of probe rotation relative to the orientation of the grain distribution/microstructure, but these variations were not significant.

From a review of the results provided in Table 6.2, mechanical fatigue cracks in the SCSS specimens exhibited signal-to-noise ratios ranging between 8.0 dB and 11.5 dB. The ET data from thermal fatigue cracks in the SCSS specimens exhibited similar signal-to-noise ratios ranging between 10.5 dB and 11.4 dB. In contrast, for CCSS specimens, mechanical fatigue cracks in the specimens resulted in signal-to-noise ratios ranging from 14.1 dB to 16.4 dB. Also, for thermal fatigue cracks in CCSS, the ET data resulted in higher signal-to-noise ratios as well, ranging between 12.5 dB and 15.8 dB. Thus, regardless of the type of fatigue crack detected, the ET data indicate a lower overall SNR in SCSS material (by nearly a factor of 6 dB) than in CCSS material. For all CCSS specimens examined in this study (with the exception of ONP-D-2), degaussing did not improve the SNR; however, the data indicate that degaussing was generally more effective in SCSS specimens.

There are a number of primary factors that contribute to the wide variation in the SNR resulting from this study. These factors can be correlated to the coupling of the ET sensor to the ID surface (a function of the

surface roughness and ID geometry), flaw orientation, morphology (relative to the sensor orientation and geometrical features on the ID), microstructural variations, changes in ferritic content as a function of spatial position (and near surface depth to a lesser degree), and variations in permeability. It is difficult to isolate which of these factors are dominate in their effects on the SNR with the limited amount of sample specimens and number of inspection trials conducted. However, the general trend does indeed indicate that when employing the ET methodology, detection of surface-breaking cracks is relatively easier on CCSS material than on SCSS material due to the consistent difference in SNR. Since the average range of grain diameters in SCSS (12 mm to 15 mm) is less than that of their CCSS counterparts (17 mm to 20 mm), with all other variables being relatively equal, this suggests that the ET SNR may be primarily driven by changes attributed to the number of grains at the surface, their orientation and the material variations in ferritic content and/or permeability, rather than sensor orientation, lift-off, geometry or crack characteristics. In the CCSS specimens studied here, the number of grain boundaries per unit area is generally less, due to their larger average grain diameter, than in SCSS, thus leading to an increase in SNR for cracks in CCSS specimens and a relative decrease in SNR for cracks in SCSS specimens.

The chemical composition of CSS material may vary widely by weight percent, and the ferrite content, spacing (distribution), and morphology can vary widely as well. In some cases, as with the CF-8M grade of CSS material, the ferrite content can approach 30% by volume (Chopra 1991). Over time, it is thought that the ferrite content in CSS materials will become magnetized and aligned, perhaps by the earth's magnetic field. The magnetic characteristics of the ferrite in CSS will have an effect upon the eddy current response at the surface of the part.

To reduce this effect and essentially randomize the magnetization of the ferrite material, a degaussing process was implemented. Degaussing was performed by using a 30.5-cm (12-in.)-diameter coil of wire hooked up to 120 V alternating current and then slowly moving the coil close to and across the inspection surface.

Demagnetizing the inspection zones proved useful in 8 out of 19 cases (42% of the time) where the degaussing process resulted in a quantifiably higher SNR. The magnitude plot in Figure 7.2 is the original magnitude representation of the ET data for specimen POP-7. In contrast, the degaussed magnitude plot in Figure 7.3 of the same specimen illustrates a significant enhancement of the SNR for this specimen. It is unclear why this process improves the magnitude response from the flaws and reduces background noise and surrounding clutter in nearly half of the specimens but fails to show any improvement in the other half.

Overall, the ET methodology was very effective with regard to detection performance in that all of the cracks were detected. Both magnitude and phase response images often were useful in detecting the cracks. As with all NDE inspections, advances in probe design eventually lead to improved detection performance; it is worth noting that the off-angle sensitivity issues discussed and quantified in Section 4 play a key role in defining the detection performance for ET as a function of crack orientation and directionality. It is evident from this study that even by employing a plus-point probe for enhanced dual-axis sensitivity; one must consider a multiple scan protocol where the probe is rotated incrementally as a function of angle to provide suitable sensitivity for detection of cracking across the full spectrum of angular orientations. Probe decoupling was evident on a few data sets, requiring subsequent re-scanning of these areas. The need to employ smaller, highly sensitive ET probe assemblies that allow for more

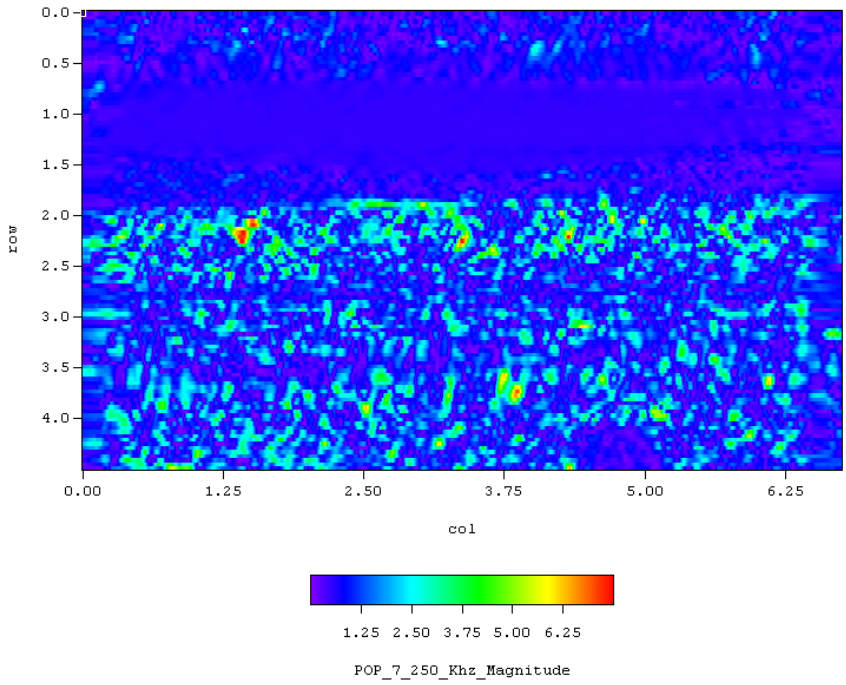

Figure 7.2 Original Magnitude Plot of WOG Specimen POP-7 at 250 kHz. To convert English units to metric, multiply by 2.54 (1 in. = 2.54 cm).

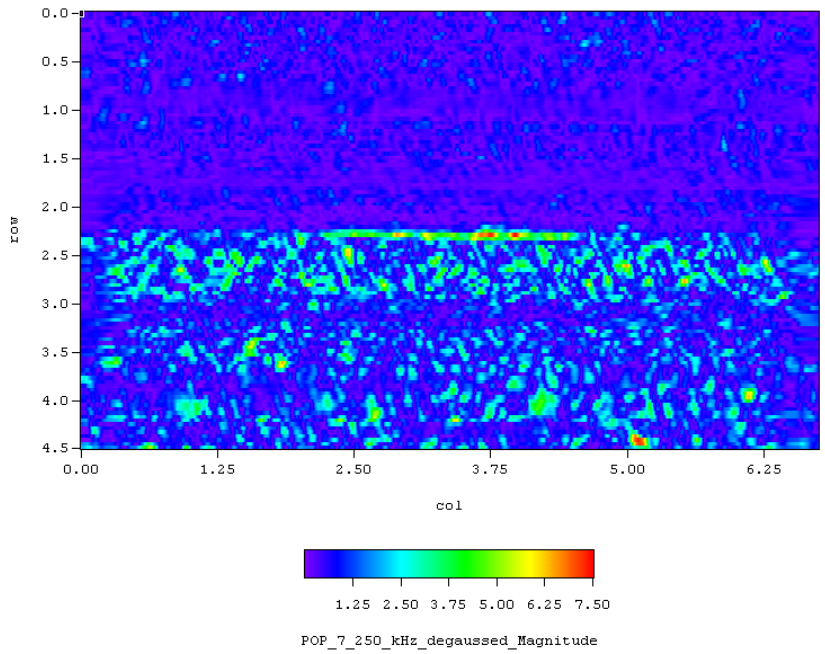

Figure 7.3 Degaussed Magnitude Plot of WOG Specimen POP-7 at 250 kHz. To convert English units to metric, multiply by 2.54 (1 in. = 2.54 cm).

effective coupling at the counterbore transitions is key to addressing all of the challenging ID conditions that may be encountered in the field. Finally, probe orientation issues should be addressed to maximize the potential for detecting off-angle cracking, clustering, and faceting of some types of cracks. The data here do not indicate that probe orientation will significantly affect background noise levels as microstructures and grain size/distribution vary, but direct evidence from this work shows increased sensitivity to off-angle flaws by reorienting the probe by 45º.

Characterizing the causes for anomalous high-amplitude signals based upon a better understanding of the physical phenomena between the eddy current field and the various microstructures would greatly benefit data analysis and interpretation. The results of this work indicate that the effects of the eddy current field as a function of microstructure, grain size, orientation, and distribution as well as probe frequency and spatial variations in permeability will not degrade probe sensitivity or detection performance of an ET approach if access to the ID is available. For industry to employ an effective ET approach from the ID, a number of issues still remain unresolved. These include quantifying the effects of worst-case ID surface conditions on the performance reliability of the technique and addressing closure weld conditions and detection reliability for both circumferential and axial cracking in CSS and dissimilar metal weld components. Also, with regard to probe design and implementation, a better understanding of the sensitivity and response characteristics of plus-point ET probes is needed as they pertain to crack morphology and crack orientation in CSS materials. Finally, data associated with identifying and assessing detection capabilities and weaknesses associated with crack orientation variability and crack type (e.g., cracking resulting from intergranular stress corrosion, irradiation-assisted stress corrosion, primary water stress corrosion, thermal fatigue, mechanical fatigue) in CSS components would help develop the foundation for a more effective and reliable implementation of this approach by industry.

Should industry consider the use of ET in the ISI of primary loop components, the use of remote visual inspection in combination with the ET methodology may provide improvements in detection performance by combining the two methodologies on a single platform. In this way, the inspector could more effectively correlate visual surface conditions with eddy current responses in near real time (Cumblidge et al. 2004).

In summary, if the inner surface is accessible, the ET method demonstrated here is very effective for detection of surface-breaking cracks. It should be noted that this technique provided valuable detection capabilities and length sizing but will not provide depth sizing information. The crack identification criteria employed in this study essentially eliminated all responses less than 12.5 mm (0.50 in.) from consideration as a crack, and as such, no false calls were reported from these data. Both magnitude and phase response information provided value in detecting cracks in these materials, while demagnetization enhanced overall SNR in approximately 42% of the specimens.

8 References

ASTM International. 1997. "Metals Test Methods and Analytical Procedures, Volume 03.03, Nondestructive Testing." Section 3 in *Annual Book of ASTM Standards*. American Society for Testing and Materials, West Conshohocken, Pennsylvania.

Cecco VS, G Van Drunen, and FL Sharp. 1983. "Test Method." Volume 1 in *Eddy Current Manual*. AECL-7523 Rev. 1, Atomic Energy of Canada Limited, Chalk River Nuclear Laboratories, Chalk River, Ontario, Canada.

Chopra OK. 1991. *Long-Term Embrittlement of Cast Duplex Stainless Steels in LWR Systems*. Semiannual Report, October 1990 – March 1991. ANL-91/22, NUREG/CR-4744, Vol. 6, No.1, U.S. Nuclear Regulatory Commission, Washington, D.C.

Cumblidge SE, MT Anderson, and SR Doctor. 2004. *An Assessment of Visual Testing*. NUREG/CR-6860, U.S. Nuclear Regulatory Commission, Washington, D.C.

Diaz AA, SR Doctor, BP Hildebrand, FA Simonen, GJ Schuster, ES Andersen, GP McDonald, and RD Hasse. 1998. *Evaluation of Ultrasonic Inspection Techniques for Coarse-Grained Materials*. NUREG/CR-6594, PNNL-11171, U.S. Nuclear Regulatory Commission, Washington, D.C.

Doctor SR, MT Anderson, AA Diaz, and SE Cumblidge. 2005. "Progress in the Reliable Inspection of Cast Stainless Steel Reactor Piping Components." Presented to the 18th International Conference on Structural Mechanics in Reactor Technology (SMiRT 18), August 7-12, 2005, Beijing, China.

Fortner Research LLC. 1996. *Transform User's Guide (Windows Version)*. Fortner Research LLC, Sterling, Virginia.

General Dynamics. 1979. *Nondestructive Testing – Eddy Current*. 2nd ed. Classroom Training Handbook CT-6-5, Convair Division, General Dynamics, San Diego, California.

Hagemaier DJ. 1990. *Fundamentals of Eddy Current Testing*. American Society for Nondestructive Testing, Columbus, Ohio.

Lamtenzan D, G Washer, and M Lozev. 2000. *Detection and Sizing of Cracks in Structural Steel Using the Eddy Current Method*. Report No. FHWA-RD-00-018, U.S. Department of Transportation, Federal Highway Administration, Washington, D.C.

Libby HL. 1971. *Introduction to Electromagnetic Nondestructive Test Methods*. John Wiley & Sons, Inc., New York.

McIntire P (ed.). 1986. "Electromagnetic Testing – Eddy Current, Flux Leakage and Microwave Nondestructive Testing." Volume 4 in *Nondestructive Testing Handbook*. American Society for Nondestructive Testing, Columbus, Ohio.

Rao GV, DE Seeger, Jr, C DeFlitch, JA Hoffman, RA Rees, and WR Junker. 2001. *Metallurgical Investigation of Cracking in the Reactor Vessel Alpha Loop Hot Leg Nozzle to Pipe Weld at the V. C. Summer Nuclear Generating Station*. WCAP-15616, Westinghouse Electric Company LLC, Pittsburgh, Pennsylvania.

Taylor TT. 1984. *An Evaluation of Manual Ultrasonic Inspection of Cast Stainless Steel Piping*. NUREG/CR-3753, PNL-5070, U.S. Nuclear Regulatory Commission, Washington, D.C.

Appendix A

Supplemental Photographs of Cast Stainless Steel Specimens

Appendix A

Supplemental Photographs of Cast Stainless Steel Specimens

All rulers shown in the Appendix A figures are in units of inches (25.4 mm).

Figure A.1 WOG Specimen APE-1

Figure A.2 WOG Specimen APE-4

Figure A.3 WOG Specimen INE-A-1

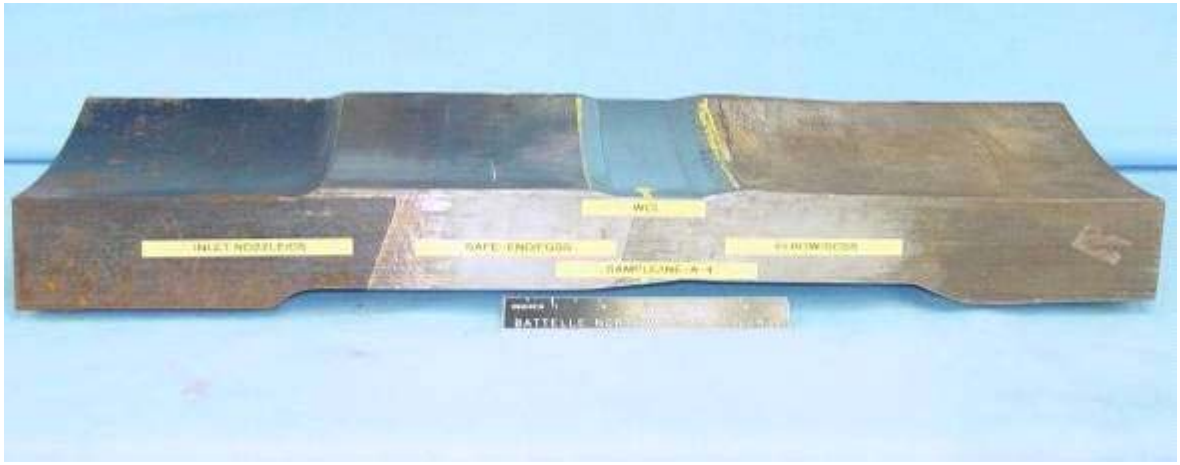

Figure A.4 WOG Specimen INE-A-4

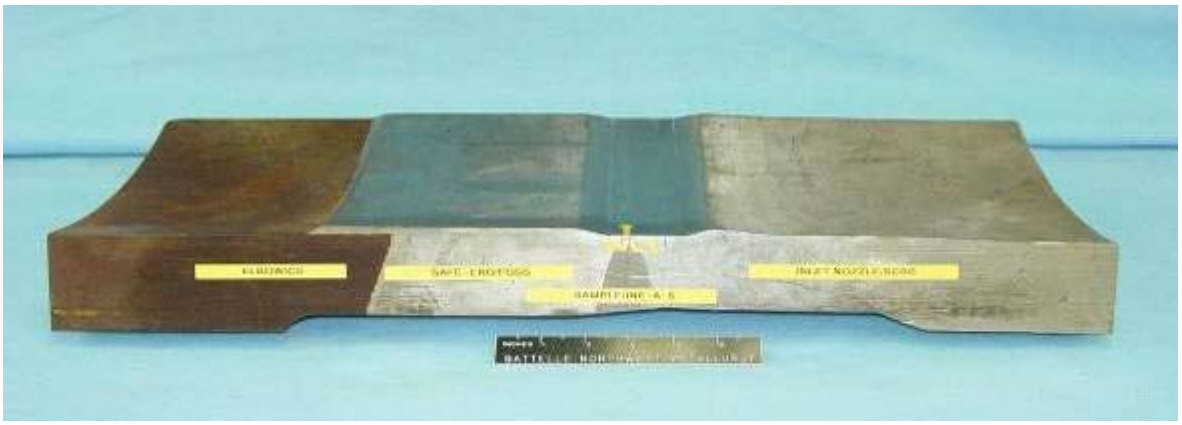

Figure A.5 WOG Specimen INE-A-5

Figure A.6 WOG Specimen MPE-3

Figure A.7 WOG Specimen MPE-6

Figure A.8 WOG Specimen ONP-D-2

Figure A.9 WOG Specimen ONP-D-5

Figure A.10 WOG Specimen ONP-3-5

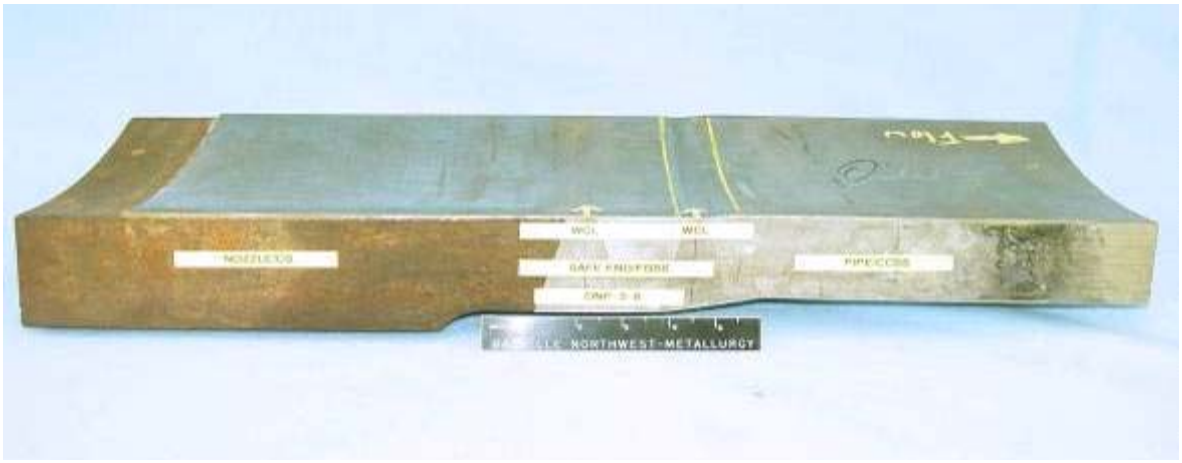

Figure A.11 WOG Specimen ONP-3-8

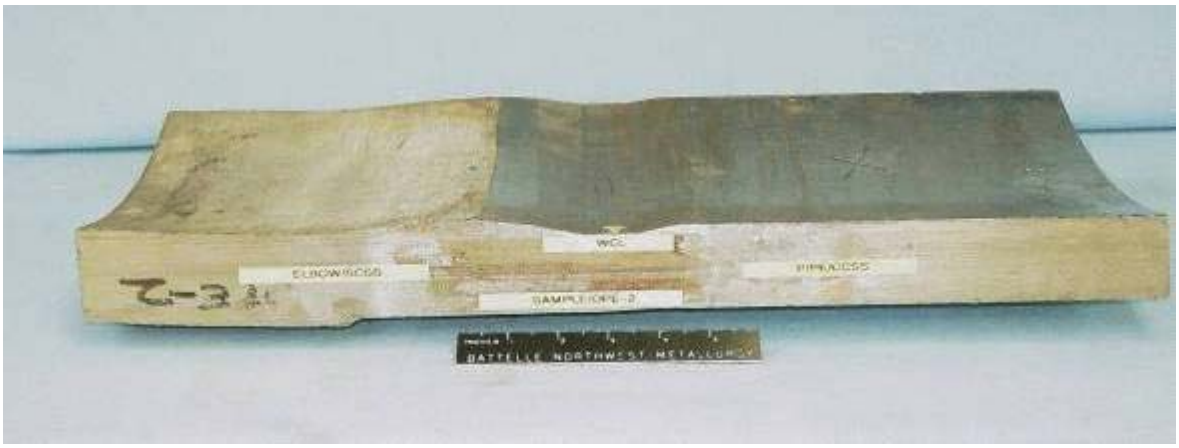

Figure A.12 WOG Specimen OPE-2

Figure A.13 WOG Specimen OPE-5

Figure A.14 WOG Specimen POP-7

Figure A.15 WOG Specimen POP-8

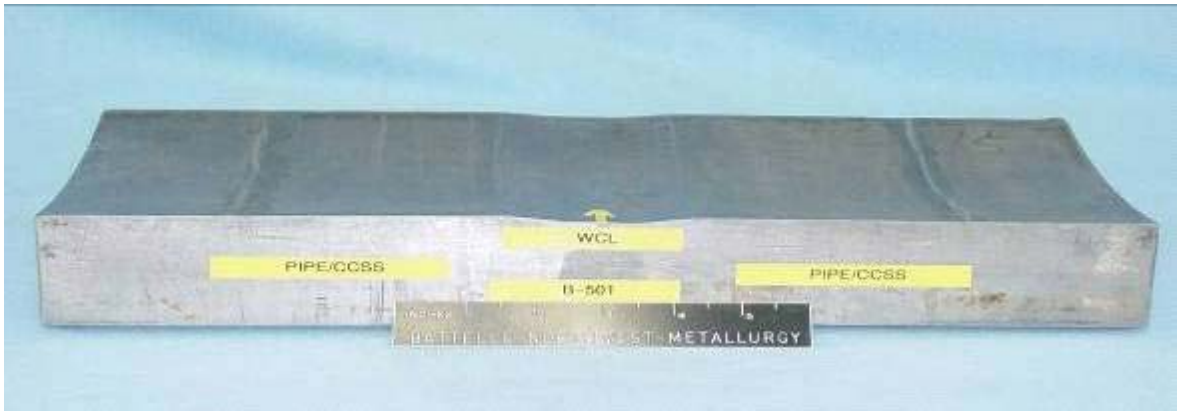

Figure A.16 PNNL Specimen B-501

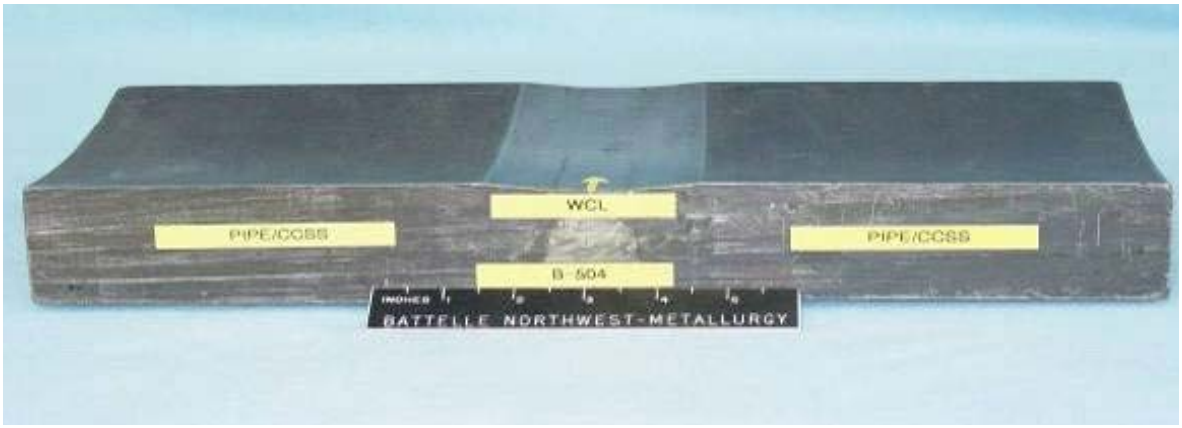

Figure A.17 PNNL Specimen B-504

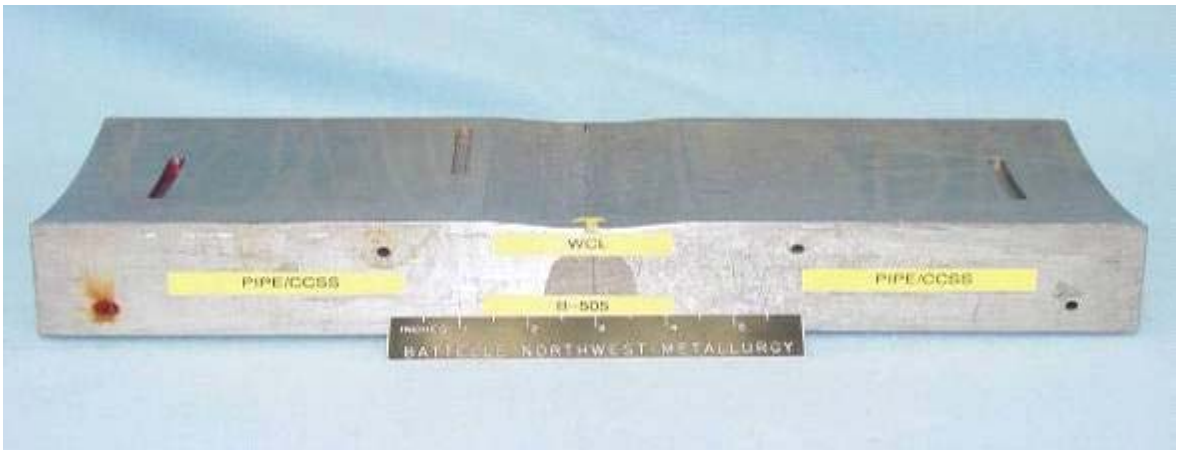

Figure A.18 PNNL Specimen B-505

Figure A.19 PNNL Specimen B-515

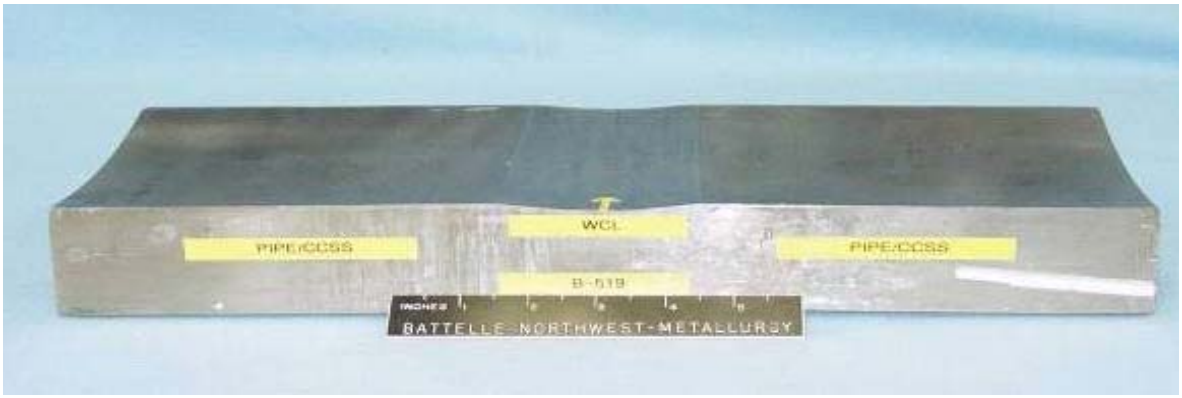

Figure A.20 PNNL Specimen B-519

Figure A.21 Southwest Research Institute Specimen AAD#1

Figure A.22 Southwest Research Institute Specimen AAD#2

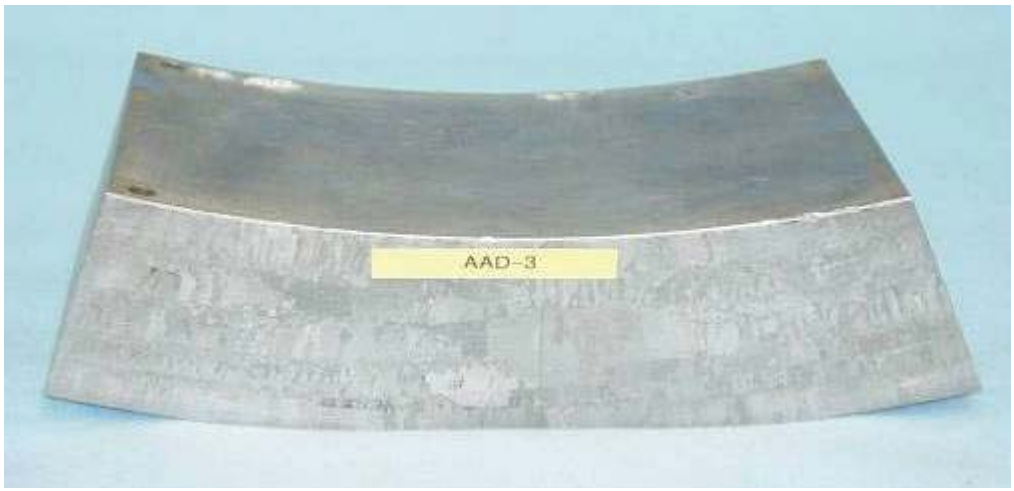

Figure A.23 Southwest Research Institute Specimen AAD#3

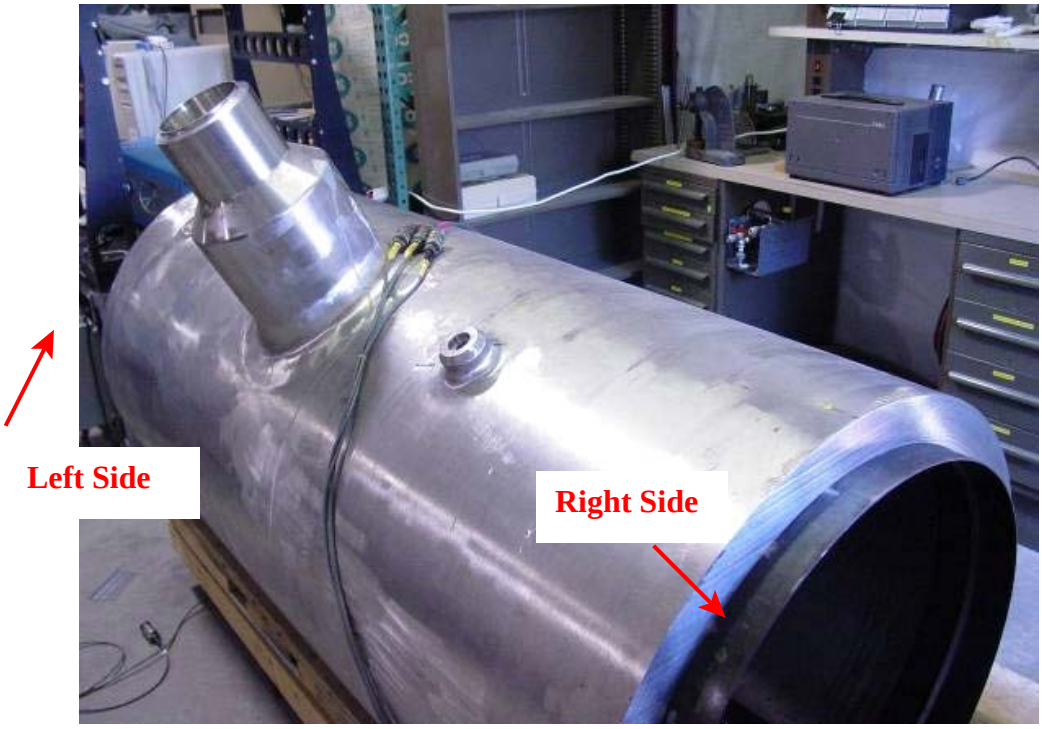

Figure A.24 EPRI NDE Center, Spanish Spool Piece Specimen

Figure A.25 EPRI NDE Center, Spanish Spool Piece Specimen, Polished and Etched Ring

Figure A.26 Westinghouse Spool Piece Specimen

Figure A.27 IHI Southwest Technologies Inc. Spool Piece Specimen

Figure A.28 Westinghouse and IHI Southwest Technologies Inc. Spool Pieces after Polishing and Etching

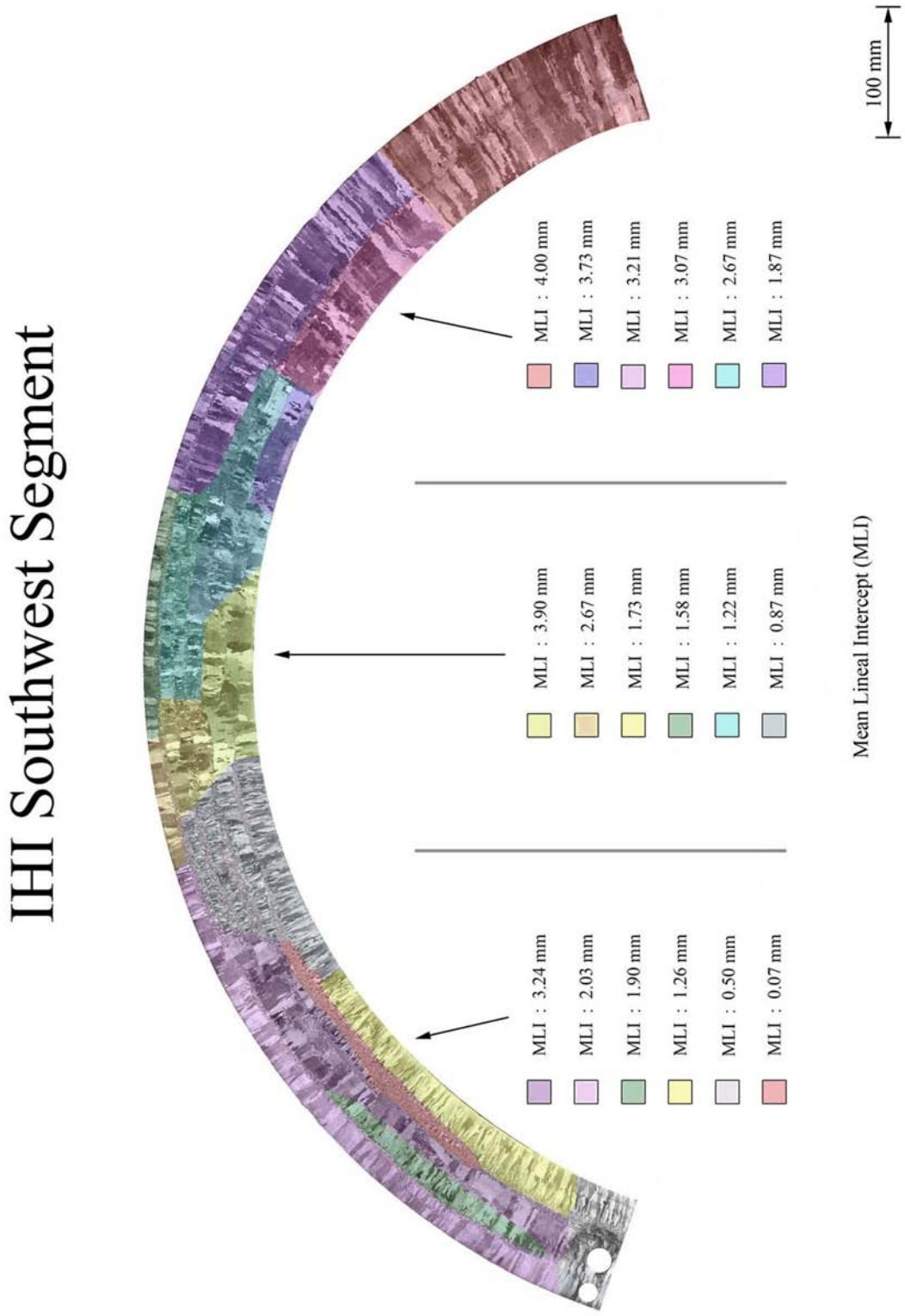

Figure A.29 False-Color Map Depicting Variation of Grains in CCSS Piping from IHI Southwest Technologies, Inc.

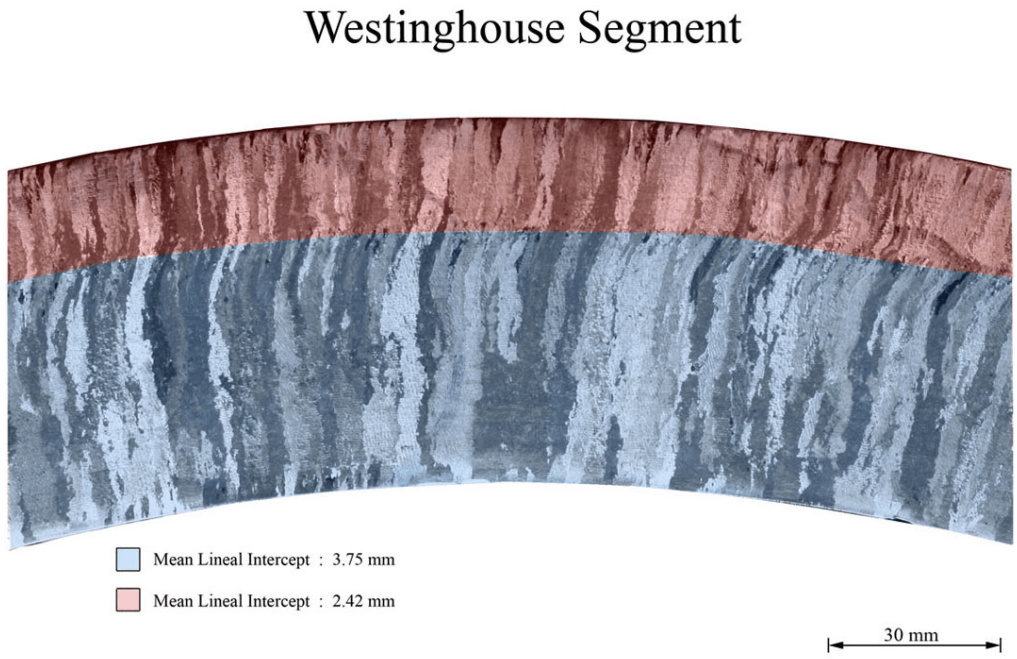

Figure A.30 Portion of CCSS Piping Specimen from Westinghouse, Inc., Showing Dendritic Grain Structure Observed to be Consistent Throughout Circumference

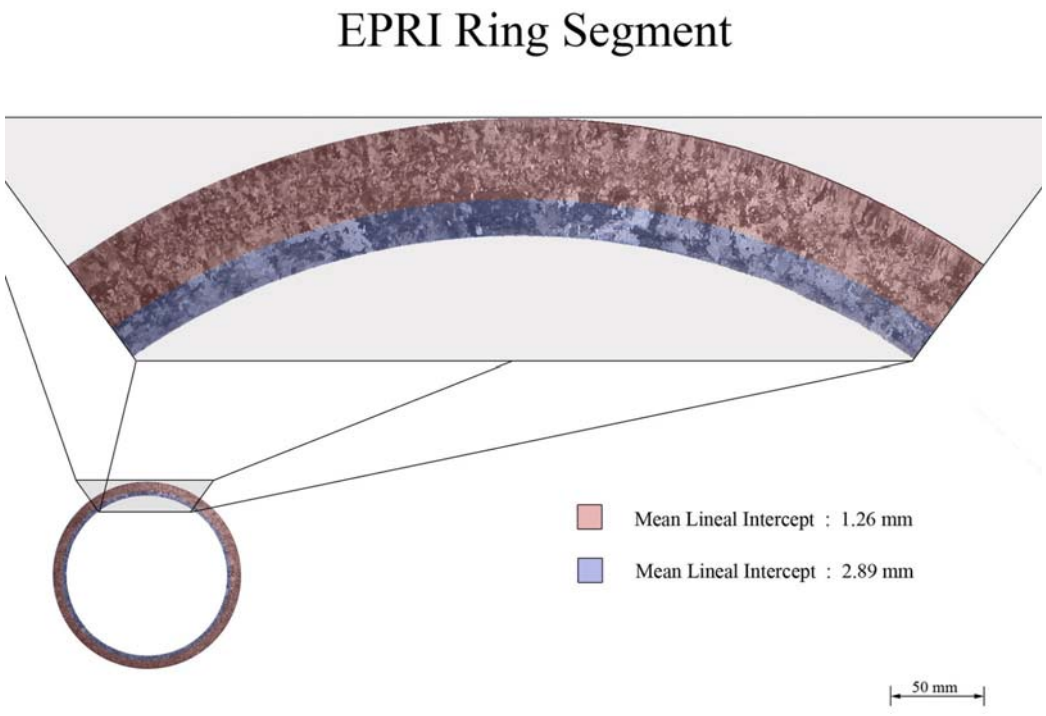

Figure A.31 Portion of Westinghouse, Inc. CCSS Piping Segment Showing Dendritic Grain Structure Observed To Be Consistent Throughout Circumference

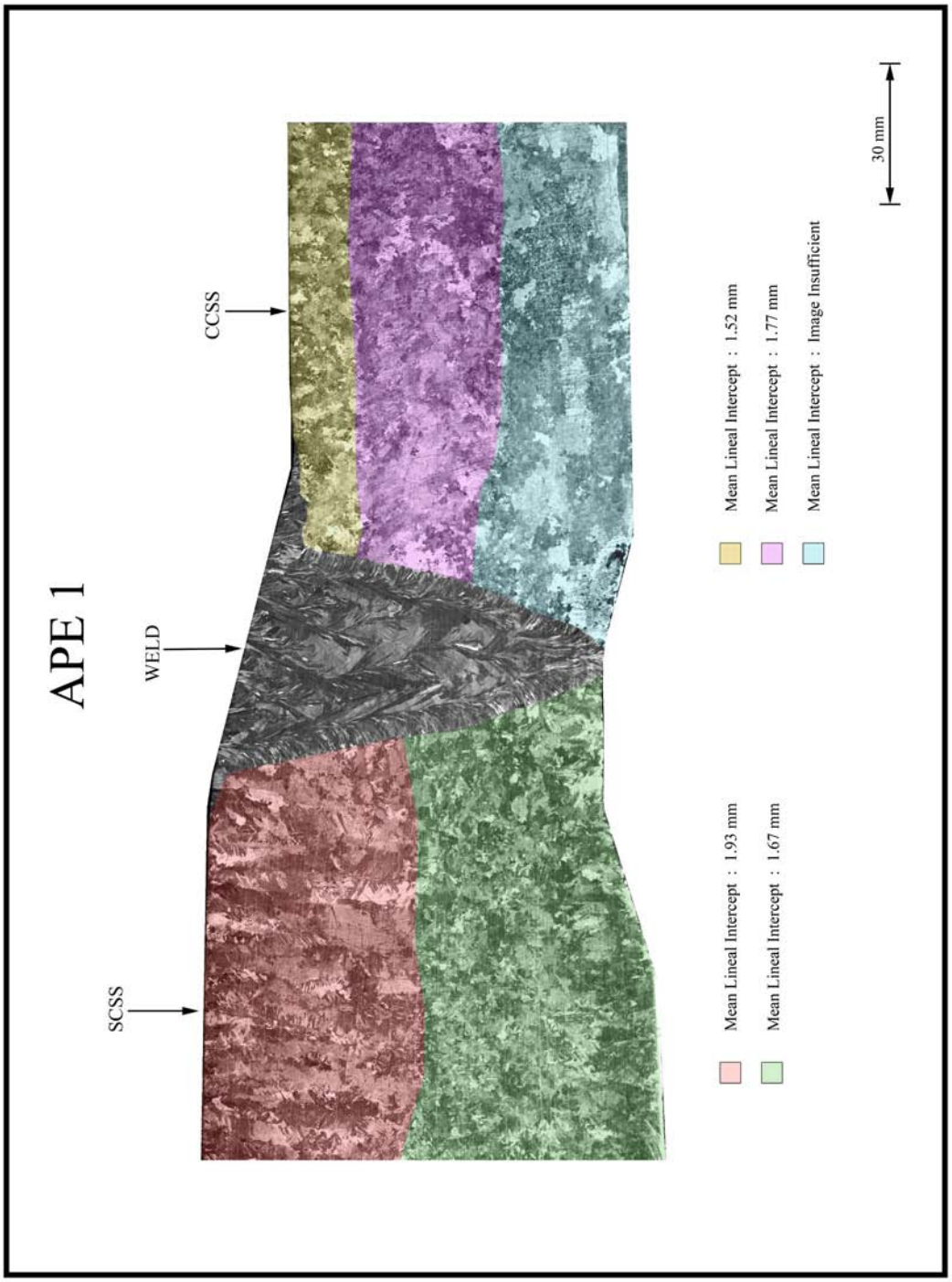

Figure A.32 Axial-Radial Cross Section of WOG Specimen APE-1, Showing Outside and Inside Diameter Geometry, and Grain Size, Typical of APE Configuration

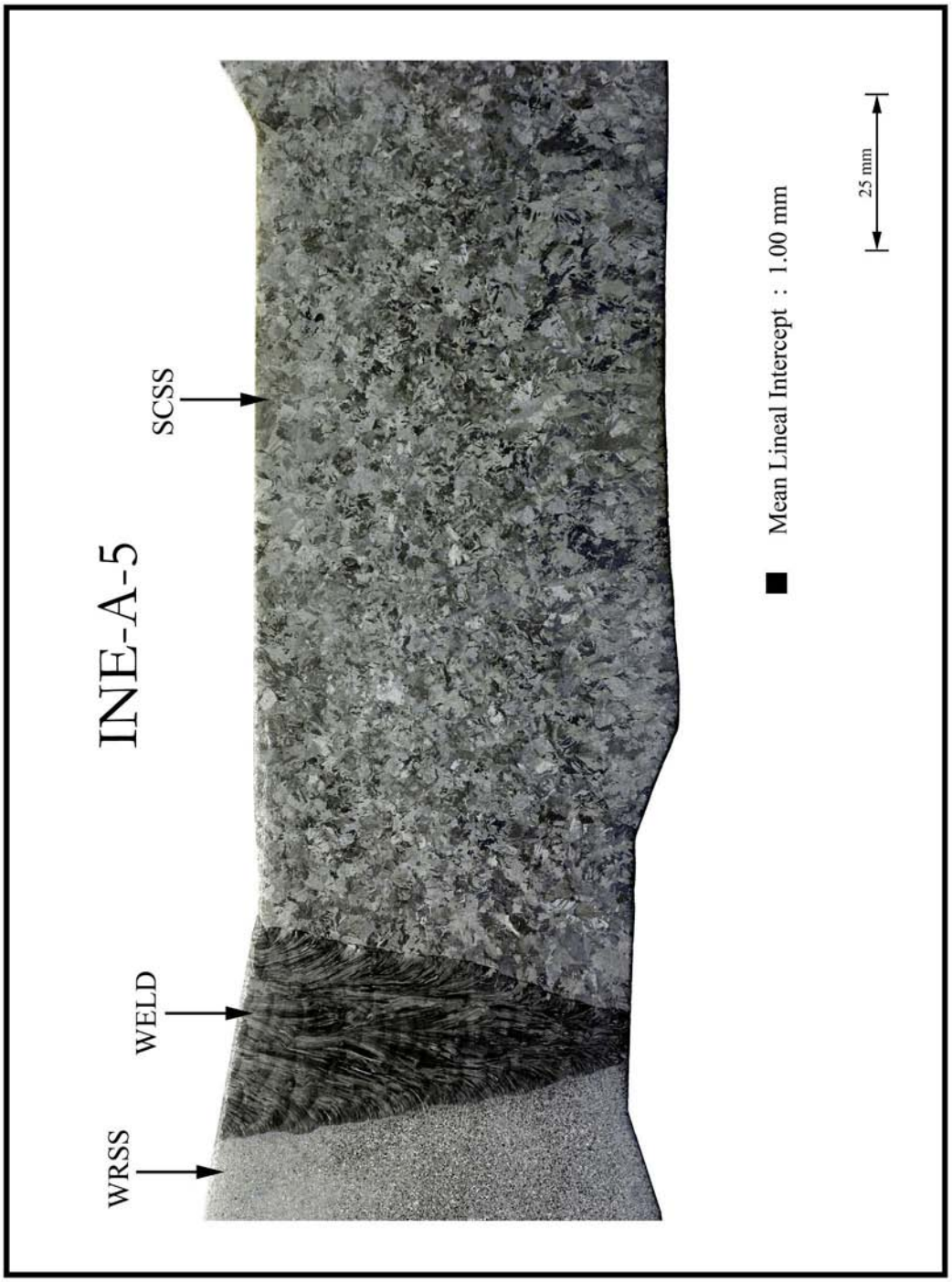

Figure A.33 Axial-Radial Cross Section of WOG Specimen INE-A-5, Showing Outside and Inside Diameter Geometry, and Grain Size, Typical of INE-A Configuration

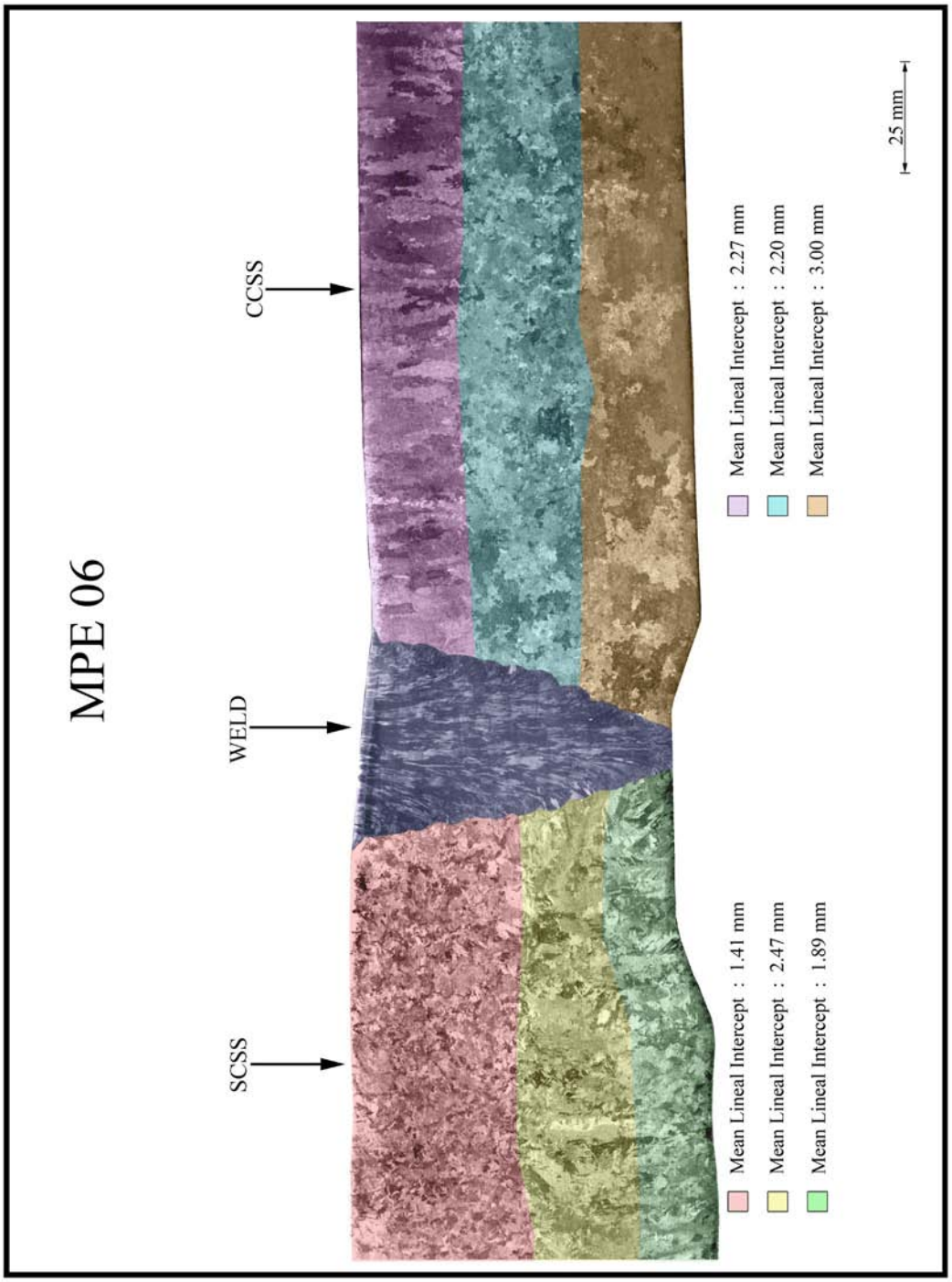

Figure A.34 Axial-Radial Cross Section of WOG Specimen MPE-06, Showing Outside and Inside Diameter Geometry, and Grain Size, Typical of MPE Configuration

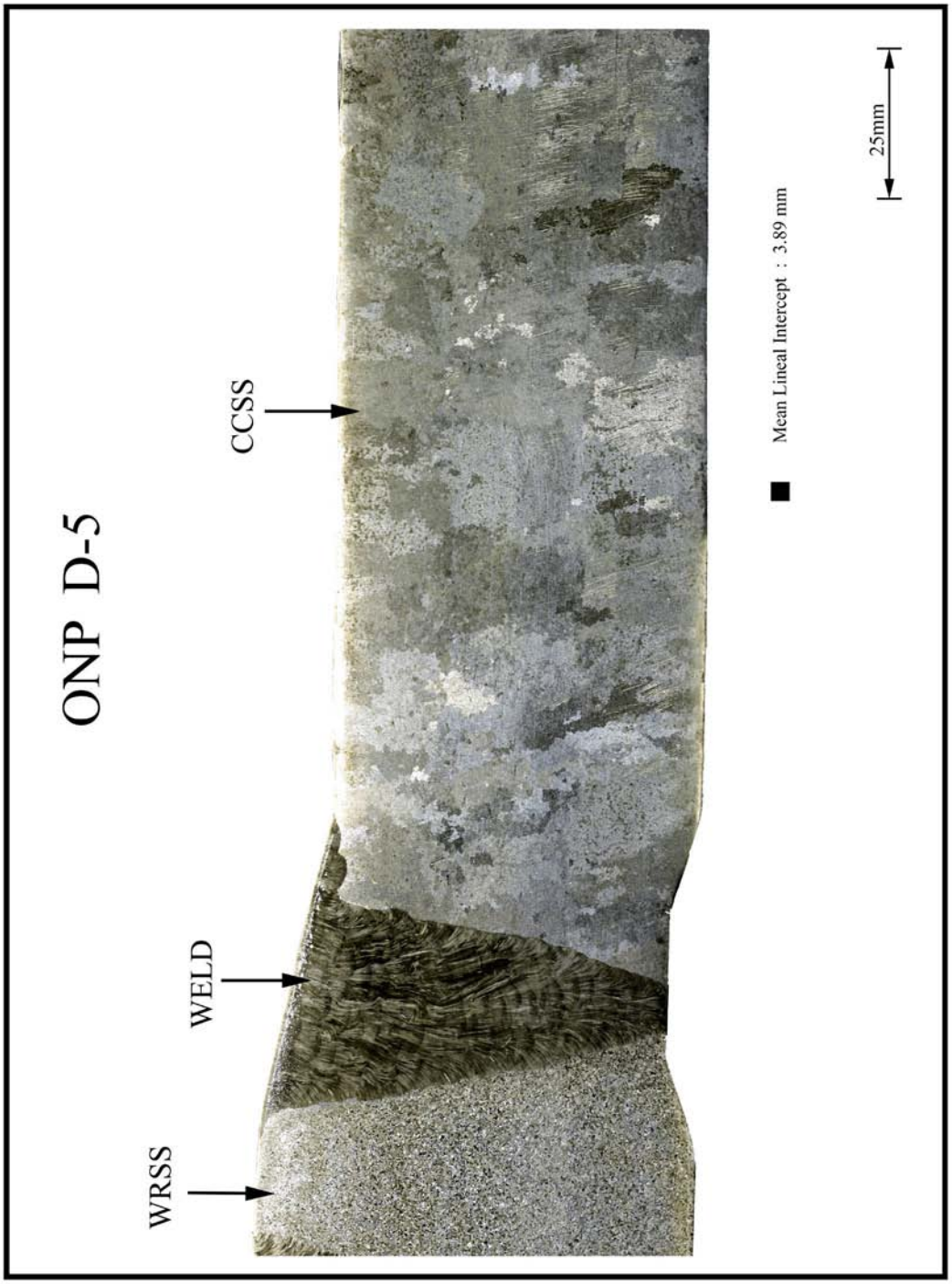

Figure A.35 Axial-Radial Cross Section of WOG Specimen ONP-D-5, Showing Outside and Inside Diameter Geometry, and Grain Size, Typical of ONP-D Configuration

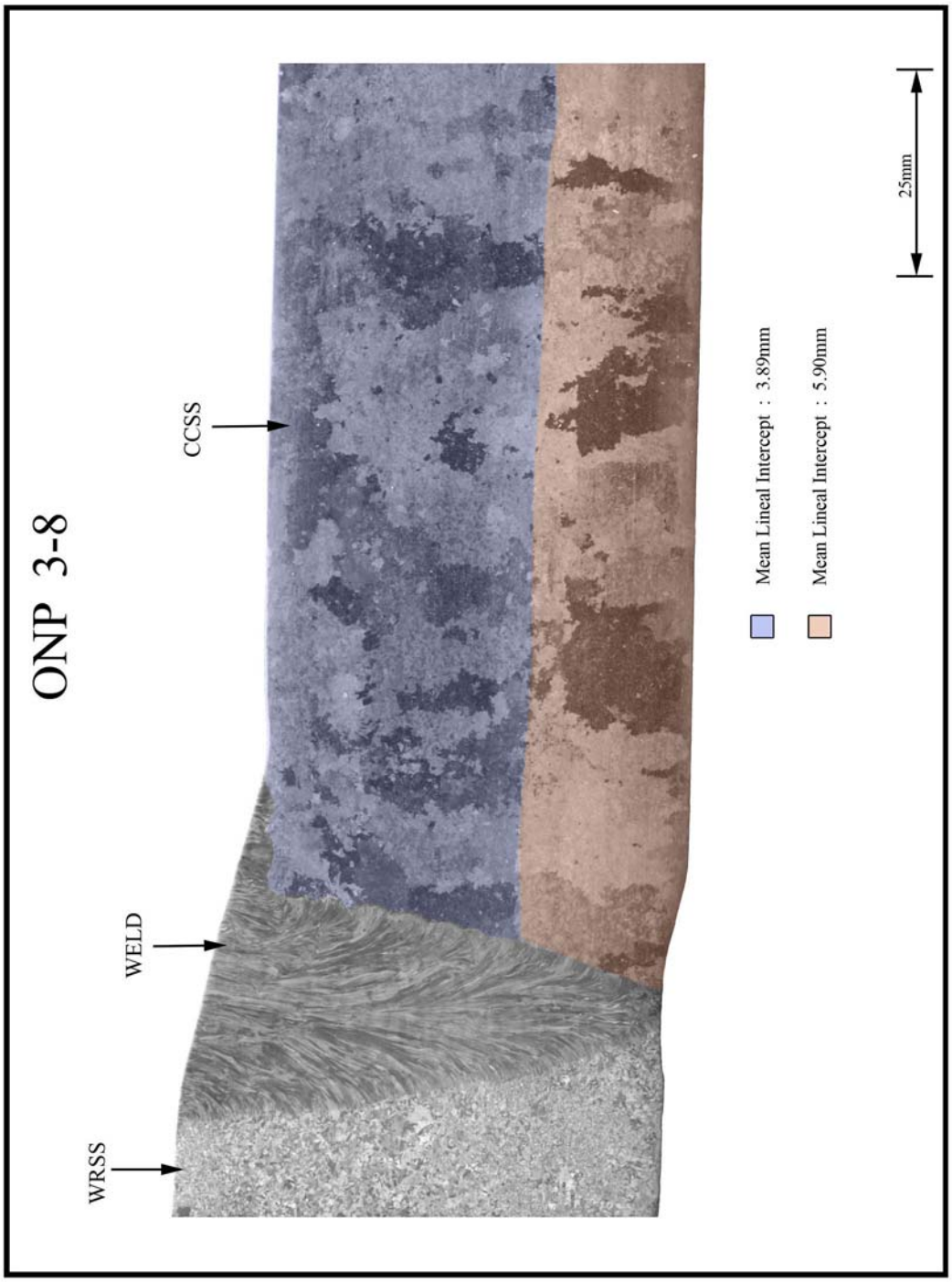

Figure A.36 Axial-Radial Cross Section of WOG Specimen ONP-3-8, Showing Outside and Inside Diameter Geometry, and Grain Size, Typical of ONP Configuration

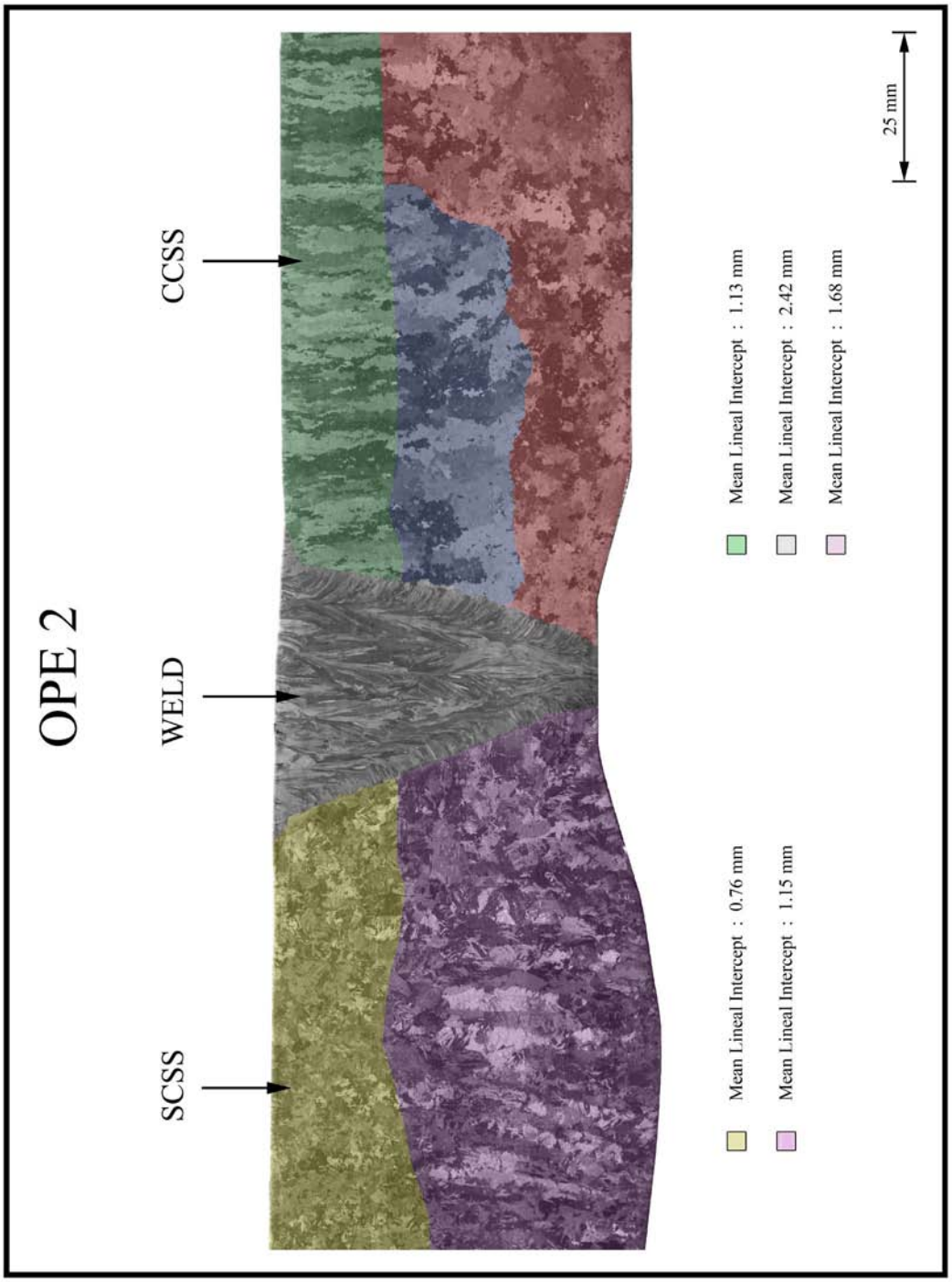

Figure A.37 Axial-Radial Cross Section of WOG Specimen OPE-2, Showing Outside and Inside Diameter Geometry, and Grain Size, Typical of OPE Configuration

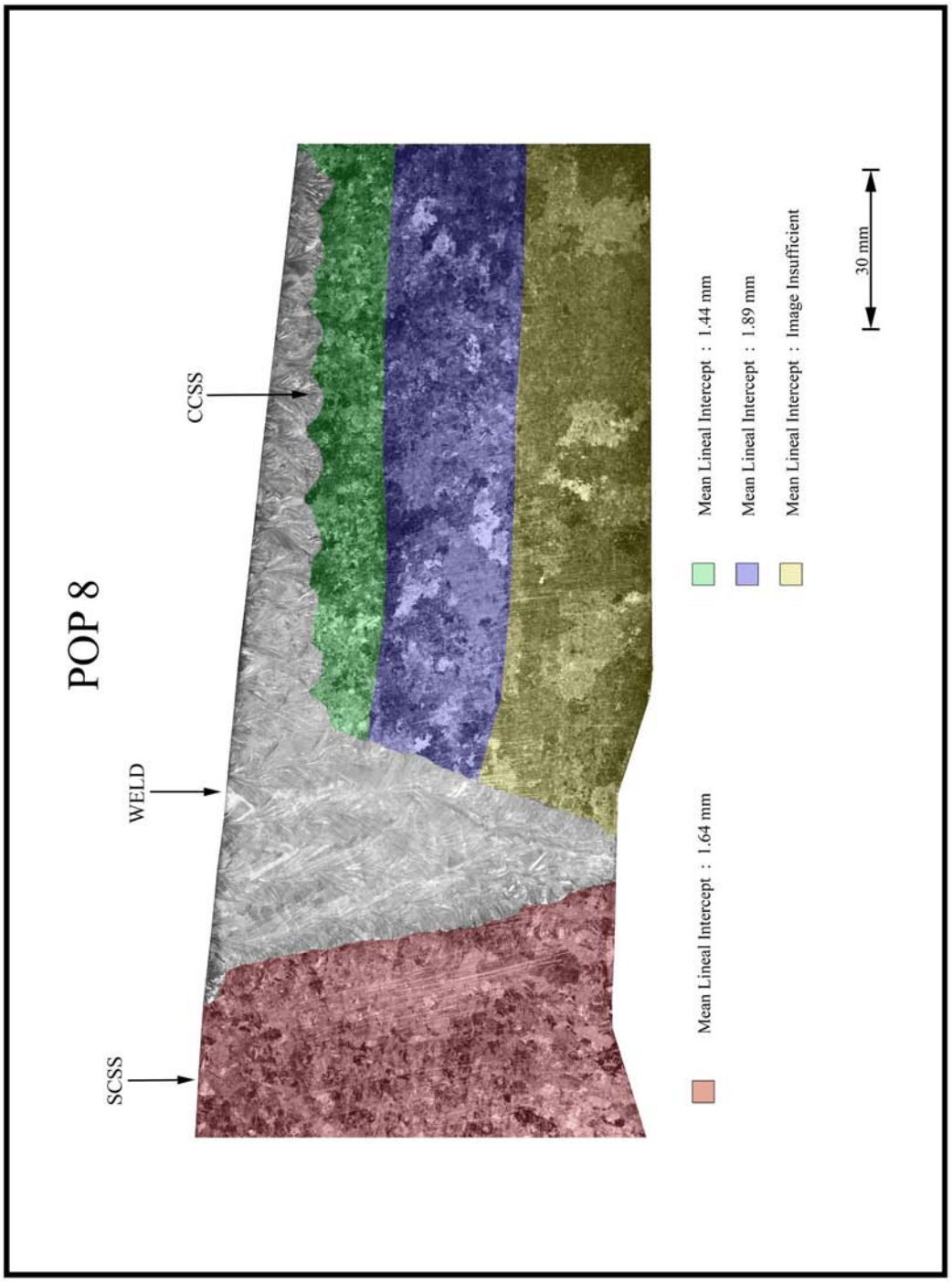

Figure A.38 Axial-Radial Cross Section of WOG Specimen POP-8, Showing Outside and Inside Diameter Geometry, and Grain Size, Typical of POP Configuration

Appendix B

Magnitude Plots from Eddy Current Data

Appendix B

Magnitude Plots from Eddy Current Data

All vertical and horizontal axes shown in these Appendix B plots are in units of inches (25.4 mm).

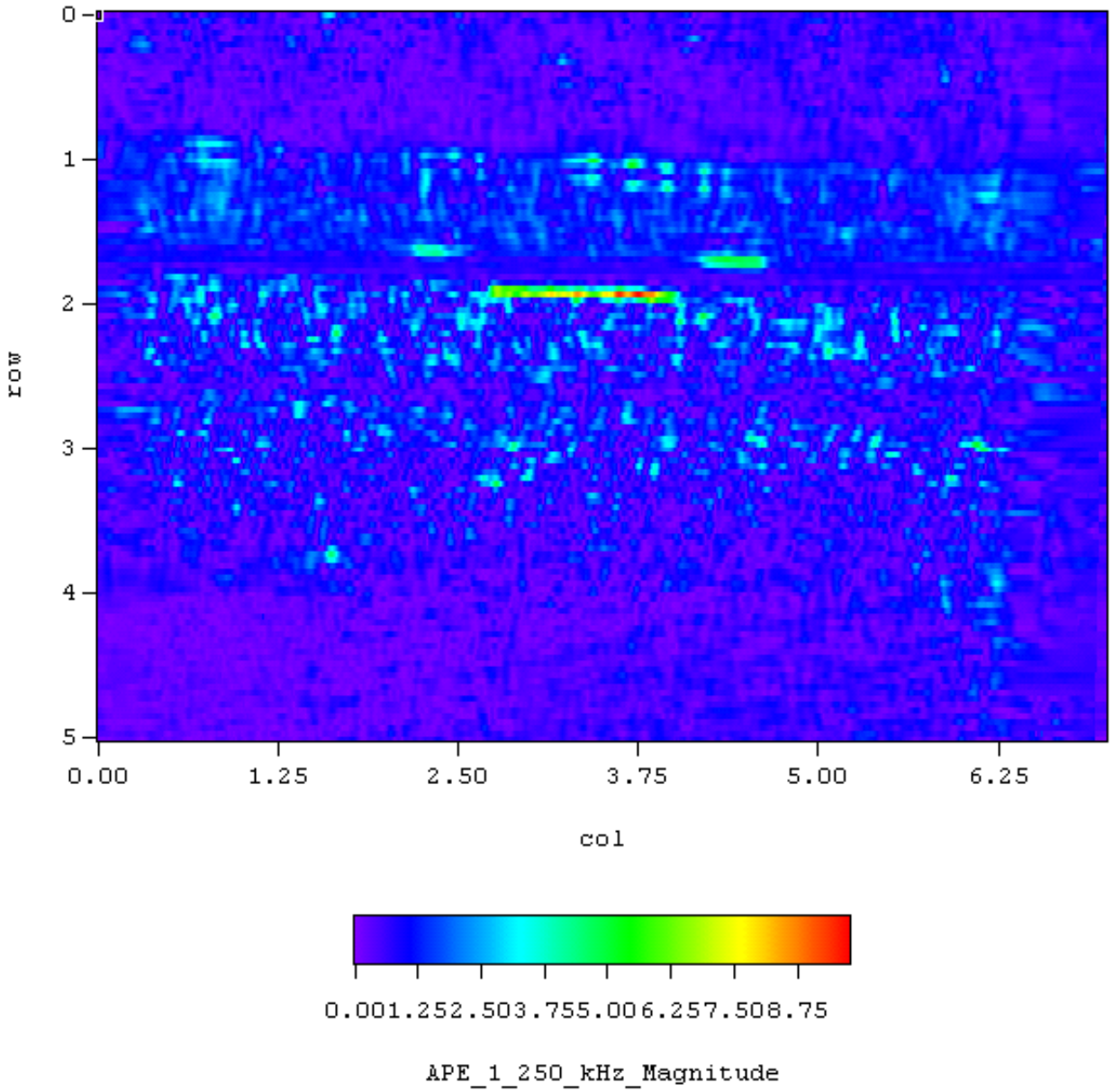

Figure B.1 Magnitude Plot of WOG Specimen APE-1

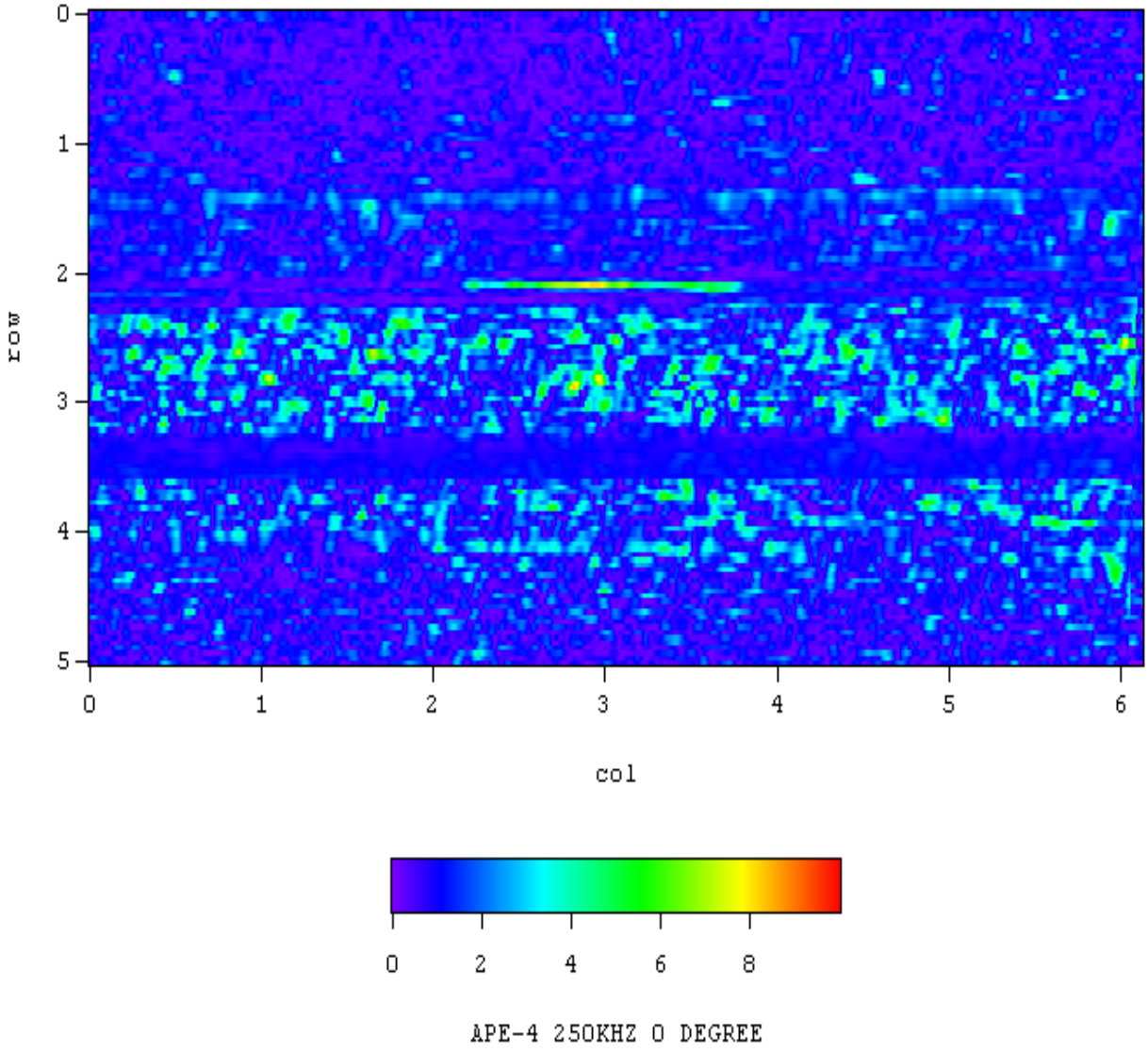

Figure B.2 Magnitude Plot of WOG Specimen APE-4

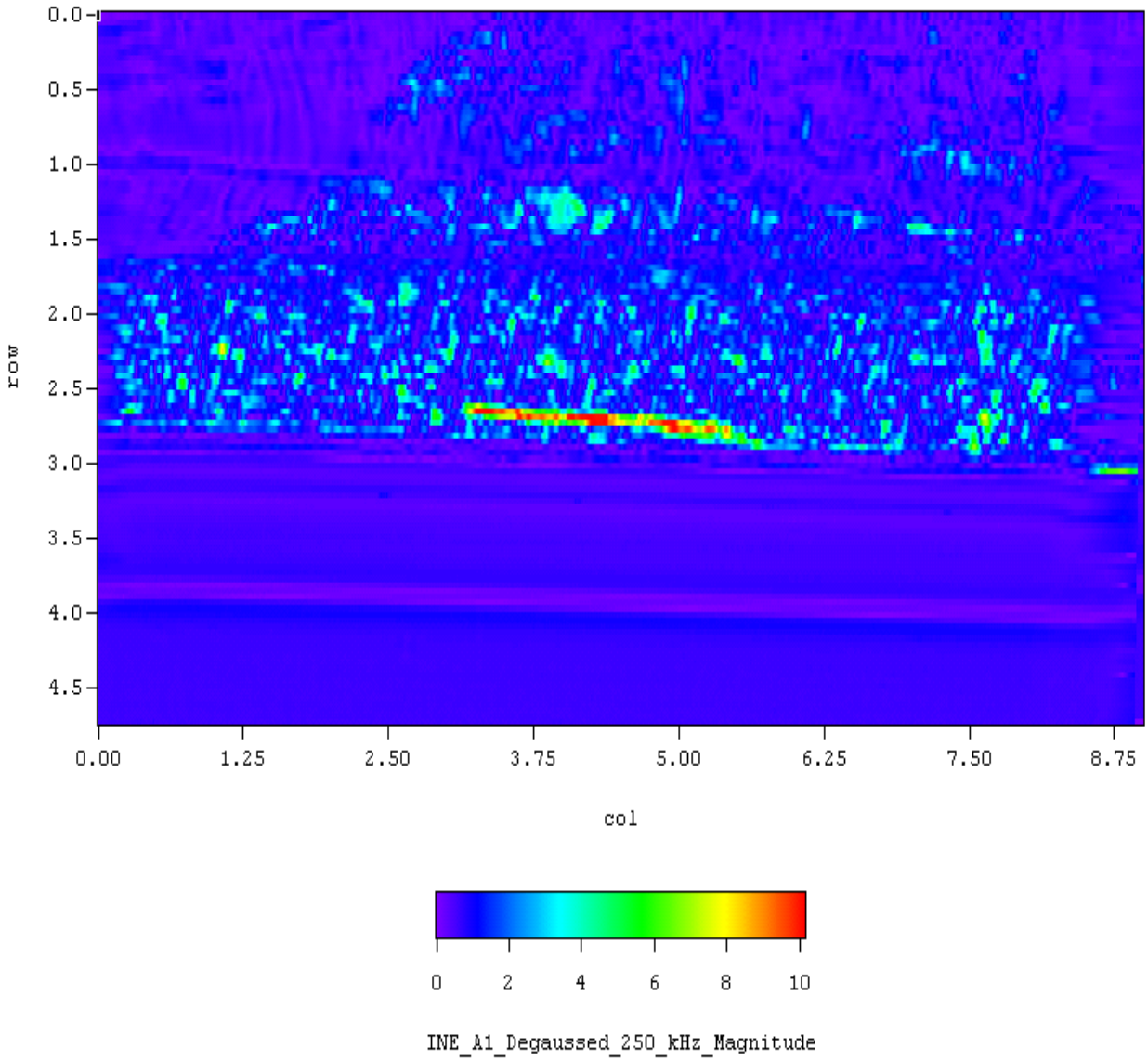

Figure B.3 Magnitude Plot of WOG Specimen INE-A-1

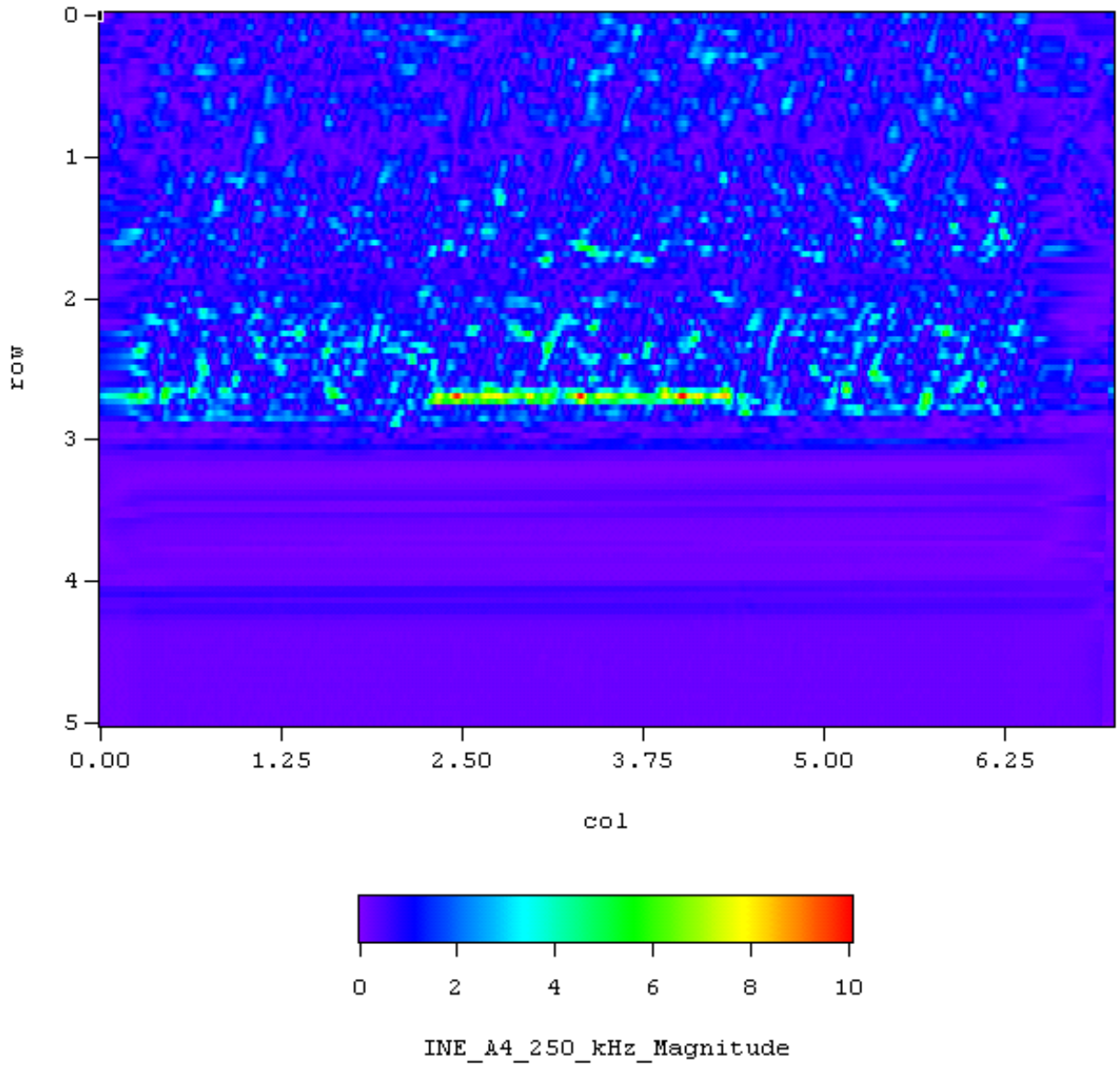

Figure B.4 Magnitude Plot of WOG Specimen INE-A-4

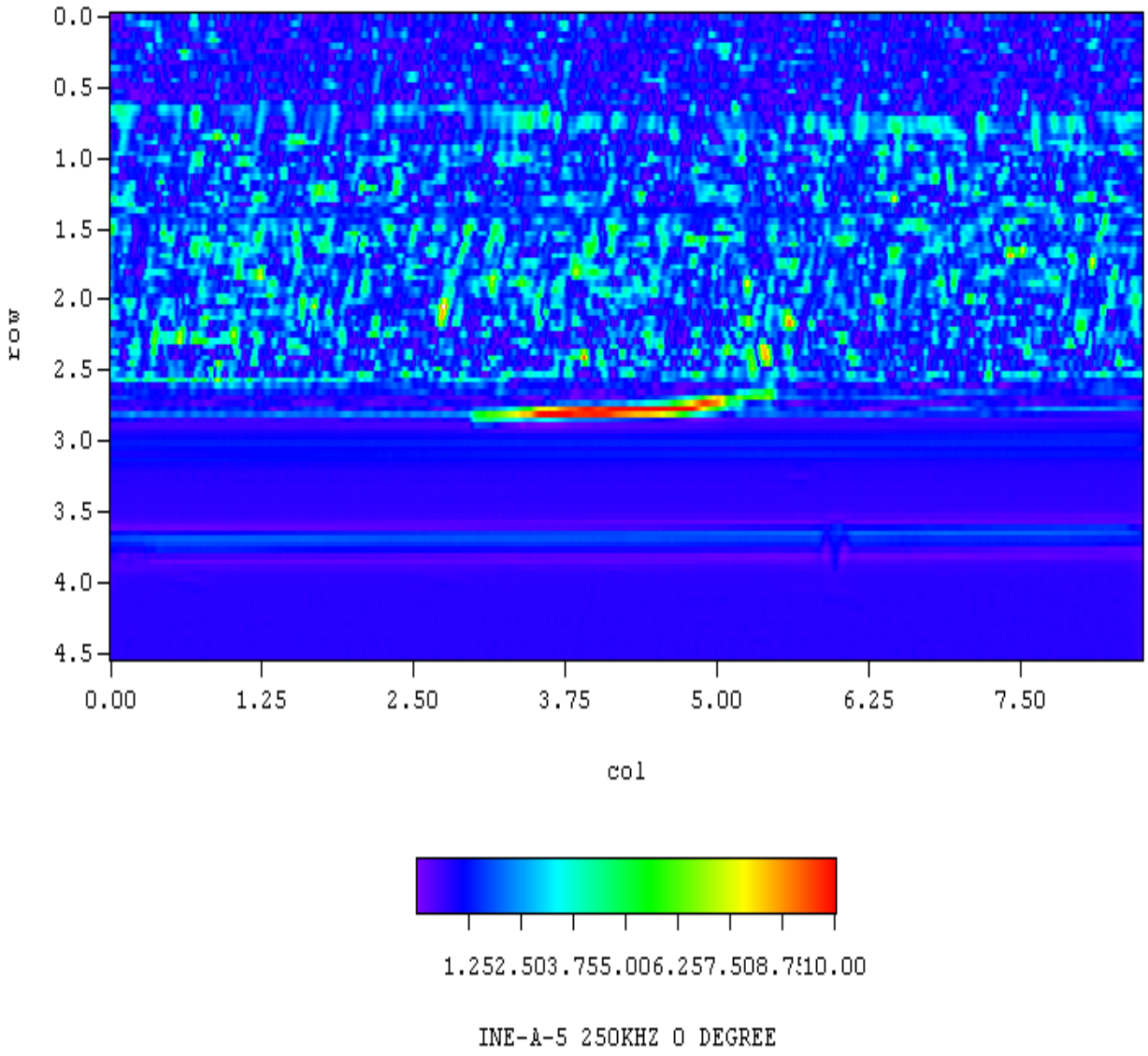

Figure B.5 Magnitude Plot of WOG Specimen INE-A-5

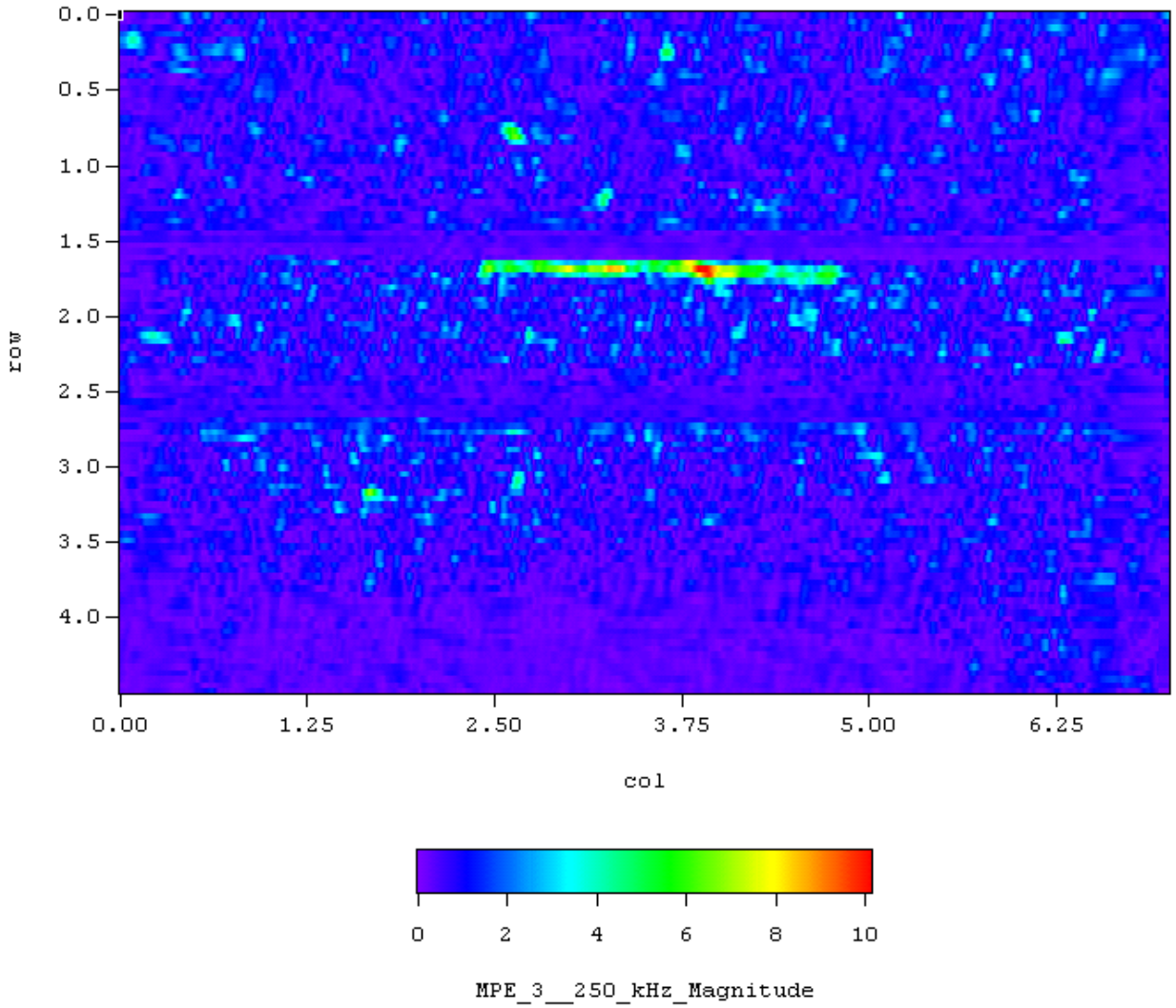

Figure B.6 Magnitude Plot of WOG Specimen MPE-3

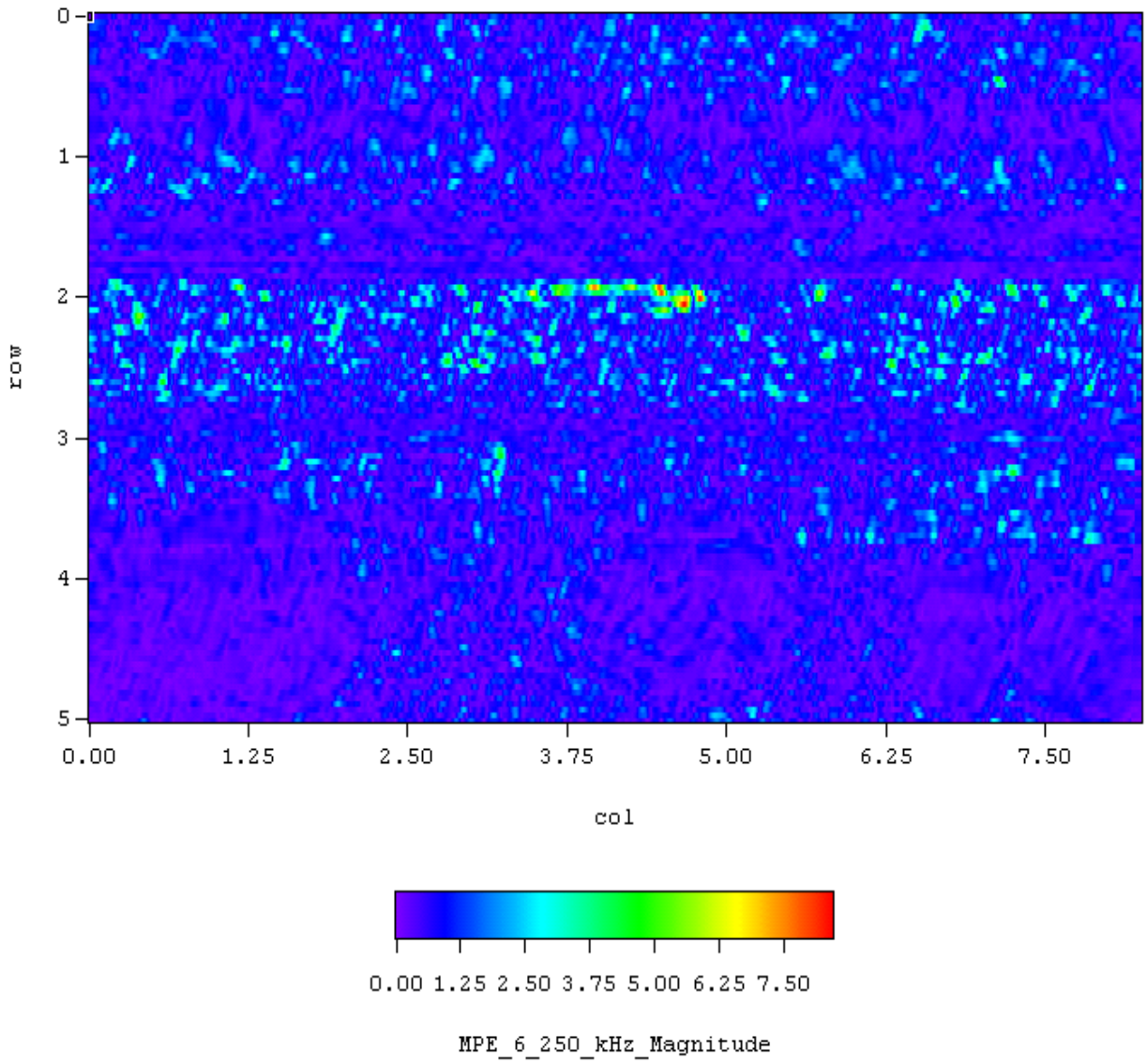

Figure B.7 Magnitude Plot of WOG Specimen MPE-6

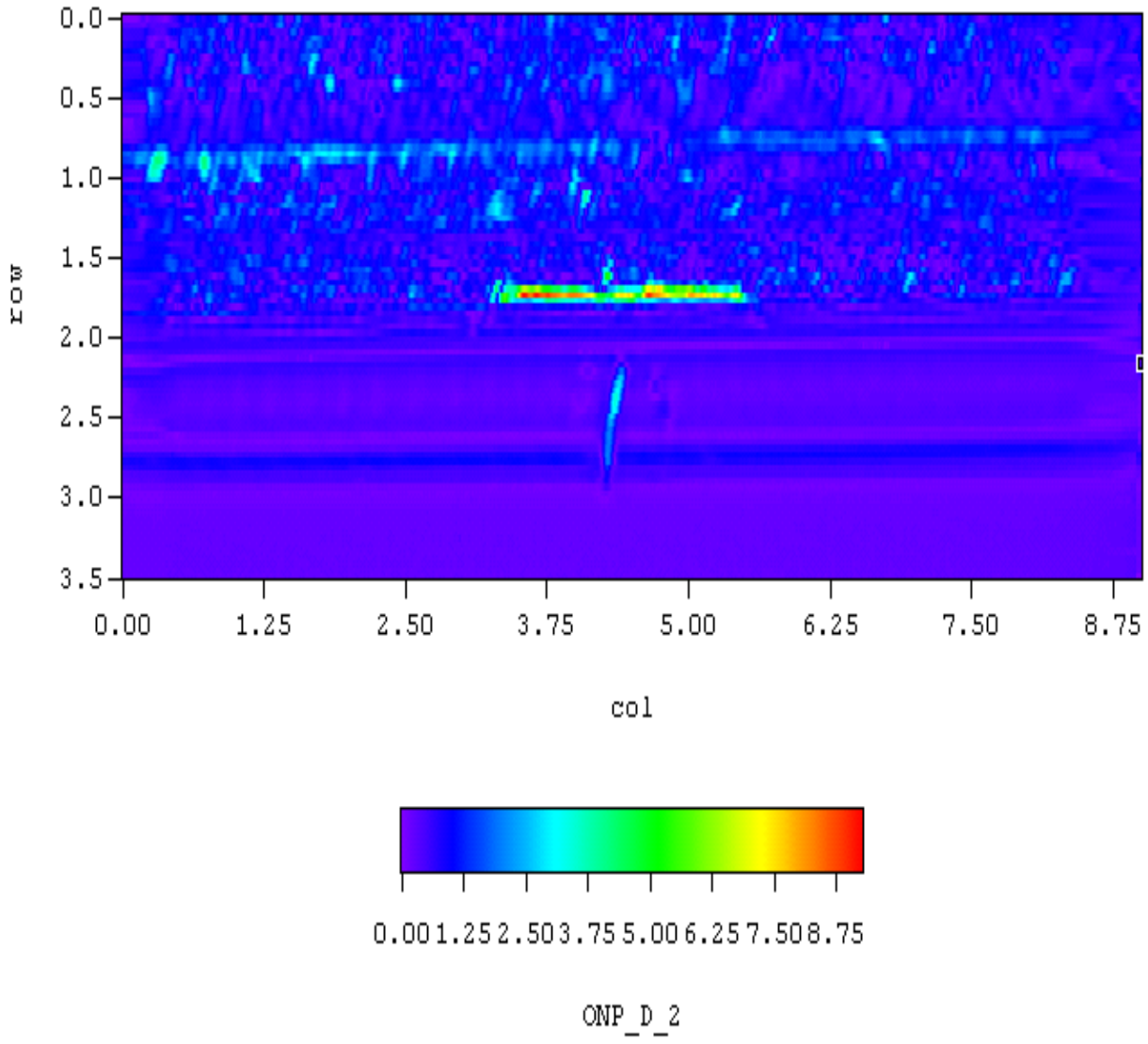

Figure B.8 Magnitude Plot of WOG Specimen ONP-D-2

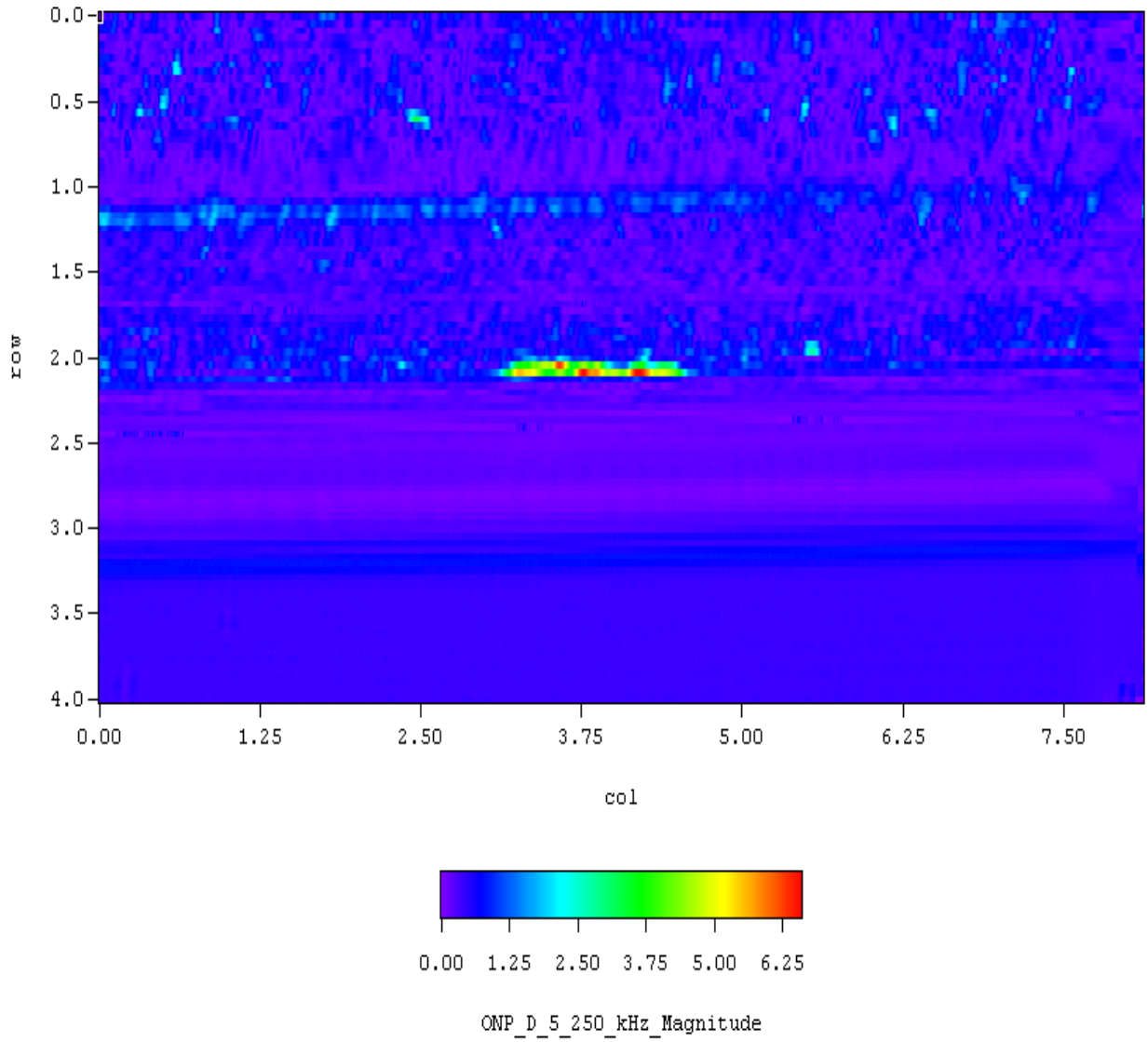

Figure B.9 Magnitude Plot of WOG Specimen ONP-D-5

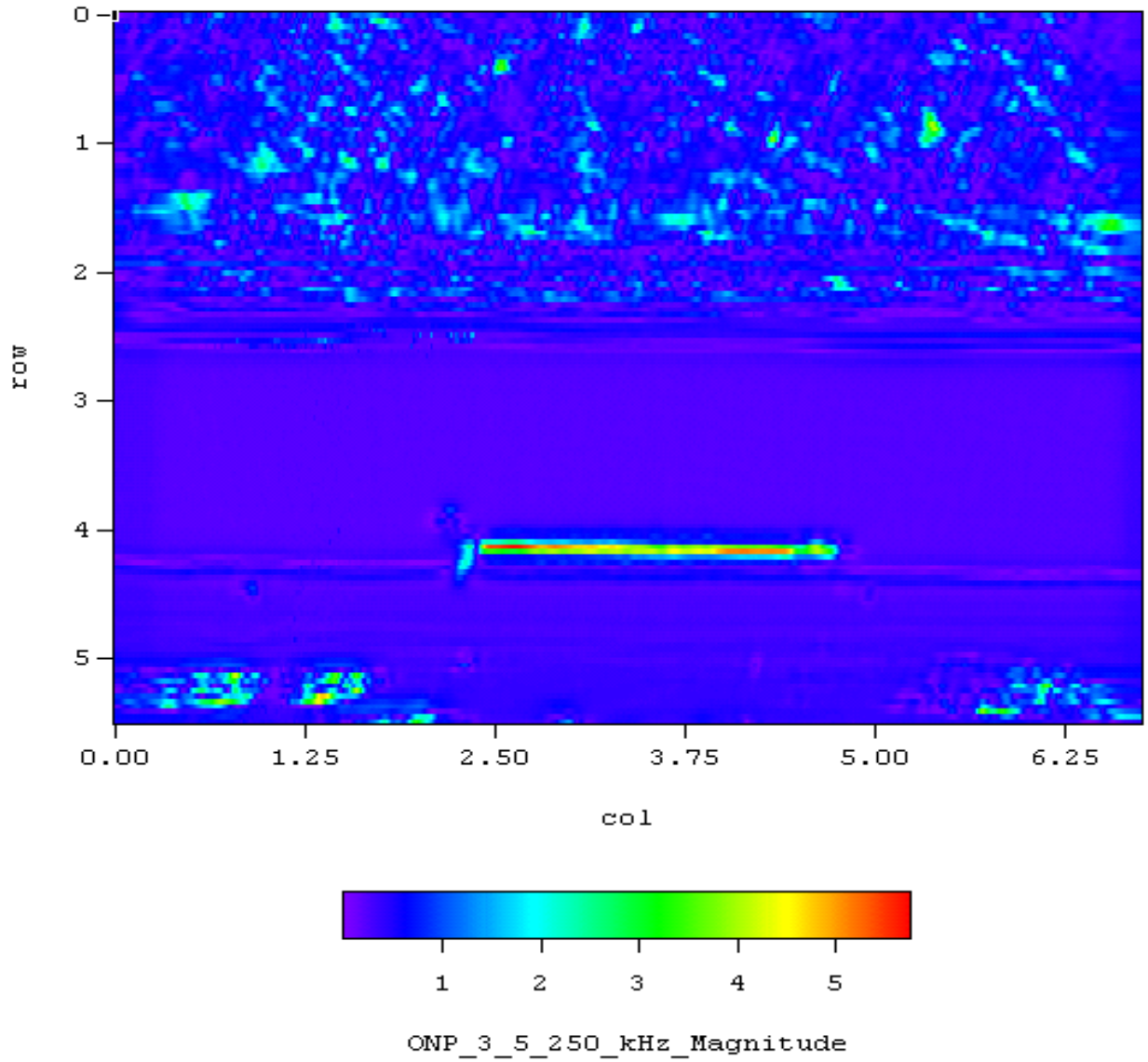

Figure B.10 Magnitude Plot of WOG Specimen ONP-3-5

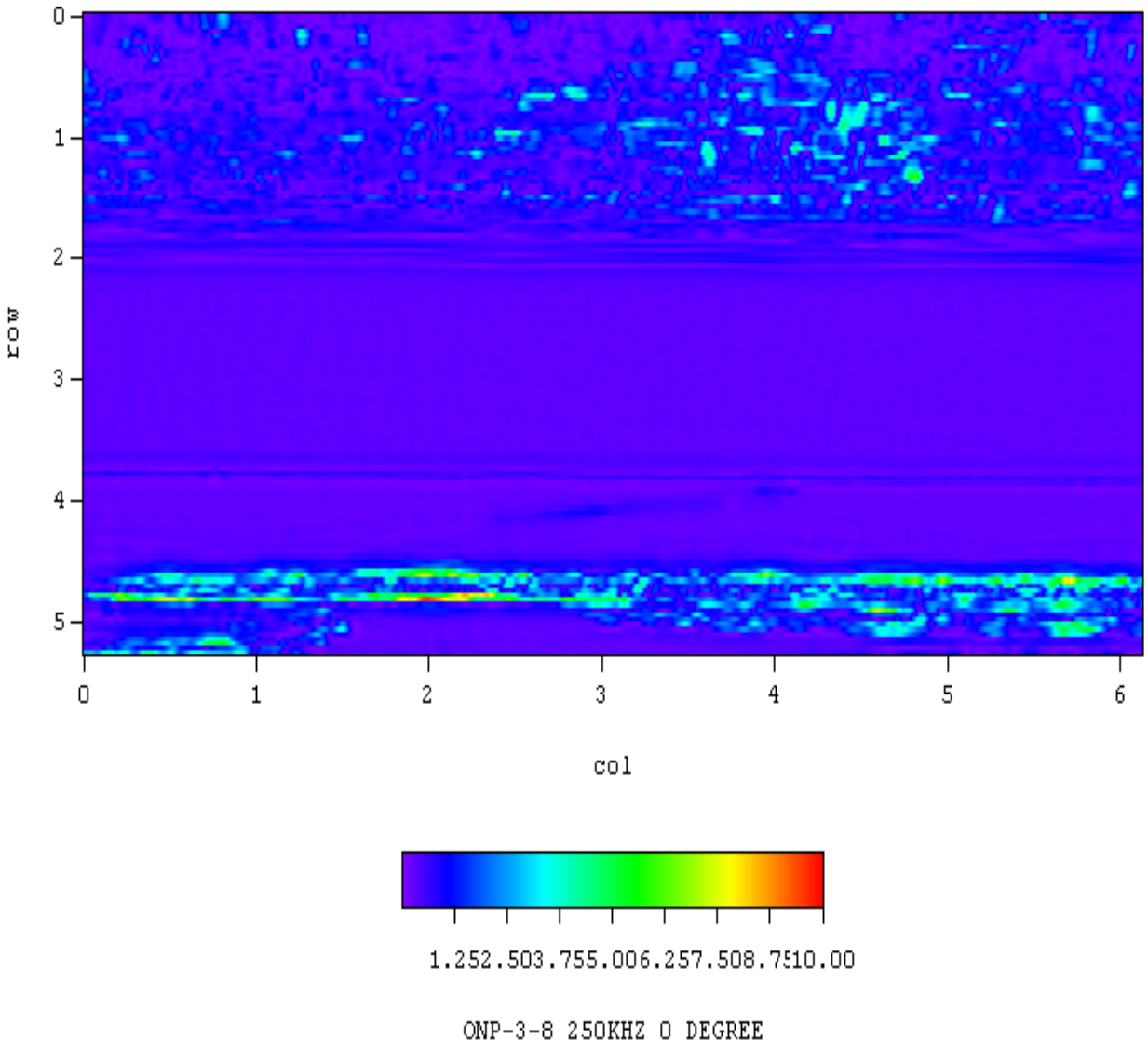

Figure B.11 Magnitude Plot of WOG Specimen ONP-3-8

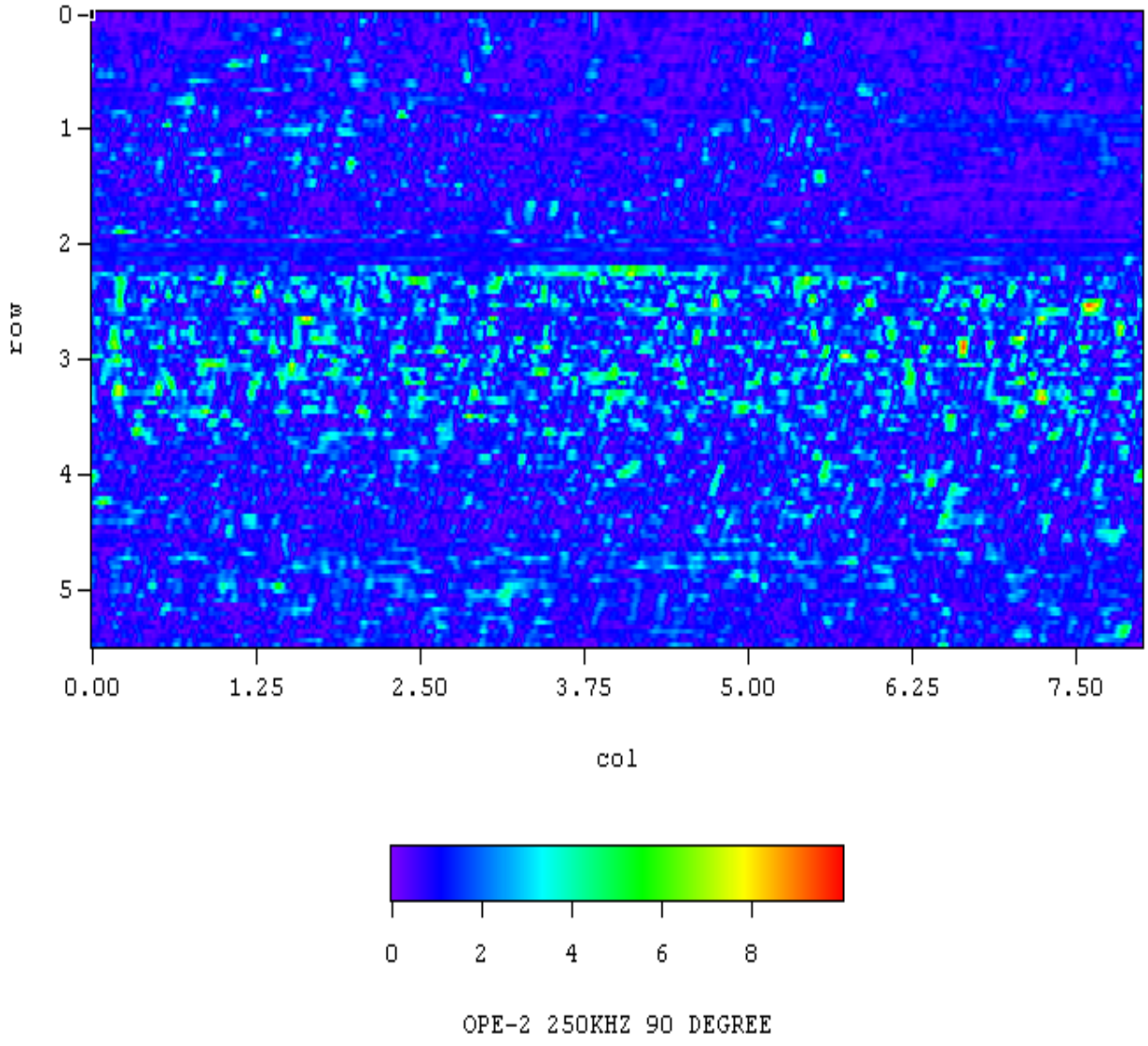

Figure B.12 Magnitude Plot of WOG Specimen OPE-2

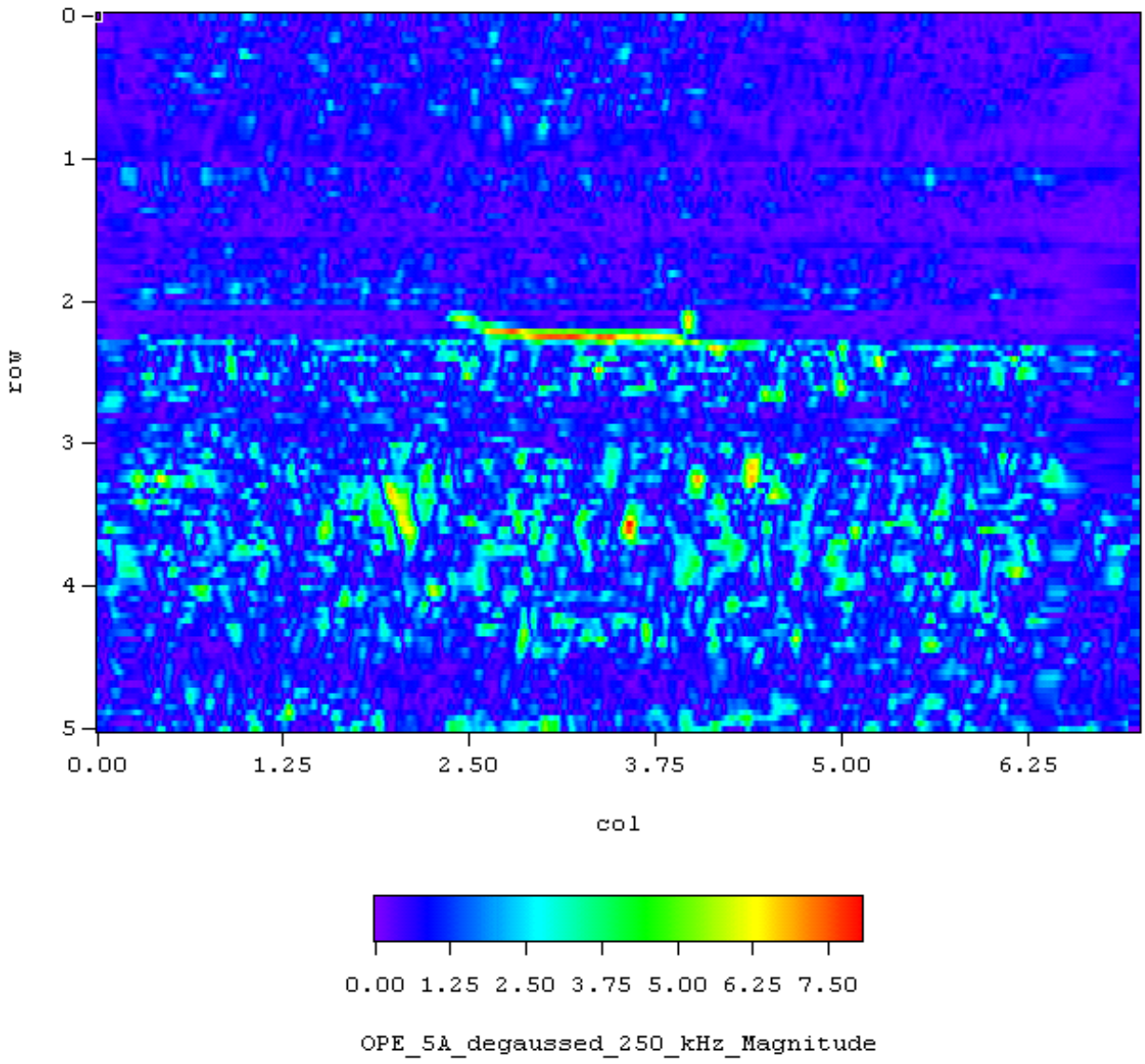

Figure B.13 Magnitude Plot of WOG Specimen OPE-5

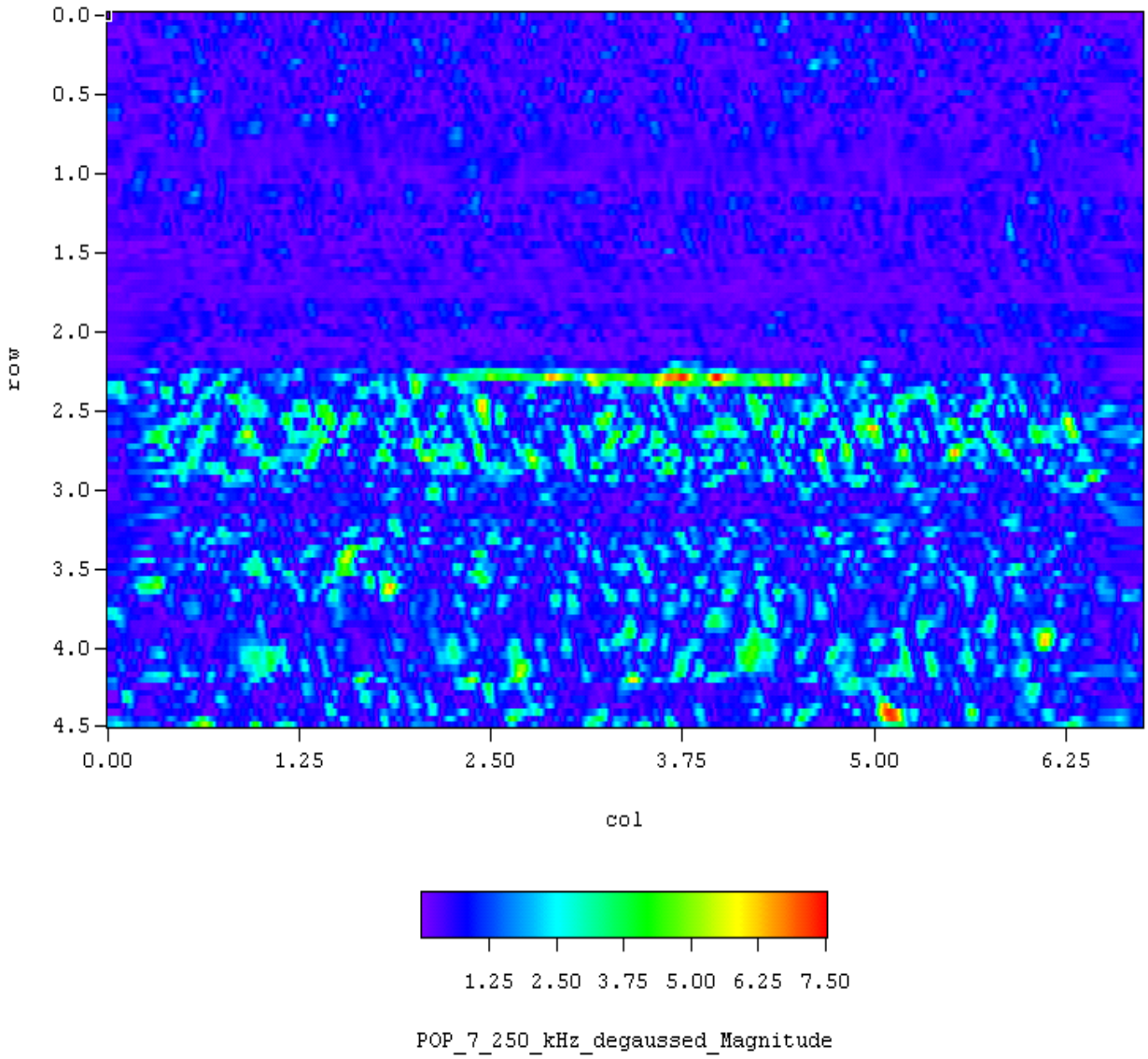

Figure B.14 Magnitude Plot of WOG Specimen POP-7

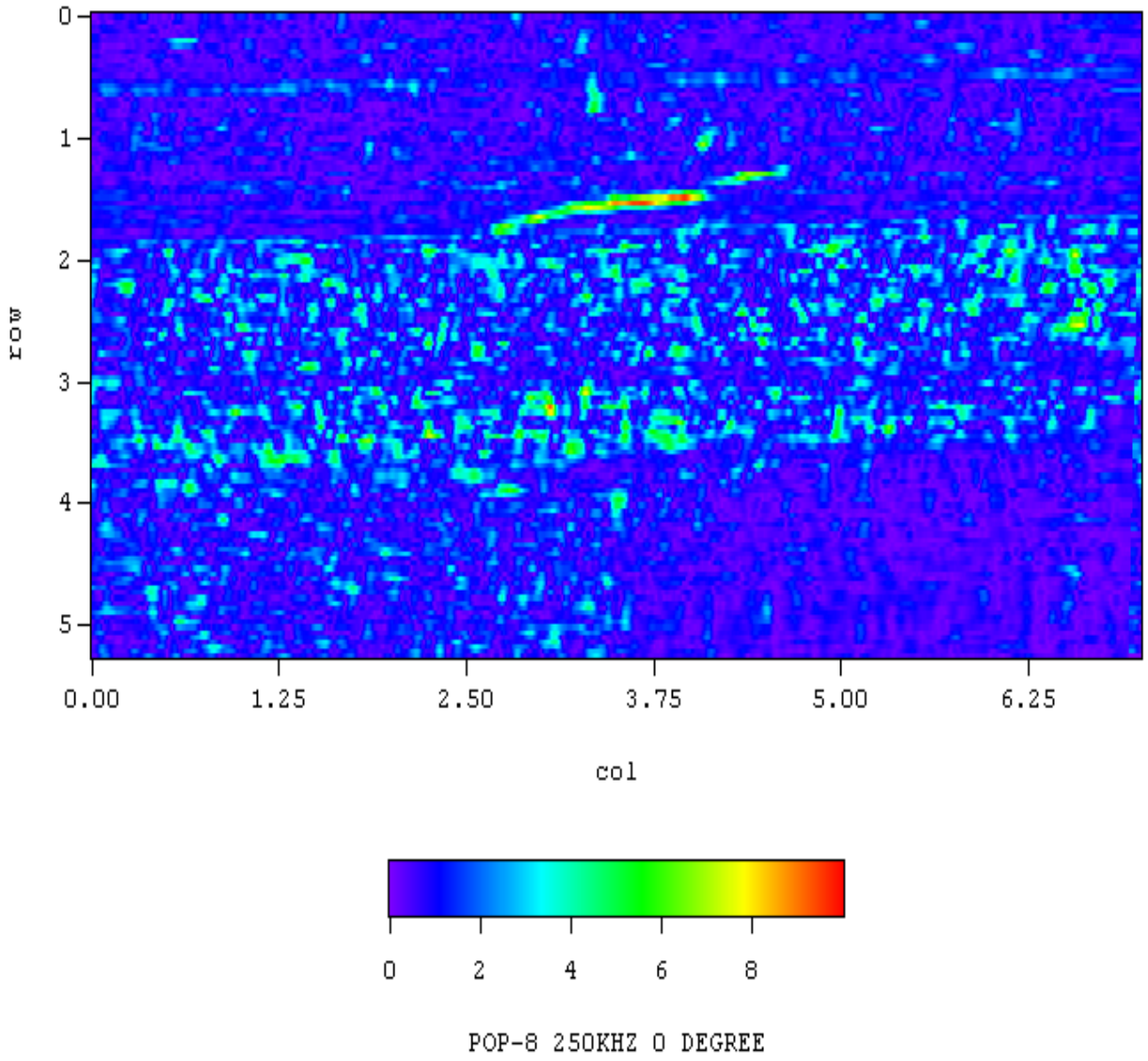

Figure B.15 Magnitude Plot of WOG Specimen POP-8

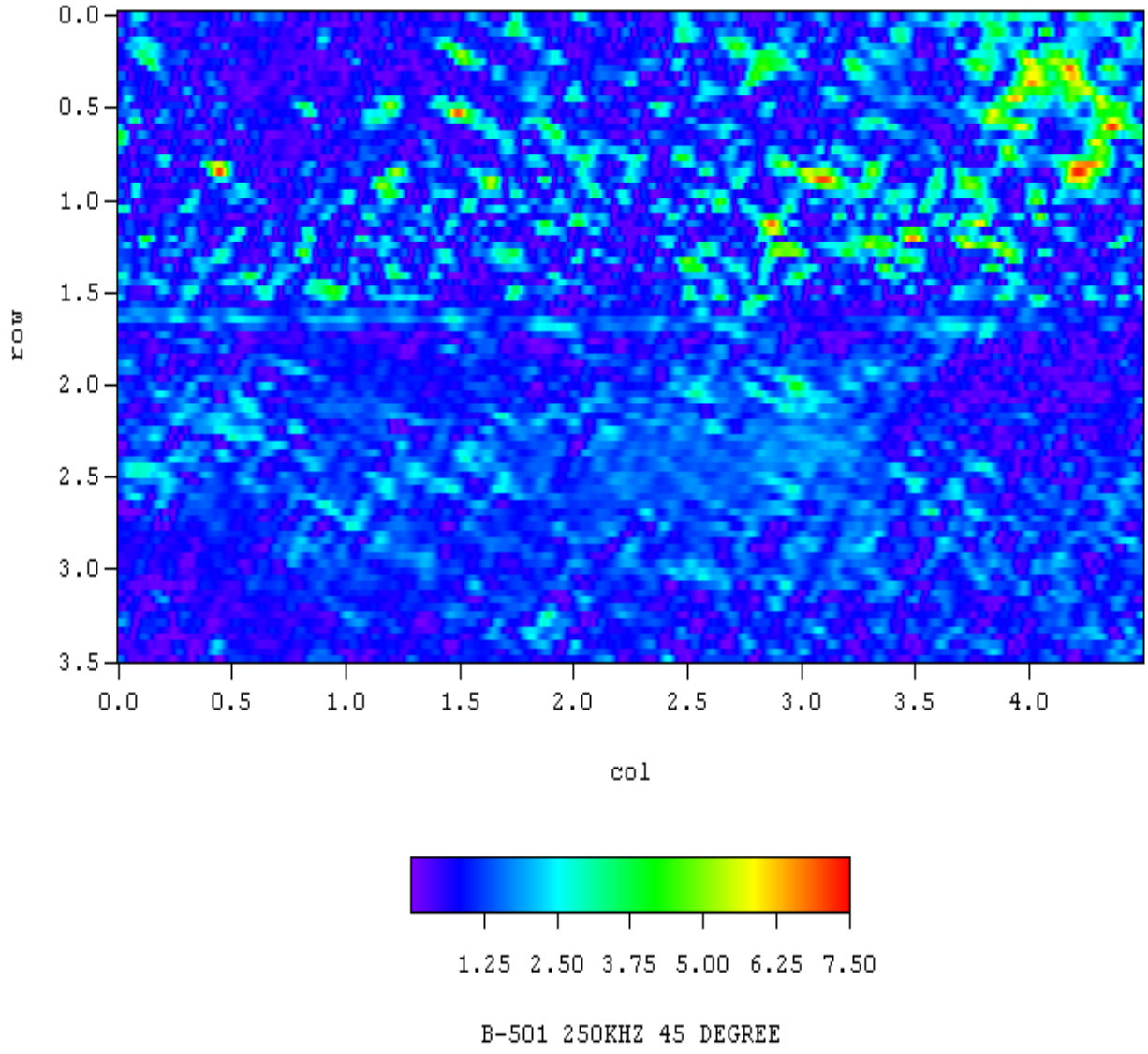

Figure B.16 Magnitude Plot of PNNL Specimen B-501

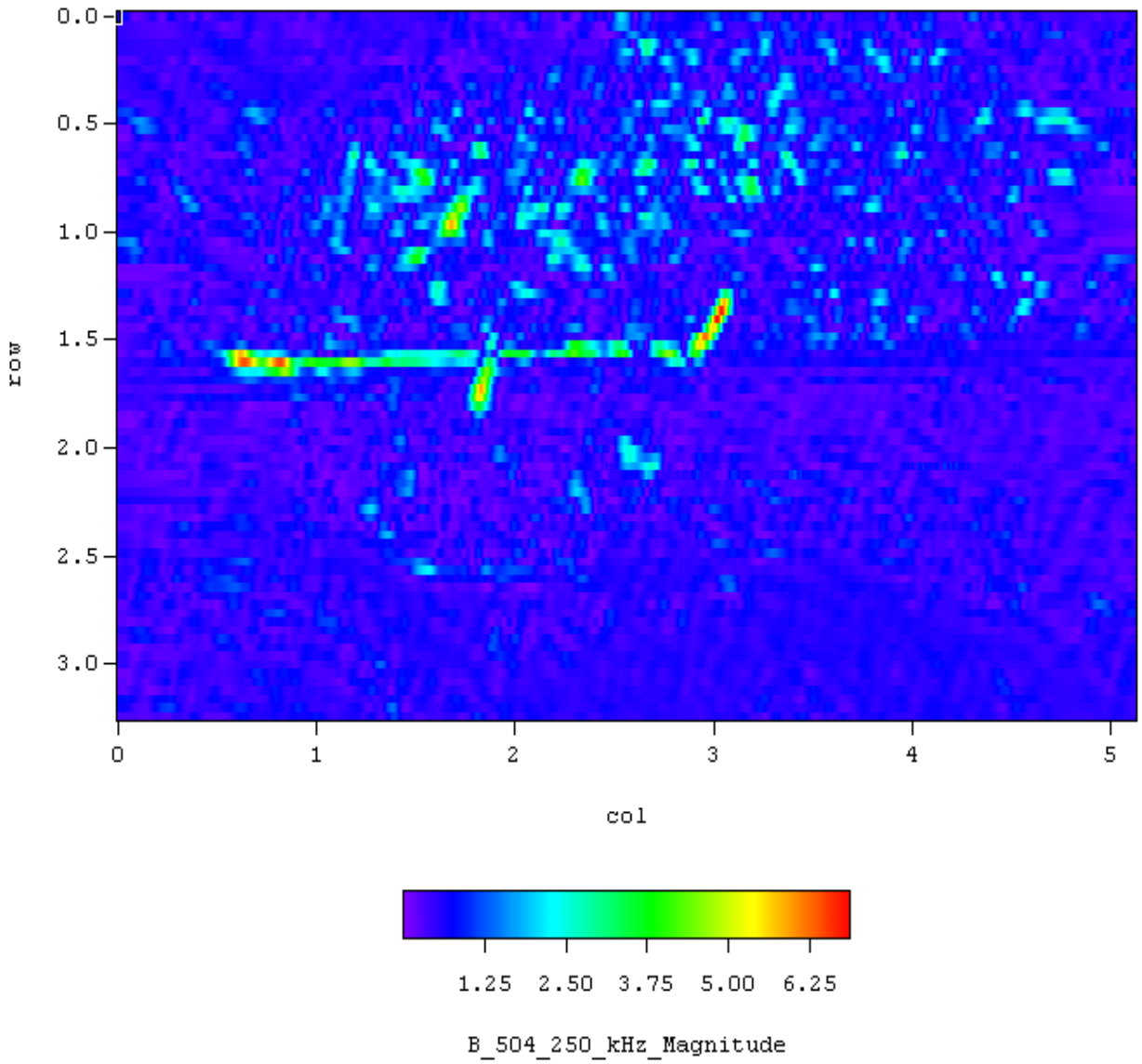

Figure B.17 Magnitude Plot of PNNL Specimen B-504

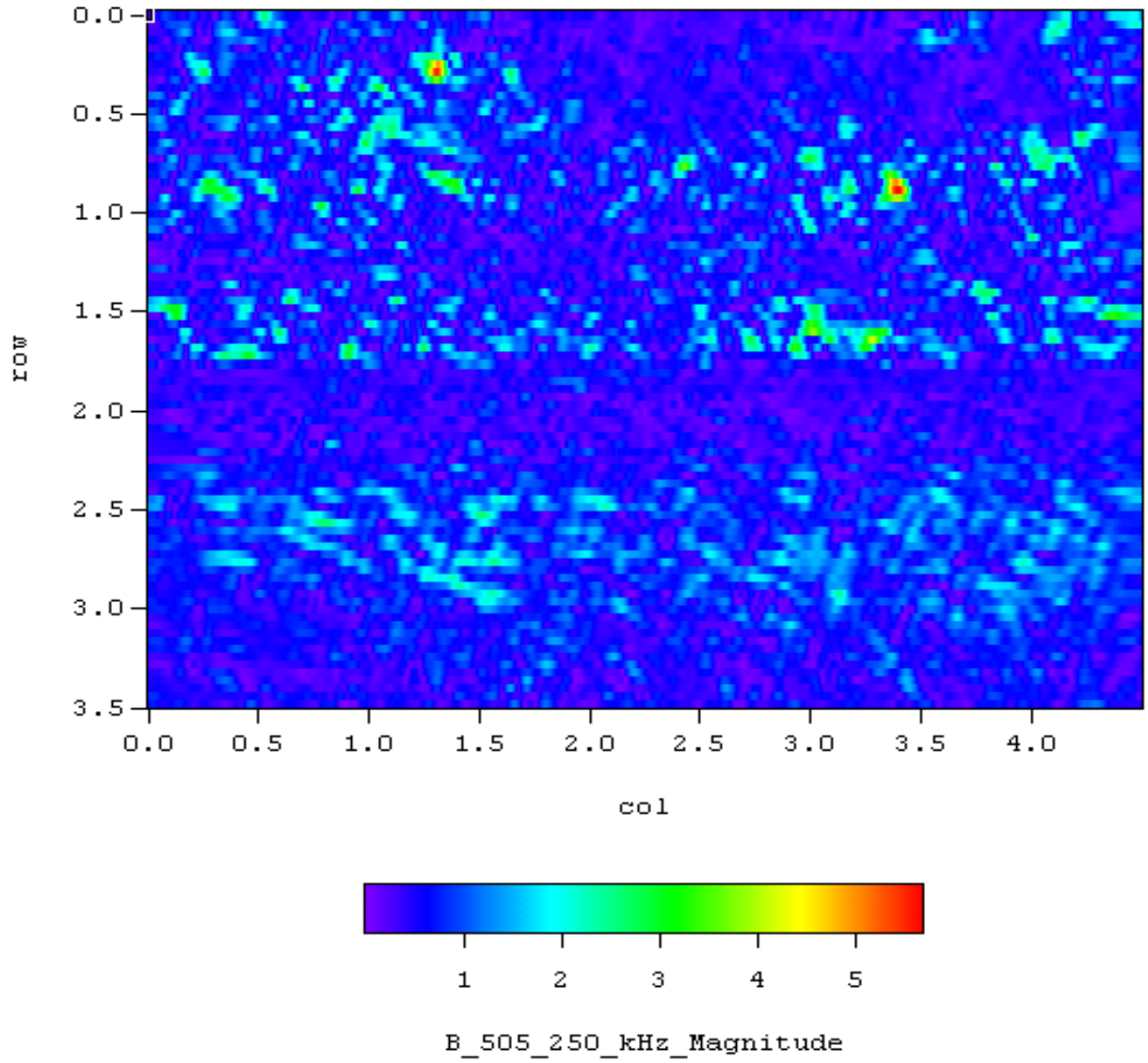

Figure B.18 Magnitude Plot of PNNL Specimen B-505

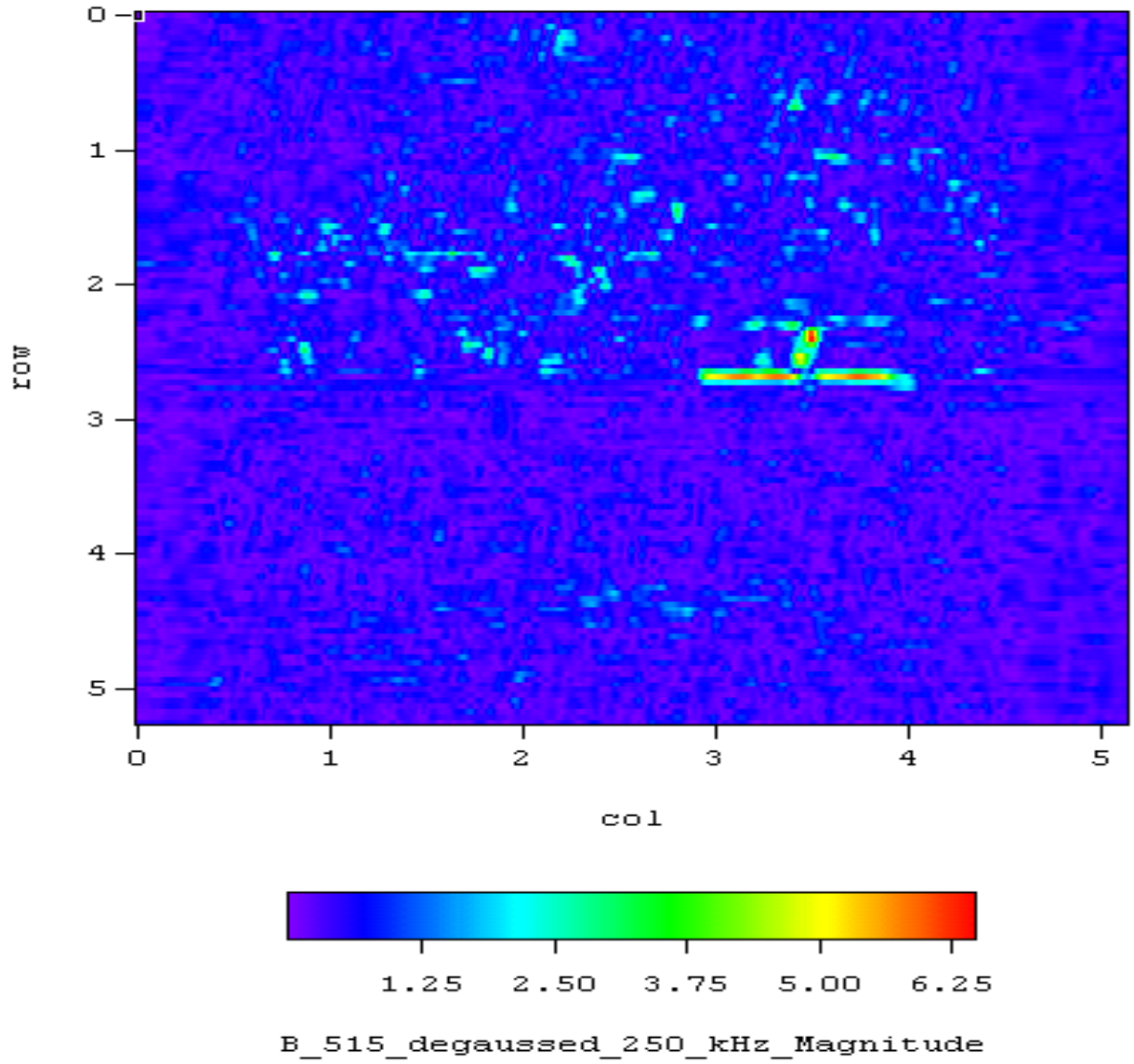

Figure B.19 Magnitude Plot of PNNL Specimen B-515

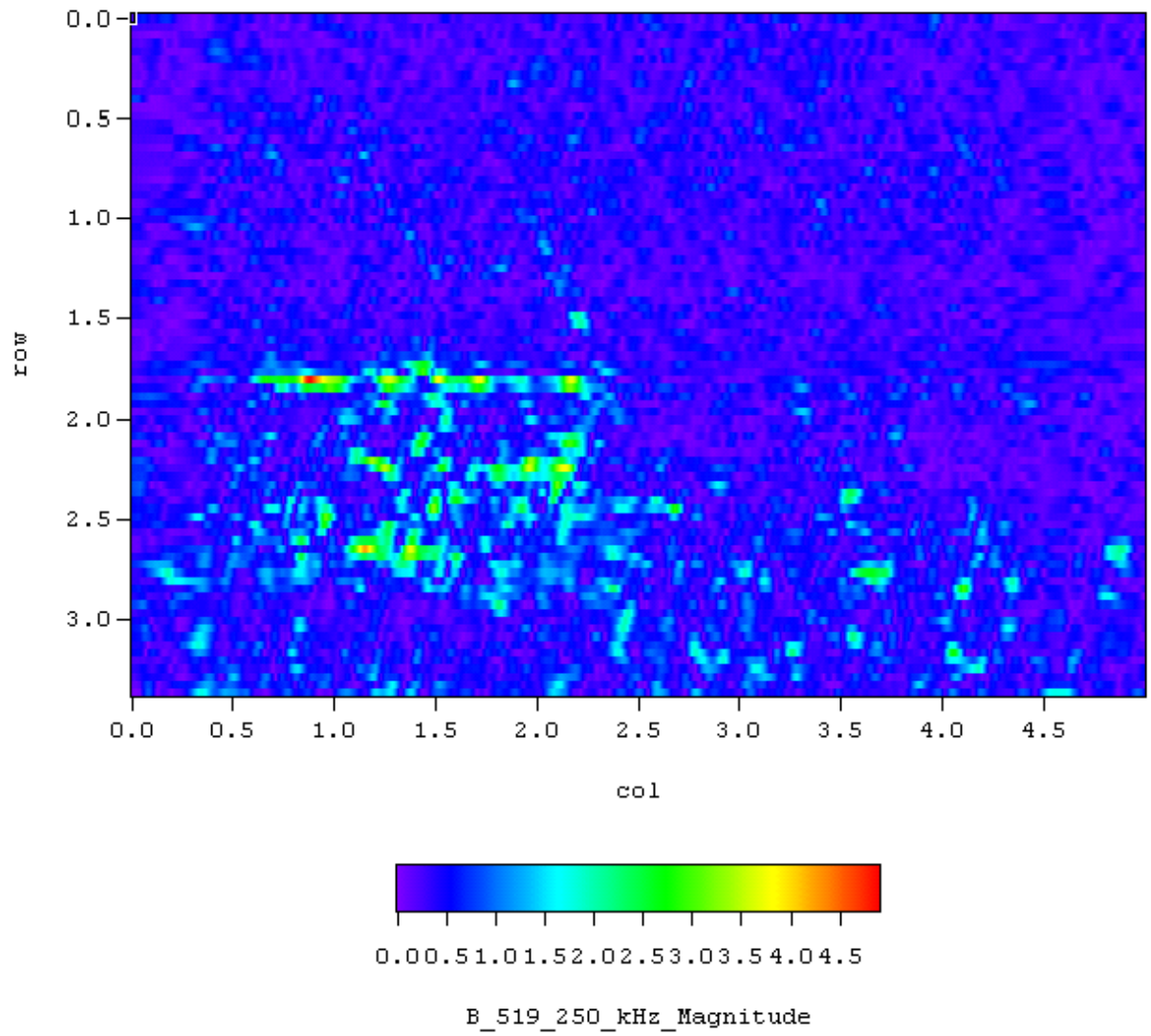

Figure B.20 Magnitude Plot of PNNL Specimen B-519

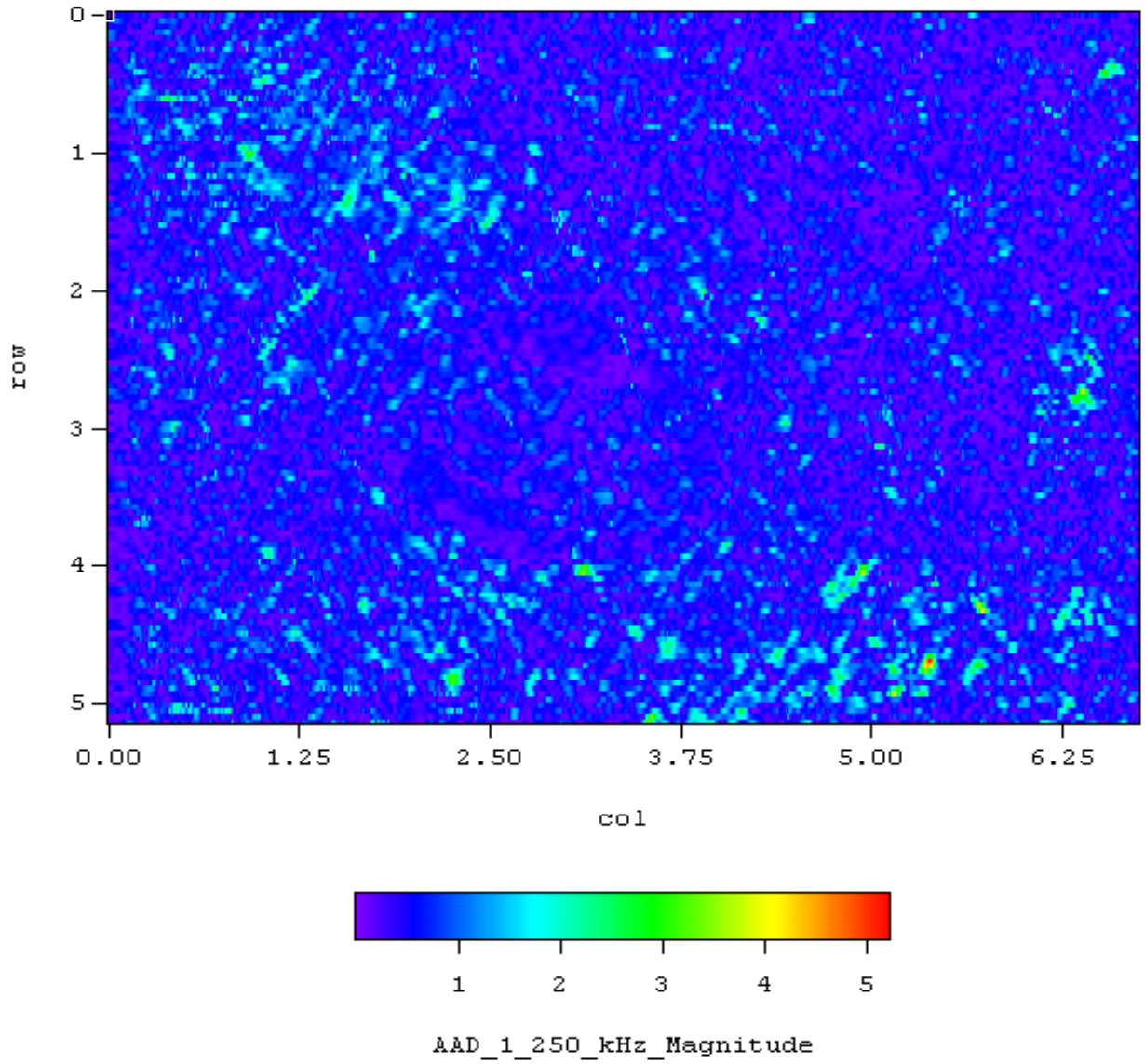

Figure B.21 Magnitude Plot of Southwest Research Institute Specimen AAD-1

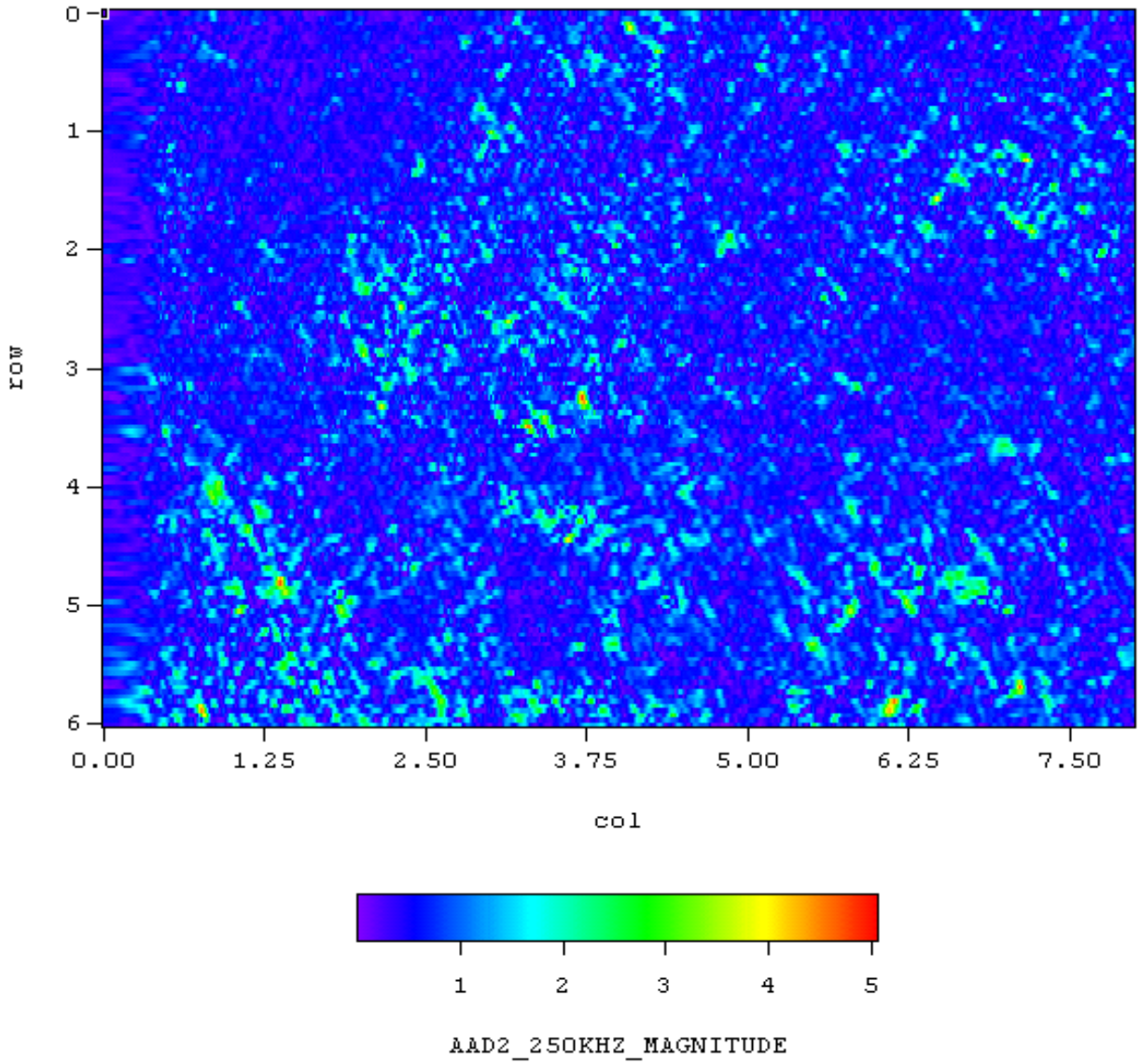

Figure B.22 Magnitude Plot of Southwest Research Institute Specimen AAD-2

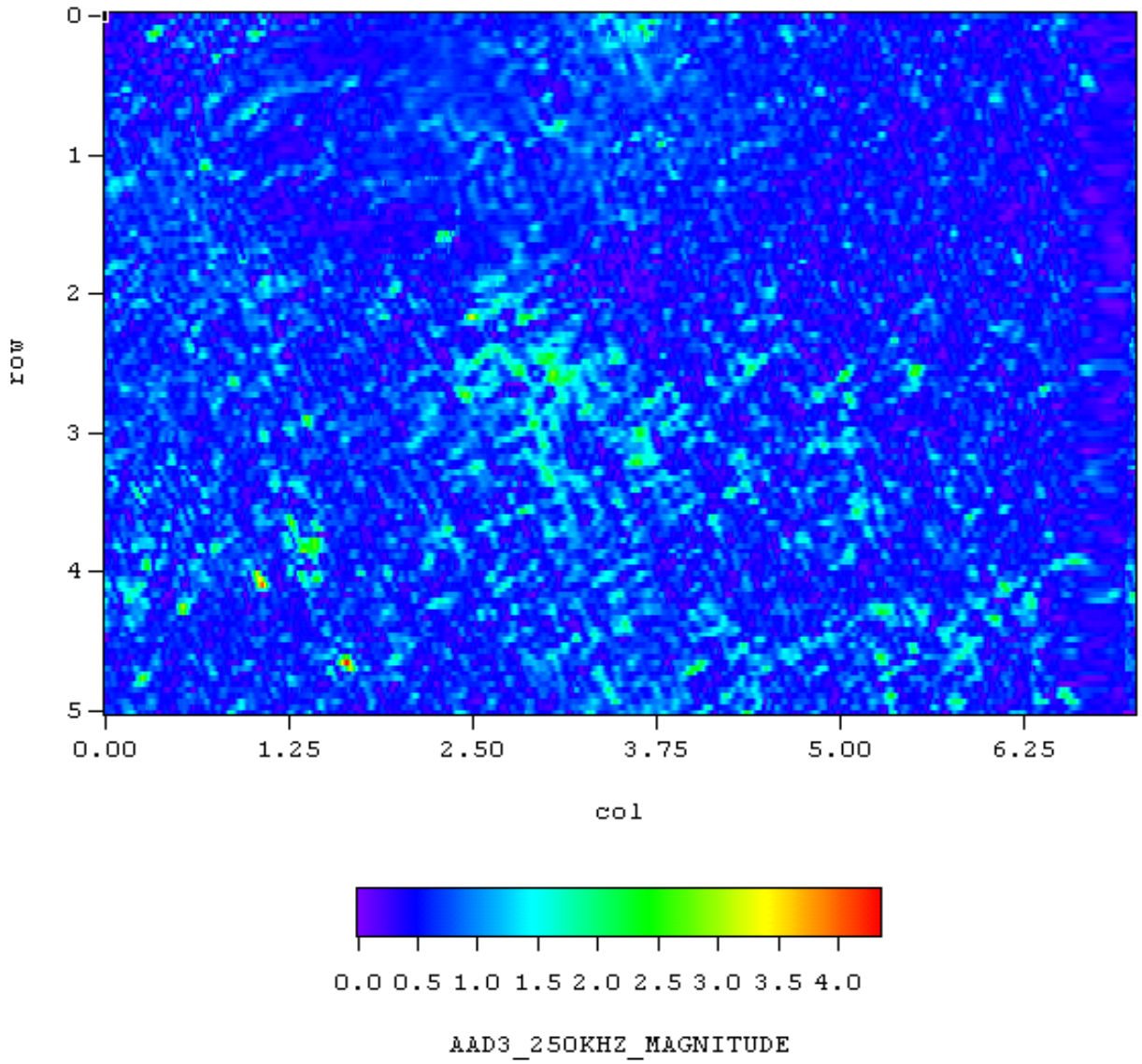

Figure B.23 Magnitude Plot of Southwest Research Institute Specimen AAD-3

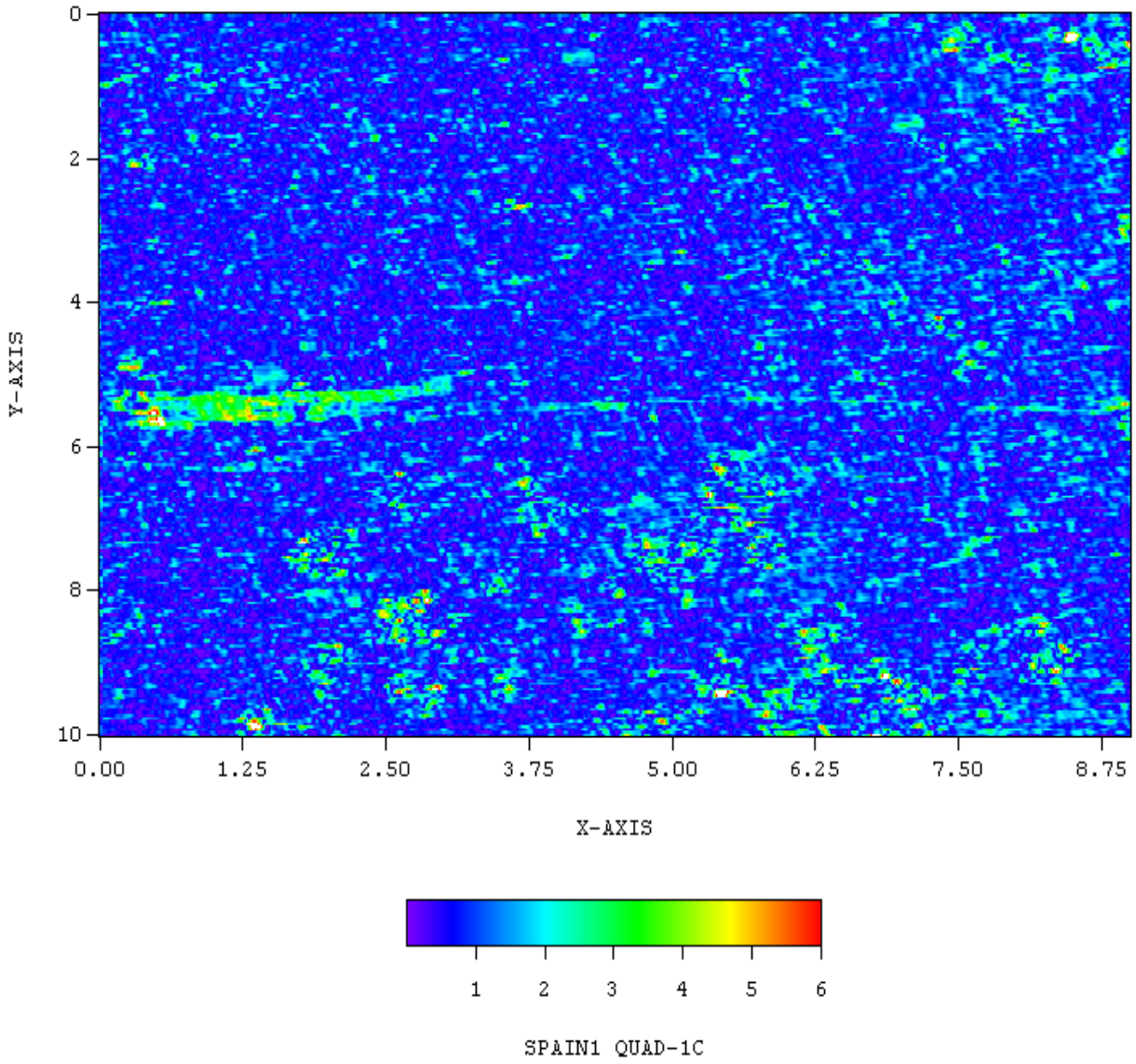

Figure B.24 Magnitude Plot of EPRI NDE Center Spanish Spool Piece Specimen (right side, Quadrant 1)

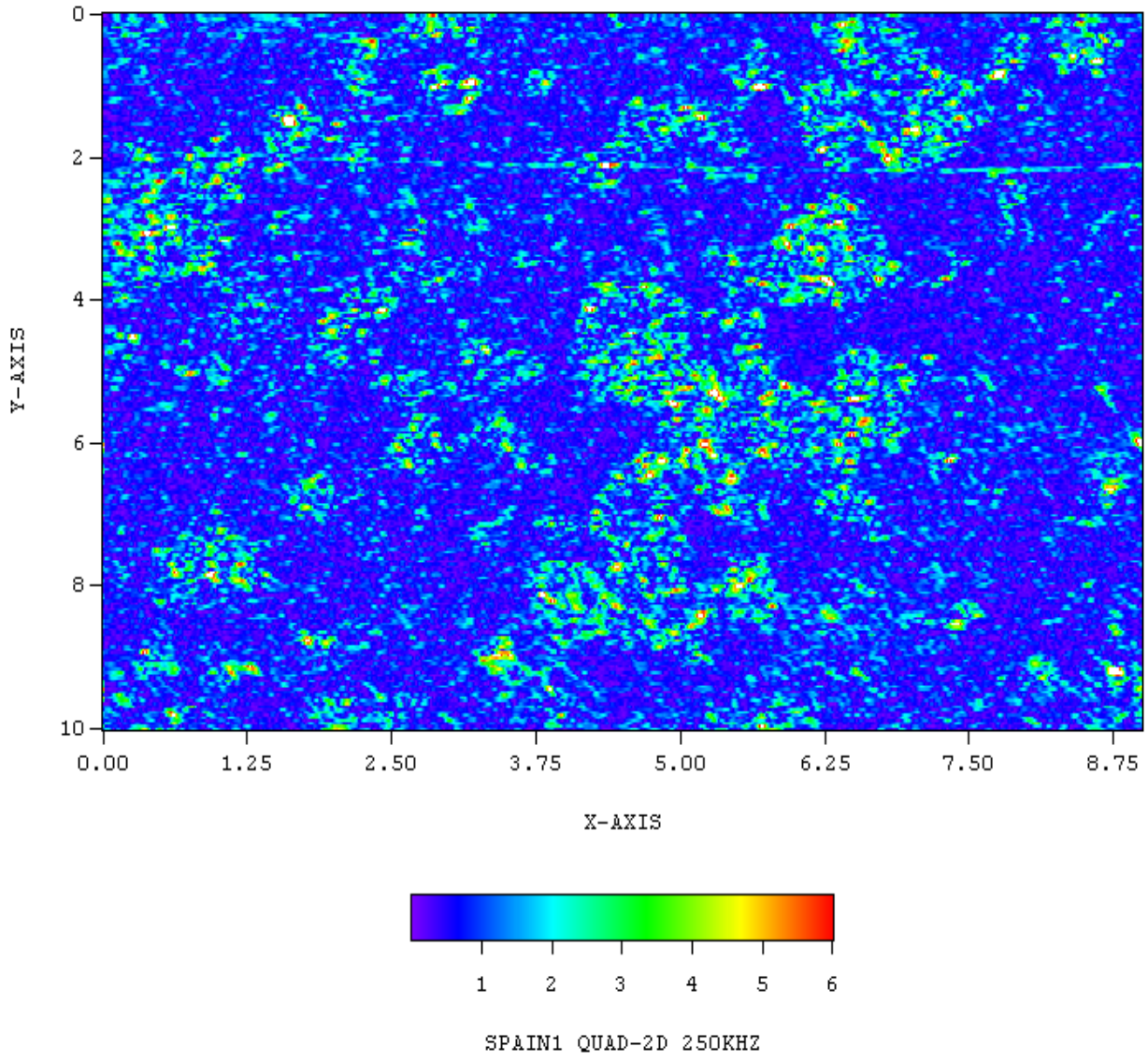

Figure B.25 Magnitude Plot of EPRI NDE Center Spanish Spool Piece Specimen (right side, Quadrant 2)

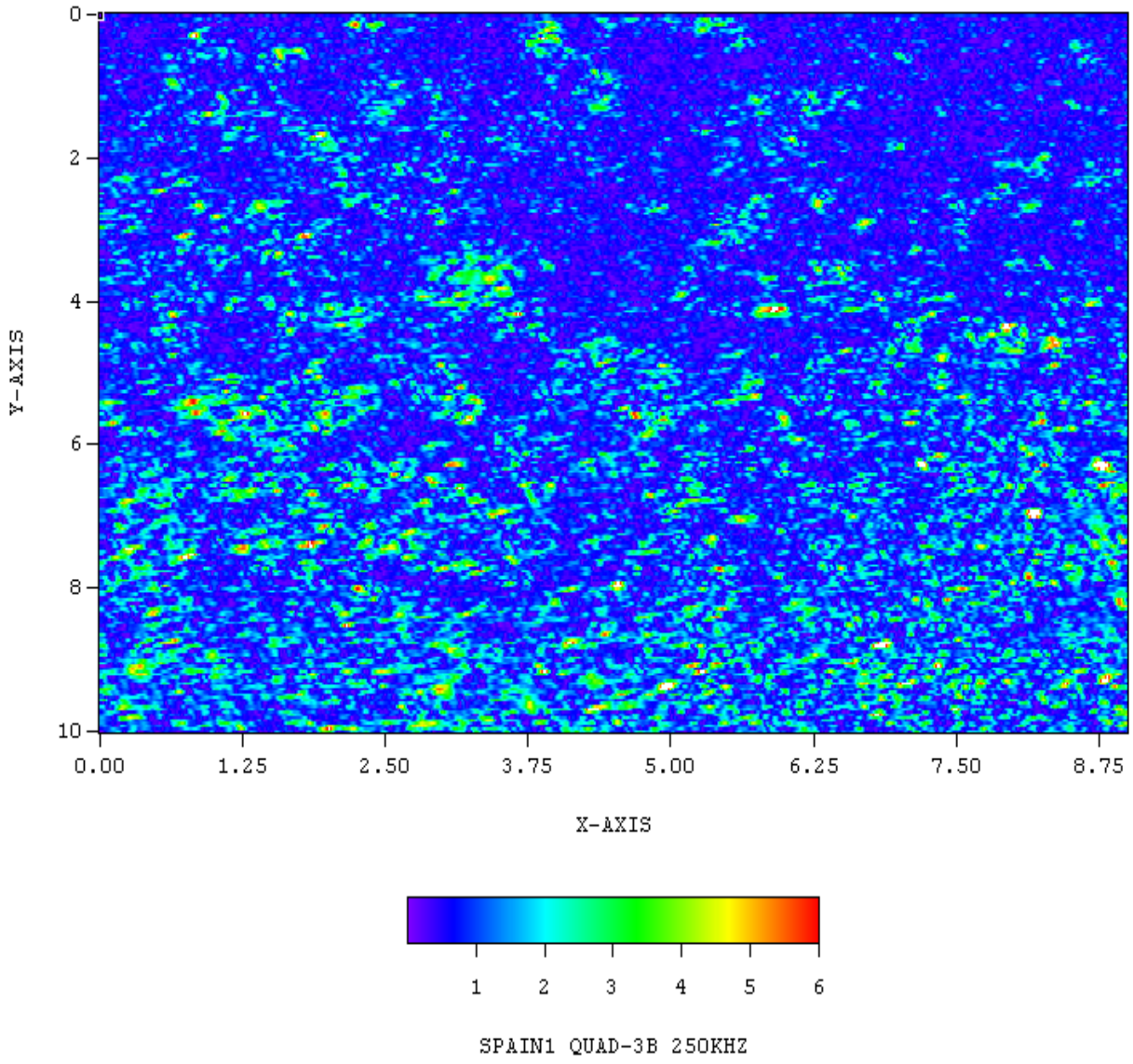

Figure B.26 Magnitude Plot of EPRI NDE Center Spanish Spool Piece Specimen (right side, Quadrant 3)

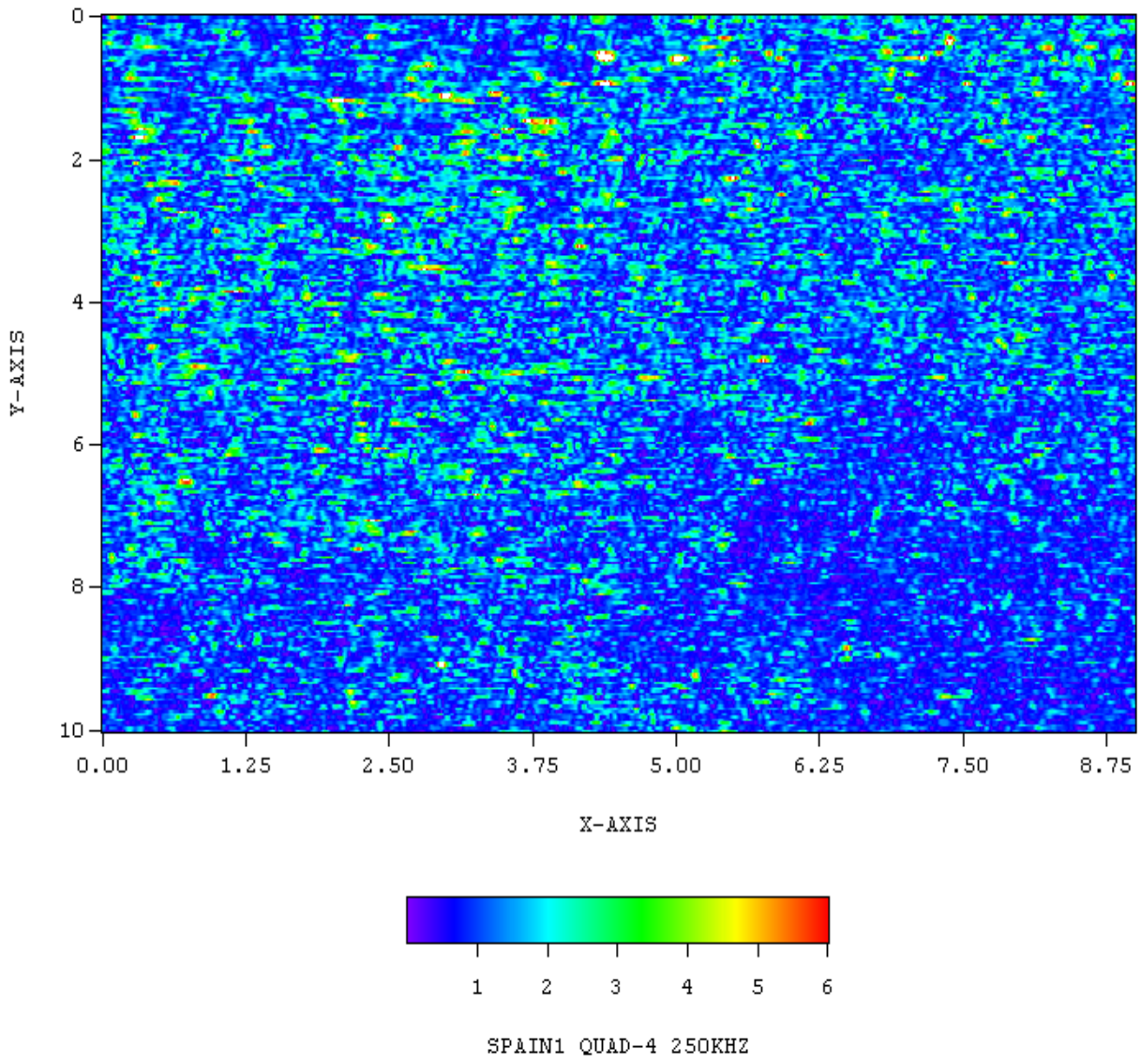

Figure B.27 Magnitude Plot of EPRI NDE Center Spanish Spool Piece Specimen (right side, Quadrant 4)

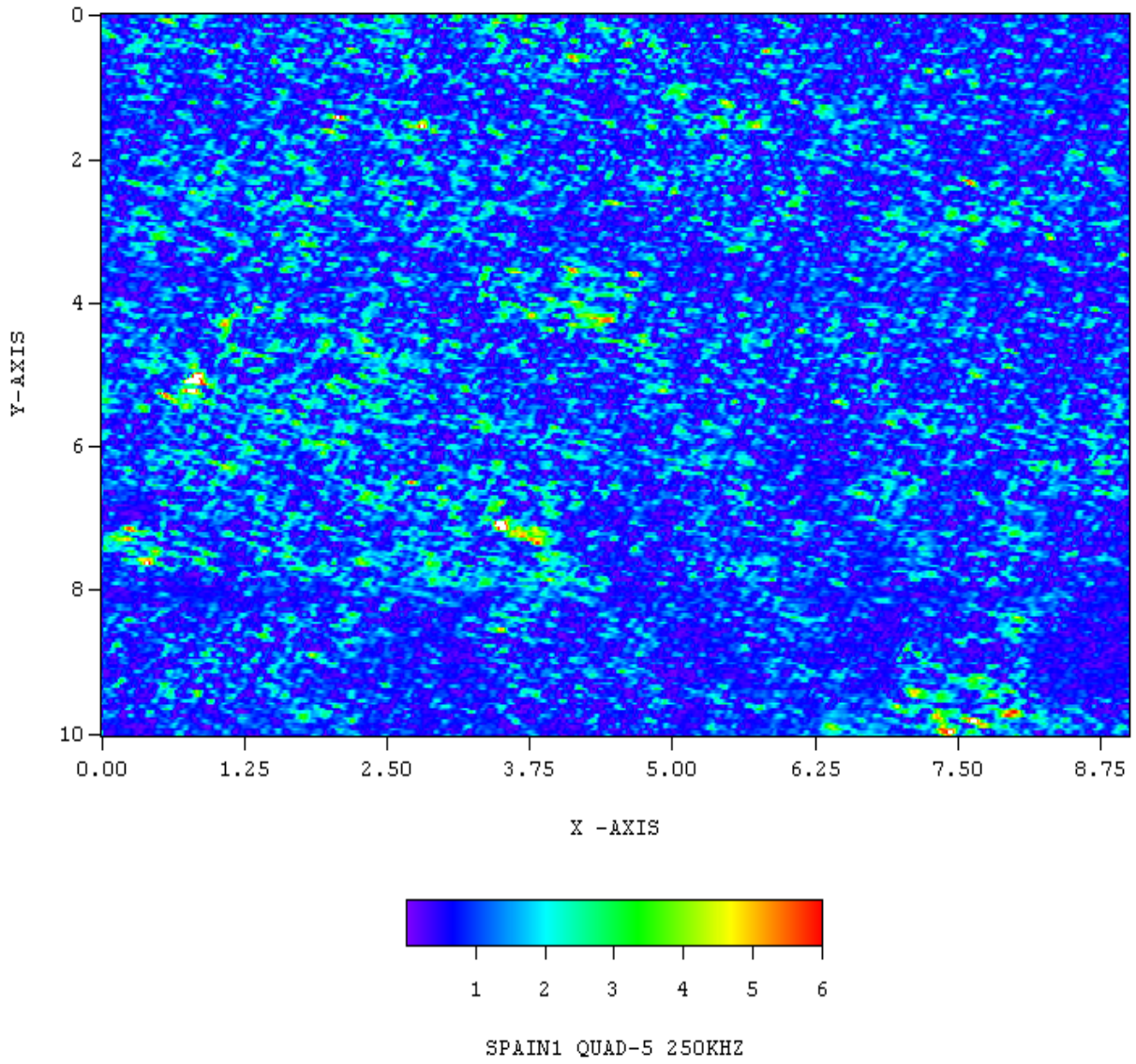

Figure B.28 Magnitude Plot of EPRI NDE Center Spanish Spool Piece Specimen (right side, Quadrant 5)

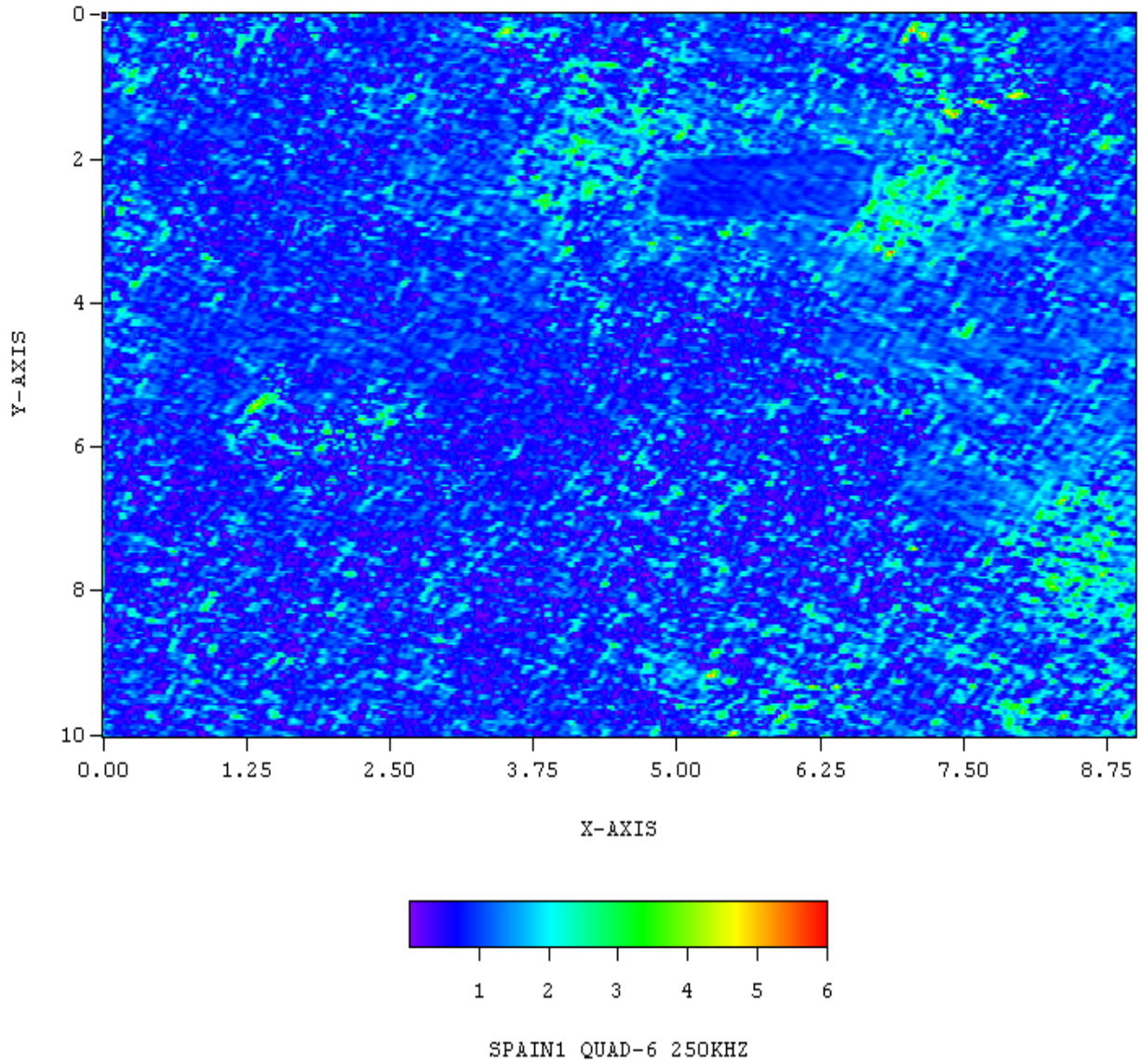

Figure B.29 Magnitude Plot of EPRI NDE Center Spanish Spool Piece Specimen (right side, Quadrant 6)

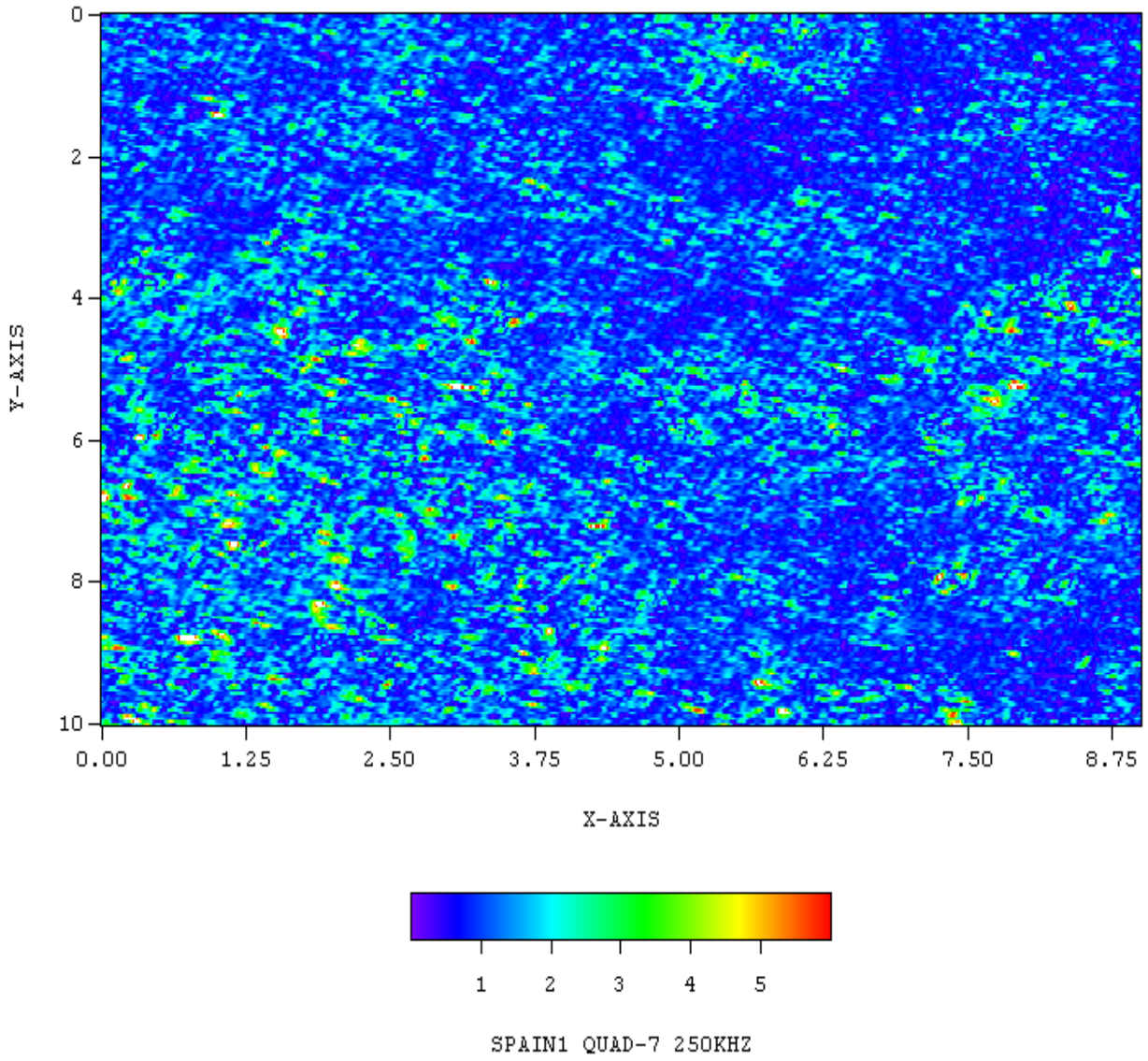

Figure B.30 Magnitude Plot of EPRI NDE Center Spanish Spool Piece Specimen (right side, Quadrant 7)

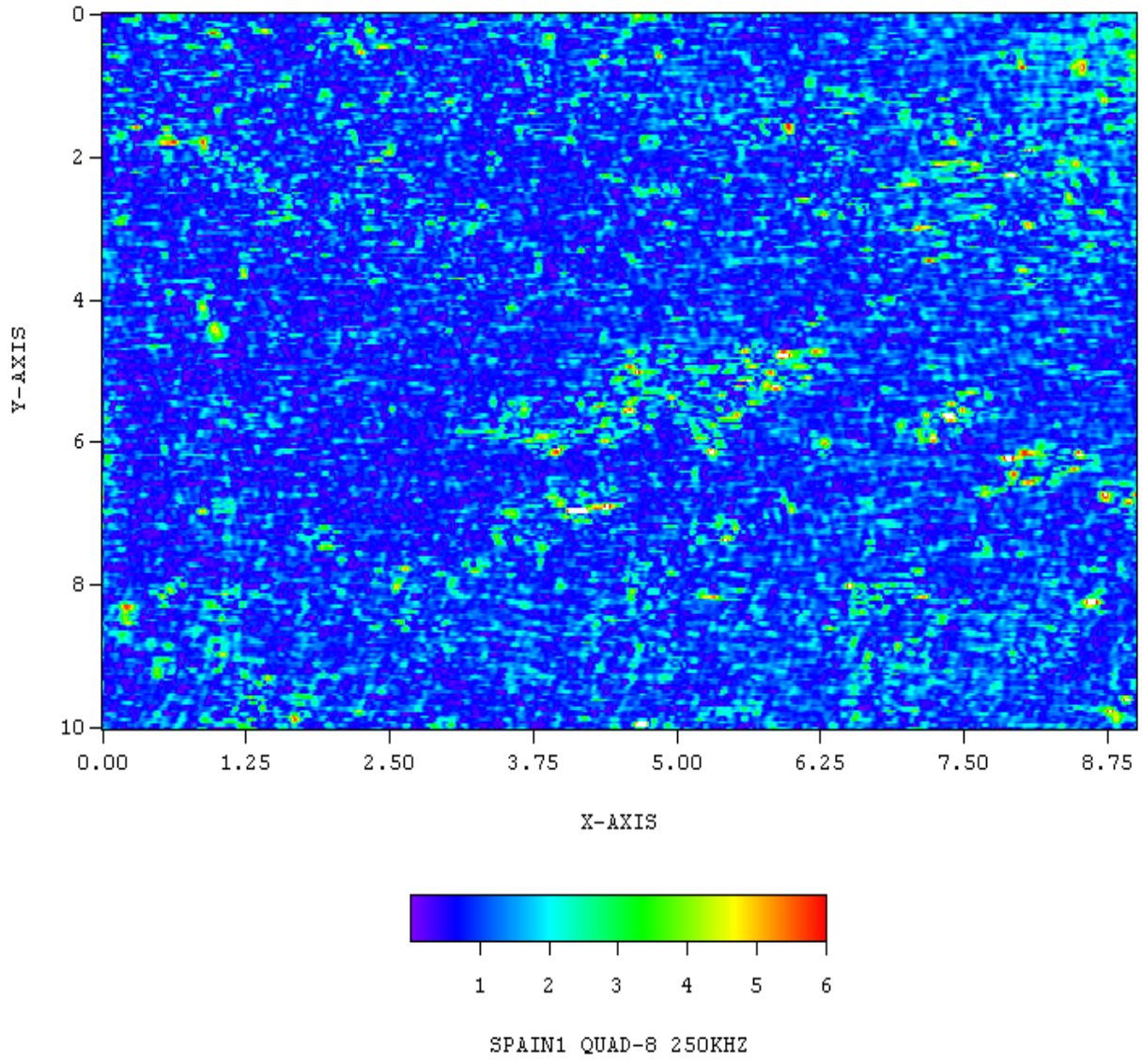

Figure B.31 Magnitude Plot of EPRI NDE Center Spanish Spool Piece Specimen (right side, Quadrant 8)

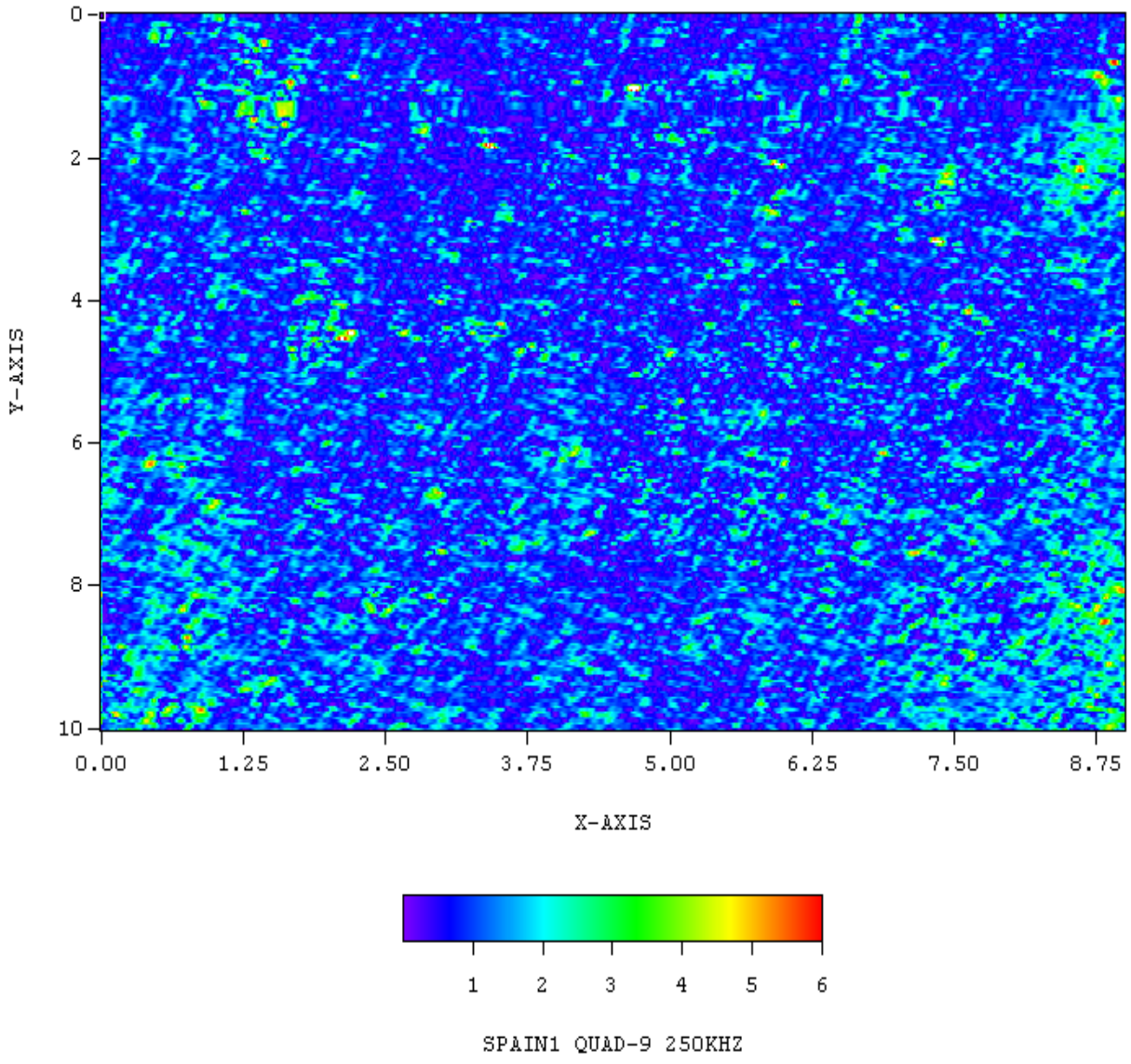

Figure B.32 Magnitude Plot of EPRI NDE Center Spanish Spool Piece Specimen (right side, Quadrant 9)

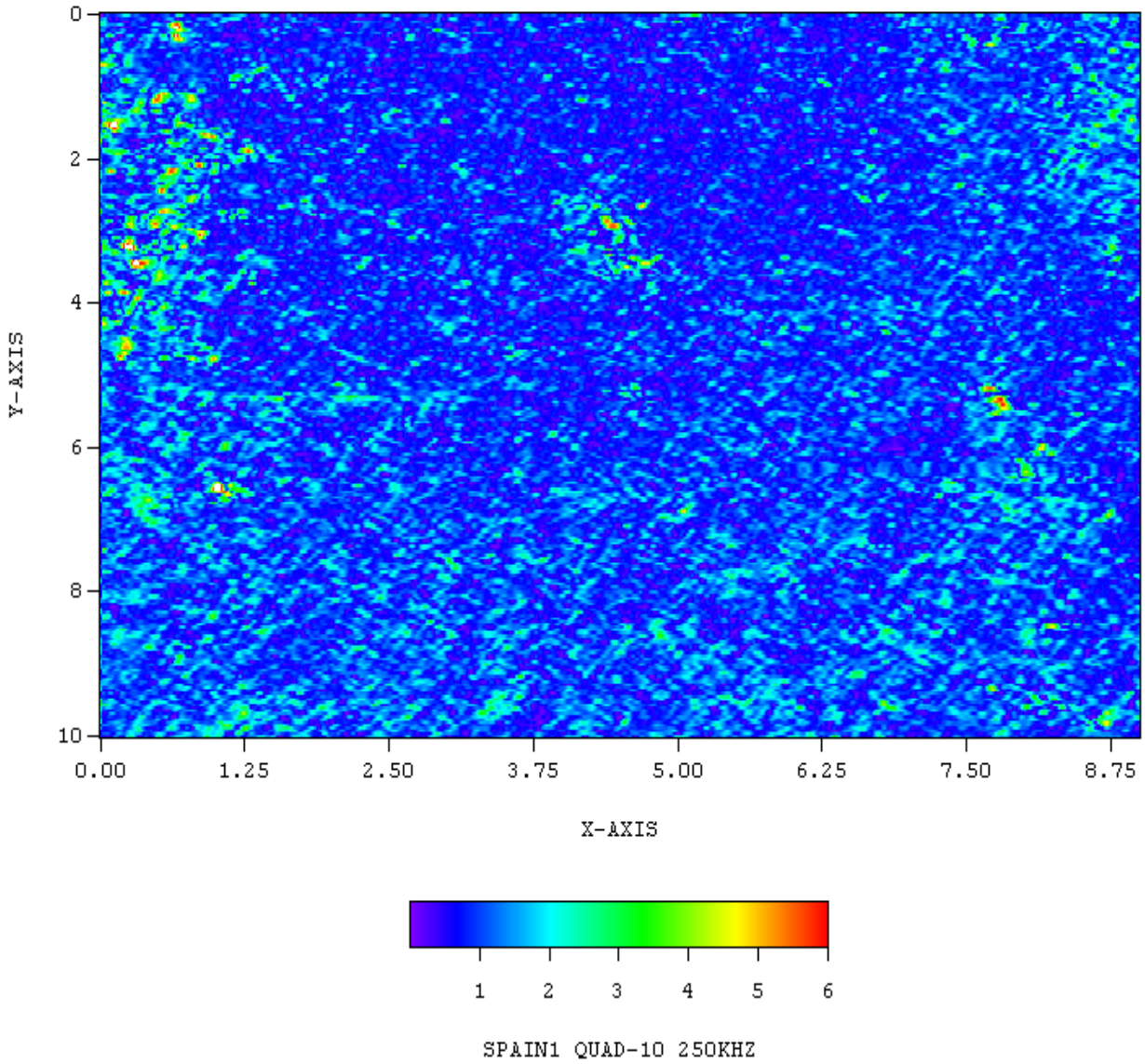

Figure B.33 Magnitude Plot of EPRI NDE Center Spanish Spool Piece Specimen (right side, Quadrant 10)

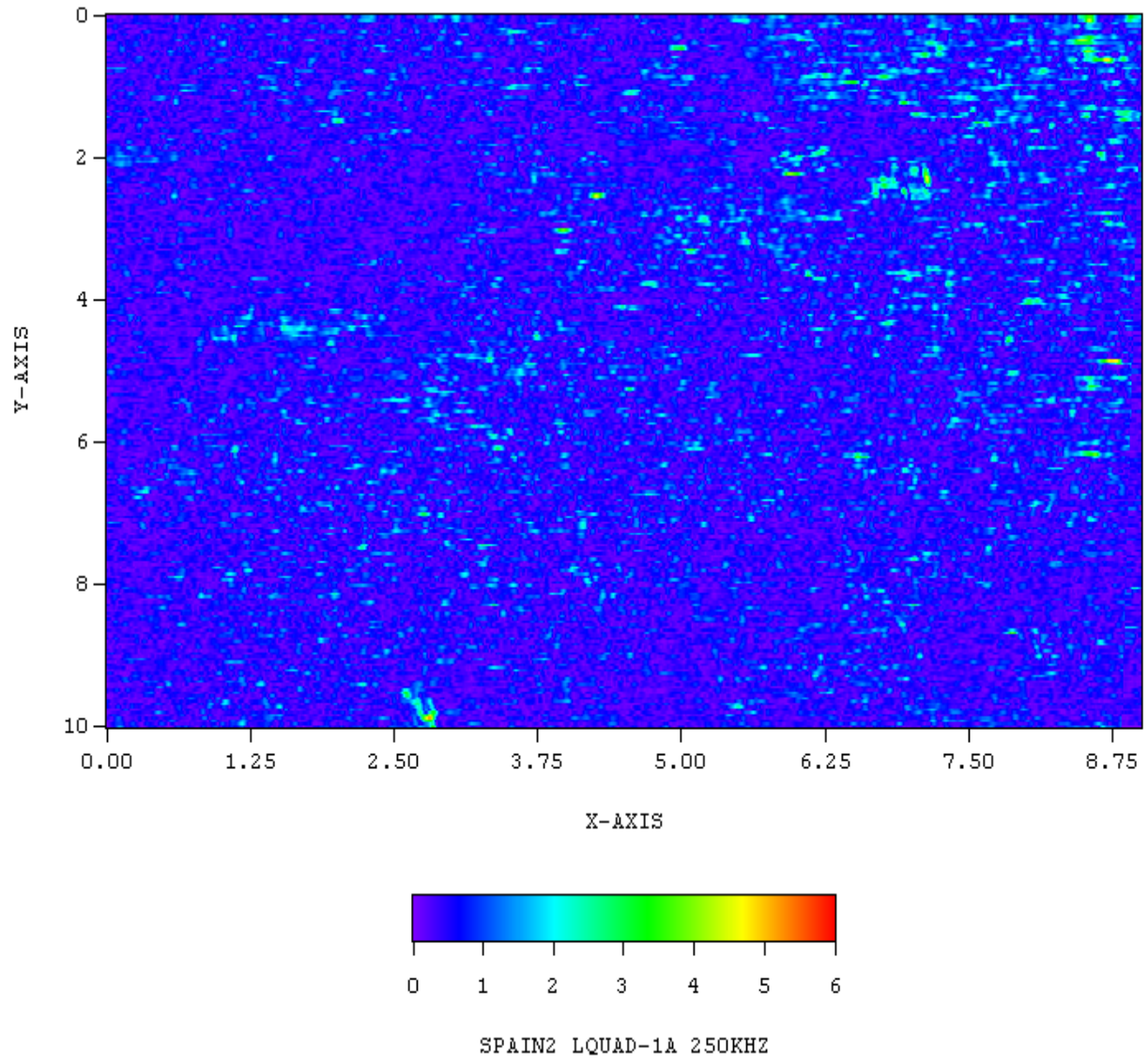

Figure B.34 Magnitude Plot of EPRI NDE Center Spanish Spool Piece Specimen (left side, Quadrant 1)

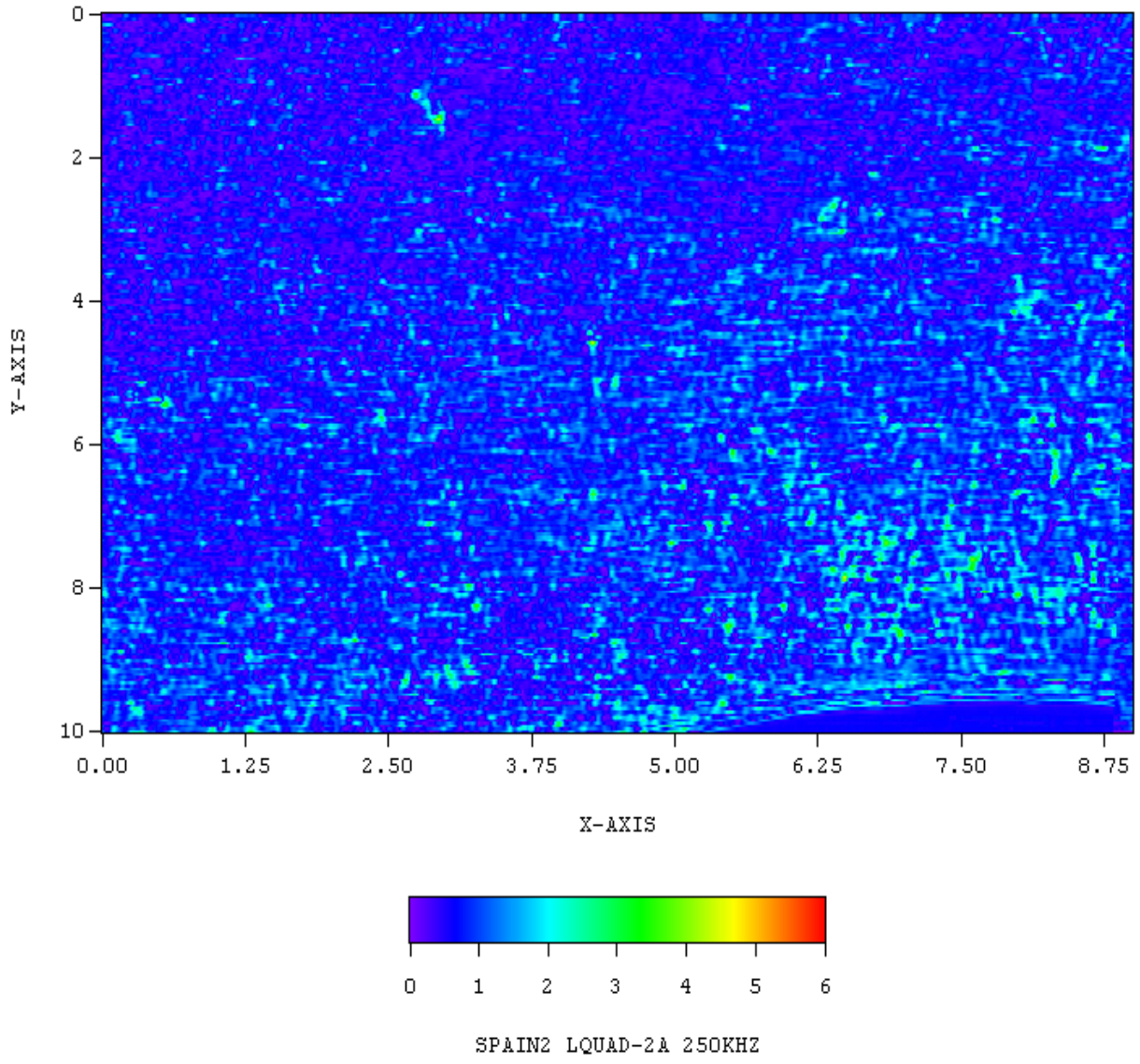

Figure B.35 Magnitude Plot of EPRI NDE Center Spanish Spool Piece Specimen (left side, Quadrant 2)

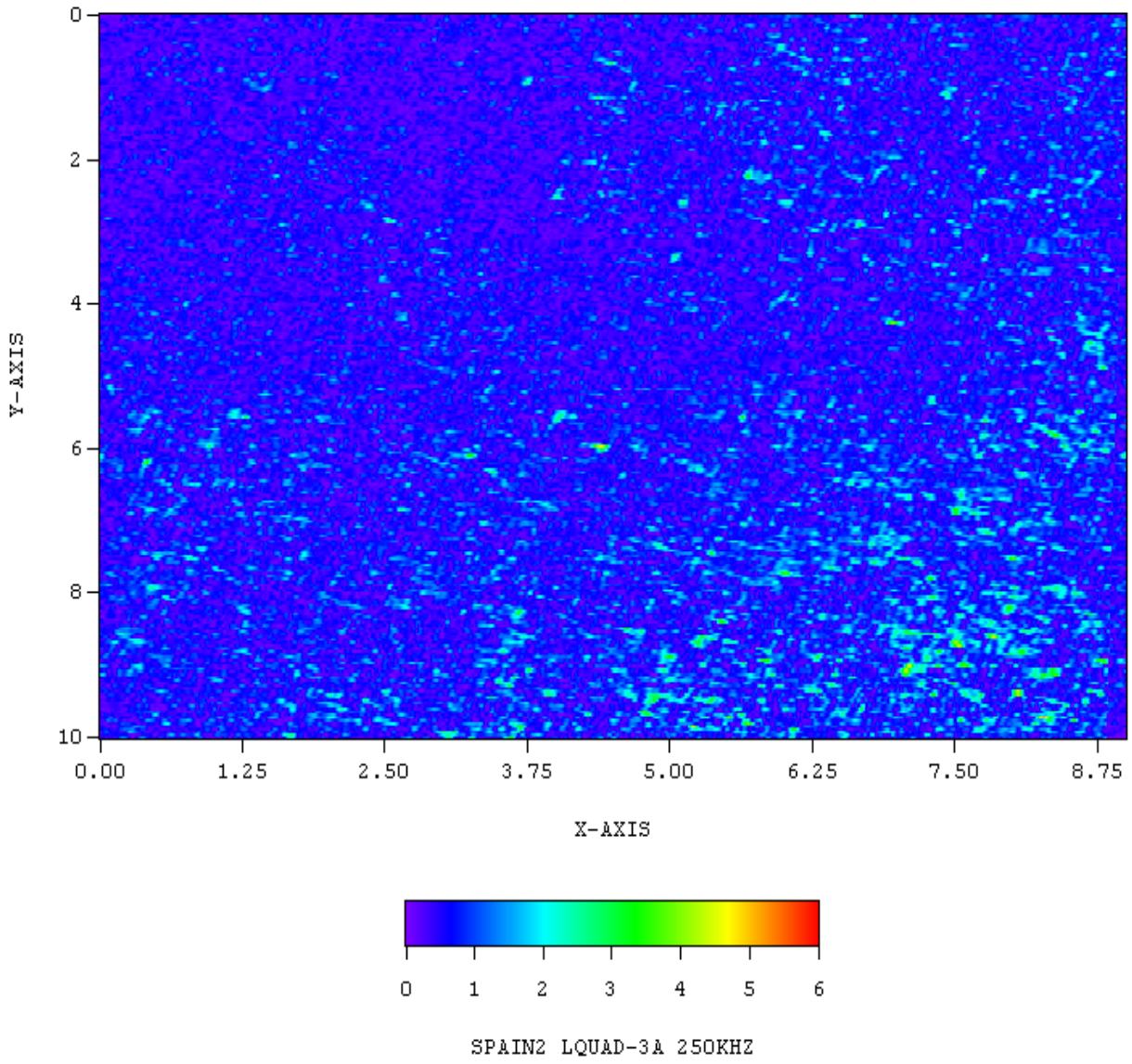

Figure B.36 Magnitude Plot of EPRI NDE Center Spanish Spool Piece Specimen (left side, Quadrant 3)

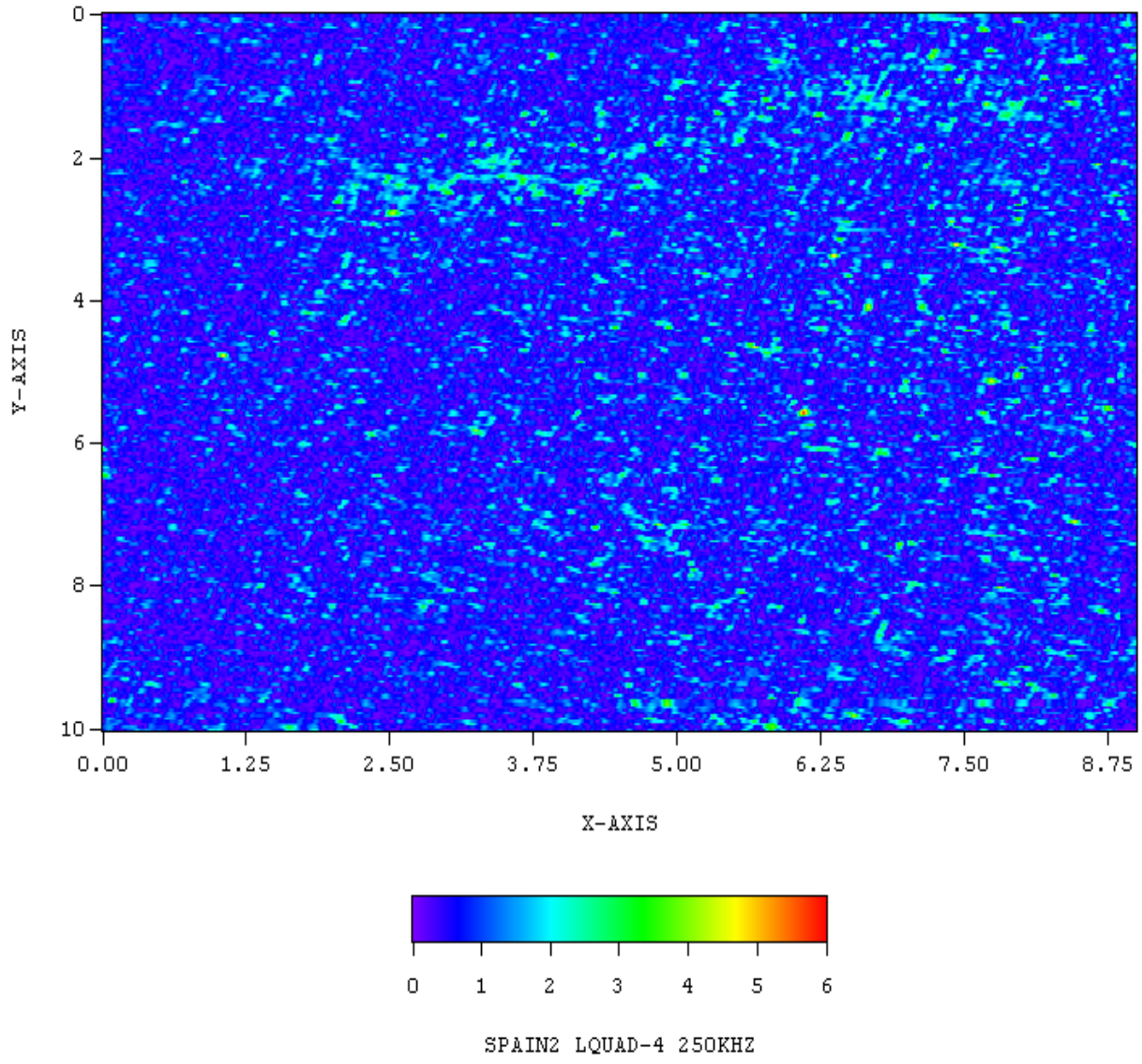

Figure B.37 Magnitude Plot of EPRI NDE Center Spanish Spool Piece Specimen (left side, Quadrant 4)

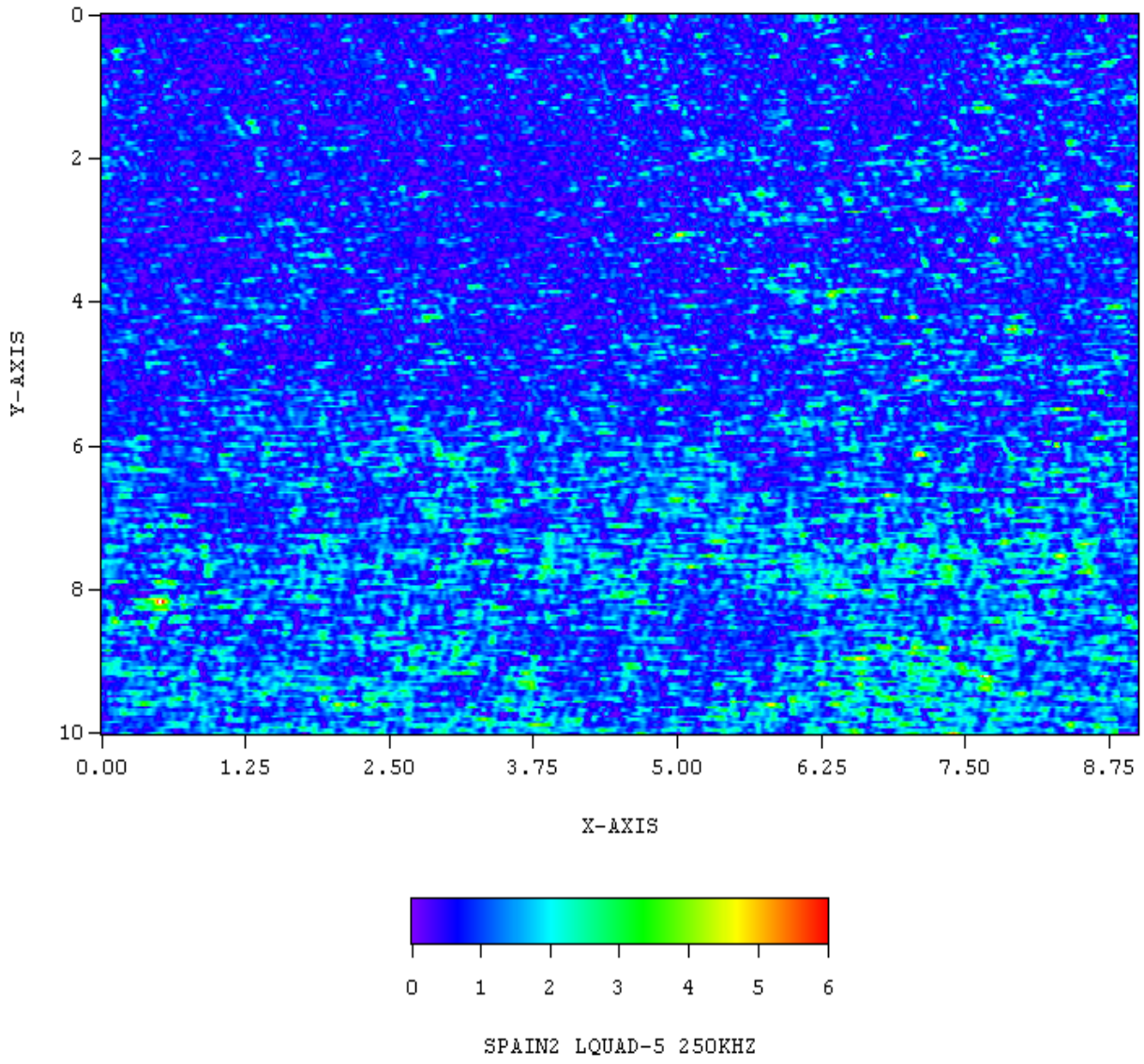

Figure B.38 Magnitude Plot of EPRI NDE Center Spanish Spool Piece Specimen (left side, Quadrant 5)

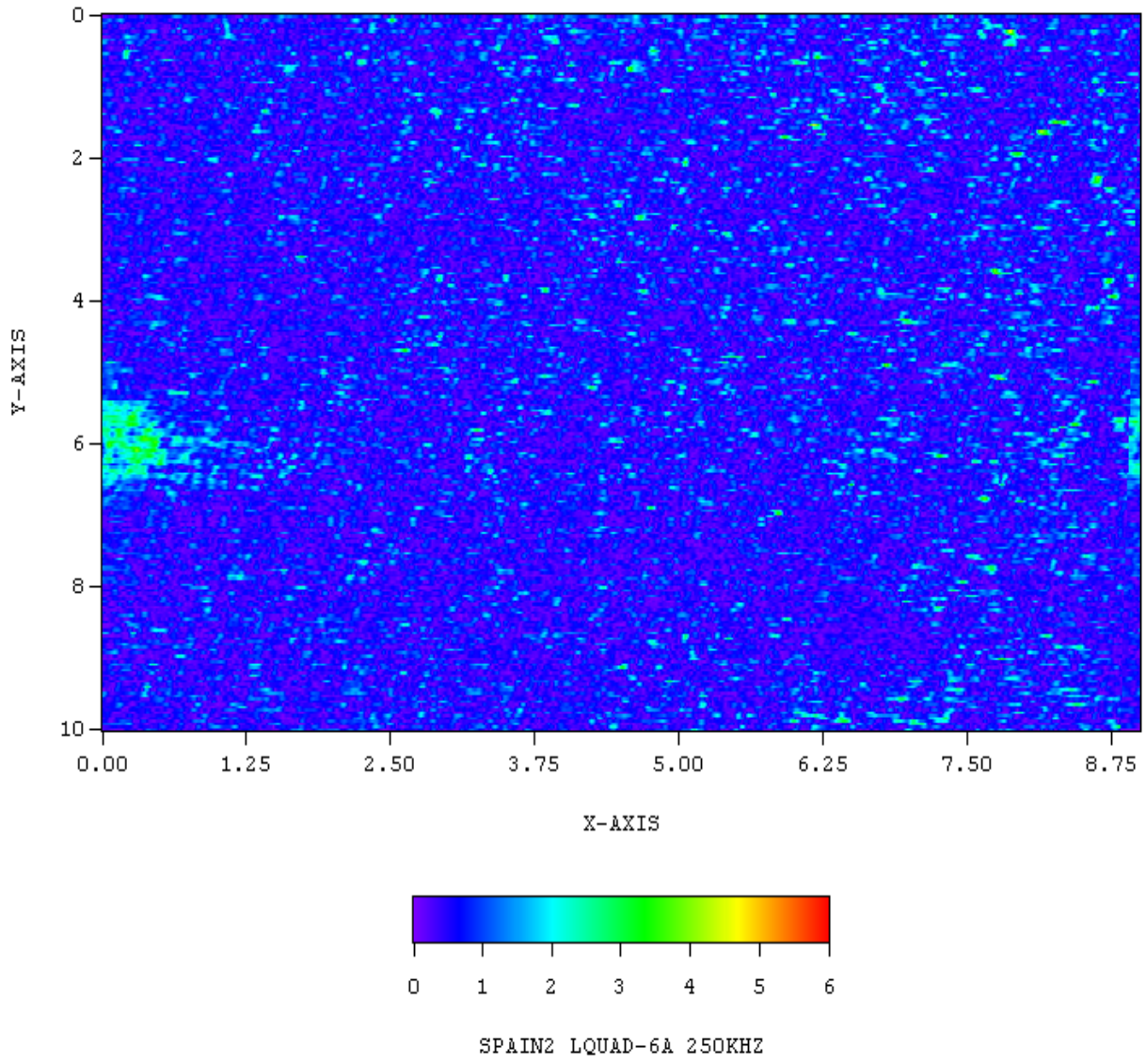

Figure B.39 Magnitude Plot of EPRI NDE Center Spanish Spool Piece Specimen (left side, Quadrant 6)

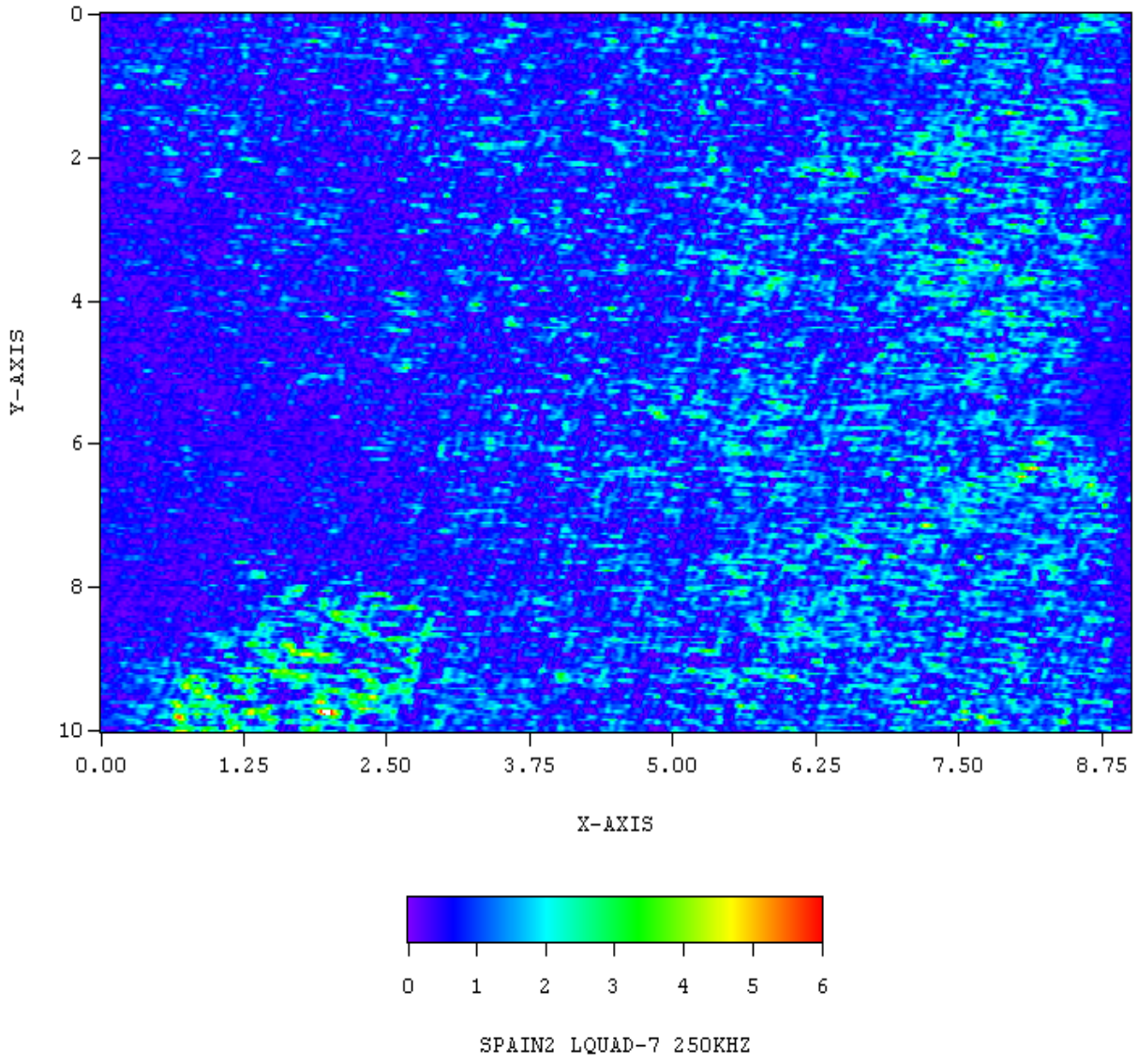

Figure B.40 Magnitude Plot of EPRI NDE Center Spanish Spool Piece Specimen (left side, Quadrant 7)

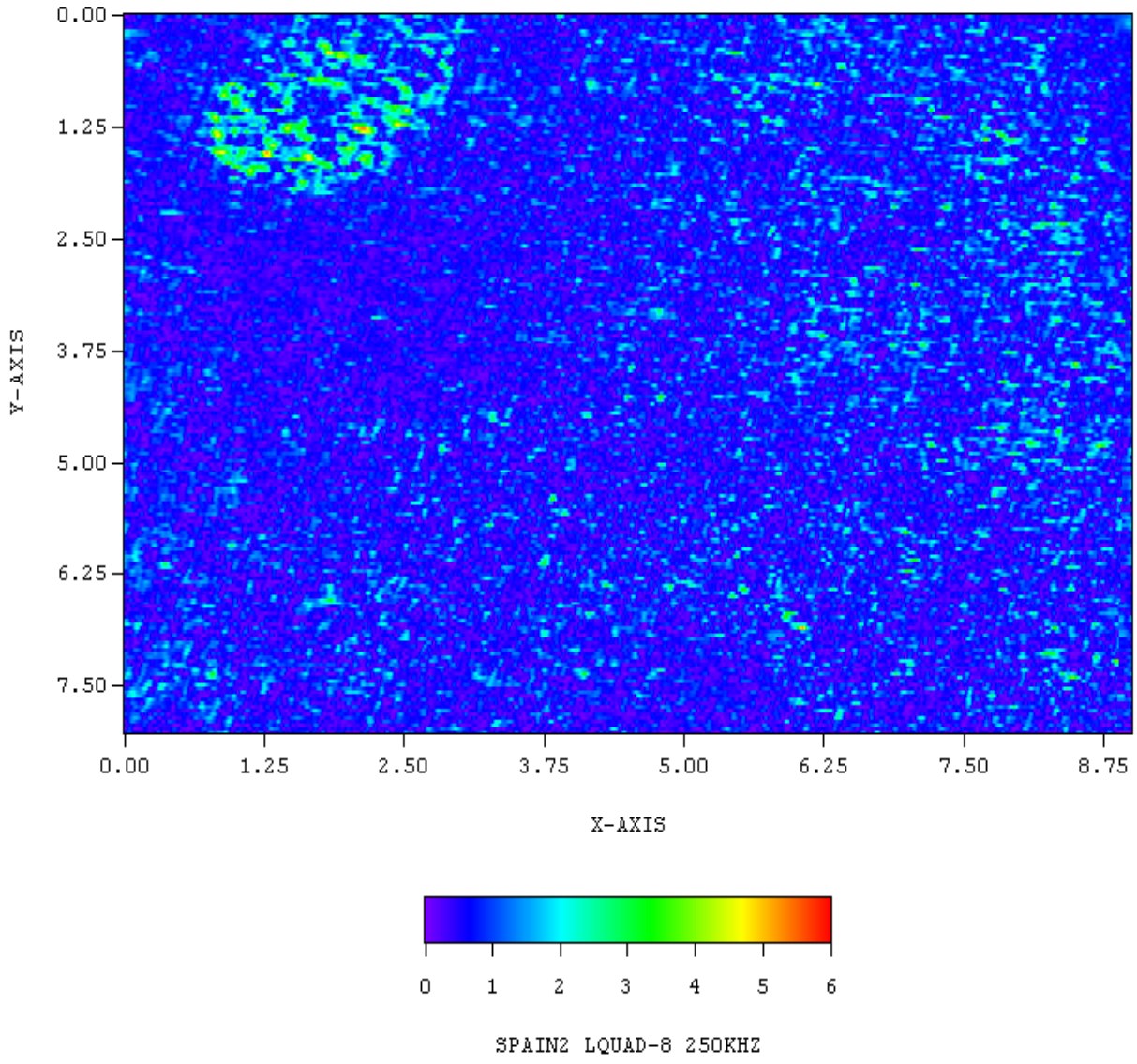

Figure B.41 Magnitude Plot of EPRI NDE Center Spanish Spool Piece Specimen (left side, Quadrant 8)

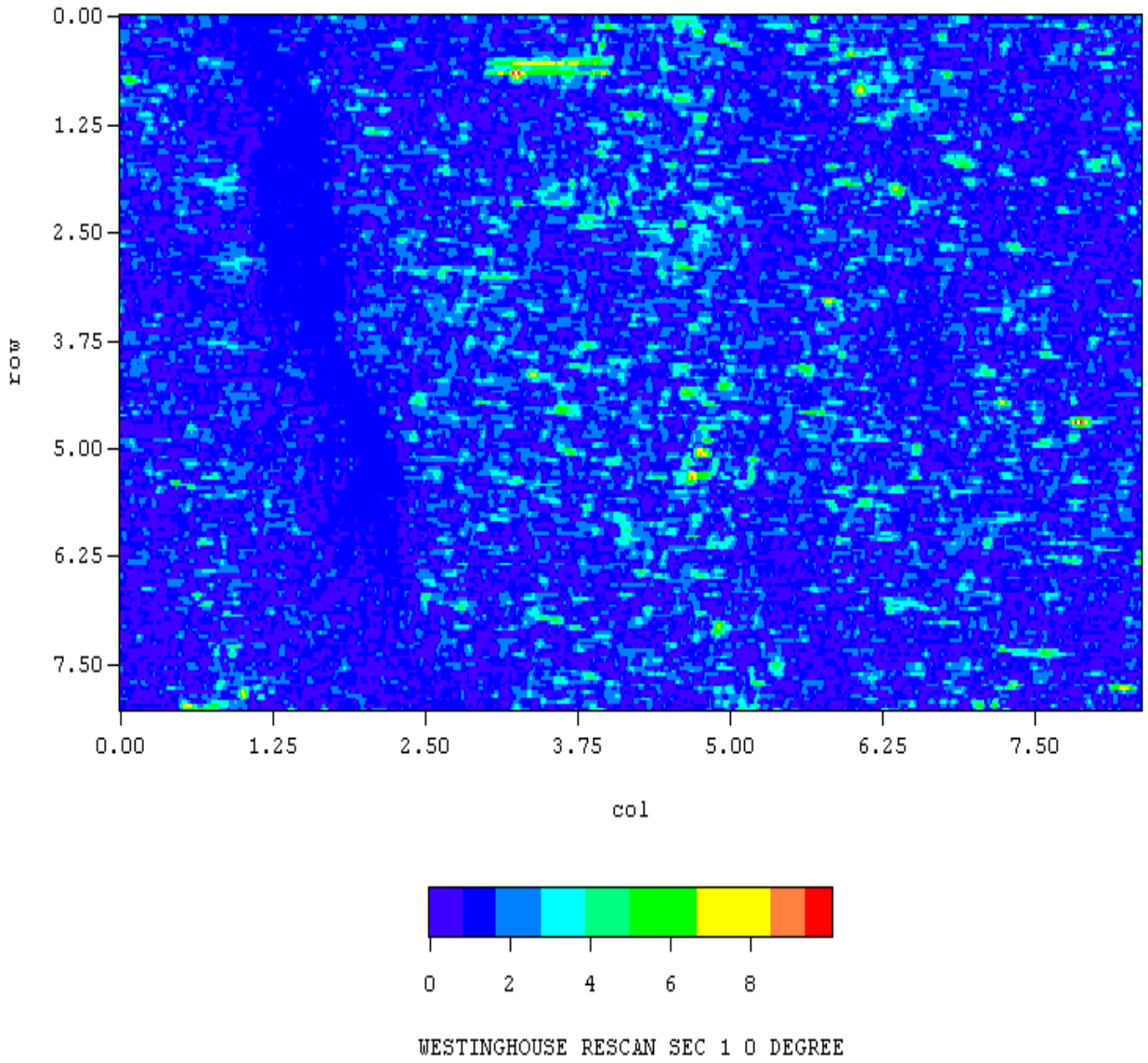

Figure B.42 Magnitude Plot of Westinghouse Spool Piece Specimen Quadrant 1

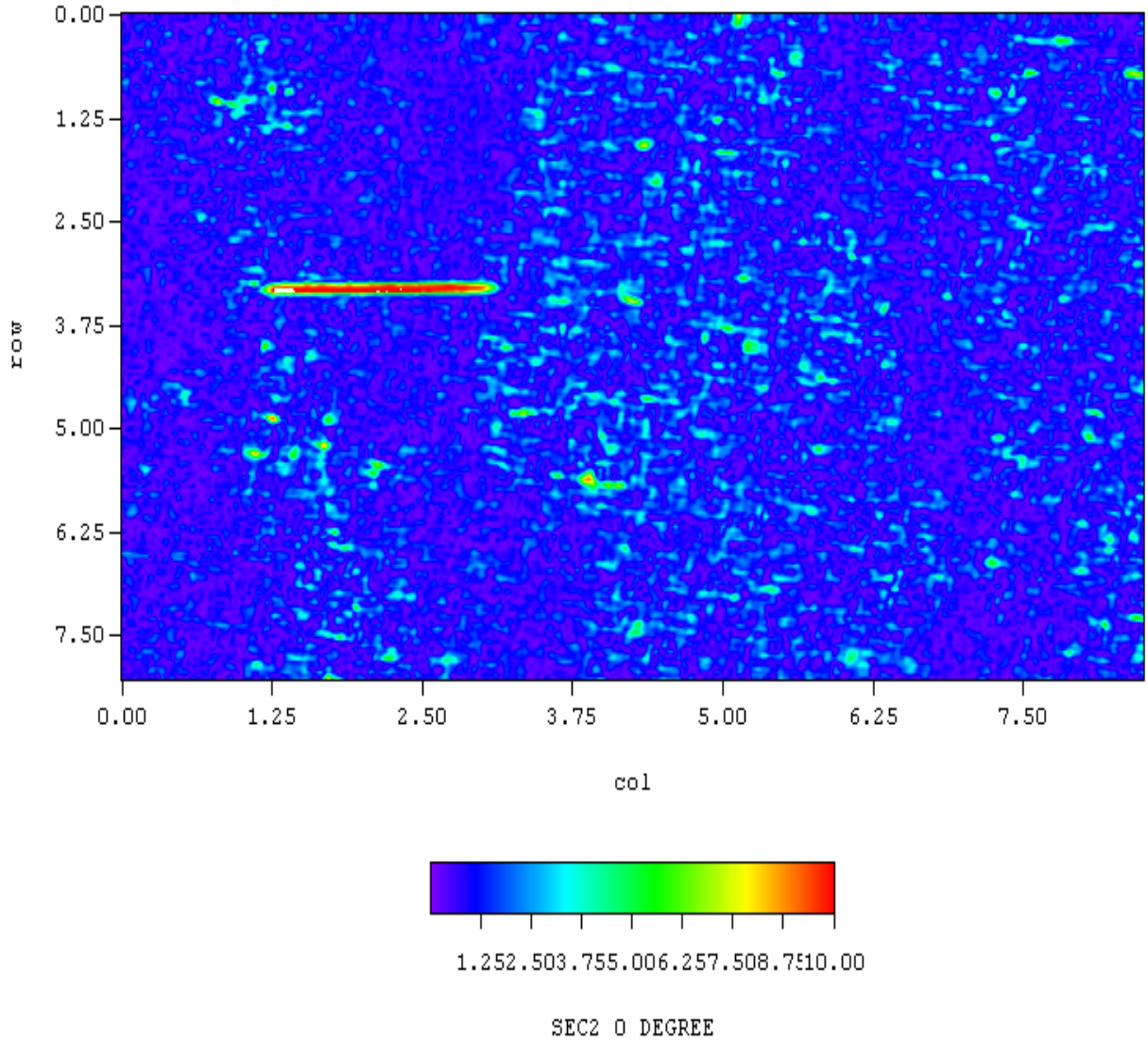

Figure B.43 Magnitude Plot of Westinghouse Spool Piece Specimen Quadrant 2

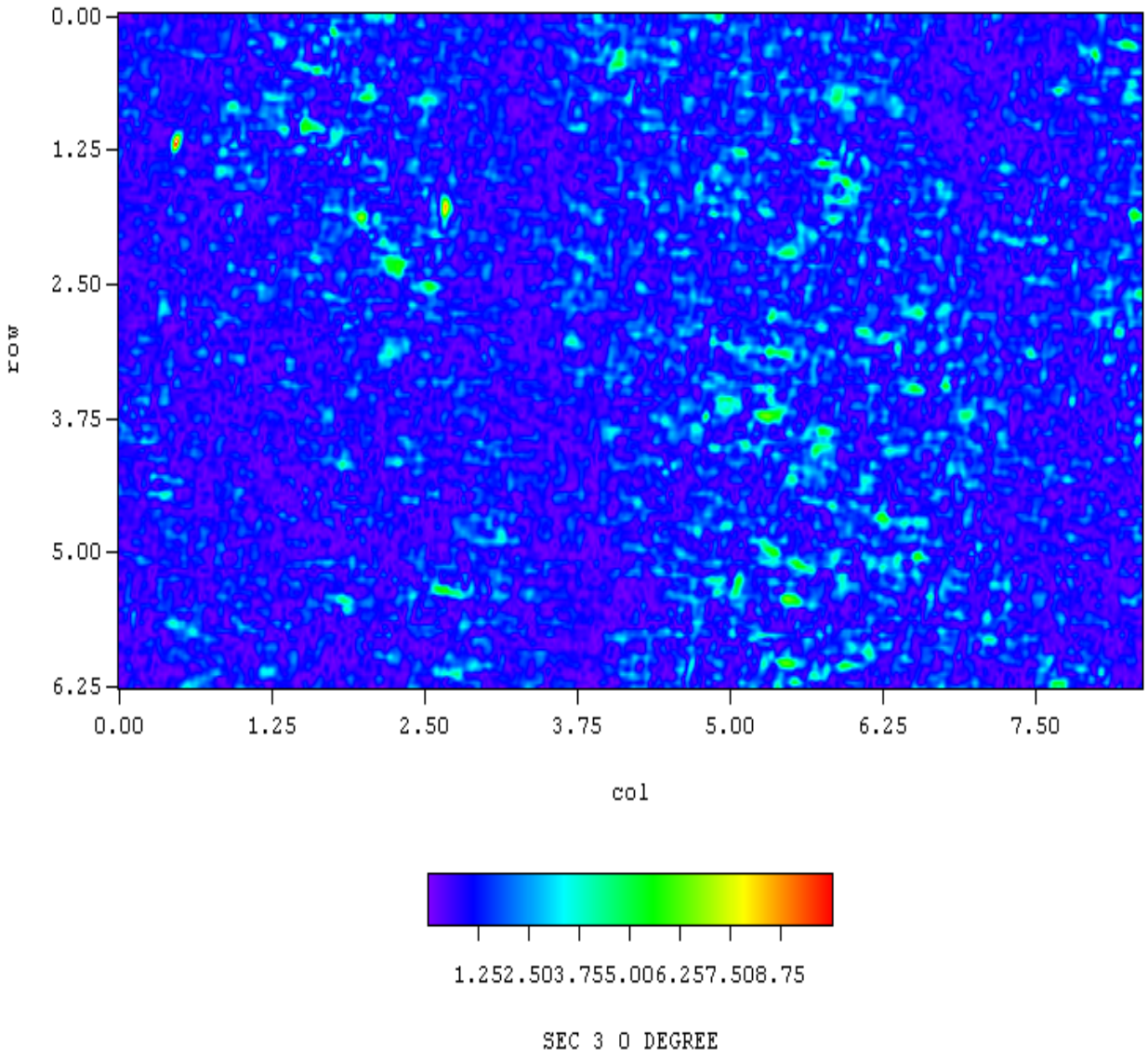

Figure B.44 Magnitude Plot of Westinghouse Spool Piece Specimen Quadrant 3

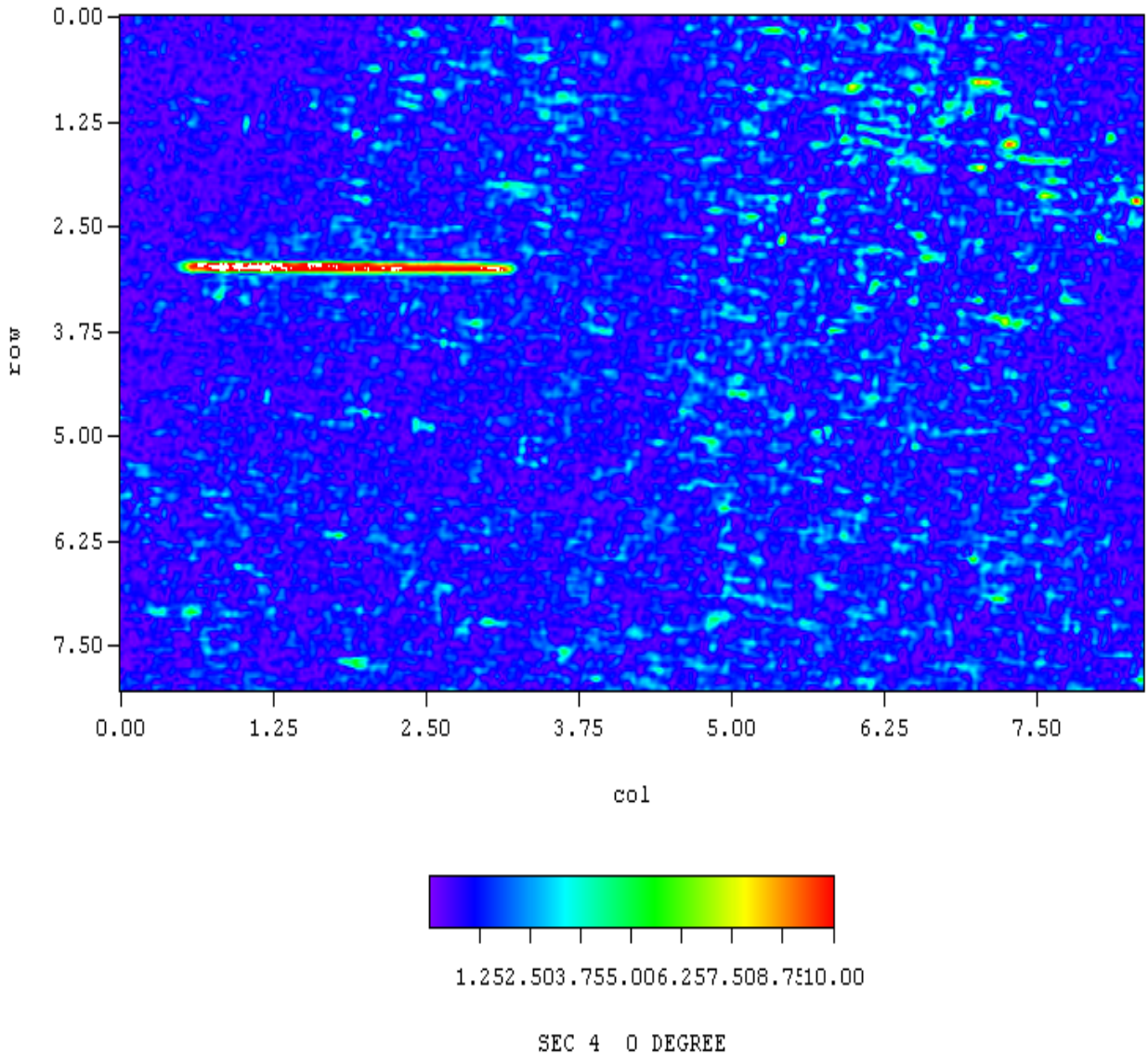

Figure B.45 Magnitude Plot of Westinghouse Spool Piece Specimen Quadrant 4

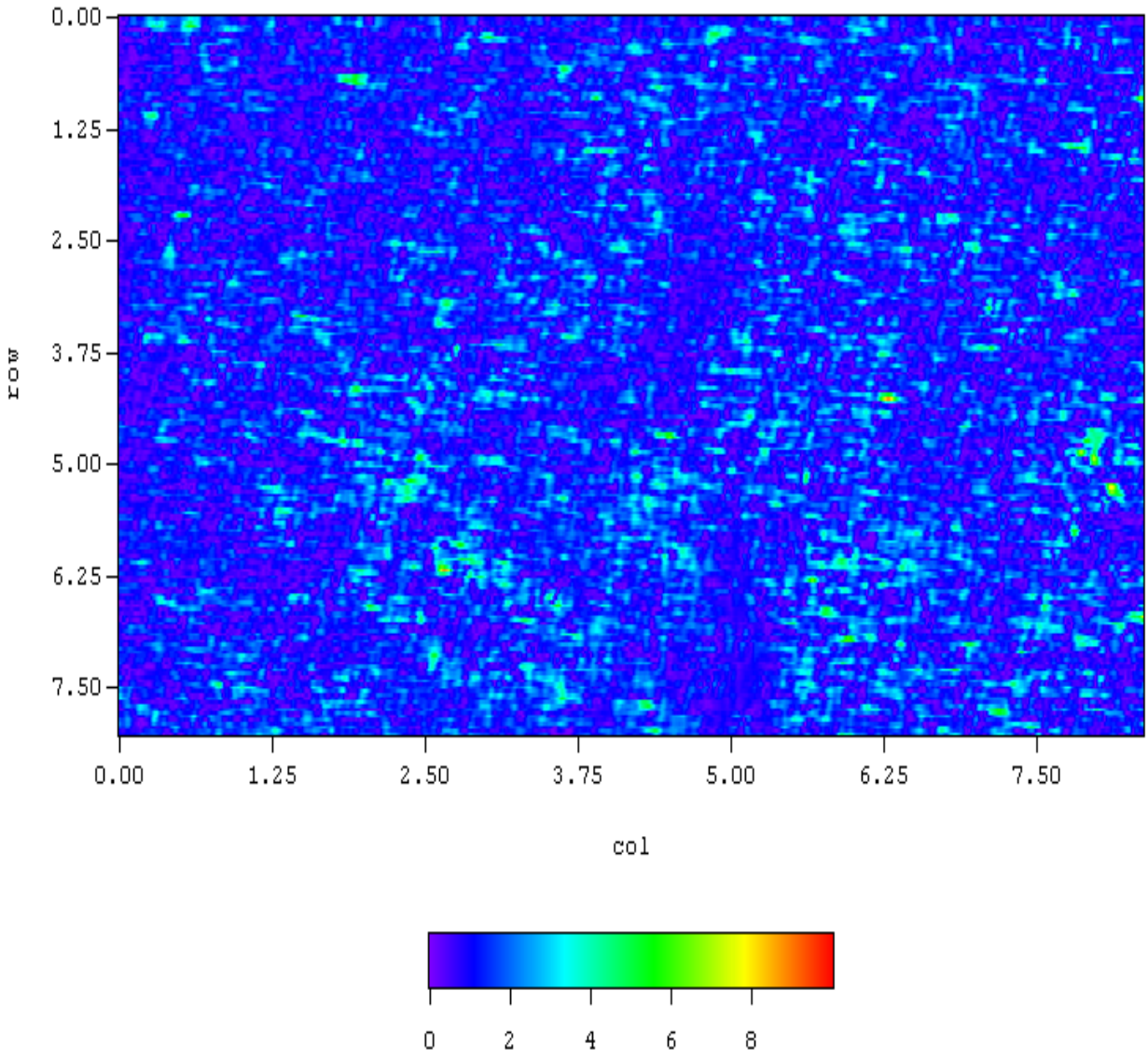

Figure B.46 Magnitude Plot of Westinghouse Spool Piece Specimen Quadrant 5

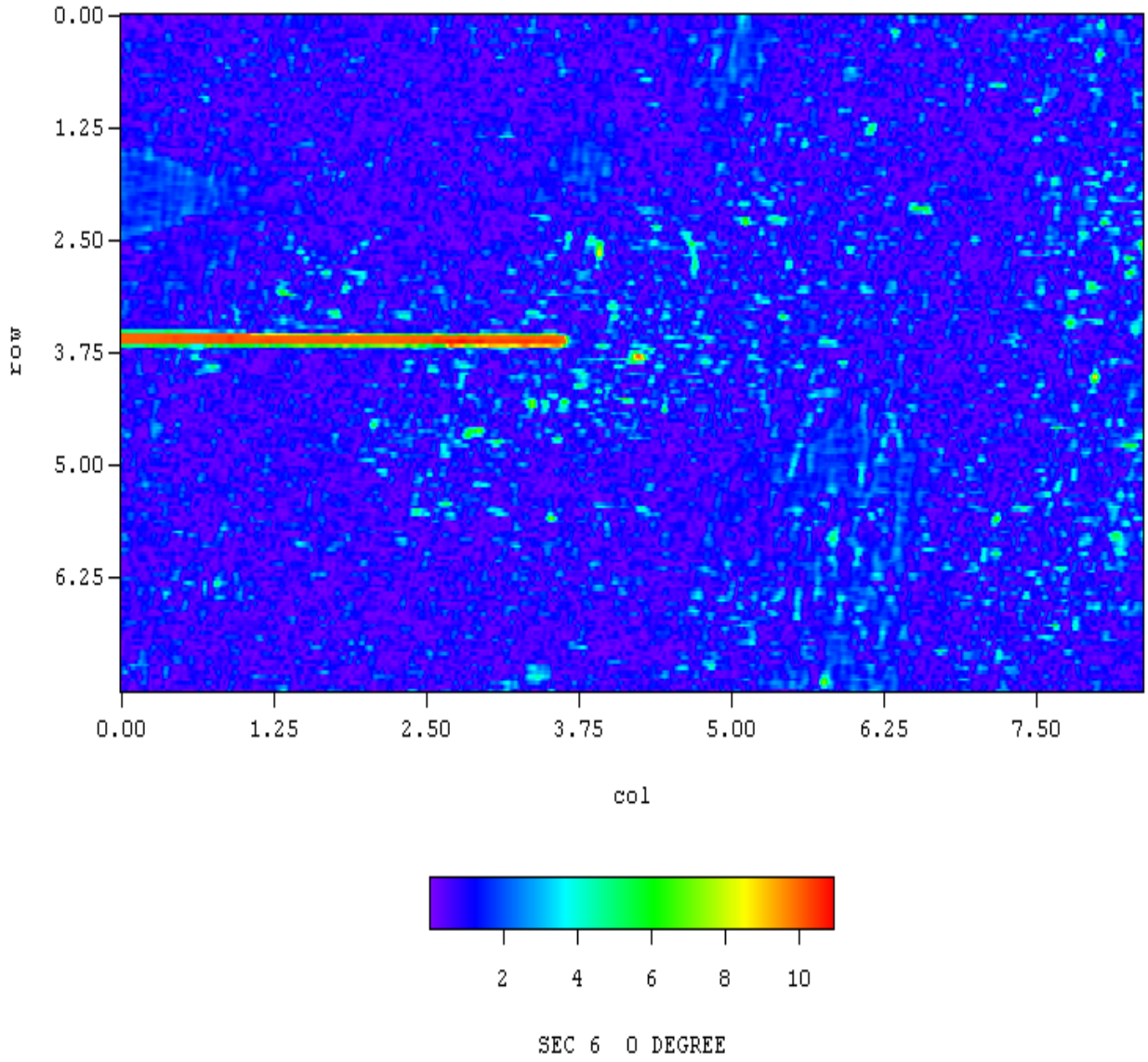

Figure B.47 Magnitude Plot of Westinghouse Spool Piece Specimen Quadrant 6

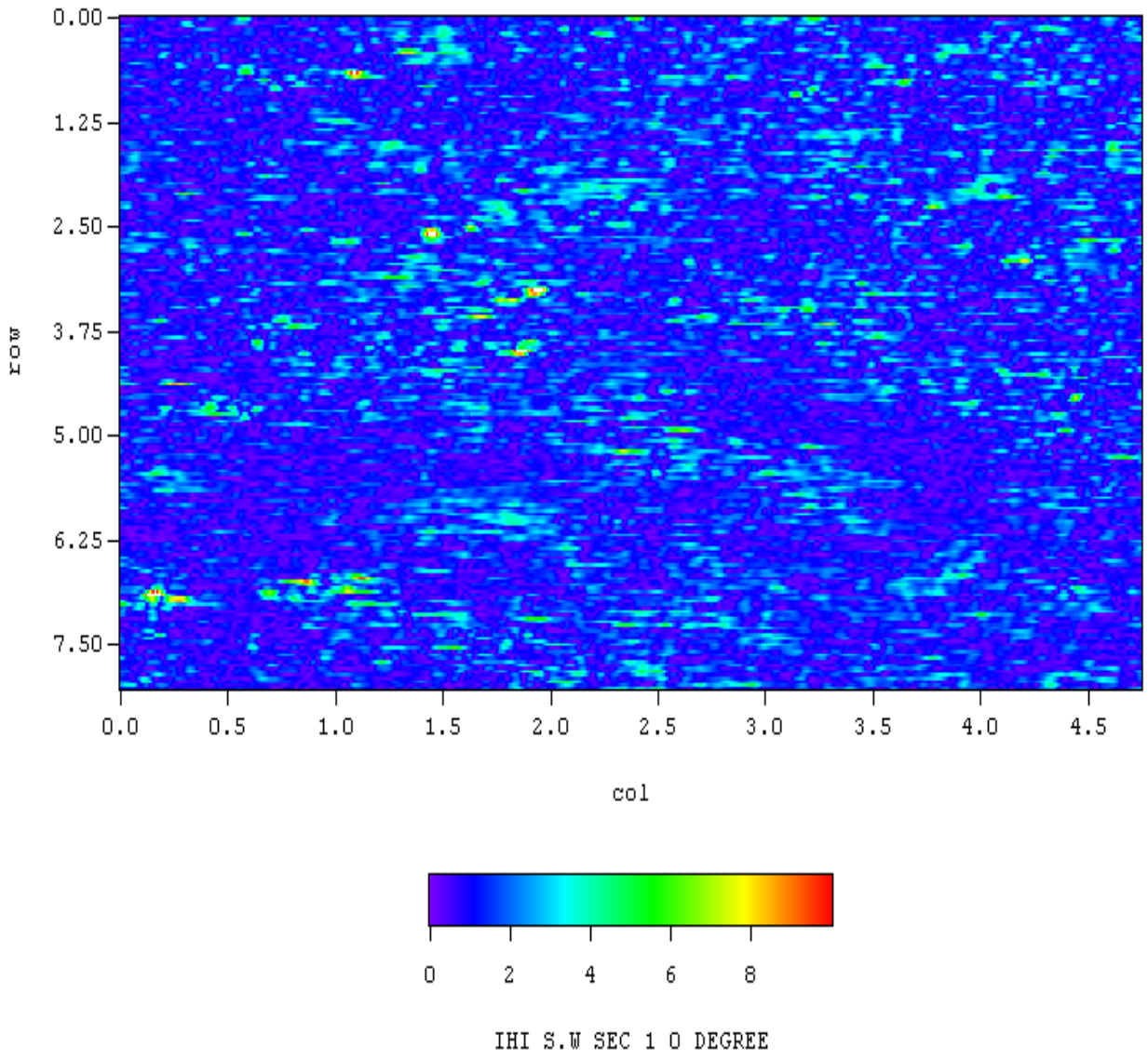

Figure B.48 Magnitude Plot of IHI Southwest Technologies Inc. Spool Piece Specimen Quadrant 1

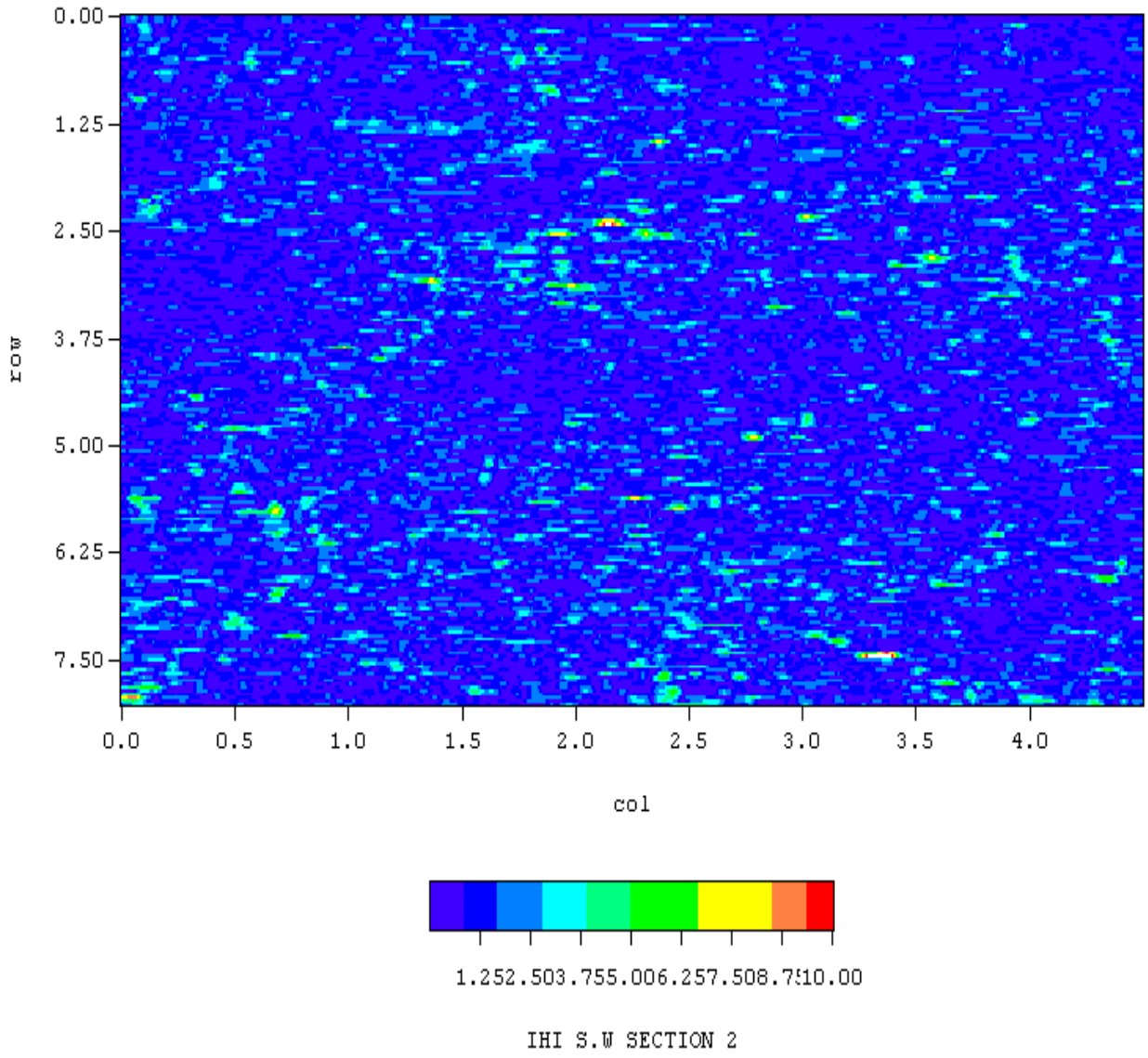

Figure B.49 Magnitude Plot of IHI Southwest Technologies Inc. Spool Piece Specimen Quadrant 2

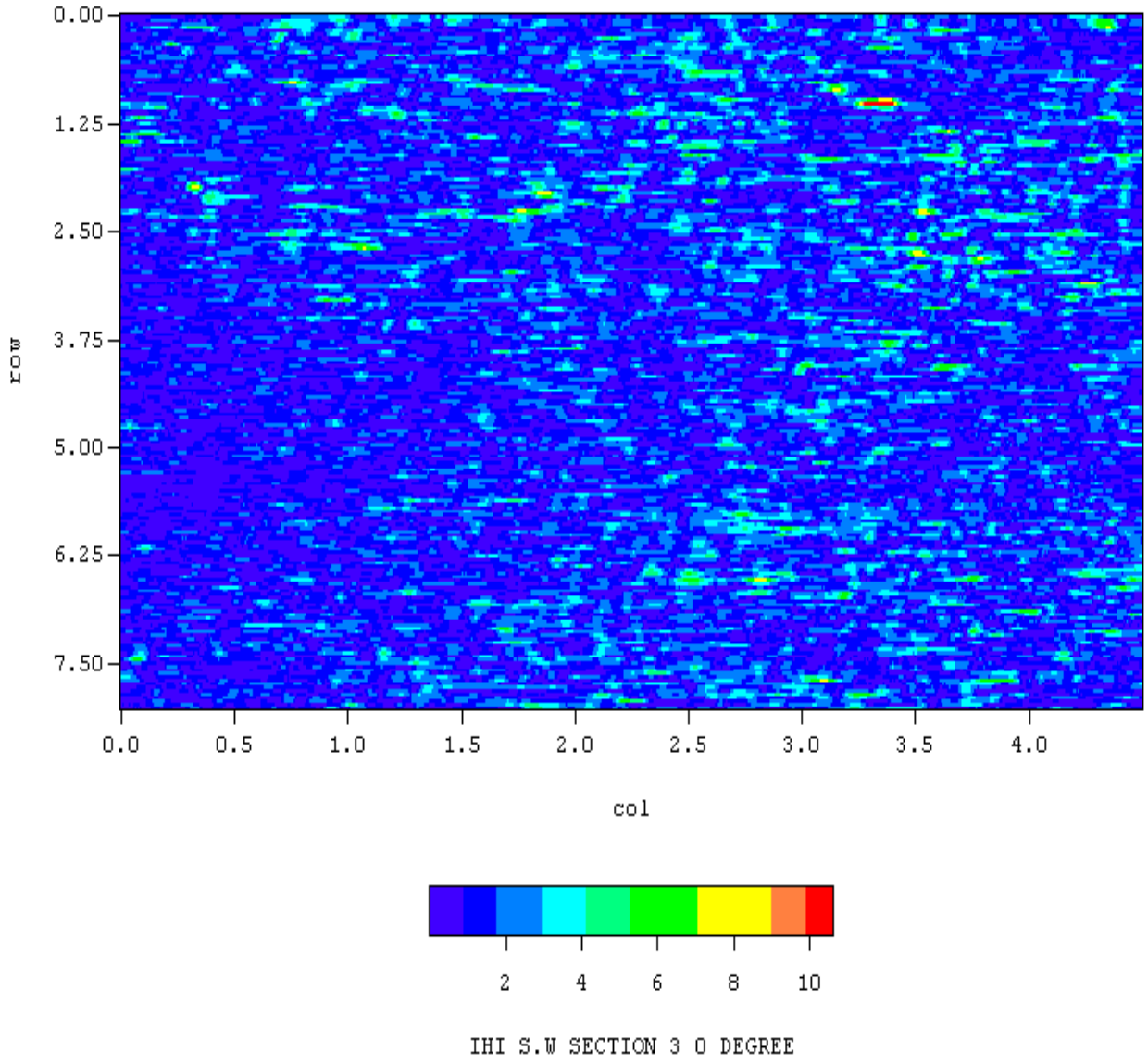

Figure B.50 Magnitude Plot of IHI Southwest Technologies Inc. Spool Piece Specimen Quadrant 3

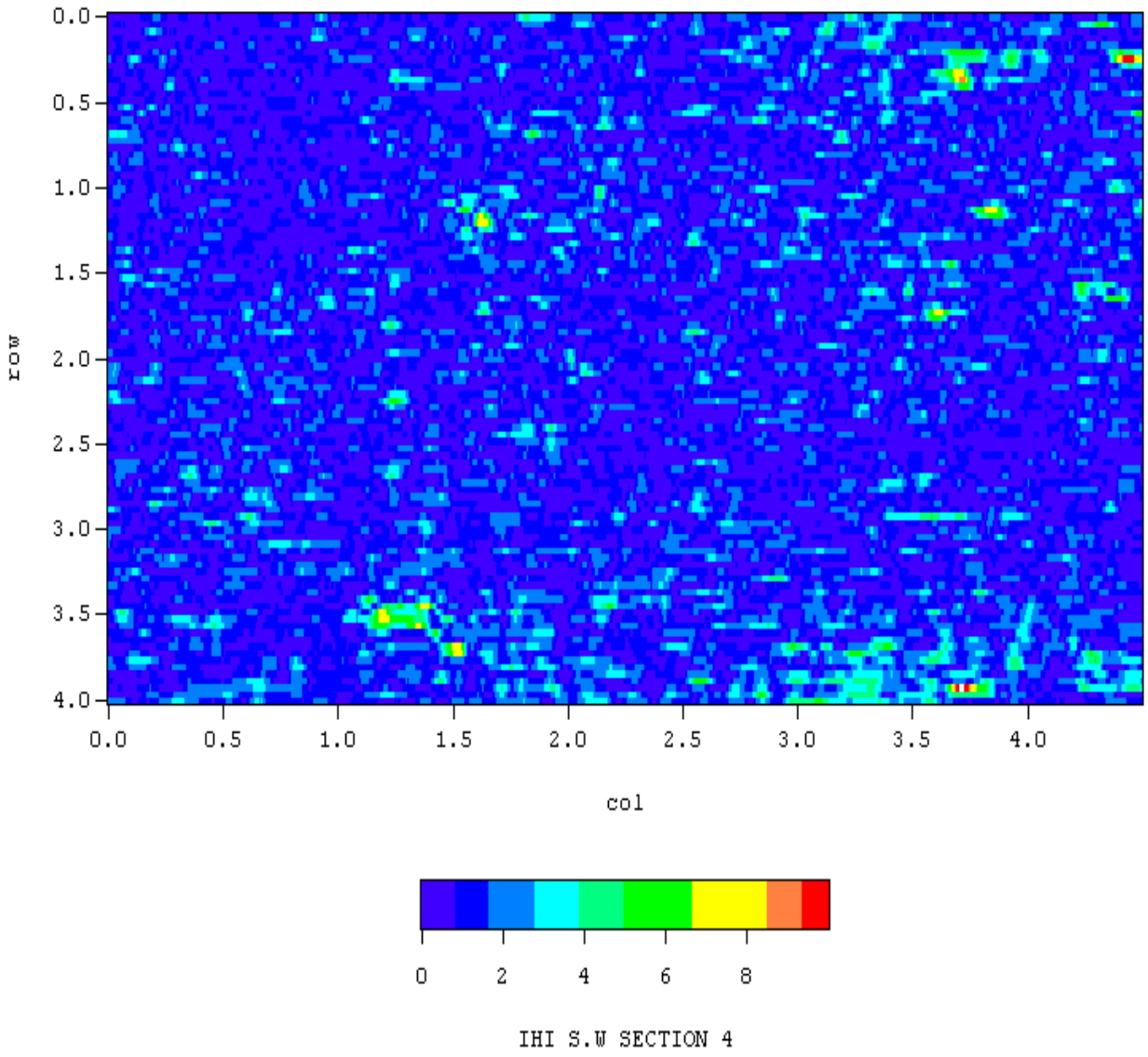

Figure B.51 Magnitude Plot of IHI Southwest Technologies Inc. Spool Piece Specimen Quadrant 4

Appendix C

Phase Plots from Eddy Current Data

Appendix C

Phase Plots from Eddy Current Data

All plots in Appendix C have vertical and horizontal axes that are in units of inches (25.4 mm).

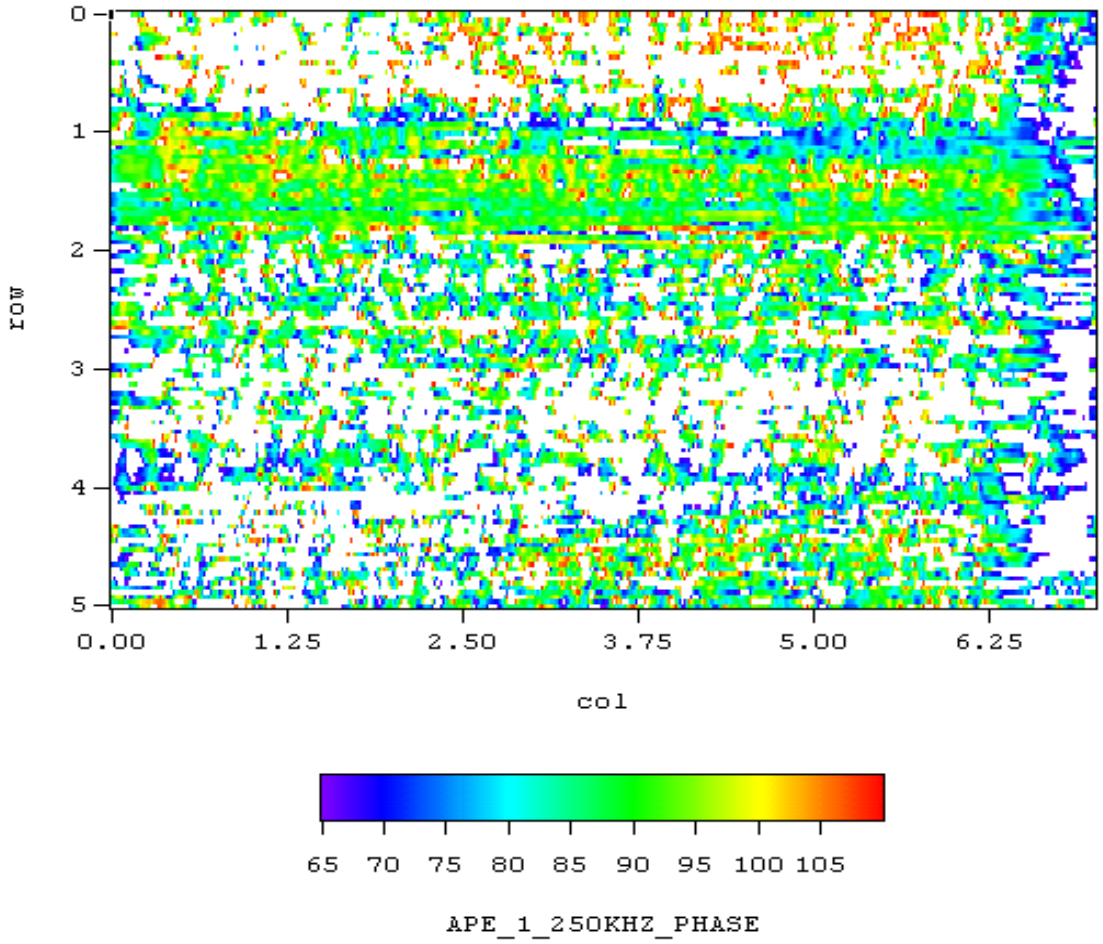

Figure C.1 Phase Response Plot of WOG Specimen APE-1

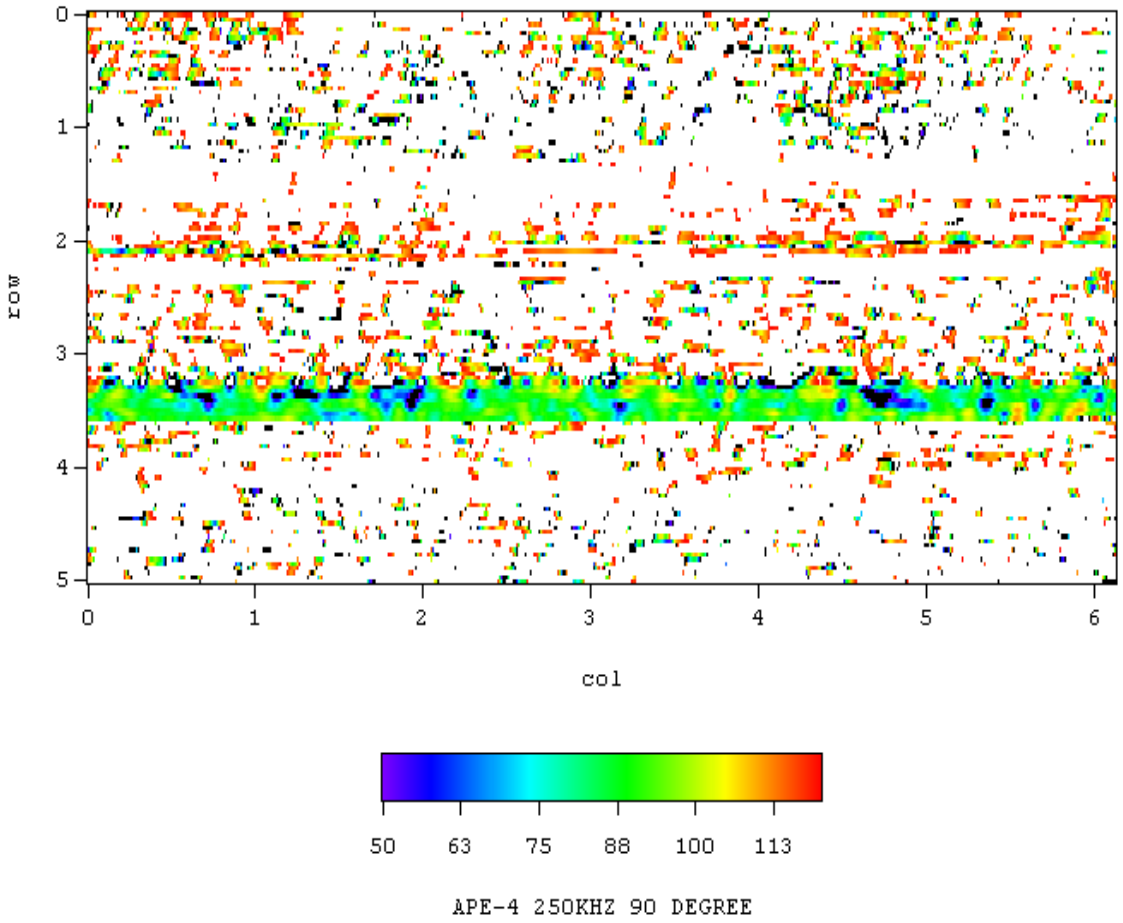

Figure C.2 Phase Response Plot of WOG Specimen APE-4

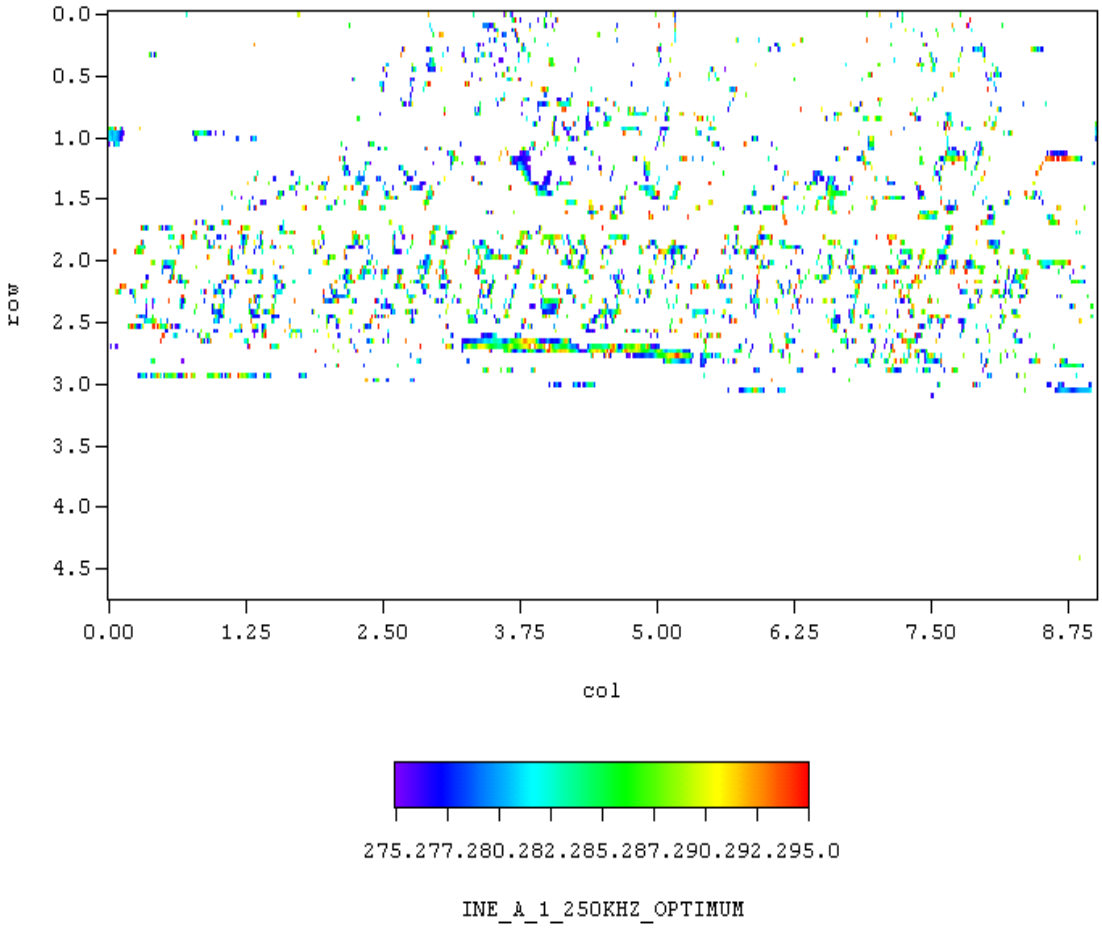

Figure C.3 Phase Response Plot of WOG Specimen INE-A-1

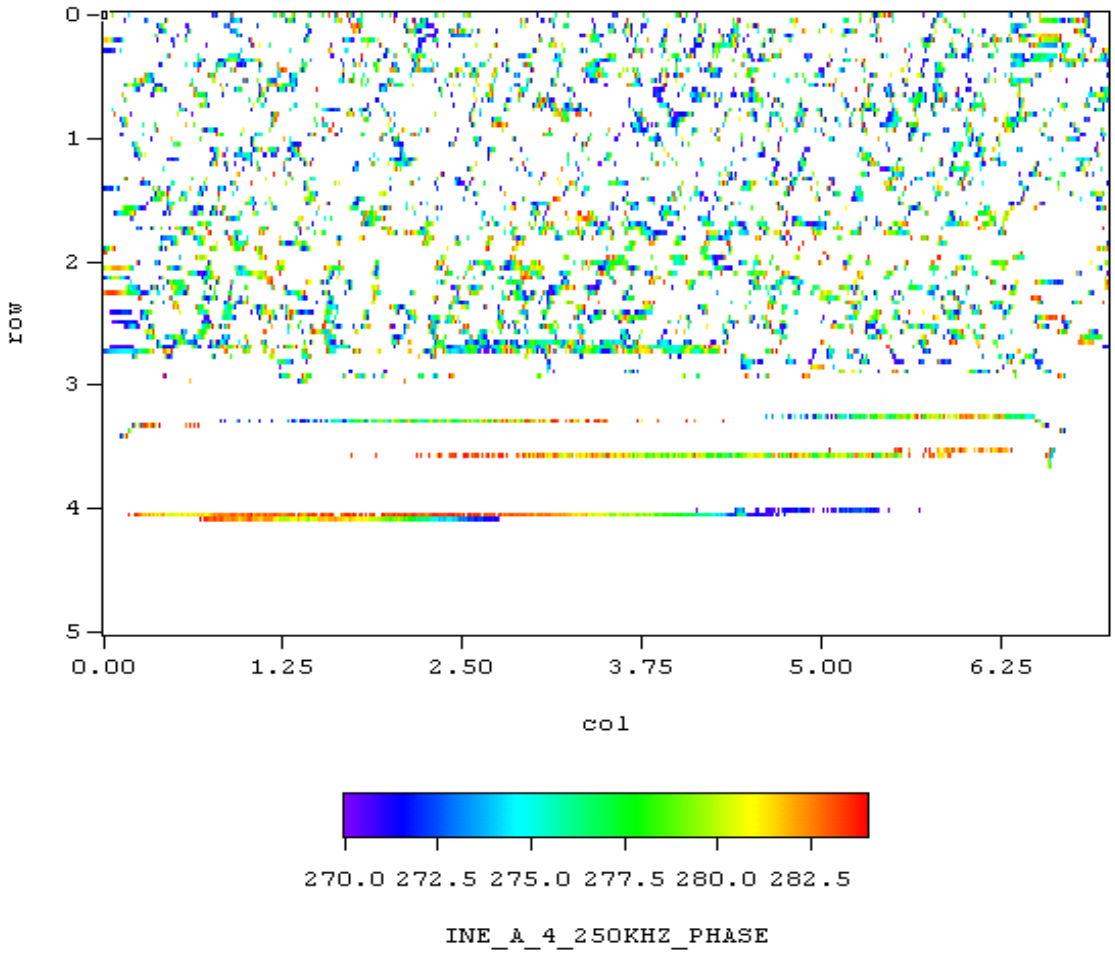

Figure C.4 Phase Response Plot of WOG Specimen INE-A-4

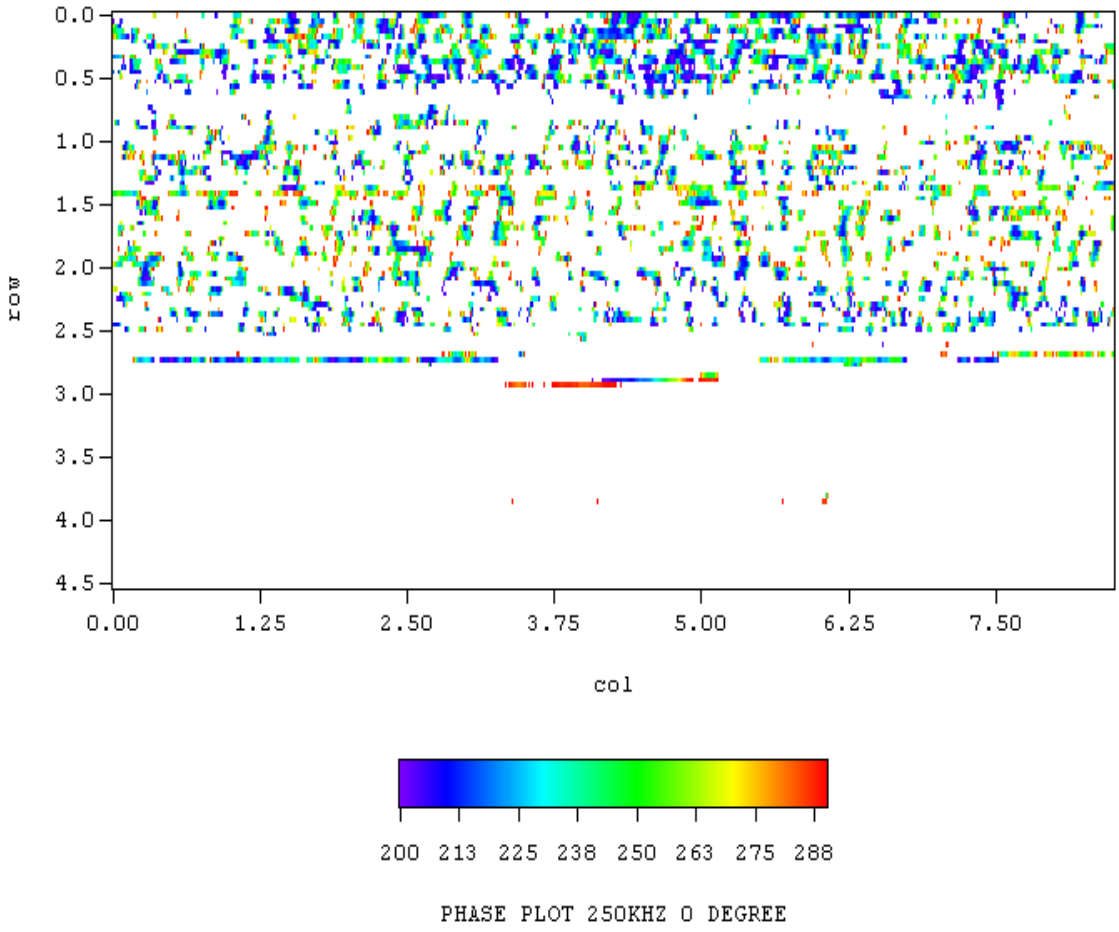

Figure C.5 Phase Response Plot of WOG Specimen INE-A-5

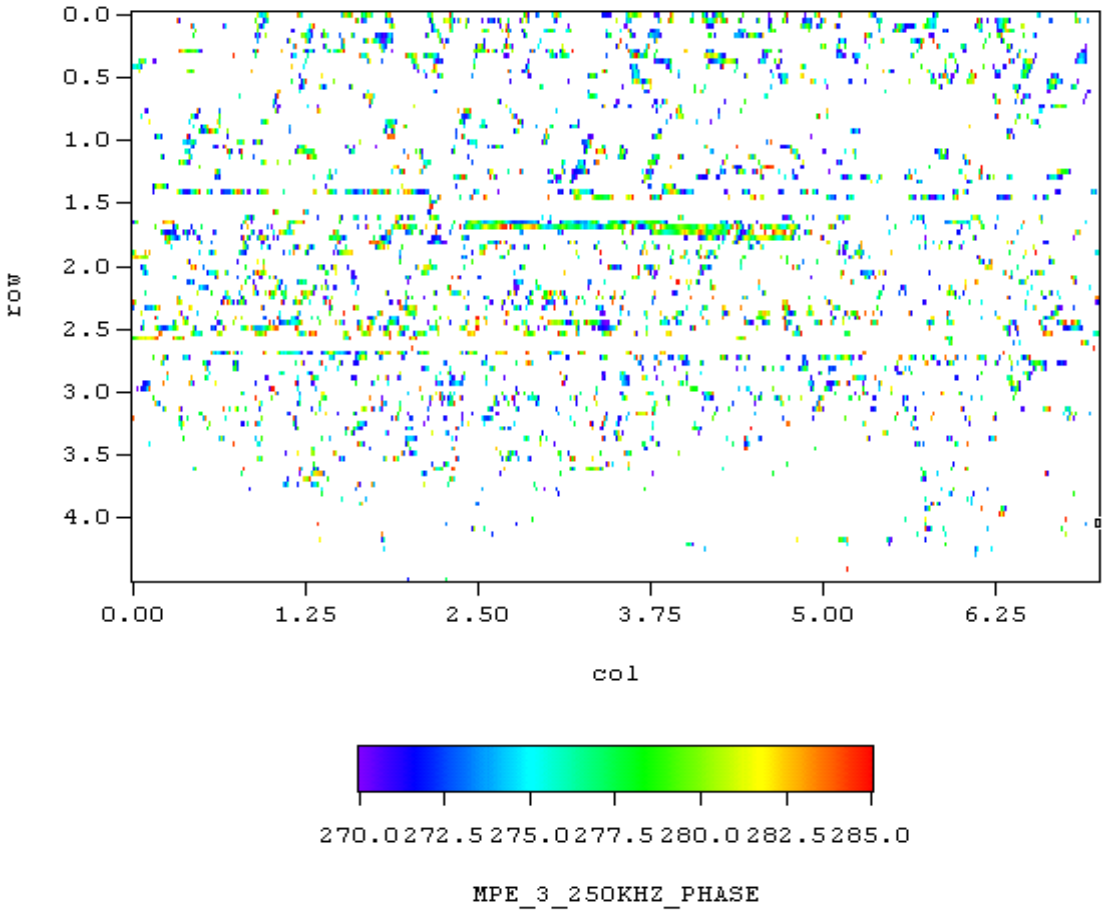

Figure C.6 Phase Response Plot of WOG Specimen MPE-3

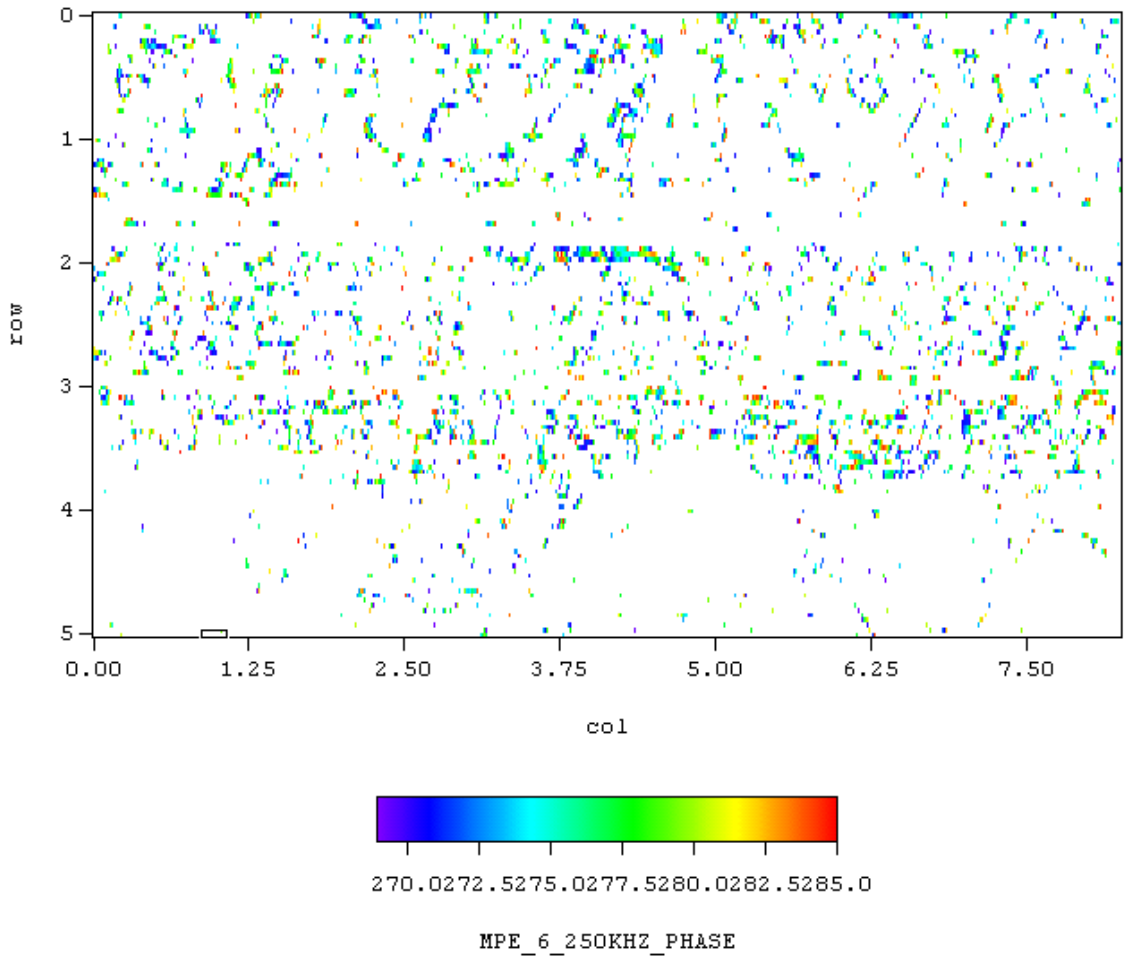

Figure C.7 Phase Response Plot of WOG Specimen MPE-6

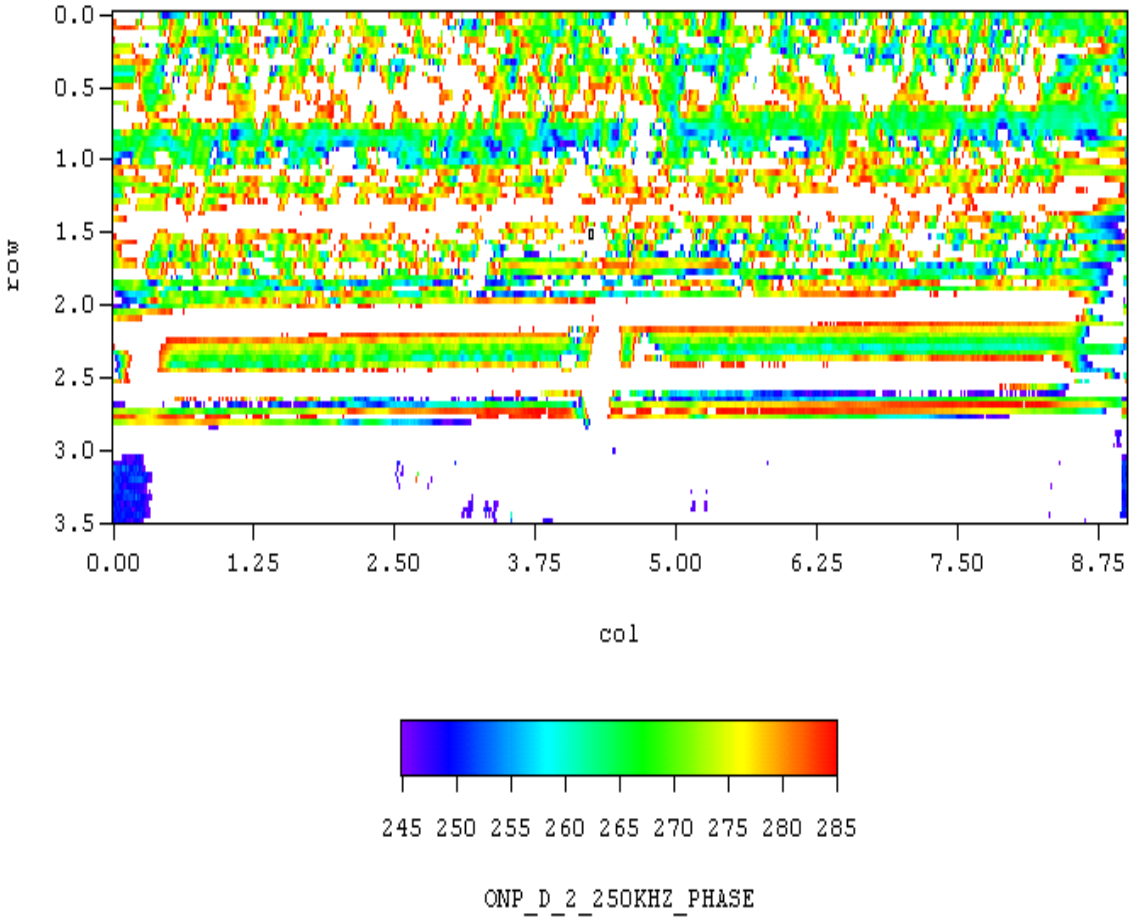

Figure C.8 Phase Response Plot of WOG Specimen ONP-D-2

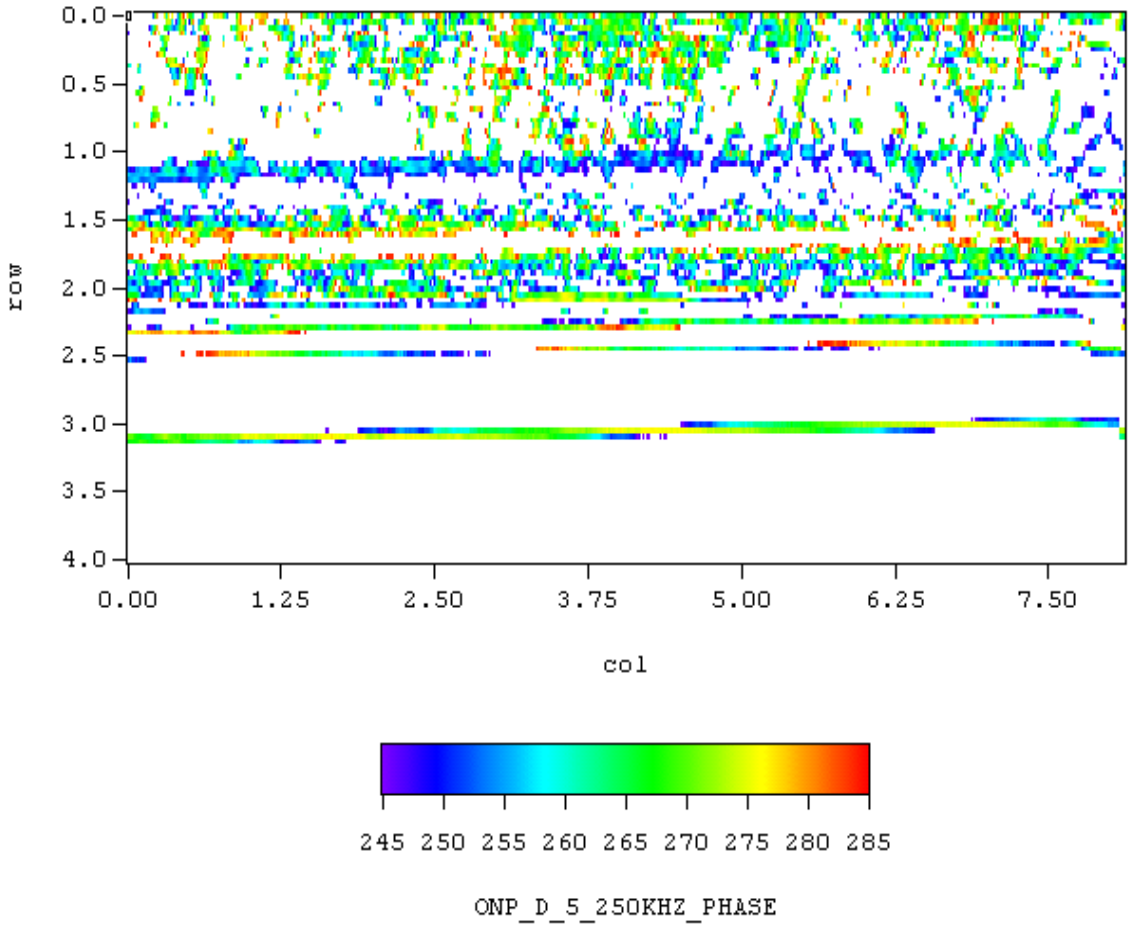

Figure C.9 Phase Response Plot of WOG Specimen ONP-D-5

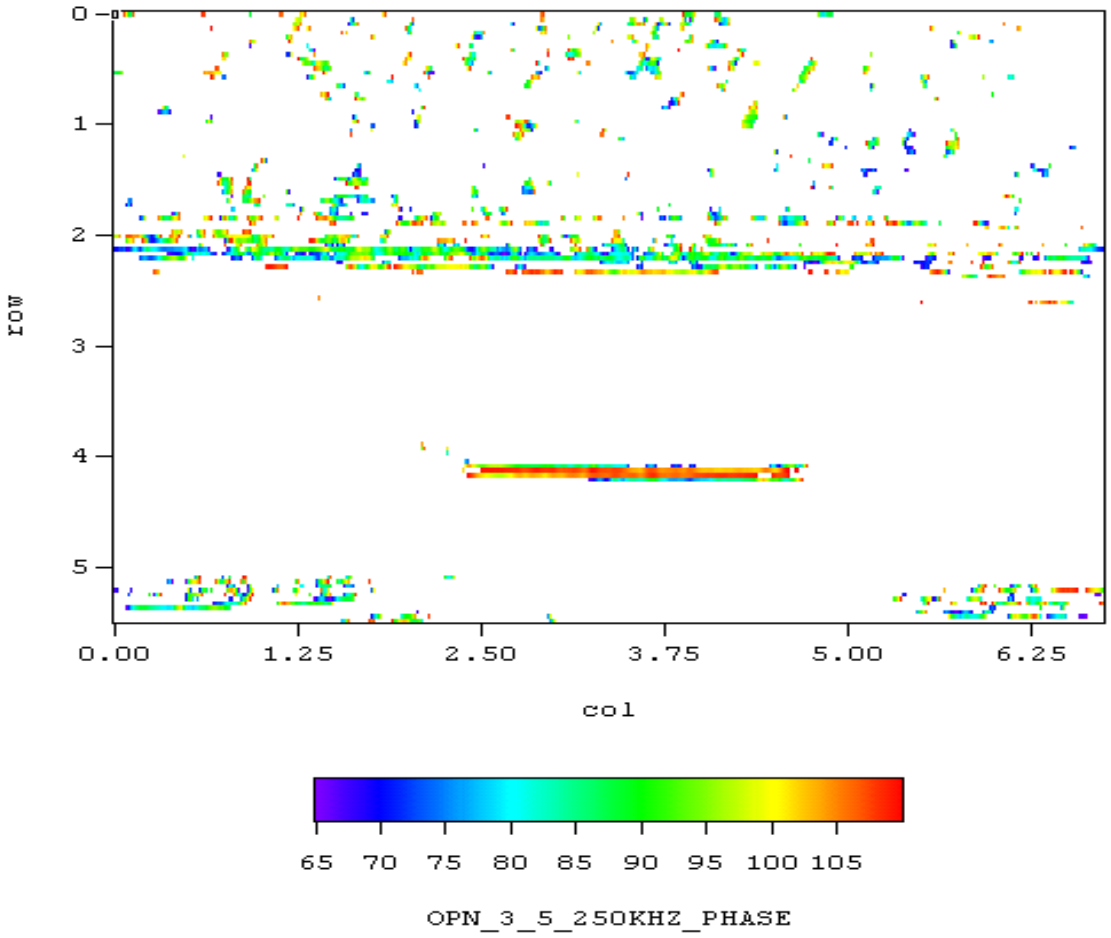

Figure C.10 Phase Response Plot of WOG Specimen ONP-3-5

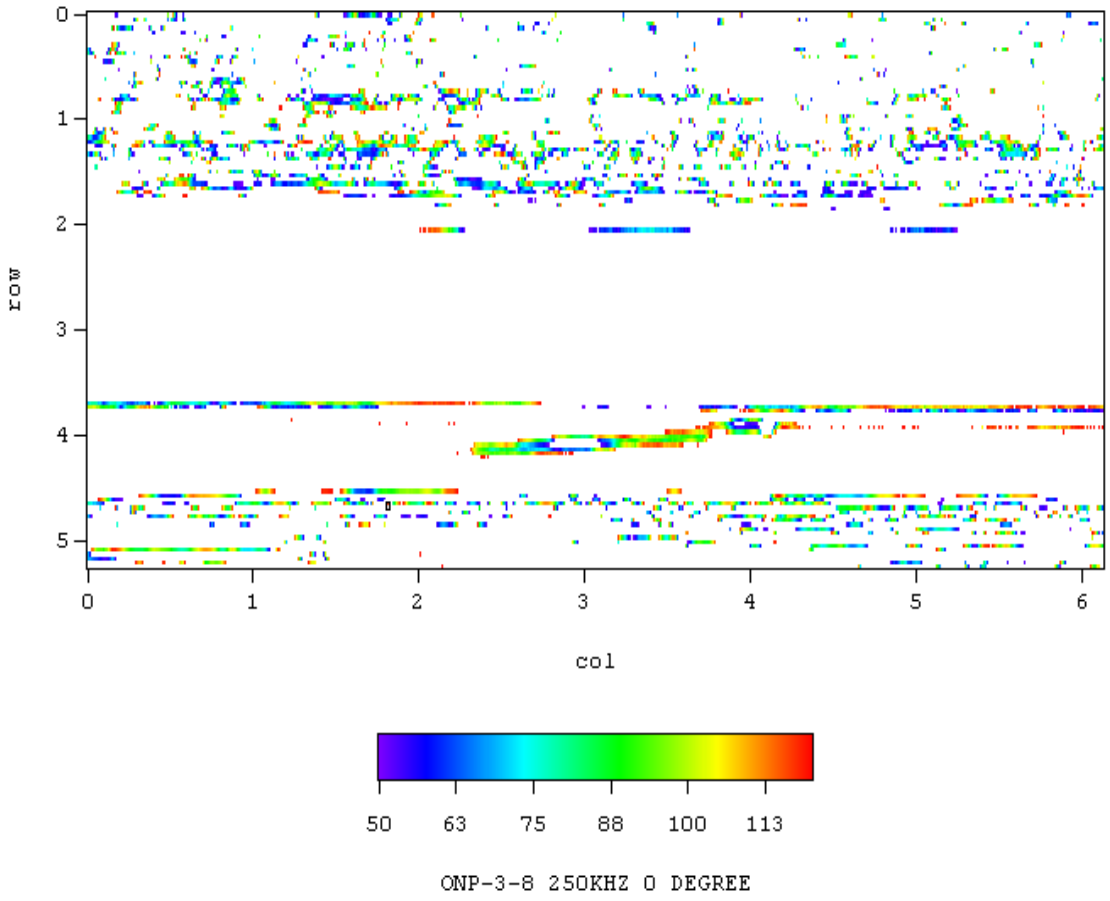

Figure C.11 Phased Response Plot of WOG Specimen ONP-3-8

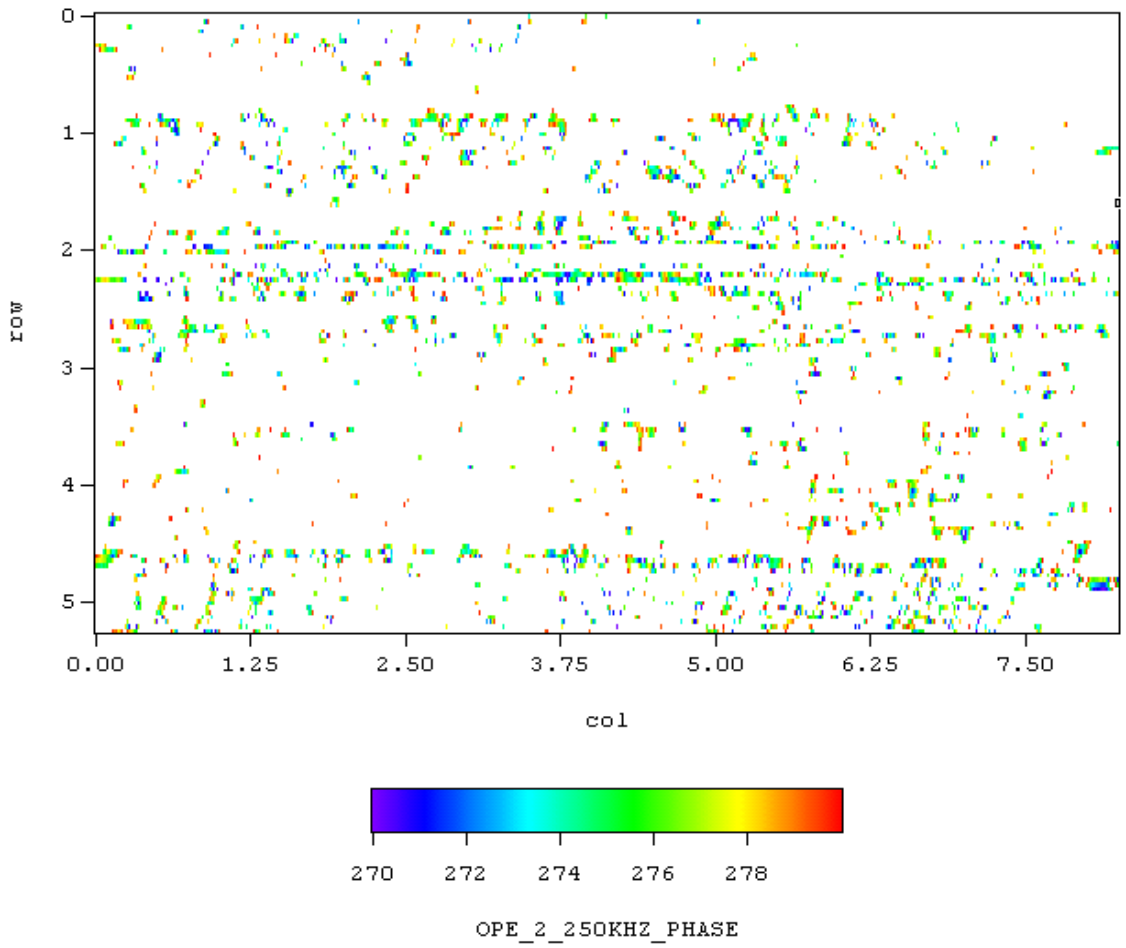

Figure C.12 Phase Response Plot of WOG Specimen OPE-2

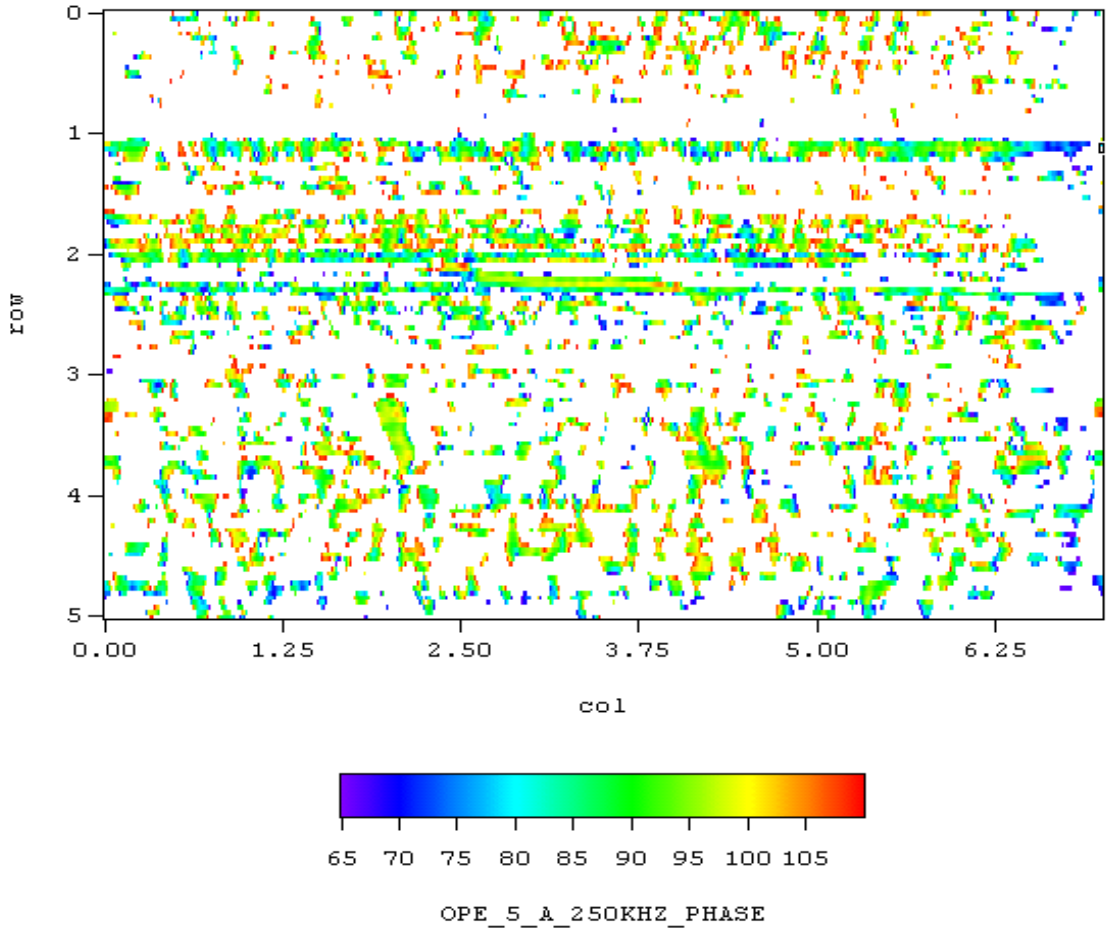

Figure C.13 Phase Response Plot of WOG Specimen OPE-5-A

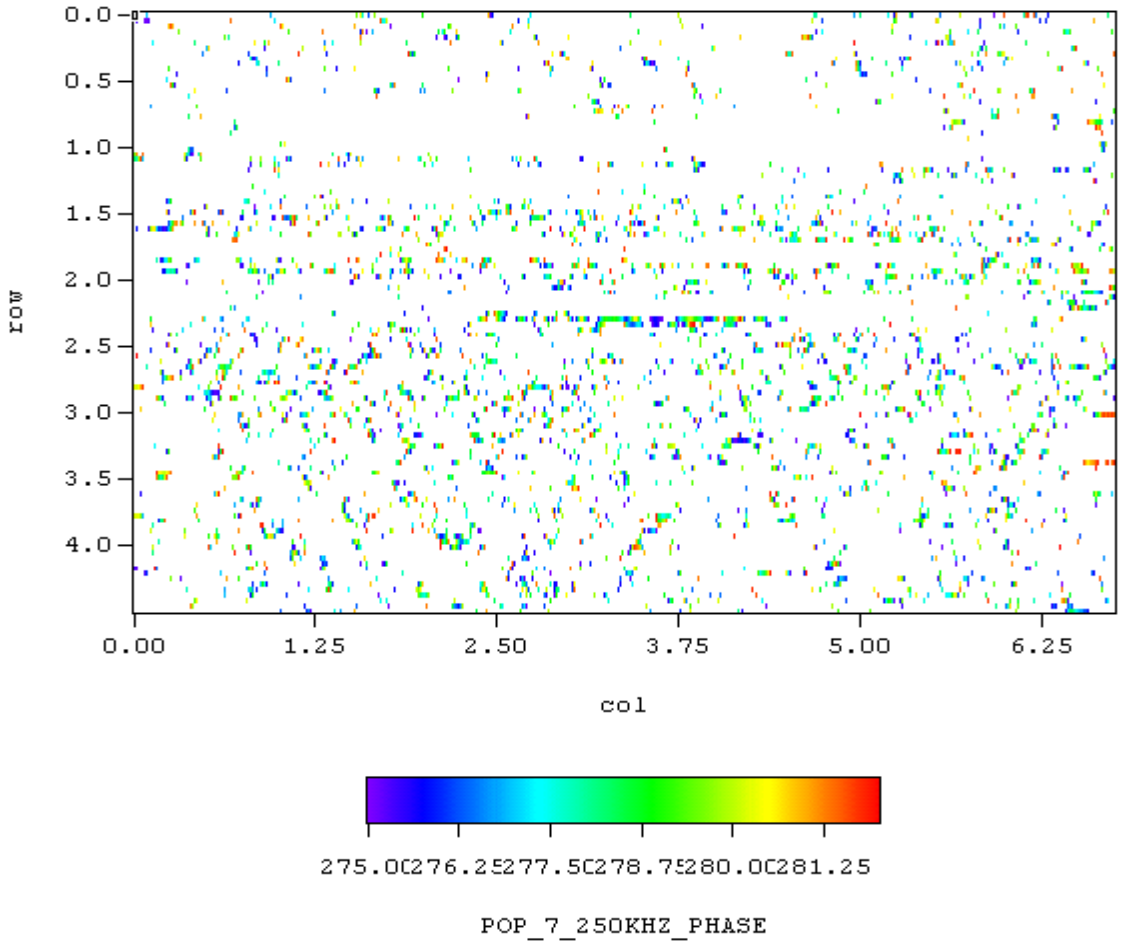

Figure C.14 Phase Response Plot of WOG Specimen POP-7

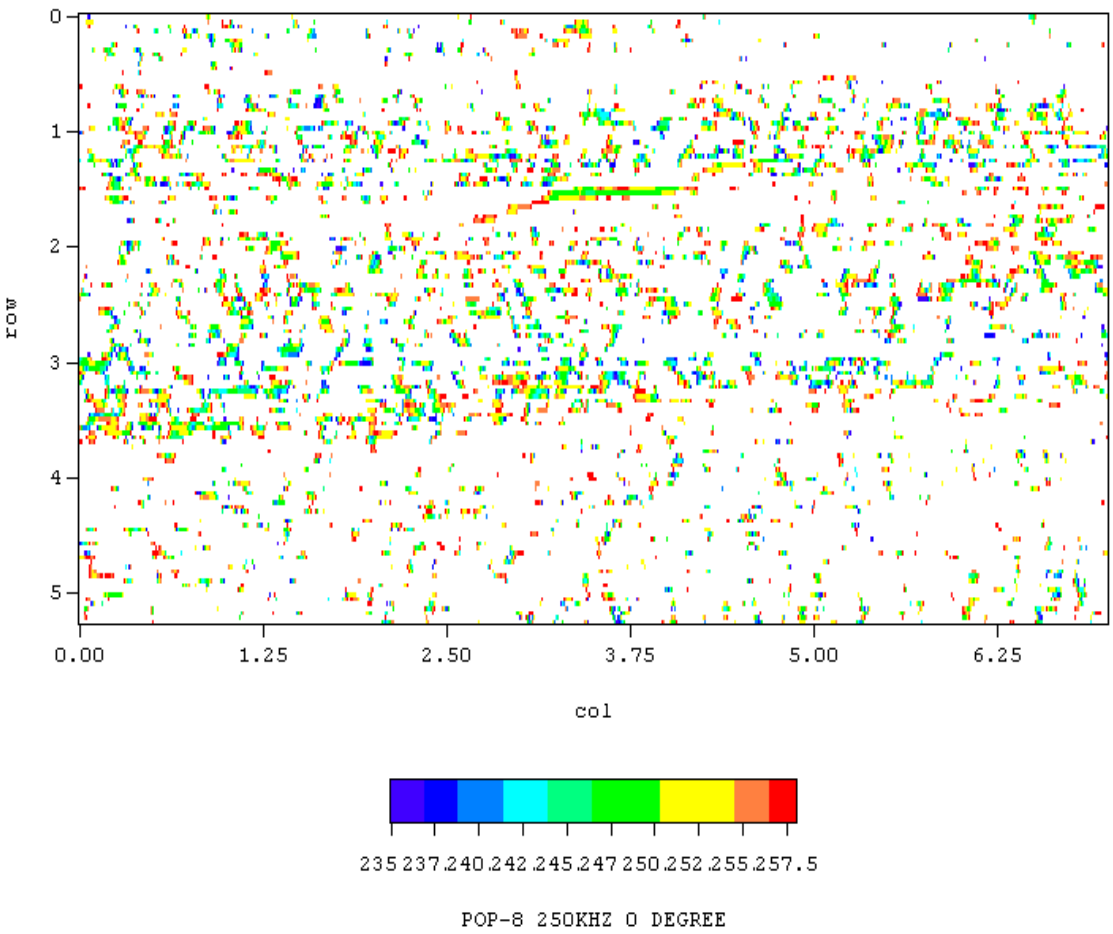

Figure C.15 Phase Response Plot of WOG Specimen POP-8

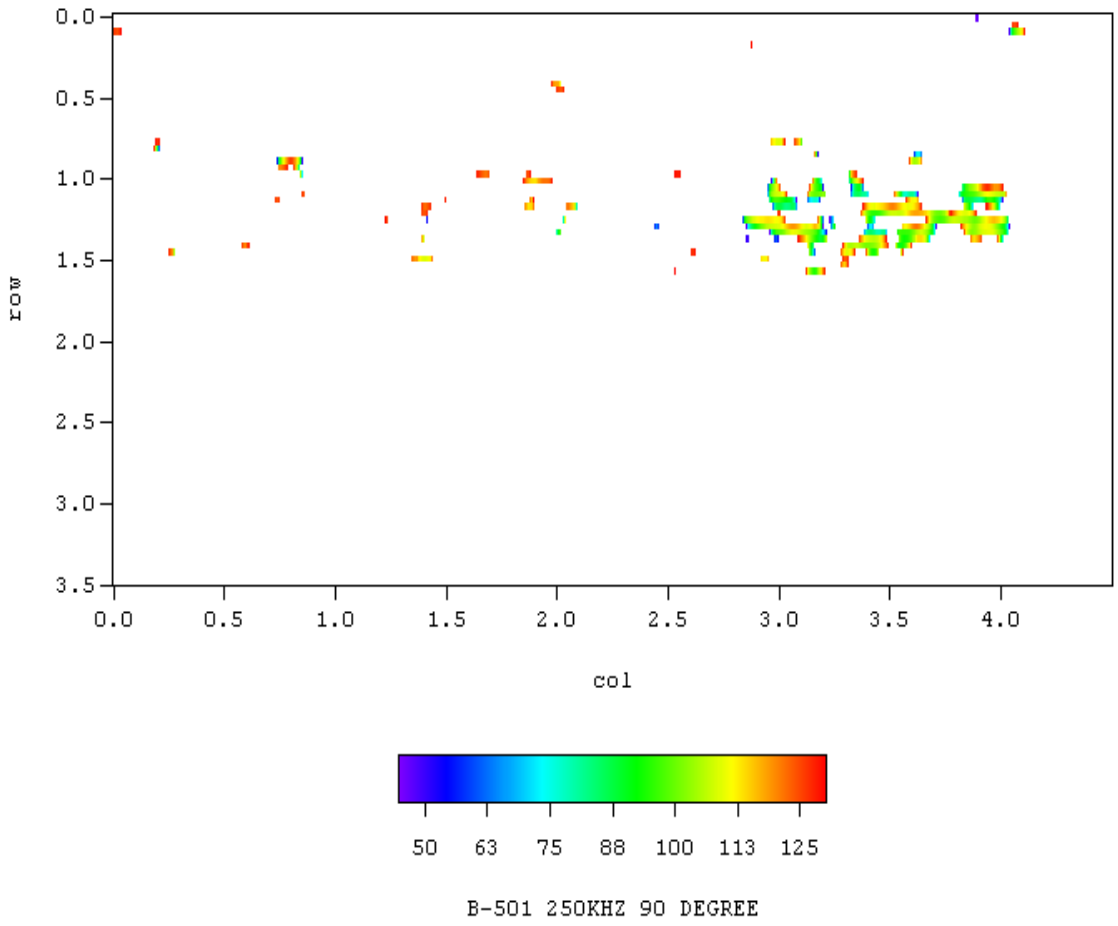

Figure C.16 Phase Response Plot of PNNL Specimen B-501

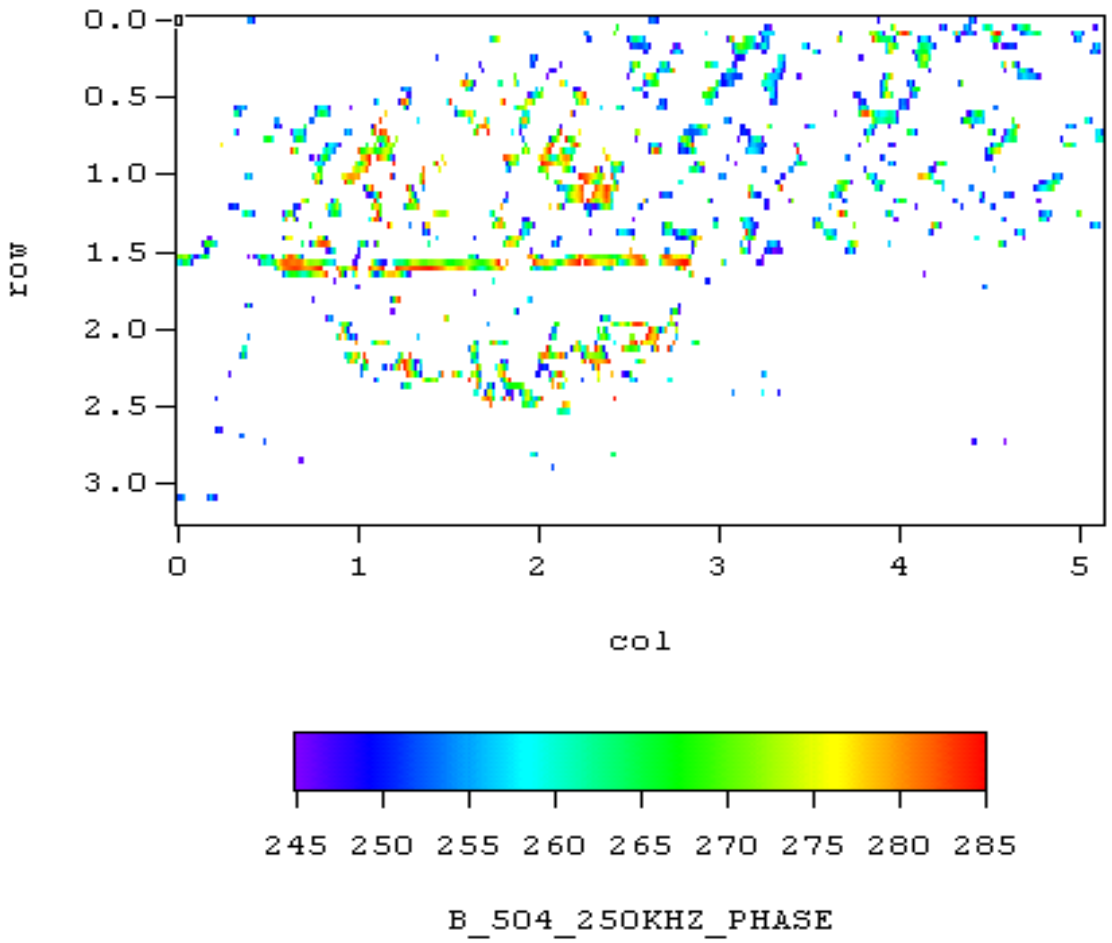

Figure C.17 Phase Response Plot of PNNL Specimen B-504

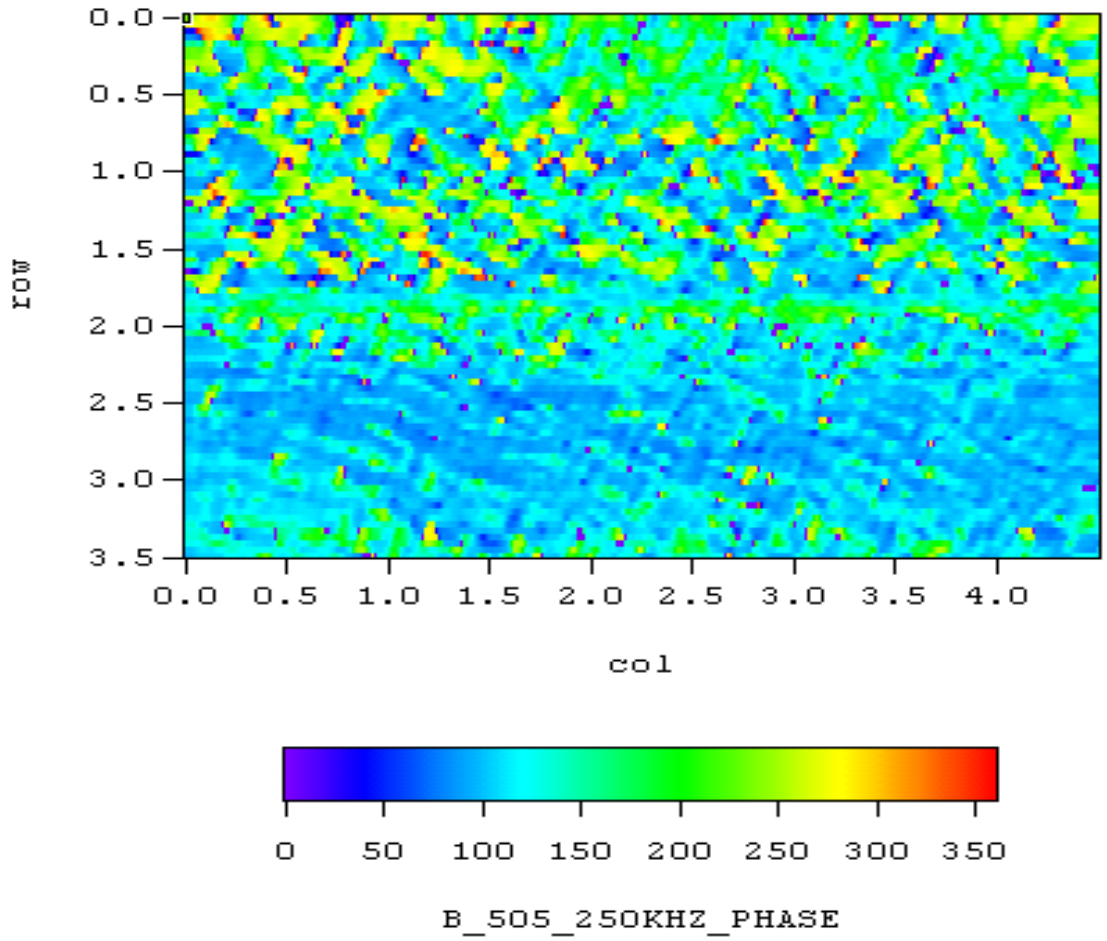

Figure C.18 Phase Response Plot of PNNL Specimen B

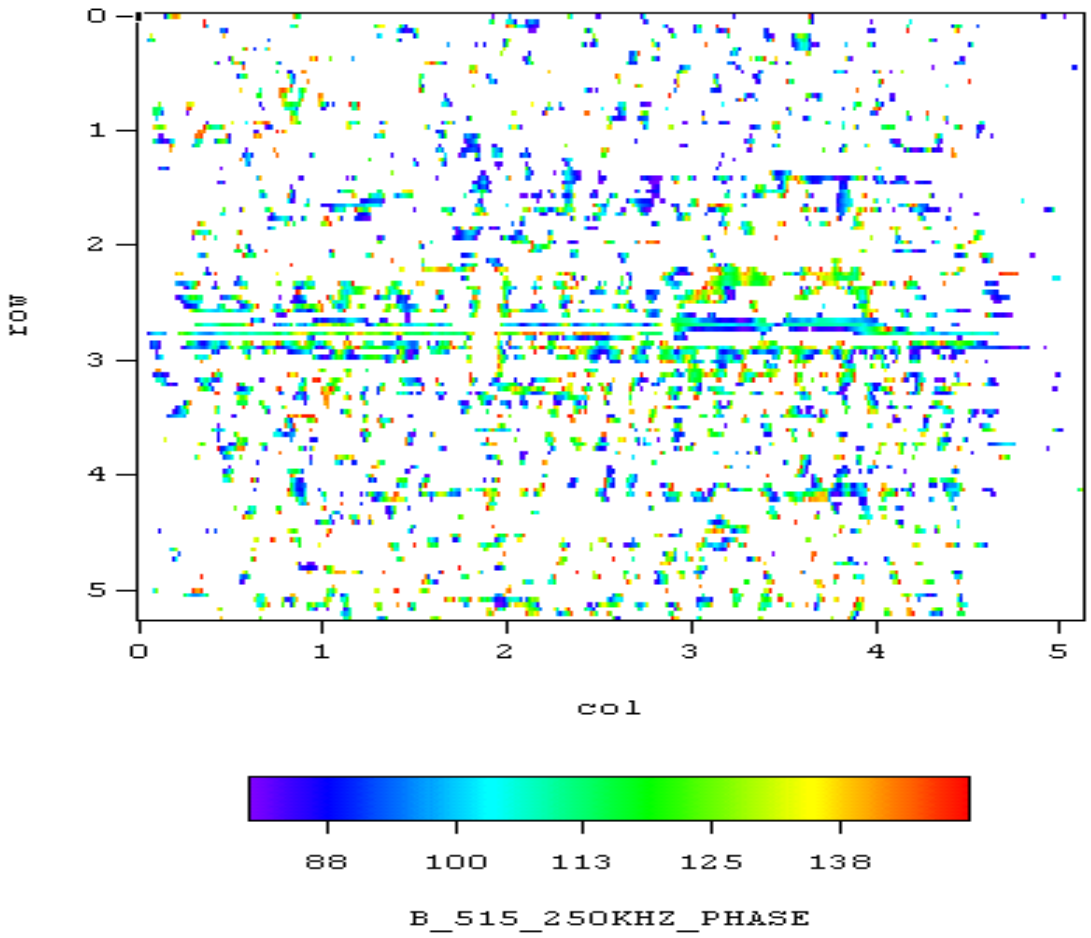

Figure C.19 Phase Response Plot of PNNL Specimen B-515

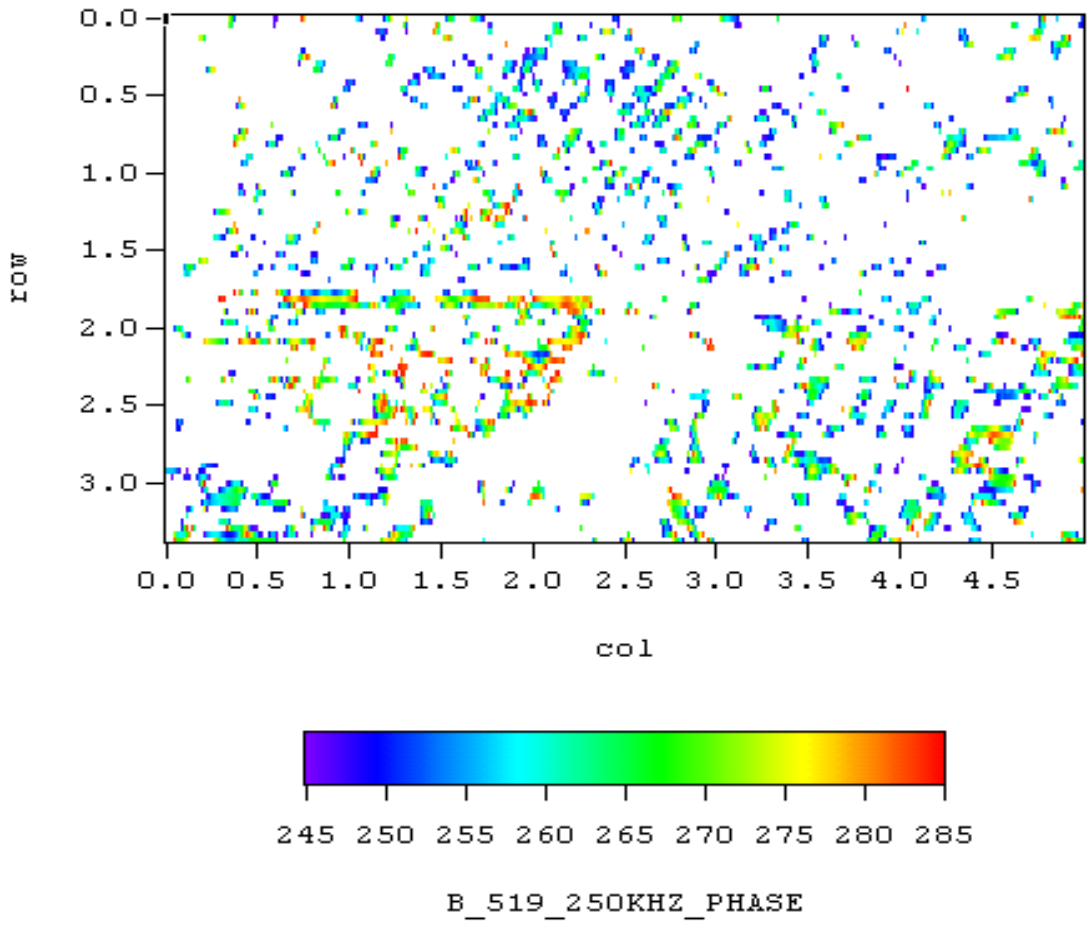

Figure C.20 Phase Response Plot of PNNL Specimen B-519

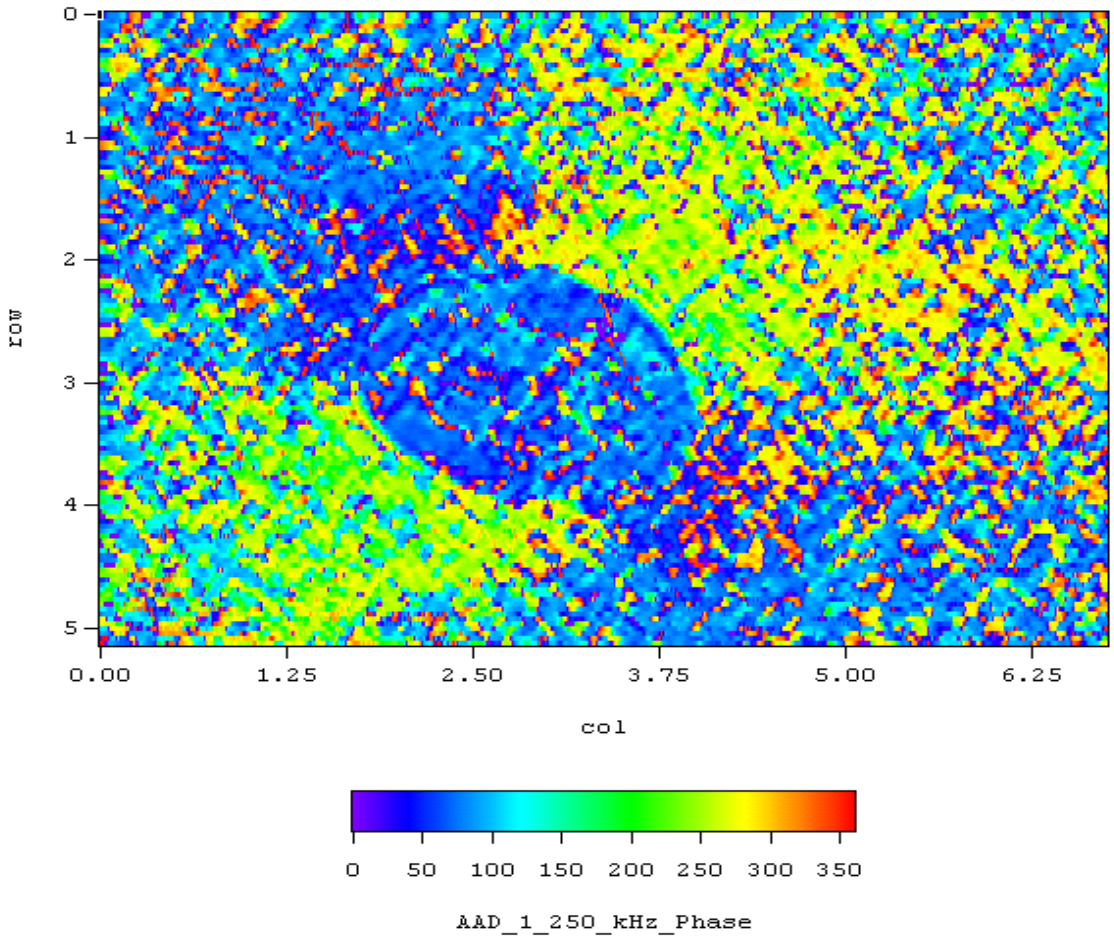

Figure C.21 Phase Response Plot of Southwest Research Institute Specimen AAD

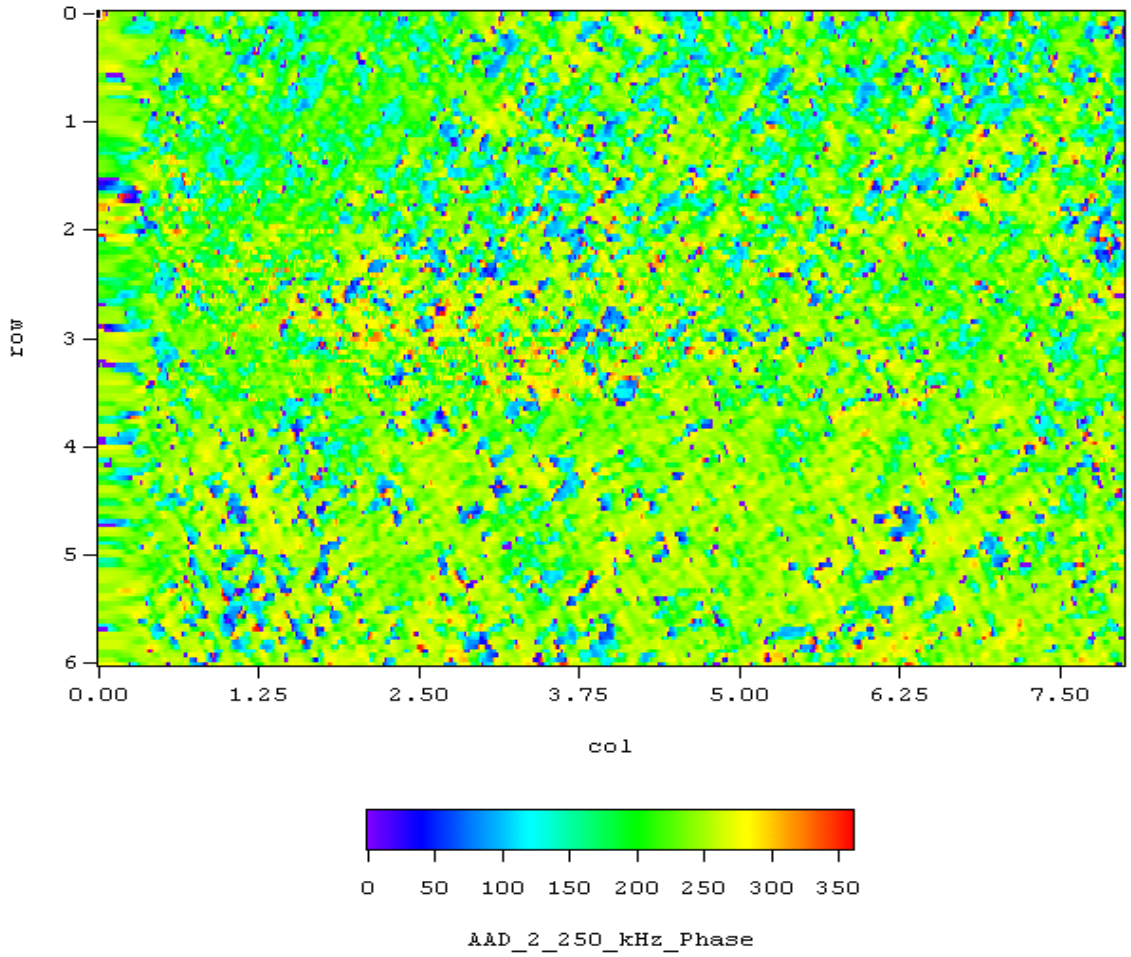

Figure C.22 Phase Response Plot of Southwest Research Institute Specimen AAD-2

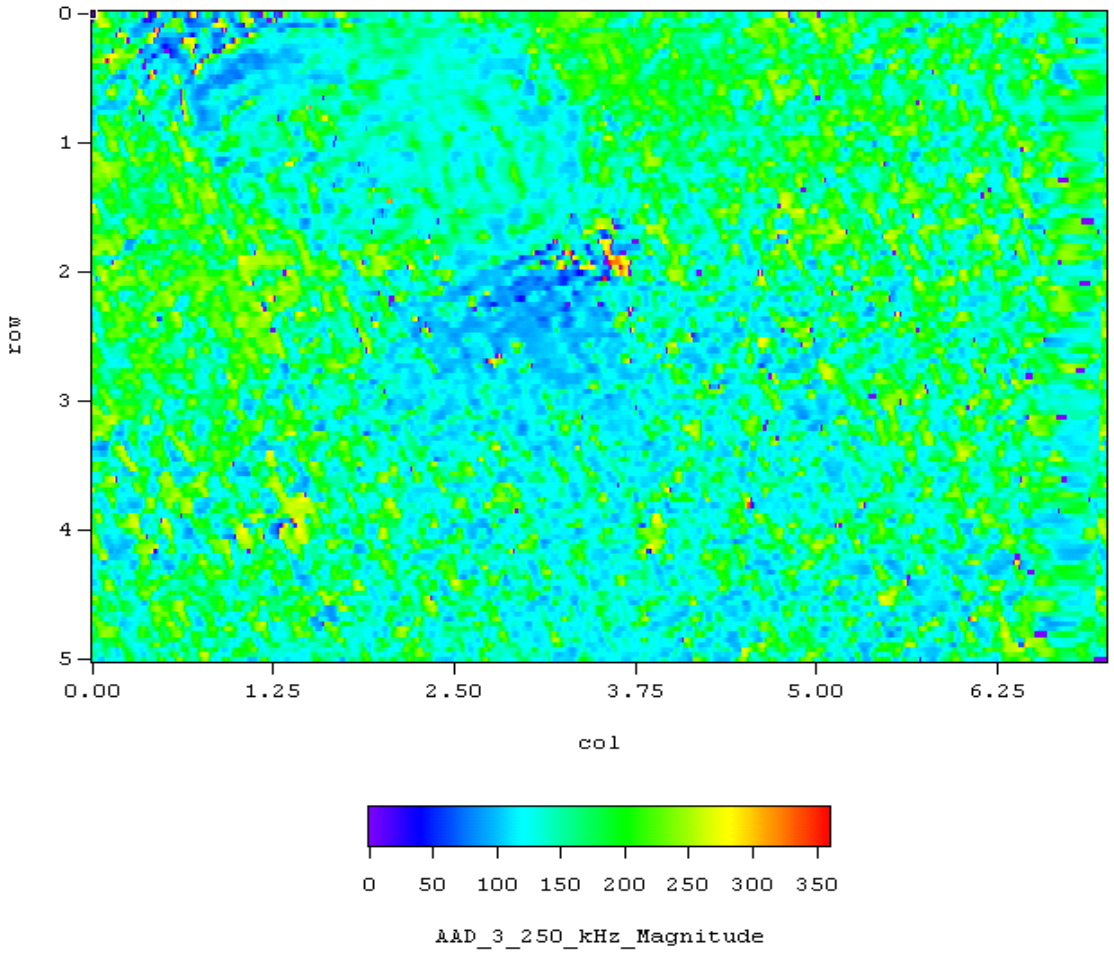

Figure C.23 Phase Response Plot of Southwest Research Institute Specimen AAD-3

Appendix D

Line Plots from Eddy Current Data

Appendix D

Line Plots from Eddy Current Data

All plots in Appendix D have horizontal axes that are in units of inches (2.54 mm).

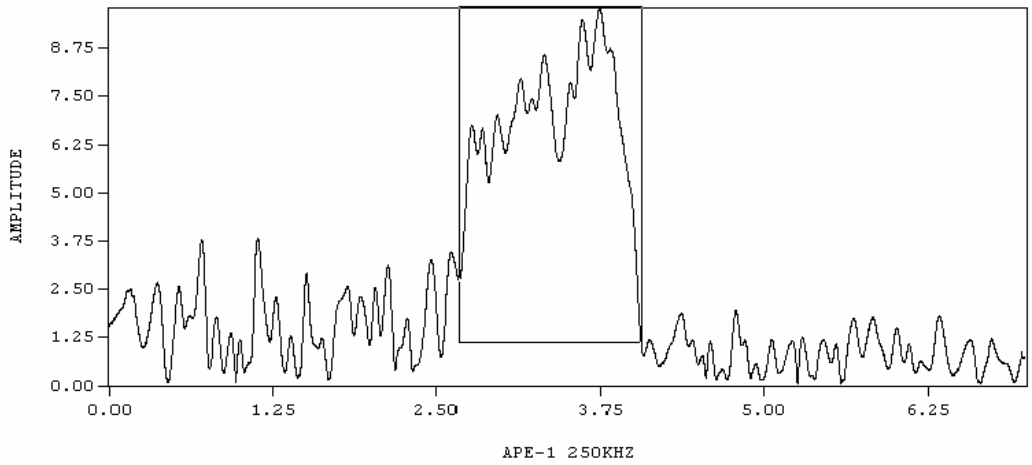

Figure D.1 Line Plot Representation of Magnitude for WOG Specimen APE-1

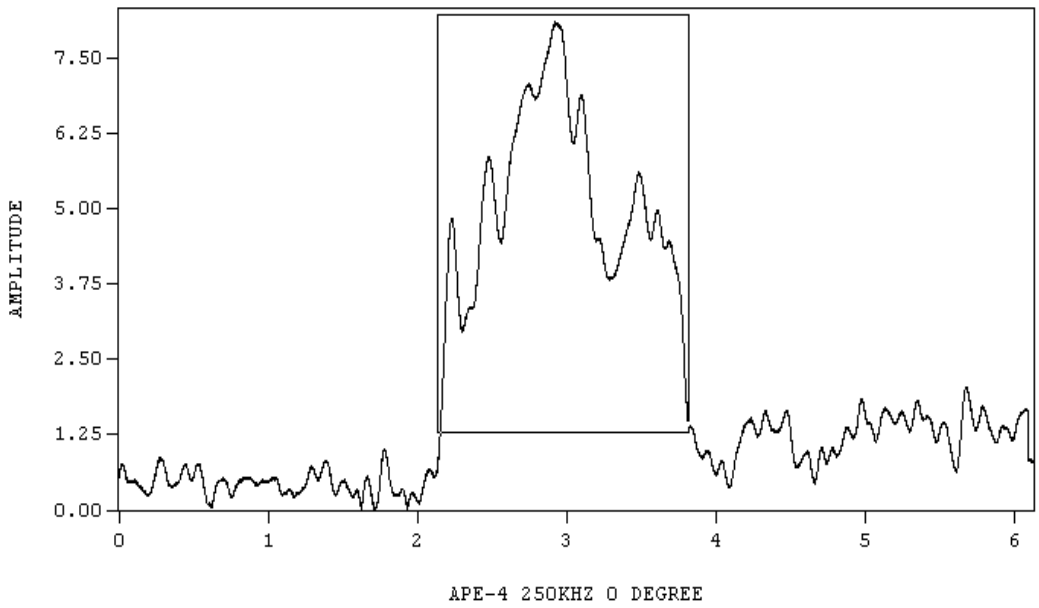

Figure D.2 Line Plot Representation of Magnitude for WOG Specimen APE-4

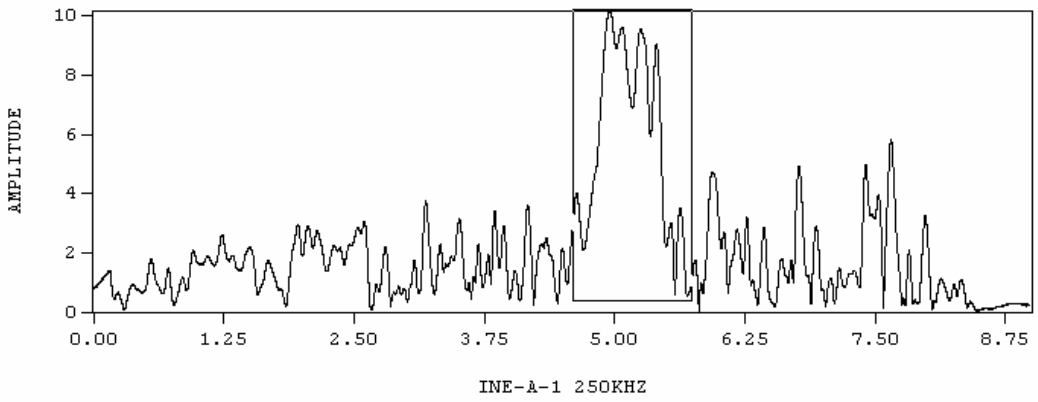

Figure D.3 Line Plot Representation of Magnitude for WOG Specimen INE-A-1

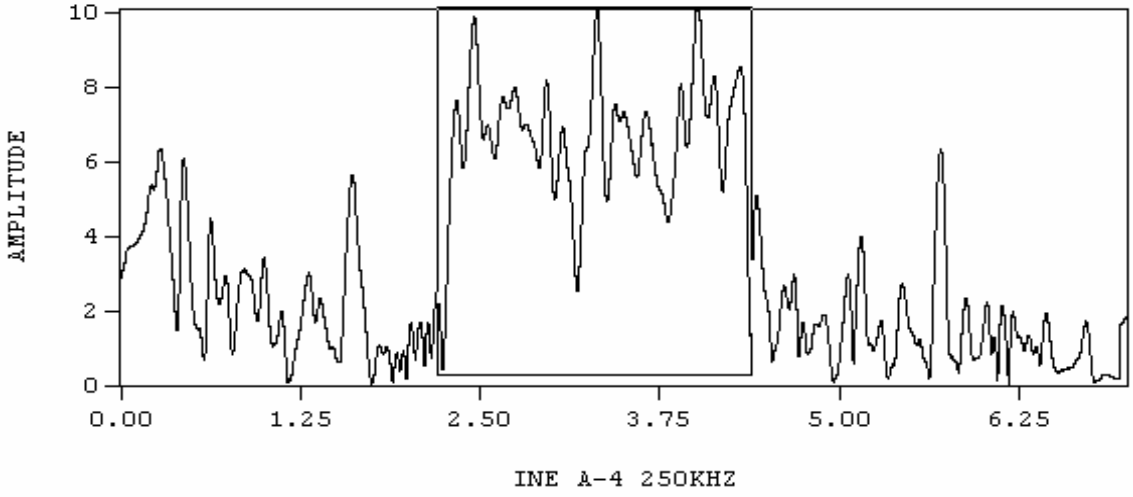

Figure D.4 Line Plot Representation of Magnitude for WOG Specimen INE-A-4

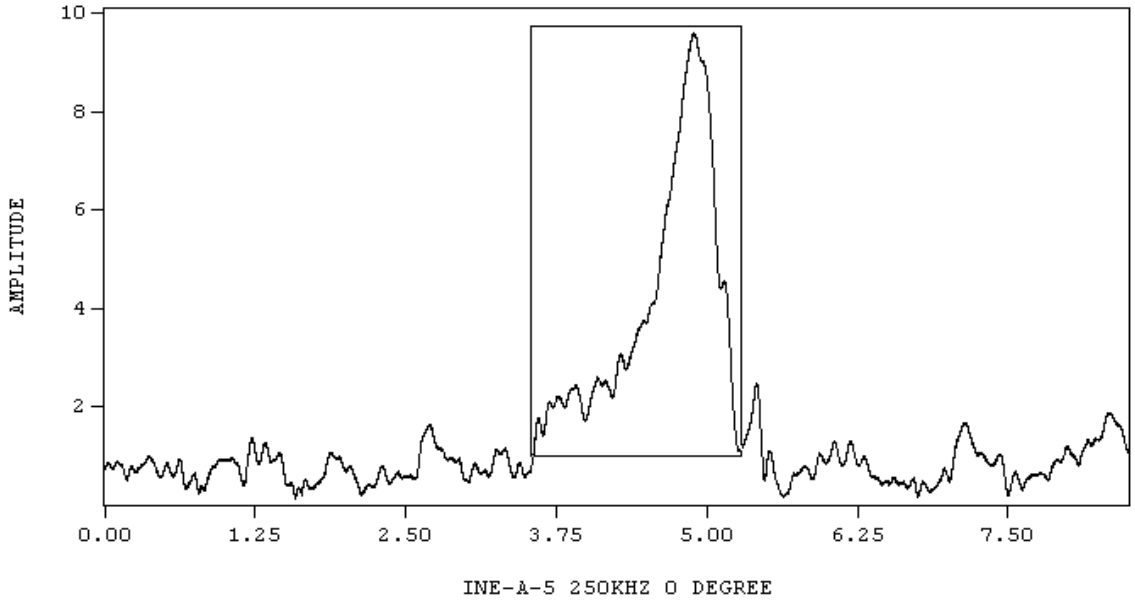

Figure D.5 Line Plot Representation of Magnitude for WOG Specimen INE-A-5

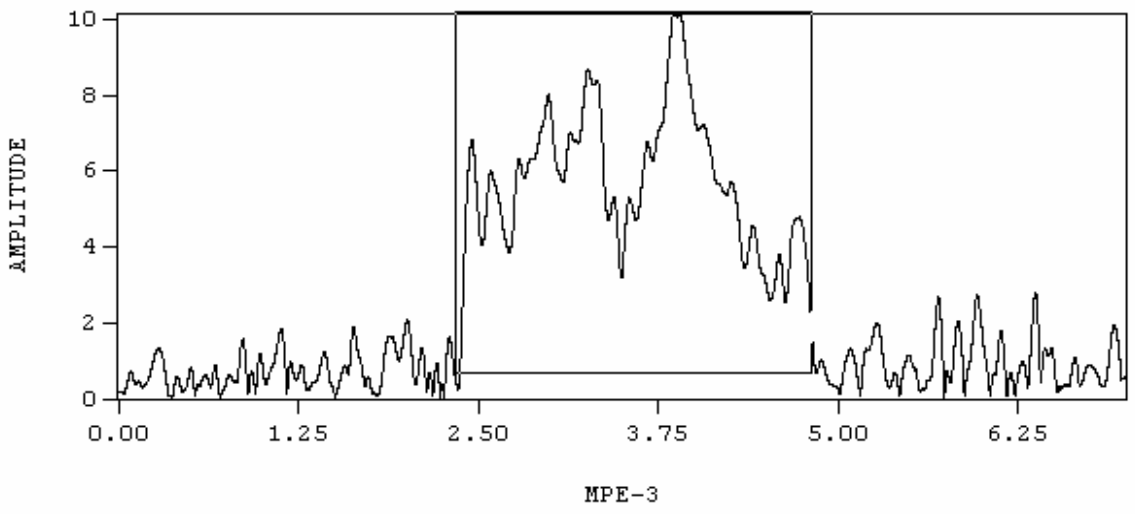

Figure D.6 Line Plot Representation of Magnitude for WOG Specimen MPE-3

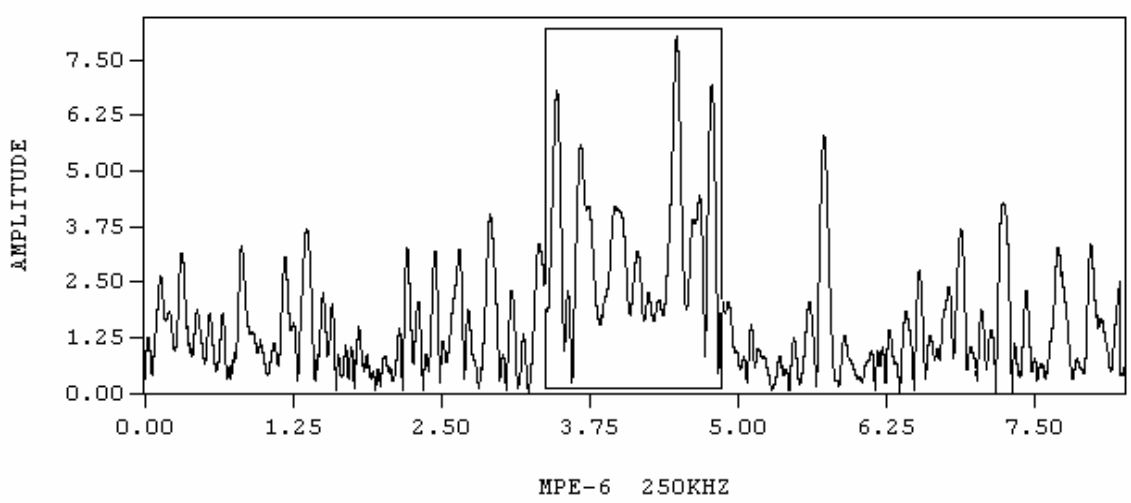

Figure D.7 Line Plot Representation of Magnitude for WOG Specimen MPE-6

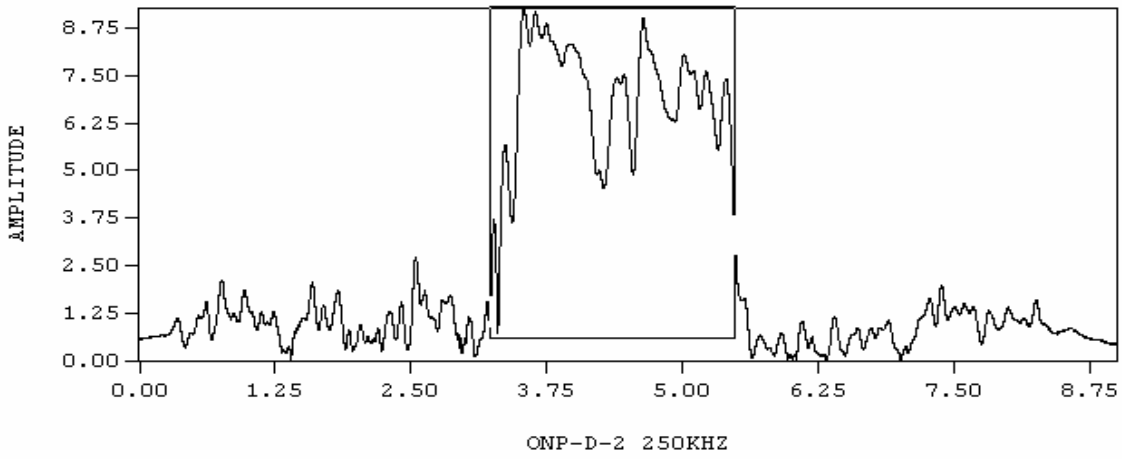

Figure D.8 Line Plot Representation of Magnitude for WOG Specimen ONP-D-2

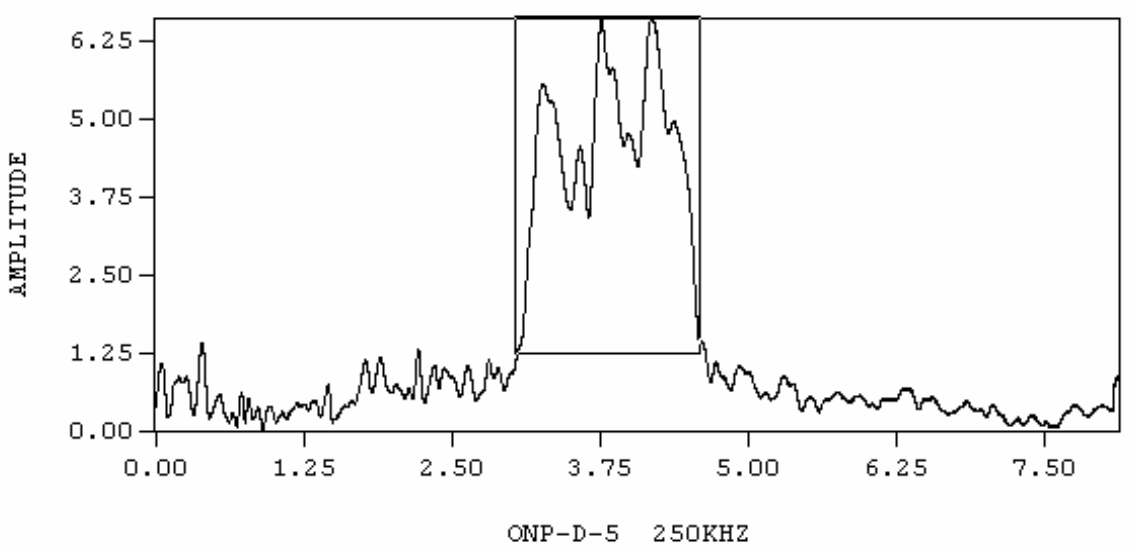

Figure D.9 Line Plot Representation of Magnitude for WOG Specimen ONP-D-5

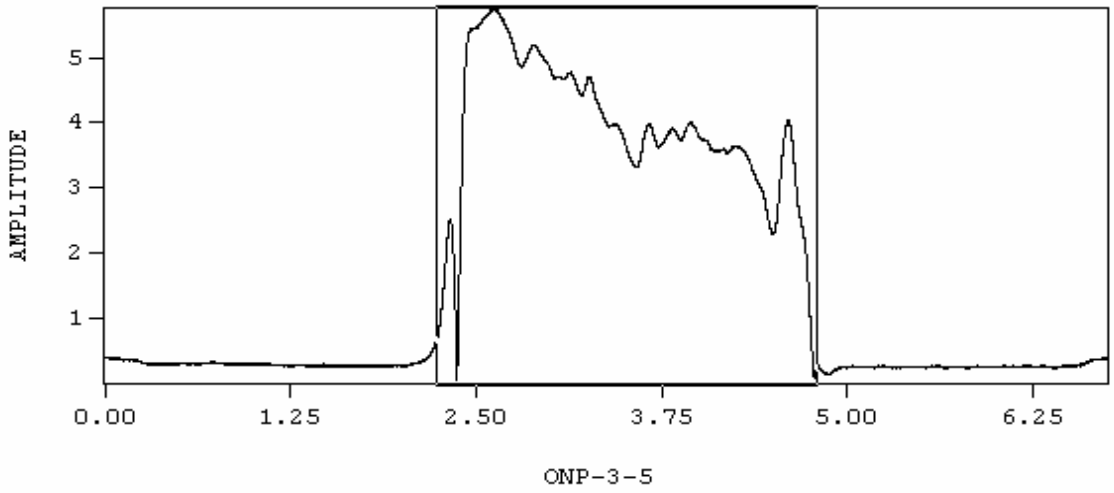

Figure D.10 Line Plot Representation of Magnitude for WOG Specimen ONP-3-5

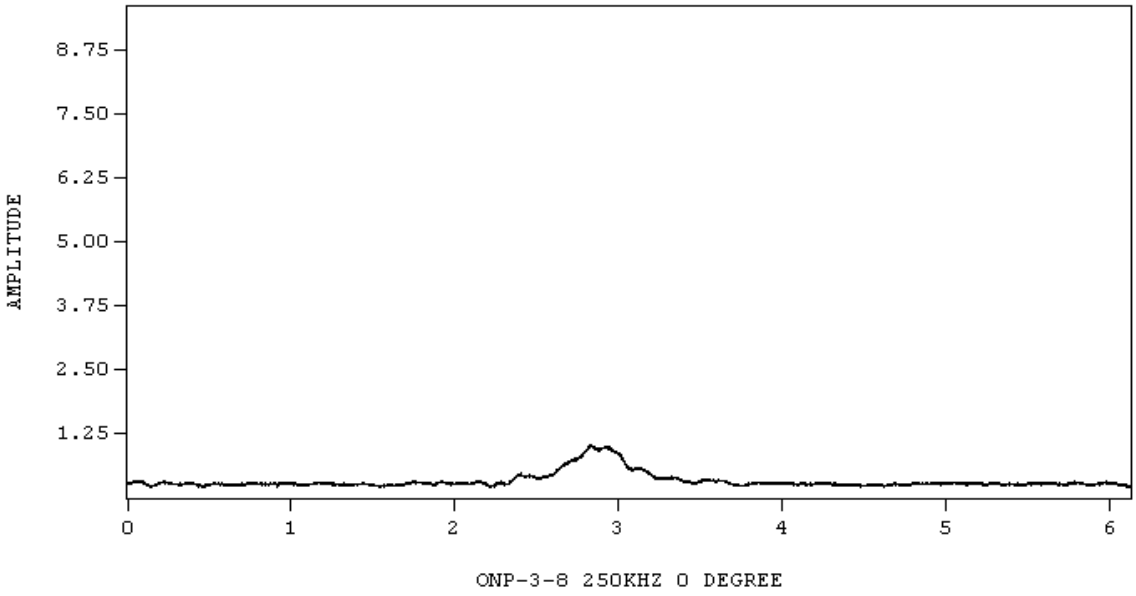

Figure D.11 Line Plot Representation of Magnitude for WOG Specimen ONP-3-8

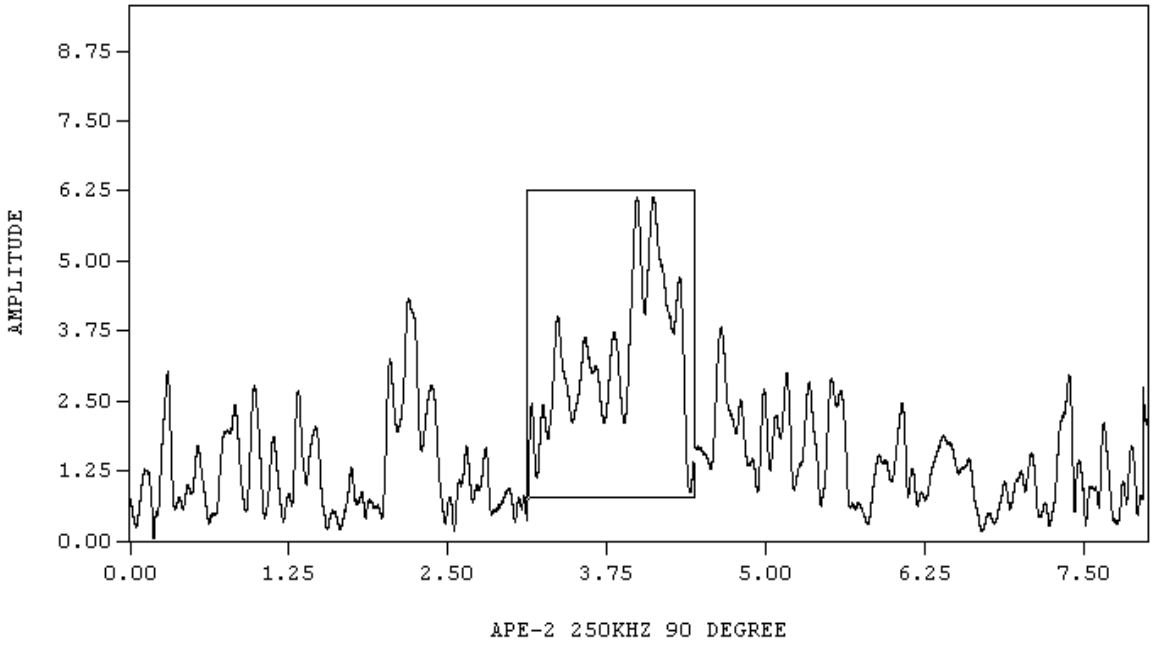

Figure D.12 Line Plot Representation of Magnitude for WOG Specimen OPE-2

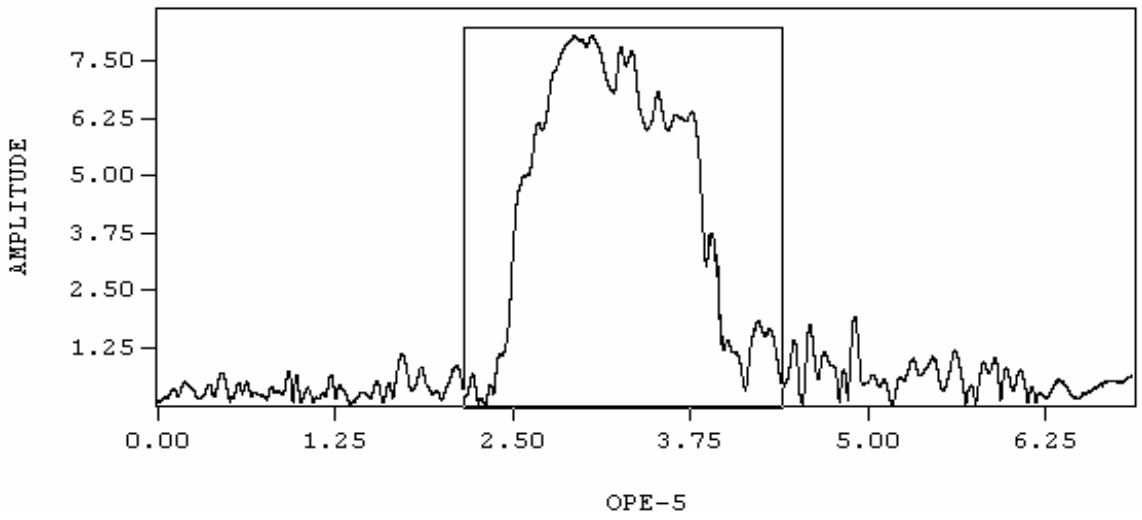

Figure D.13 Line Plot Representation of Magnitude for WOG Specimen OPE-5

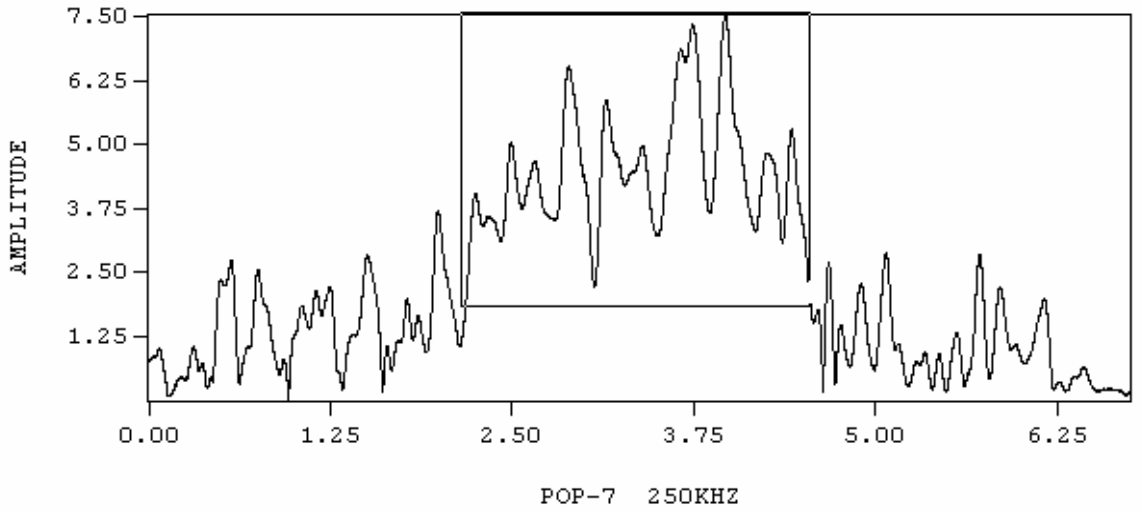

Figure D.14 Line Plot Representation of Magnitude for WOG Specimen POP-7

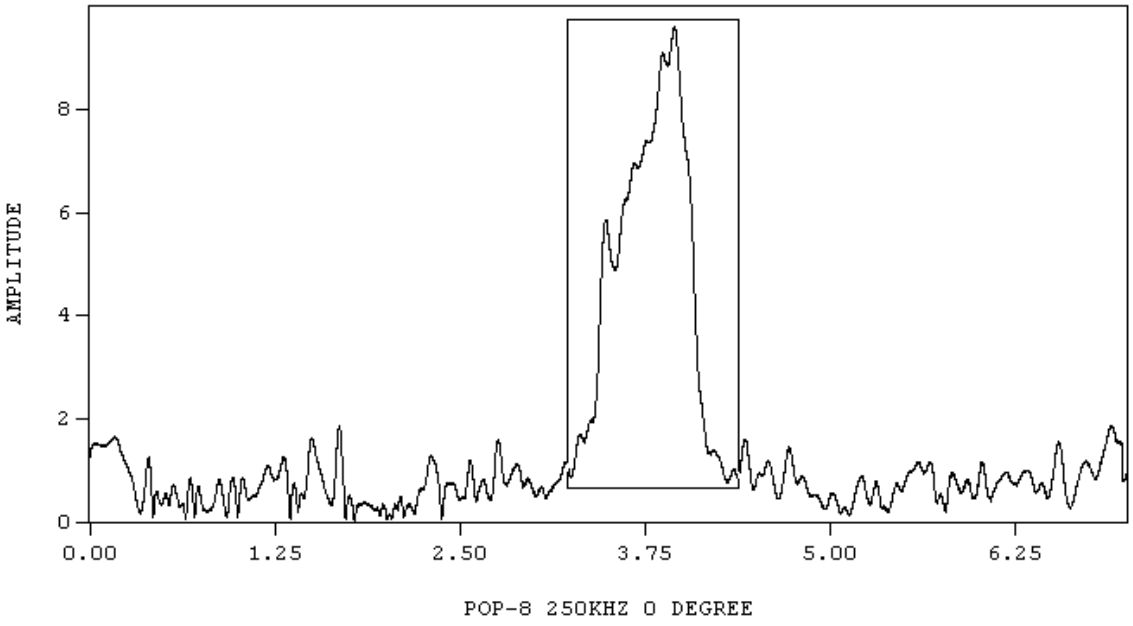

Figure D.15 Line Plot Representation of Magnitude for WOG Specimen POP-8